Obduction Processes of the Taitao Ophiolite (Southern Chile) in the South American Forearc: Implications for Accretion Style of Oceanic Blocks

A Dissertation Submitted to

the Graduate School of Life and Environmental Sciences,

the University of Tsukuba

in Partial Fulfillment of the Requirements

for the Degree of Doctor of Philosophy in Science

(Doctoral Program in Integrative Environmental Sciences)

Eugenio Andrés VELOSO ESPINOSA

Table of contents

Abstract

The repeated subduction of three short spreading centers of the Chile ridge system, due to north and southward migration of the Chile Triple Junction during the last 6 My, took place offshore the Taitao peninsula (46° Lat. S). This resulted in unique stress field conditions applied to the South American forearc in the Taitao area. In the area, the most prominent feature is the presence of the young Taitao ophiolite (<13 Ma), which is believed to be a piece of oceanic lithosphere obducted above the continental plate, and associated granitic rocks. Due to the young age of the ophiolite, the processes of ophiolite obduction (unlike other old ophiolites in the world) can be easily linked to the well known geodynamic environment of the region. This provides an excellent opportunity to study the obduction processes of mid-oceanic ridge onto active continental margins.

Fault-slip data were collected from the plutonic units of the ophiolite, and it was used to determine the different stress fields involved during and after the obduction processes. In addition, oriented rock samples were collected from all the ophiolite rock units (including plutonic units, dike complexes and volcani-clastics). These samples were analyzed by means of rock magnetic methods, including: (1) isolation of remanent magnetic vectors, (2) thermomagnetic experiments and (3) anisotropy of magnetic susceptibility; which aid to determine: (1) folding and rotational events, (2) ferromagnetic phases and (3) paleocurrent and depositional characteristics of clastic sediments in the northern edge of the ophiolite.

Analysis of fault-slip data revealed heterogeneous stress fields acting on the ophiolite through time. The non-orthogonal compressional stress field induced by the subduction of the Nazca-Antarctic plates and the active Chile Ridge resulted in compressional and strike-slip fault zones developed inside and in the eastern margin of the ophiolite respectively. Oldest identified compressional component ("B") generated thrust faults zones in the plutonic units while the strike-slip component ("C") produced a progressive counterclockwise rotation of the ophiolite,

ca. 60°, along the dextral Bahía Barrientos Fault Zone in the eastern margin. As this rotation continued, faults previously generated in the plutonic units (by "B" stress field) were no longer able to absorb the induced compression and as a result new thrust faults were generated in the plutonic units by the still acting compression (younger identified "A" stress field).

Restoration of remanent magnetic vectors (carried by magnetite crystals) for all analyzed units, indicates that the ophiolite experienced two rotations and a folding event before and during the obduction processes. Plutonic units were *ca.* 90° clockwise rotated, before ca. 6 Ma, about an NW-ward inclined rotational axis as the ophiolite was progressively incorporated onto the forearc. Further, the ophiolite entered into an accommodation phase *ca.* 6 Ma ago, in which the plutonic units were counterclockwise rotated, about NE to E-ward inclined axes, and complexly folded. This accommodation resulted in the thinning of the forearc crust and generation of tectonic gaps along the north and east contacts of the ophiolite with the forearc basement. Gaps were filled by volcanic products, erupted through the thinned forearc crust, and by clastic rocks.

Rotation of the ophiolite produced a dextral-normal fault zone in its northern margin, which built up slope instabilities on the inner walls of the Estero Cono. This triggered turbidite currents which flowed towards NW-W following the coastal shape of Estero Cono. As velocity and energy of the flow decreased, transported sediments were left in a NW-W-facing slope.

Newly generated units, erupted and deposited in the tectonic gaps, were also rotated synchronously with the rest of the ophiolite as the later continued the accommodation process. Such units rotated about NE to E-ward inclined rotational axes, recording the later portion of the counterclockwise rotation experienced by the plutonic units of the ophiolite. Calculated rotational amounts and rates suggest that rotation of the ophiolite had constantly slow down for the last *ca.* 6 Ma, reaching probably equilibrium state in the last 1 My.

Keywords: Obduction, Ophiolite, Paleomagnetism, AMS, Inclined rotational axes, Stress field.

Tables Index

Figures Index

Photos Index

Chapter 1: Introduction

The presence of a piece of heavy oceanic lithosphere above light (buoyant) continental lithosphere implies that important geological processes had transport, and emplaced, such piece (or block) into its present location. This emplaced (process known as obduction) piece of oceanic lithosphere is called "*ophiolite*" (e.g. Nicolas, 1995) (Fig. 1.1). Commonly, ophiolites have being interpreted as oceanic lithosphere once created in a normal spreading ridge system or continental rift setting (Nicolas, 1995; Moores, 1982).

An ophiolite sequence is typically consists of: (1) ultramafic rocks (harzburgites or lherzolites) commonly altered to serpentinite, (2) massive and/or layered gabbros, (3) sheeted dikes complexes, (4) pillow lavas and (5) sedimentary cover which may include chert and pelagic sediments (e.g. Nicolas, 1995; Vaughan and Scarrow, 2003). These lithological association has being reported from many ophiolites in the world as well as from diving observations of insitu oceanic lithosphere developed along modern spreading ridge systems (e.g. Hurst et al., 1994; Varga et al., 2004) (Fig. 1.2).

Global reconstructions of ancient and modern plate motions show that most of the known ophiolites in the world are located along ancient or modern active continental margins (Fig. 1.2). However, proposed obduction models are usually controversial (Vaughan and Scarrow, 2003). These include: (1) overthrusting of oceanic lithosphere onto passive-margin or arc rocks, (2) splitting off and overthrusting of the upper section of the subducted slab, or (3) underthrusting of oceanic lithosphere into an accretionary prism that fringes the continental plates (Condie, 1997). All these models require a good knowledge of the geodynamic setting at the time of obduction, which usually arises from the global reconstruction of plate motions. However, reconstructions of plate motions are only possible (with a good precision) between present and Jurassic times (oldest known oceanic floor age) by means of magnetic reversals (Larson, 1991). Pre-Jurassic reconstructions usually involve larger uncertainties.

The presence of the young Taitao ophiolite (<13 Ma) in the south-western margin of the South American plate (Fig. 1.2) provides one of the best examples of accretion of mid-oceanic ridge. Due to the youngest age of the ophiolite (Guivel et al., 1996), relationships between the obduction processes and the tectonic environment in the area, for the last 20 My time (e.g. Cande and Leslie, 1986), are straightforward. The different structures developed inside the ophiolite and surrounding units (such as compositional layering, faulting, folding, foliation, etc) are related to the ophiolite generation at the Chile Ridge (CR) system and/or to the obduction and no to other major tectonic event that affected the Taitao area. This unique setting is not observed in others ophiolites in the world, where later regional tectonic events had obliterated origin and obduction-related structures. Thus, once the different structures of the Taitao ophiolite are characterized and related to either the generation of the ophiolite or to the obduction, they can be related to other ophiolites in the world.

1.1. Study area

The westernmost part of Taitao peninsula is the westernmost edge of the Chilean coast in the southwestern margin of the South American plate. It is located approximately between 46°30' and 47°00' Lat S, and 75°15' and 75°30' Long W; just 40 km SE of the actual location of the Chile Triple Junction (CTJ), where the oceanic Nazca and Antarctic and the continental South American plates meet (Fig. 1.3). The ca. 220 km^2 that represents the study area are divided between the Taitao ophiolite (ca. 180 km^2) and small intrusive bodies (ca. 40 km^2).

The rock units observed in this area are: (1) ultramafic rocks, (2) massive and layered gabbros, (3) basaltic to andesitic dike complexes, (4) thick sequences of pillow lavas, pillow breccias and clastic sediments, and (5) several small hornblende and biotite-bearing tonalites and granodiorites. All these rock units are encased into Los Chonos Metamorphic Complex (LCMC) of Pre-Jurassic age, which corresponds to the basement of the Aysén region.

The Taitao ophiolite, also referred as the "*Bahía Barrientos Ophiolite*" (Guivel et al., 1999; Lagabrielle et al., 2000) (Fig. 1.4), was considered to expose a complete ophiolitic sequence (e.g. Forsythe et al., 1986; Nelson et al., 1993). It was later suggested by Lagabrielle et al. (1994, 2000) and Guivel et al. (1996, 1999) that volcani-clastic deposits located in the east and northern edges of the ophiolite do not belong to it but instead they are genetically linked to the obduction process. The term Taitao ophiolite, in this study, follows that proposed by Nelson et al. (1993), regardless of the different tectonic and magmatic origin of each one of its rock units (Fig. 1.4). Thus, the Taitao ophiolite refers to a NW-ward tilted sequence of ultramafic rocks, massive and layered gabbros, sheeted dike complex and volcani-clastic deposits. These outcrops in the inner part of the westernmost Taitao peninsula (Fig. 1.4, 1.5).

The study area can only be reached by sea or by helicopter, which departure from the closest city in the region, Puerto Aysén, located in the inner part of the Seno Aysén (Fig. 1.3). Sail from Puerto Aysén to Taitao peninsula is done in between the numerous islands of the southern part of the Chonos Archipelago, crossing the Moraleda Channel up to Anna Pink bay. From there, southward until the northern extreme of Golfo de Penas, to further reach the interior of the Taitao peninsula (Bahía Barrientos bay). Once in Bahía Barrientos, outcrops of the different rock units can be reached by foot or by zodiac boats.

1.2. Objectives

Although several studies had been carried out on the Taitao ophiolite and surrounding intrusive bodies, important structural questions remain unclear. Structural characteristics of the different rock units of the ophiolite had been not established yet, like:

- The different units of the ophiolite are systematically NW-ward inclined, and the whole ophiolite section has been exposed in a northward sequence;
- Most of the internal contacts between each one of the different sections of the ophiolite are

not primary; instead they are strike-slip and/or thrust faults;

- Dike complexes at Estero Cono and Caleta Mitford-Rees (Fig. 1.5) have almost perpendicular trending orientations with respect to each other; and their orientations do not coincide with the CR spreading system either;
- Depositional settings for clastic sediments located in the northern edge of the ophiolite are not established structurally.

Thus, the aim of this study is to determine the obduction processes experienced by the Taitao ophiolite, its deformational history for the last *ca.* 10 My and the consequences of the obduction into the South American forearc.

For this, several aspects need to be established:

- Recognition and separation between primary (spreading ridge-related) and secondary (obduction-related) structures;
- Original orientation of the different ophiolite units before the obduction;
- Original location of the ophiolite with respect to the CR spreading axis;
- Stress field that affected the ophiolite during the obduction event;
- Mechanism of intrusion and sedimentation of the volcani-clastic deposits located in the east and northern edges of the ophiolite.

1.3. Used approaches

To achieve these objectives three different and independent approaches were used: (1) determination of heterogeneous stress field, (2) isolation of remanent magnetic (RM) vectors (paleomagnetism), and (3) anisotropy of magnetic susceptibility fabrics.

Strike-slip and dip-slip brittle faults structures observed in the plutonic units of the ophiolite (formally ultramafic and gabbro units) and in its eastern edge were used to calculate the heterogeneous stress field that activated them. Orientation and characteristics of the stress field

were determined by means of the "*multi-inverse*" method, proposed by Yamaji (2000, 2003).

Isolation of RM vectors is probably one the most powerful tools to determine the tectonic evolution of tectonically affected terrains. It has been widely used to provide qualitative data about the tectonic evolution of continent and oceanic plates as well as independent block terrains (Butler, 1982; Tauxe, 1998). This technique was used to determine the different tectonics rotations experienced by the different blocks of the Taitao ophiolite since its generation in the oceanic spreading ridge (ca. 13 Ma) until its present configuration.

Anisotropy of Magnetic Susceptibility (AMS) has probe to be a useful tool to determine orientation of mineral fabric (Tarling and Hrouda, 1993) based on the close dependence of sedimentary AMS fabric orientation and depositional current and slope settings (Rees, 1965; Rees et al. 1968; Ellwood and Ledbetter, 1977, 1979; Ellwood et al., 1979; Taira and Lienert, 1979; Ellwood, 1980; Ledbetter and Ellwood, 1980; Schieber and Ellwood, 1993; Piper et al. 1996; Abdeldayem, 1999; Liu et al., 2001). This technique was used to determine paleocurrent flow and depositional settings of the clastic sediments located in the northernmost edge of the ophiolite. Despite if clastic sediments belong or not to the ophiolite (Nelson et al., 1993; Lagabrielle et al., 1994; Guivel et al., 1996, 1999), a better characterization of the transport and sedimentation mechanisms of the clastic sediments is necessary in order to qualitatively determine the post-obduction processes that affected the Taitao ophiolite and the surrounding forearc area for the last *ca.* 3 My time.

In this study, new stress field determinations, paleomagnetic data and AMS fabrics from the different rock units of the Taitao ophiolite are discussed, justified and interpreted to obtain a reliable model for the driving forces responsible for the obduction and deformation of the ophiolite, and the tectonic processes that affected the ophiolite before, during and after its obduction onto the South American forearc.

1.4. Previous studies

The first reference to the rocks located in the westernmost part of the Taitao peninsula was an isolated K/Ar age obtained for the Cabo Raper pluton (Fig. 1.5) by Munizaga (1970). The presence of an ophiolitic body in the westernmost part of the Taitao peninsula was first reported by Forsythe et al. (1985), who lithologically described the different rock units in addition to fossils recovered from volcani-clastic sediments. Thus, the Taitao ophiolite was defined as a pseudostratified succession of ultramafic rocks, gabbros, dike complexes and volcani-clastic deposits (located both north and east of the previous units) (Fig. 1.5).

The first geochronological data for the rocks in the area (including the ophiolitic and granitic bodies) was reported by Mpodozis et al. (1985) using K/Ar method. Using this available data, Hervé et al. (1985) linked these geochronological constraints with the several collisions of the CR system in the area.

Cande and Leslie (1986) suggested the migration of the CR system, for the last 18 Ma, by analyses of the sea-floor magnetic anomalies on both the Nazca and Antarctic plates. They determine the basic geodynamic framework for the Taitao area, in which several segment of the CR system collided with the South American plate. Forsythe et al. (1986) used this geodynamic framework to relate the emplacement of the calcalkaline granitic bodies in the Taitao peninsula with the collision events of the CR system and the migration of the CTJ.

Geochemical studies of the rock units of the Taitao peninsula started in the 1990s. Keading et al. (1990) determine the possible magmatic sources of the calcalkaline plutons that surround the ophiolite. Later, Allen et al. (1991) established some geochemical characteristics of the dikes in the ophiolitic body based on the abundances of rare earth elements.

The Taitao ridge, located offshore of the Taitao peninsula and being perhaps the submarine continuation of the ophiolite (Kurnosov et al., 1995), and adjacent areas were drilled in 1992 by the "Ocean Drilling Project" (ODP) during Leg 141 at sites 859 to 863 (Fig. 3.1). In this series of

studies bathymetry, magnetometry and gravimetry (for the area centered on the CTJ) were determined (e.g. Forsythe and Prior, 1992; Bangs et al., 1992).

Perhaps one of the most complete reports about the rocks of the Taitao ophiolite is the one of Nelson et al. (1993). Here, detailed lithological and petrological characteristics of each rock unit were reported and, for the first time, two opposite models were proposed for the development of the Taitao ophiolite; generation in a short-lived extensional marginal basin in the forearc or obduction of a piece of oceanic crust.

Bourgois et al. (1993) pointed out that volcani-clastic deposits of the ophiolite, located north and east of the rest rock units (Fig. 1.5), are not part of the ophiolitic sequence; instead, these deposits are genetically linked to the ophiolite. Two new units were defined based on geochemical differences between the ophiolite and those volcani-clastic units, and spatial relations with other rock units in the area. These are: (1) the Main Volcanic Unit (MVU), compromising volcani-clastic deposits in the northern margin of the ophiolite (Fig. 1.5); and (2) the Chile Margin Unit (CMU), including pillow lavas, pillow breccias and some sedimentary deposits that outcrops the eastern margin of the ophiolite (Bahía Barrientos area; Fig. 1.5). Geochemical analysis of these volcani-clastic deposits lead Lagabrielle et al. (1994) and Guivel et al. (1996) to establish the different magmatic sources of these, which correspond to normal and enriched MORB (Mid-Oceanic Ridge Basalt). Thus, Lagabrielle et al. (1994) and Guivel et al. (1996) re-defined the ophiolitic sequence and the term "*Bahía Barrientos Ophiolite*" was defined (Fig. 1.4).

Numerous studies on petrology, paleomagnetism, sedimentology, etc were carried out during ODP Leg 141 and summarized by Lewis et al. (1995). Later, Bourgois et al. (1996) used a geochemical model for the emplacement of the Cabo Raper pluton (Fig. 1.5), which was used to establish the rate of tectonic erosion that had affected the southwestern coast of the South American plate. Later on, seismic anisotropies of the region beneath the CTJ area were determined by Murdie and Russo (1999), using a net of seismometers installed in the Taitao

region. Such anisotropies were interpreted in order to establish a possible location for the subducted CR spreading axis beneath the Taitao area.

The thermal effects induced in the forearc region produced by the subduction of an active spreading ridge, like the CR system, were discussed by Lagabrielle et al. (2000) by using geochemical constraints between the different volcanic and intrusive products in the Taitao area. They argue that the geothermal gradient in the area was highly increased by the subduction of the active CR system. As a product, melting of the underplated portions of the young oceanic lithosphere occurred and calcalkaline magmas with MORB-type affinities were generated.

Almost 20 years had passed since the presence of an ophiolitic body was first reported in the westernmost part of the Taitao peninsula. However, important questions seem not be answered yet: Which are the processes that the Taitao ophiolite experienced during its obduction into the South American forearc? Which was the orientation of the primary structures of the ophiolite with respect to CR spreading ridge system? Where was the original locale of the ophiolite with respect to the spreading ridge axis? Which was the mode of emplacement of the ophiolite onto the forearc region? When, and how, were developed the secondary structures of the ophiolite (such as folds and brittle faults)? What are the consequences of the ophiolite obduction in the forearc region? among many others.

1.5. Previous models proposed for the Taitao ophiolite

Many studies have been carried on the Taitao ophiolite but the obduction processes are still not fully constrained with the present available data; instead many had focused on understanding the possible causes that generated the ophiolite (e.g. Nelson et al., 1993; Forsythe and Nelson, 1985; Guivel et al., 1996, 1999; Lagabrielle et al., 1994) by means of petrological, geochemical and geochronological studies.

The first proposed model for the generation of the Taitao ophiolite corresponds to Nelson et al.

(1993). According to the available data at the time Nelson et al. (1993) proposed two opposite models for the generation of the ophiolite: (1) in an oceanic spreading center or (2) in a short-lived rifting system of the forearc environment. The key for both models were the interpretation of the shallow to medium-depth depositional and extrusive characteristics of the volcano-clastic deposits at the Estero Cono area (Fig. 1.5). In the first model, volcani-clastic deposits do not belong to the ophiolite and they had been erupted through fisural volcanism product of the CR subduction beneath the South American forearc. In the second model, volcani-clastic deposits belong to the ophiolite in which the whole ophiolitic sequence was generated in a small rifting inside the forearc.

Guivel et al. (1996, 1999) established that volcano-clastic deposits at Estero Cono do not belong to the Taitao ophiolite, but they are genetically linked to its obduction. Thus, the second model of Nelson et al. (1993) was overruled. In addition, Guivel et al. (1996, 1999) and Lagabrielle et al. (1994) also proved, based on geochemical similarities between the ophiolite and several samples recovered from the CR, that the ophiolite was originally generated in an oceanic spreading ridge environment, statement also proved by some other authors (e.g. Forsythe et al., 1995; Kurnosov et al., 1995). If the creation of the Taitao ophiolite occurred in an oceanic spreading center, then the actual location of the CR system implies that the ophiolite package was obducted over the forearc.

Chapter 2: The oceanic lithosphere and its evolution through time

The oceanic lithosphere is a dynamic system which evolves through time, beginning with its creation in the so-called spreading centers or spreading ridges (Fig. 2.1c) where new oceanic lithosphere is created everyday. The new lithosphere consists of a pseudo stratified sequence, comprising, from bottom to top: (1) ultramafic rocks (upper mantle), (2) layered gabbros, (3) dike complexes and (4) massive lava flows (Fig. 1.1). As the new lithosphere is created, it pushes the old one away from the spreading center, creating a large sheet-like surface called oceanic plate. However, oceanic plates are not a smooth surface, containing irregularities such as valleys and mountains chains. Sediments are then progressively deposited on top of the plate as it moves away from the spreading center.

The oceanic lithosphere reaches, eventually, its edge to the boundary with another plate (continental or oceanic) (Fig. 2.1b). If the oceanic plate meets with a continental plate, it sinks down beneath the continental plate because of the gravity force acting on the heavier oceanic plate; process is known as "*subduction*". During this process the oceanic plate is decomposed progressively on the way back to the mantle.

Sometimes, a piece or section of the oceanic lithosphere refuses to sink beneath the continental plate and instead it goes up (becoming attached to the continental plate margin) (Fig. 2.1c). This process is known as "*obduction*" (Fig. 2.1a), which can be a very complex process. Suggested obduction models include slices attached progressively to the continent (e.g. van den Beukel, 1990; Kerr et al., 1998), or sheet-like thrusts of the whole section of oceanic crust and mantle (e.g. Thomas et al., 1988), or different blocks accreted to the continental margin, or a mixing between these processes.

2.1. Oceanic ridges, the birth of the oceanic floor

Fracturing of the oceanic lithosphere causes a wedge-like upwelling of hot partially molten asthenosphere. Basaltic liquid extracted from this wedge fills the fissures in the crust, creating a swarm of dikes. This episodic activity progressively weakens the oceanic crust and allows it to respond by brittle tectonic stretching (expansion) (Nicolas, 1995). The stretching is mainly controlled by normal faulting at the spreading ridge axis, as some submarine profiles on the oceanic floor had shown (e.g. Nicolas, 1995).

Basically two types of oceanic ridges exist, depending on their spreading rates (namely fast and slow spreading ridges). The expansion rate depends on the amount of basaltic material extracted from the melting of the upper mantle (Fig. 2.2). Fast spreading ridges (like the Chile and East Pacific ridges in the Pacific Ocean) have spreading rates over 2 cm/yr and as much as 15 *cm/yr* (e.g. Nicolas, 1995). The amount of extracted basalt from the molten mantle is *ca.* 20%, which creates a normal oceanic crust with a thickness of about 5-6 *km*, and a upper mantle section of about 2-3 *Km* (e.g. Nicolas, 1995). Studies of ophiolites have proposed that this type of oceanic lithosphere is composed of a thick section of ultramafic peridotites of harzburgitic composition (also called "fertile" peridotites), gabbros, dike complexes and massive lava flows on top (Nicolas, 1995). Until recently this theory was not proven from natural and/or modern examples. However, a similar series of rocks are found to be exposed at Hess Deep in the East Pacific Ridge (e.g. Hurst et al., 1994; Varga et al., 2004). The spreading results in normal faulting and tilting of blocks along the ridge axis, which are rapidly filled by new effusive material derived from the spreading ridge (e.g. Hurst et al., 1994; Varga et al., 2004).

In contrast to fast spreading ridges, slow spreading ridges have spreading rates below 2 *cm/yr* down to 0.5 *cm/yr* (like the Mid Atlantic ridge). The amount of extracted basalts is about 10%, which creates a thin (ca. 3 *Km*) and "*abnormal*" oceanic crust and a thick upper mantle section of about 10 *km* (Nicolas, 1995). The upper section of the lithosphere generated at these spreading

ridges is similar to that generated at fast spreading ridges (gabbros and dike complex). The exception is the upper mantle section, which is composed of peridotites of the lherzolites composition instead of harzburgites. The spreading resulted in normal faulting (Hurst et al., 1994; Nicolas, 1995) and stretching of the lithosphere.

Oceanic ridges are not isolated features in the oceanic plate; they form large chains. A ridge system is composed of several segments (or isolated spreading ridges) bounded by fracture zones. These fractures zones displace and truncate each segment of the spreading ridge system, and they show different movement depending on the configuration segments, having a dual strike-slip fault-like movement (Fig. 2.3).

2.2. Oceanic plateaus and volcanic seamounts

Oceanic plateaus and volcanic seamounts are the most representative bathymetric features in the oceanic plate besides spreading ridges. Oceanic plateaus correspond to large flat surfaces which are elevated respect to the surrounding seafloor, supposed to be derived from a plume originated in the lower mantle (e.g. Campbell and Griffiths, 1992; Mahoney et al., 1993; Coffin and Eldholm, 1994; Kerr et al., 1998) (Fig. 2.4). Oceanic plateaus cover large areas of the ocean basins and they are characterized by a crustal thickness of about 10 *km*, well in excess of the normal oceanic crust produced at an oceanic ridge which is about 5 *km* (Kerr et al., 1998). Their composition and structures depend on several factors such as the volume of material releases by the plume, whether the plume head ascended beneath or if is off-axis of a spreading ridge, or whether there is a significant lateral flow of the plume head to exploit thin sections of the oceanic crust (Sleep, 1997; Kerr et al., 1998).

Volcanic seamounts, mountains in the sea-floor, are prominent but small compared with oceanic plateaus. They sometimes form large mountain chains as in the Hawaiian Islands. They are usually generated by hotspots activity originated in deep mantle (Fig. 2.4). However, they

can also be generated by interactions between plumes, hotspots and oceanic ridges (Bryan and Cherkis; 1995; Vogt, 1971; Morgan, 1978).

These two bathymetric features are usually hotter, due to advective heat from the deep mantle, than the surrounding seafloor. Consequently they are more buoyant than the surrounding cold oceanic lithosphere.

2.3. Subduction, the death of the oceanic floor

By the time when the moving oceanic lithosphere meets with a continental plate, usually far away from the spreading center, it has lost almost all its heat and it has become heavier. As the oceanic lithosphere sinks beneath continental plate due to its weight, hydrous minerals that compose the oceanic crust are progressively dehydrated by the heat from the lithospheric mantle/asthenosphere. Released fluids are trapped in the bottom of the continental plate where they fuse by lowering the melting temperature. Magmas are created at this stage, which start to ascend to the surface through the continental plate. The surface manifestations of this process are volcanoes on top of the continental plate and plutonic bodies which corresponds to failed volcanoes.

2.4. Accretion, the growth of the continent

If the oceanic lithosphere is young, hot and thin, it is somewhat more difficult to be subducted (Molnar and Atwater, 1978; LePichon and Blanchet, 1978; Nicolas and LePichon, 1980). Therefore, mid-oceanic ridges, oceanic plateaus and seamounts which were still hot when they reached to the subduction zone, tend to be obducted becoming amalgamated at the continental margin and contributing to the continental growth.

Chapter 3: Geodynamic and Geological Framework

3.1. Geodynamic Framework

3.1.1. The evolution of the Chile Ridge

Offshore Taitao peninsula, two oceanic plates (Nazca plate in the north and Antarctic plate in the south) subduct beneath the South American plate along the Chile-Peru trench (Fig. 3.1). These two plates are separated by oceanic spreading centers of the Chile Ridge (CR) system. Global plate tectonics reconstructions showed that the subduction convergence vector of the Nazca plate has been constant towards N85°-90°E with nearly a constant velocity of 8.5 cm/yr with respect to the South American plate for the last 20 My time. In contrast, the Antarctic plate has maintained its eastward convergence velocity of 2 cm/yr the last 10 My time (Cande et al., 1982; Cande and Leslie, 1986) (Fig. 3.1).

The CR system consists of a series of axial rift valleys that mark the position of spreading centers (with depths down to 3000 *m* below sea level) and small but prominent volcano-like bathymetric highs inside the valleys (about 1000 *m* higher than the surrounding seafloor). Each spreading center segment is demarcated by fracture zones oriented nearly N80°-70° (Behrmann et al, 1992) (Fig. 3.2) which are represented by bathymetric "jumps" of about 300 to 500 *m* which truncate and displace the ridge valleys (e.g. Behrmann et al., 1992).

Through time, the CR has migrated eastward and collided (the term collision is used herein for the beginning of the subduction of a ridge segment) several times with the western margin of the South America for the last 18 My time (Cande and Leslie, 1986) (Fig. 3.3). These collisions induced unusual and unique conditions into the forearc region, producing: (1) the obduction of a piece of oceanic lithosphere (the Taitao ophiolite, and perhaps the Taitao ridge), (2) intrusion of several small granodioritic bodies, and (3) generation and deposition of several volcani-clastic

products (e.g. Forsythe and Nelson, 1985; Mpodozis et al. 1985; Keading et al., 1990; Nelson et al, 1993; Bourgois et al., 1993, 1996; Lagabrielle et al., 1994, 2000; Kurnosov et al.,1995; Guivel et al., 1996, 1999; Veloso, 2001) in the Taitao peninsula.

3.1.2. The migration of the Chile Triple junction

The locality where a spreading center (or a fracture zone) subducts beneath the Chile-Peru trench defines the locale of the Chile Triple junction (CTJ). This junction is currently located about 40 *km* northwest of the Taitao peninsula (Fig. 3.1). Due to the orientation of the CR system (N10°W) with respect to the Chile-Peru trench (NS), the Chile Triple junction migrates fast northward when a spreading ridge is subducted but migrates slightly (and slowly) southward when a fracture zone is subducted (Fig. 3.4) (Cande and Leslie, 1986; Forsythe and Prior, 1992; Lagabrielle et al., 2000).

The CR system started to subduct beneath the South American plate when a *ca.* 700 *km* long segment south of the Esmeralda Fracture Zone (F.Z.) (Cande and Leslie, 1986) (Fig. 3.3), collided with the South American plate around 14-10 Ma ago in front of the coast of the Madre de Dios archipelago. Then, the CTJ had a TRT (trench-ridge-trench) configuration (e.g. McKenzie and Morgan, 1969). As the 700 *Km* long segment of the CR was subducted, the position of the CTJ migrated fast northward until it reaches south of the Golfo de Penas area (Fig. 3.1, 3.3), spending about 8-4 My to completely subducted.

Between the Esmeralda F.Z. (in the south) and the Darwin F.Z. (in the north) the CR was composed of three short segments; each *ca.* 100 *km* long. Just after the 700 *km* long segment subducted, the CTJ changed its configuration to a TFT (trench-fracture zone-trench; e.g. McKenzie and Morgan, 1969) configuration as the Esmeralda F.Z. started to subduct under the South American plate. As this F.Z. subducted, the CTJ migrated slightly southward west of the Golfo de Penas area (Fig. 3.3, 3.5) until the segment between Esmeralda and Tres Montes F.Z.

(hereafter called segment 1) collided with the trench. The segment 1 of the CR collided with the South American plate *ca.* 6 Ma ago (Cande and Leslie, 1986).

As this later segment was quickly subducted in front of the coast of the Taitao-Tres Montes peninsulas in about 3 My time (Fig. 3.5), the Tres Montes F.Z. started to subduct. Thus, the CTJ changed to a TFT-type configuration and as a result the position of the CTJ migrated slightly southward. However, it remained in front of the coast of the Tres Montes-Taitao peninsulas.

About 3 Ma ago the segment 2 (between Tres Montes and Taitao F.Z.) collided with the western margin of the South American plate. The CTJ changed again its configuration to TRT-type and started to migrate fast northward until this segment was completely subducted in 2.5-2.7 My time (e.g. Cande and Leslie, 1986). About 0.3 Ma ago the CTJ changed, again, to a TFT configuration as the Taitao F.Z. was subducted beneath the South American plate. The TFT-type CTJ migrated slightly southward maintaining its position in front of the Tres Montes-Taitao peninsulas area.

North of the Taitao F.Z., the next segment of the CR collided offshore the Taitao peninsula area *ca.* 0.3 Ma ago. As this segment collided with the South American plate the CTJ changed to a TRT-type configuration and it started to migrate fast northward. Today, this segment is subducting beneath the South American plate and the CTJ (Cande and Leslie, 1986).

3.2. The Geology of the Aysén Region

The geology of the coastal area of the Aysén region (southern Chile) consist of four main units: (1) a pre-Jurassic metamorphic complex, (2) large igneous intrusive complex of Cretaceous-Miocene ages, (3) thick deposits of volcani-sedimentary rocks of Miocene ages, and (4) the Taitao suite (Fig. 3.1).

Los Chonos Metamorphic complex (LCMC) is the pre-Jurassic (Davidson et al., 1987; Hervé et al., 1988; Pankhurst et al., 1999) metamorphic basement of the coastal area of the Aysén

region (Fig. 3.1). It extends as an NS-ward elongated belt, composed of two sub-areas with different lithologies and structures. The eastern sub-area consists of metasediments of turbidite origin with metachert and interbedded greenstones, which retain sedimentary structures and presents a sub-green schist metamorphism (Hervé et al., 1994). The western sub-area consists of psammitic-pelitic schist, green schist and metachert, which have lost all sedimentary structures due to the metamorphism, which ranges between green-schist up to, locally, amphibolite facies (Hervé et al., 2000). The whole LCMC has been interpreted as an accretionary complex developed since Jurassic times along the southwestern border of the South American plate (Hervé et al., 1984).

Igneous rocks, extending for more than 1000 *km* subparallel to and behind the LCMC, conforms the so-called Patagonian Batholith (Hervé et al., 2000). This batholith can be divided into two main segments north and south of the Golfo de Penas area (Fig. 3.1). The north segment (North Patagonian Batholith) has a NNE-SSW-trend, while the southern segment (South Patagonian Batholith) has a NNW-SSE-trend (Hervé et al, 2000). Both are mainly composed of biotite-hornblende-bearing granodiorites and tonalites (Pankhurst et al., 1999). The whole batholith has been interpreted as the product of subduction induced magmatism, with outer (or marginal) bodies developed in a mature crust while inner (or central) bodies developed by the fusion of mafic rocks after sub-crust volcanism (Pankhurst et al., 1999). The Patagonian Batholith intruded the LCMC and the Traiguén formation (see further) in late Cretaceous in the outer area and in Eocene-Pliocene in the central part (Hervé et al., 2000).

The Traiguén formation consists of a thick sequence of volcani-clastic rocks including abundant pillow lavas, volcanic breccias, graywackes, siltstones and turbiditic deposits. The formation outcrops in the Moraleda Channel (Fig. 3.1) (Hervé et al., 2000). A low-grade metamorphism similar to that sea-floor affected these rocks, in addition to folding about NS-trending axes (before 20 Ma; Hervé et al., 2000). This formation, in the Magdalena Island, is intruded by granitic bodies and dikes of *ca.* 20 Ma. Rb/Sr (whole rock) ages suggest that volcani-

clastic products were deposited during 40 and 20 Ma (Hervé et al., 1995). The Traiguén Formation has been interpreted as deposited in a pull-apart basin in the forearc region due to the strike-slip movement of the Liquiñe-Ofqui Fault Zone (Hervé et al., 2000).

The rocks exposed in westernmost part of the Taitao peninsula are the Taitao Ophiolite, and small granitic bodies surrounding the ophiolite (Fig. 1.5, 3.1). These granitic bodies correspond to small hornblende and biotite bearing tonalites and granodiorites, which obliterated the (possible) primary contacts between the ophiolite and the forearc basement (LCMC).

3.3. The Geology of the westernmost Taitao Peninsula

The geology of the westernmost part of the Taitao peninsula can be divided into the Taitao ophiolite – including ultramafic rocks, gabbros, dike complexes and volcani-clastic deposits (Fig. 1.4) – and the intrusive granitic bodies distributed in the southern, northern and eastern margins of the ophiolite (Fig. 1.5).

3.3.1. The Taitao Ophiolite

a. Ultramafic rocks unit

Ultramafic rocks are disrupted into several WNW-ESE-trending elongated bodies (Fig. 1.5, Photo 1a) of about 0.5 to 1.0 *km* long by 0.2 to 0.3 *km* wide dimensions and some lenticular bodies, of about 100 *m* in radius (mega-xenoliths, Photo 1b), included into the gabbro unit. These small bodies are usually intruded by numerous felsic stockworks (e.g. Nelson et al., 1993).

Strong foliation develops in the main body, in the south, in addition to lineation observed in some ultramafic outcrops. Serpentinitization is a common feature in the ultramafic bodies affecting usually more than 90% of these rocks, giving it a yellowish-brown color.

The foliation of the ultramafic bodies developed increasingly in the southern part towards the

contact with Cabo Raper pluton (Fig. 1.5). In the main ultramafic body, foliation seems to be parallel to the contact with both the granitic body to the south and the gabbro unit to the north, having a general NW-strike and dipping towards NE and SW. In the inner portion of the main body, foliation rotates and becomes NS-trending and dipping towards E (e.g. Nelson et al., 1993; Veloso, 2001).

Brittle faults developed inside the ultramafic unit exhibit abundant kinematic indicators, such as slickenlines, moon shaped steps, R and R' secondary fractures (Appendix A). These suggest a main thrusting sense of movement with local strike-slip movements. Two main sets of fault were recognized, one striking NE-ward and other striking EW-ward. Brittle faults cut and displace ductile faults, indicating that brittle deformation took place after the ductile one. EW-trending brittle faults are usually displaced by NE trending brittle faults; however, inverse crosscutting relations (i.e. NE trending faults displaced by EW trending faults) were also observed, suggesting a synchronous activity of these two sets.

Ultramafic rocks present a harzburgitic geochemical affinity (Veloso, 2001); however, some lherzolites and dunites layers are present near the contact with the gabbro section (e.g. Nelson et al., 1993). Also, Nelson et al. (1993) reported the existence of a 3 *cm* thick layer of websterite near the contact with the gabbro section. However, this was not observed during fieldwork campaigns.

Only at the northernmost contact with the gabbro unit evidence for primary contact can be seen, i.e. gabbro dikes that intruded into the ultra-mafic rocks without displacement across the basal contacts. However, the most common contact between these two sections is low angle brittle and ductile faults striking E to NE and dipping towards north and south. These faults are sometimes intruded by gabbro dikes up to 0.5 *m* thick. Fault contacts can be followed several meters until they are covered by the intense vegetation of the area or submerge in the Bahía Barrientos bay (Fig. 1.5). The southern contact of the ultramafic unit with the Cabo Raper granite is most probably a dextral strike-slip fault.

b. Gabbro unit

This unit is distributed into three bodies, a main body covering an approximately area of approximately 24 km^2 (located in the inner part of the peninsula) and two small EW elongated bodies covering an area of about 3-4 km^2 (in the southeastern part of the ophiolite) (Fig. 1.5). In total, the gabbro unit covers an area of about 30 km^2 and its thickness is about 4-5 *km* when measured perpendicular to the compositional layering (Nelson et al., 1993).

Instead of the well developed foliation observed in the ultramafic unit, gabbros commonly exhibit compositional layers and well preserved sedimentary structures – such as grading, cross-lamination, etc – that indicate younging direction and top of the sequence (Photo 2a). The rarely developed foliation strikes NW-SE and dips towards north and south. Gabbros occur also as dikes intruding into themselves. Layered gabbros are extensively and complexly folded, usually about EW trending fold axes (Photo 2b).

The thickness of compositional layers is generally about 10-30 *cm*. Each layer consists of pyroxene-rich and plagioclase-rich sub-layers; the first commonly contains fine-grained crystals (0.3-1.0 *cm*) normally grading upward up to 7.0 *cm* long crystals each; while the second consists of a mix of fine-grained pyroxene and plagioclase crystals.

Contacts of the gabbro unit with the surrounding units are still unclear; only in the southernmost edge of this unit evidence of primary contact with the ultramafic unit was observed. However, fault contact is the most common (usually striking NW to WNW). Contact with the dike complex was not observed; however, the gabbro unit is intruded by numerous dikes which are more frequent towards to the dike complex. This suggests that the contact between gabbro and dike complex might be primary.

Brittle deformation also affected this unit, similar to that observed in the ultramafic unit, with similar sets of brittle faults, i.e. NE trending strikes and EW trending strikes with double crosscutting relationships, suggesting that both sets were acting simultaneously.

c. Bimodal dike complex unit

Remaining the most unexplored section of the Taitao ophiolite, the Bimodal Dike Complex covers ca. 25 km^2, extending from its southern contact with the gabbro section up to the contact with volcani-clastic deposits north and east of the ophiolite. Most accessible outcrops are located in Caleta Mitford-Rees, in the Pacific coast, and in the inner part of Estero Cono (Fig. 1.5; Photo 3). The thickness of this section was estimated as approximately 6 *km* (Nelson et al., 1993).

The bimodal dike complex section consists of two different dike complexes with almost perpendicular orientations with respect to each other; one striking NW-SE, located in Caleta Rees and Caleta Mitford (hereafter referred as Mitford-Rees Dike Complex, MRDC), and other striking NNE-SSW, in the inner southern shore of Estero Cono (hereafter referred as Estero Cono Dike Complex, ECDC) (Photo 3). MRDC shows a wide range in composition from basaltic to andesitic with rare more acidic individual dikes (Nelson et al., 1993). At least 3 different intrusive events can be recognized in this complex based on composition and/or texture differences. Pillow lavas erupted from dikes were observed, suggesting that at least this part of the dike complex eventually reached the bottom of the submarine floor (Photo 3b). In contrast, ECDC shows a more restricted basaltic compositional range, although scatter andesitic dikes were observed. Nelson et al. (1993) described this complex as containing light green to grey aphanitic rocks, plagioclase and/or pyroxene phenocrysts. This dike complex shows a stronger metamorphic overprint compared to that of the MRDC. During our fieldwork campaigns, these features were observed, especially the increment in the metamorphic overprint. Approximately 120 *m* in length of the ECDC were mapped in detail, identifying (at least) 7 different episodes of intrusion (Fig. 3.6) with different textures and mineralogical associations. Under the assumption that the ECDC was created at the CR system, this outcrop represents *ca.* 2000 years of spreading activity; taking a spreading rate of 6.0 *cm/yr* (e.g. DeMets et al, 1994).

d. Volcani-clastic surrounding units

Volcani-clastic deposits cover an approximate area of about 20 km^2, divided into the CMU and the MVU (Guivel et al., 1996). CMU deposits consist mainly of pillow breccias and subordinate pillow lavas with some intercalations of conglomerate and coarse grained sandstone deposits (Photo 4). In contrast, the MVU is characterized by thick deposits of pillow lavas with minor and subordinate (only local) pillow breccias, basaltic to andesitic lava flows and at least 1000 *m* thick clastic strata of rhythmic sequences of conglomerates, sandstones and mudstones (Nelson et al, 1993). Also, MVU is intruded by numerous basaltic to andesitic (feeder?) dikes which cut the clastic sequence at Caleta Pascuas (Photo 5c). According to Lagabrielle et al. (1994) and Guivel et al. (1999) CMU deposits are more evolved than those of the MVU, presenting slightly higher metamorphic degree.

Bedding orientation of volcani-clastic strata in CMU dips usually N or S-ward with W to SW trending strikes. These orientations suggest the presence of: (1) widely open gently folds with EW trending axes or (2) EW trending normal (?) fault planes. These possibilities could not been constrained due to the outcrop scarcity in the area. The MVU sequence is consistently tilted, between 20° and 40°, towards NW to W and striking N to NE (Nelson et al., 1993). MVU deposits are distributed along one of the major (first order) lineaments in the area, Estero Cono, which has a NW-SE trending orientation (Fig. 1.5).

Another important difference between MVU and CMU is the spatial distribution of the volcanic-clastic deposits in the sequence. In the CMU, the base rests unconformable over the metamorphic basement and it is composed by at least 3-4 *km* thick deposits of pillow breccias with some intercalated pillow lavas (Nelson et al., 1993). These deposits can be observed exposed in the western shore of Bahía Barrientos bay (from Estero Lobos up to the opening of the bay northward) and in Punta Obstrucción in the eastern shore of the same bay (Fig. 1.5). Northward of these deposits, in Seno Hoppner, a more or less 1 *km* thick of conglomerates and minor coarse-grained sandstones deposits are exposed. These sediments are well exposed in a

small island named "*islote Amarillo*" (more or less 30 *m* diameter) (Photo 4b). Further northward, until the diffuse contact with the Seno Hoppner pluton, thick deposits of pillow lavas and pillow breccias are the exposed lithologies (Fig. 1.5, 30d).

In contrast, the MVU lithologies are more varied. The base of the unit is unknown but probably rest unconformable over the bimodal dike complex, in the south, and over the metamorphic basement, in the north. The base consists of a thick, about 1 *km*, deposits of basaltic to andesitic pillow lavas and minor subordinate pillow breccias exposed in the southern interior shore of Estero Cono and Caleta Monona (Fig. 1.5). Dimensions of the pillow lavas range between 10-15 *cm* and 2-3 *m*. The abundance of pillow lavas in this section indicates that the volcanic environment was mainly submarine which may became subaerial at some portions (Nelson et al., 1993) (Fig. 30a, Photo 5a).

From Caleta Monona until almost Caleta Pascuas (Fig. 1.5), in the southern shore of Estero Cono and in the southern shore of Cono Island, a rhythmic clastic sequence of sediments is well exposed. This sequence, previously named "*middle sedimentary member*" by Nelson et al. (1993), is bounded by submarine lavas deposits at the base and on top. It consists of a rhythmic sequence of conglomerates, sandstones and mudstones; which shows a decreasing grain size upsequence (i.e. NW-ward). Conglomerates are only exposed at Caleta Monona area, interbedded with medium-to-coarse grained sandstones and rare mudstone layers. Conglomerate layers are rarely present from the middle portions of the sedimentary sequence towards the top of it; instead, mudstone layers are interbedded with medium-to-fine sandstones (Fig. 3.7b). Nelson et al. (1993) defined four different sedimentary associations, named fa1 to fa4, distributed from east (fa1) to west (fa4) starting from Caleta Monona until Caleta Pascuas. These associations were interpreted as:

- fa1, at the base of the sequence, probably deposited as proximal debris flows apron adjacent to a submarine high or emergent coastline;
- fa2 (Photo 5b), probably deposited as a submarine NW-ward sediment gravity flow;

- fa3 interpreted as wave-dominated deposits formed in a shallow marine settings, where the source of sand and gravel may have been sediments gravity flows generated by storm waves in shallower water upslope from the site of deposition (i.e. SE-ward of the depositional site);
- fa4, interpreted as a probable series of distal turbidite deposits of a submarine fan at water depths in excess of the storm wave base (Nelson et al., 1993).

Only at fa2 and fa4 Nelson et al. (1993) reported the presence of abundant sedimentary structures (such as cross lamination, convolute folds, etc) which indicate a NW-ward paleocurrent flow of the sediments.

On top of the sedimentary sequence, basaltic to andesitic pillow lavas and lava flows interbedded with fine grained sandstones, of probable turbiditic origin, are exposed in the southern shore of Estero Cono from Caleta Pascuas until the western end of Estero Cono (Fig. 1.5). Pillow breccias are not present in this part of the sequence; instead, basaltic to basaltic-andesitic feeder dikes (Photo 5c) that cut the whole sequence were commonly observed. Pillow lavas show no evidence of explosive submarine volcanism (possible below the pressure compensation level; e.g. Fisher, 1984) suggesting off-axis volcanism (Nelson et al., 1993). Nelson et al. (1993) proposed a deepening basin depositional environment for this sequence, more distal from the source than the "*middle sedimentary member*" (Fig. 3.7c).

The presence of pillow breccias in both sequences (especially abundant in CMU) and abundant lava flows in MVU, together with their E-MORB (MVU) and N-MORB (CMU) affinities, suggests that lavas were erupted under shallow-water conditions (Guivel et al., 1996, 1999; Lagabrielle et al., 1994, 2000). The abundance of subaerial pyroclastic material leaded Guivel et al. (1999) to interpret these deposits as independent units not part of the Taitao ophiolite. According to Lagabrielle et al. (1994), CMU and MVU units were emplaced in or close to their present location by MORB-derived magmas erupted through the Chilean continental basement.

3.3.2. Intrusive units

Six plutonic bodies have been mapped in the westernmost Taitao peninsula, five surrounding the ophiolite and one located in the center of it near the contact between the gabbro and the bimodal dike complex units (Fig. 1.5). These intrusive bodies cover approximately 140 km^2, with individual bodies ranging in size from 32 km^2 down to *ca.* 4 km^2.

Their chemical composition ranges between hornblende-biotite-bearing granodiorites and tonalites (Nelson et al., 1993; Lagabrielle et al., 2000; Veloso, 2001). They present trondhjemitic affinities (TTG series) based on their contents of normative Albite, Anortite and Orthoclase (Bourgois et al., 1996; Keading et al., 1990; Veloso, 2001), suggesting that parental magmas were generated by the partial fusion of a young oceanic crust (e.g. Martin, 1994, 1999).

Some important differences between intrusive bodies were observed, and two main groups can be defined, including: (1) Cabo Raper (south), Estero Cono (north) and Barrientos (in Caleta Buena at Tres Montes peninsula) plutons; and (2) Seno Hoppner (north) and Tres Montes (southwestern shore of Tres Montes peninsula) (Fig. 1.5, Photo 6). The first group presents massive and locally magmatic flow textures (Photo 6a), while the second shows evidence of, at least, two intrusion stages, high degree of deformation, and intrusion of basaltic to andesitic dikes (Guivel et al., 1999).

The intrusion of both the Estero Cono and the Barrientos plutons, into the metamorphic basement, obliterated the contact between the basement and the Taitao ophiolite, especially in its northern part. In contrast, it is not clear whether the Cabo Raper pluton intrudes the metamorphic basement or the ophiolite. However, strongly foliated lenticular blocks (ca. 3x5 m^2) of the plutonic body are enclosed within the ultramafic unit of the ophiolite near their contact, suggesting that a major ductile fault zone is the main contact between these two units (Nelson et al., 1993).

These two granitic bodies intruded the metamorphic basement (Seno Hoppner pluton in the

northeastern edge of the ophiolite and Tres Montes pluton in the southwestern margin of the Tres Montes peninsula), obliterating the contacts between the ophiolite and the metamorphic basement. Contact metamorphic aureoles, northward of Seno Hoppner pluton (Photo 6c), were observed. The Tres Montes pluton shows tonalitic to granodioritic compositions and consists of magmatic breccias which show evidence of hydraulic fracturing, locally including clasts of green-schist facies dolerites (Guivel et al., 1999).

The so-called Central pluton has been mapped in (or near) the contact between the gabbro and the bimodal dike complex units (Fig. 1.5) (Nelson et al., 1993; Guivel et al., 1999). This mapping has been only possible by helicopter landings. However, during fieldwork expeditions was not possible to access that area by foot. According to Nelson et al. (1993), this felsic, tonalitic pluton is porphyric and contains large xenoliths of roof pendants of diabase. Exhibits an irregularly developed flow foliation near its margin and shows a propylitic alteration. Also, it has a trondhjemitic affinity, with a strong alteration (Guivel et al., 1999).

3.4. Ages constraints

Age constraints for the different units of the Taitao peninsula (including the ophiolite, and intrusive bodies) had been obtained by means of K/Ar, $^{40}Ar/^{39}Ar$, U-Pb SHRIMP and Fission Track methods (Table 1, Fig. 3.8) (Munizaga, 1970; Mpodozis et al., 1985; Bourgois et al., 1993; Le Moigne, 1994; Guivel et al., 1996; Hervé et al., 2003).

Bourgois et al. (1993) and Le Moigne (1994) obtained two ages (K/Ar method), of about 13 Ma and 6 Ma on a hornblendite vein and a doleritic dike that cut the gabbro unit respectively. Other ages obtained from the different units of the ophiolite and intrusive units are not consistent with the *ca.* 13 Ma K/Ar age but with the *ca.* 6 Ma (see further). The older age may be overestimated due to an excess of Ar in the sample (Orihashi, Y., personal communication).

Encased in the aim of this project, two more ages were obtained from the gabbro unit by

means of U-Pb Fission track method in recovered zircon crystals. Samples were collected in the eastern coast (in front of Caleta Buena) and in the western margin of the ophiolite (near the contact between gabbro and the bimodal dike complex sections) (Fig. 1.5). Obtained Fission Track ages yielded 5.93±0.41 Ma and 5.79±0.22 Ma. These Fission track ages do not represent the age of the rock; instead they are interpreted as the exhumation ages for the gabbro unit and therefore for the ophiolite. This age coincides with the *ca.* 6 Ma age (Le Moigne et al., 1994).

In summary, an accurate age for the Taitao ophiolite is not yet available but an exhumation age of *ca.* 6 Ma. This age is coincident with the arrival and collision of the CR segment delimited by Esmeralda and Tres Montes F.Z. (Fig. 3.5), suggesting that exhumation (obduction?) of the Taitao ophiolite was triggered by the collision of this CR segment with the South American plate offshore of the Taitao area.

Unlike the plutonic units, volcani-clastic units (CMU and MVU) had been extensively dated by means of K/Ar (whole rock) method and microfossil techniques (Mpodozis et al., 1985; Guivel et al. 1996). Four ages for the CMU of about 3.5 Ma were obtained (K/Ar, whole rock) (Mpodozis et al., 1985; Guivel et al., 1996), while for the MVU slightly younger ages of *ca.* 3.0 Ma were obtained (whole rock K/Ar and microfossils) (Mpodozis et al., 1985; Bourgois et al., 1993). Since none of the rocks of the peninsula is completely "fresh", obtained K/Ar ages represent a maximum age for these rocks. Younger than ages for the plutonic units, K/Ar ages from volcani-clastic units are coincident with the collision of the CR segment delimited by Tres Montes and Taitao F.Z. (Fig. 3.5).

Probably the most extensive geochronological record, from of the rocks of the westernmost Taitao peninsula, corresponds to those obtained from the intrusive plutonic bodies. Used methods include K/Ar (biotite and hornblende), $^{40}Ar/^{39}Ar$ and U-Pb SHRIMP and Fission track in zircon and apatite (Mpodozis et al., 1985; Guivel et al., 1999; Hervé et al., 2003) (Table 1, Fig. 3.8).

K/Ar analyses of Cabo Raper pluton samples yield ages of 3.6±0.6 and 3.3±0.3 Ma, for biotite, and 4.1±2.4 and 3.4±0.8 Ma, for hornblende (Mpodozis et al., 1985). Inconsistent with

K/Ar ages and significantly older, $^{40}Ar/^{39}Ar$ (Biotite) ages yield 5.1±0.6 and 4.8±0.3 Ma (Guivel et al., 1999). U-Pb SHRIMP ages indicate a crystallization age of about 3.9 Ma, slightly older than those reported by Mpodozis et al. (1985) but within their large errors; and younger than those reported by Guivel et al. (1999) (Hervé et al., 2003). These data indicate that cooling of the Cabo Raper pluton occurred in an interval no longer than 2 My time (Hervé et al., 2003). Obtained ages from Cabo Raper pluton suggest that crystallization occurred before or coeval with the second impact of the CR in the Taitao peninsula area; and the rapid exhumation occurred coeval or after this impact.

Only K/Ar (whole rock) and $^{40}Ar/^{39}Ar$ (biotite and hornblende) ages have been reported for Seno Hoppner pluton (Mpodozis et al., 1985; Guivel et al., 1999); yielding consistent ages of about 6 Ma. This data suggest that the crystallization of the Seno Hoppner pluton occurred contemporaneous with the first collision of the CR and with the uplift of the Taitao ophiolite.

For Estero Cono pluton only one U-Pb Fission track age (zircon) is available (Hervé et al., 2003), which is 3.49±0.27 Ma. Several similarities between Cabo Raper and Estero Cono plutons lead to consider them generated from the same source and crystallized at similar times (Hervé et al., 2003). Again, geochronological data suggest that the exhumation of this intrusive body occurred synchronously with the collision of the second segment of the CR.

Two Fission track ages were reported by Hervé et al. (2003) for the Estero Cono pluton: (1) 3.47±0.22 (zircon), and (2) 3.14±0.30 (apatite). The proximity of this ages with those from Cabo Raper and Estero Cono pluton suggest that the exhumation of these bodies occurred very fast, probably in no more than 2 My time (Hervé et al., 2003), before or contemporaneous with the second collision of the CR in front of the coast of the Taitao peninsula.

Different geochronological data indicates that crystallization and exhumation for the intrusive bodies is closely related to the series of collisions of the CR in the area. Thus, based on the geochronological and petrological characteristics, two groups are defined and correlated with the evolution of the CR for the last 6 Ma (e.g. Lagabrielle et al., 1994; Guivel et al., 1999; Veloso,

2001). The first, including Seno Hoppner and Tres Montes plutons, with crystallization ages of *ca.* 6 Ma is coeval with the first collision of the CR (Fig. 3.5); while the second, including Cabo Raper, Barrientos and Estero Cono plutons, with crystallization ages of about 3.5-4.0 Ma and rapid exhumation (*ca.* 2 My time) are coeval with the collision of the second segment of the CR (about 3 Ma).

Chapter 4: Methodology

4.1. Data collection

4.1.1. Fieldwork campaigns

Two fieldwork campaigns were conducted during the months of December and January 2000-2001 and during same months of 2002-2003. During first campaign, structural data (fault-slip data, bedding attitudes, lithological contacts orientations and characteristics, etc) along the eastern and western coast of Bahía Barrientos, northern and southern coast of Estero Cono, southeastern part of the plutonic units and from the southern coast of the Taitao and Tres Montes peninsulas were collected (Fig. 4.1).

Few oriented samples and oriented cores of rock were extracted from: (1) pillow lavas and pillow breccias at Bahía Barrientos, (2) Dike complex at Estero Cono (ECDC), (3) ultramafic and gabbro units and (4) from the two plutonic bodies in the south of the Taitao and Tres Montes peninsulas. During this first campaign, samples were labeled TPA, TPB, TPC and TPD followed by the correspondent sample number (for example TPC001).

During second fieldwork campaign, a larger amount of data was collected and more sites were visited. New structural data was collected along the western coast of Bahía Barrientos, southern coast of Taitao and Tres Montes peninsula, northern and southern coast of Estero Cono, western coast of Taitao peninsula (Caleta Rees and Caleta Mitford) and from the inner part of the plutonic units (Fig. 4.1).

This time, several oriented samples and cores of rock were obtained from: (1) the plutonic units, (2) pillow lavas, pillow breccias, massive lava flows and feeder dikes at Estero Cono, and (3) dikes and gabbro from Caleta Rees and Caleta Mitford (MRDC). At the innermost part of Estero Cono, a systematic drilling survey was performed at the ECDC. During this campaign,

samples were labeled TPE, TPG and TPH while obtained cores from the ECDC were labeled C (for example C08).

4.1.2. Collection sets of data and samples

Basically, fault-slip data consists in a set of orientations including: (1) the orientation of the fault surface (measured as strike and dip), (2) the direction of the striae or any other kinematic indicator which reveals the direction of movement (Appendix B), and (3) sense of movement, described as normal, reverse, etc (Fig. 4.2). Unfortunately, collected fault-slip data was not always the complete set of directions. Usually, it was only possible to measure the orientation of the fault surface and the sense of displacement, lacking information about the orientation of the striae. Among the collected fault-slip data only 53 data-sets contained all necessary information, 38 located in the plutonic units and 15 along the Bahía Barrientos bay (Fig. 4.1).

Cores were drilled with a manual drilled, which can extract rock cores of about 2.2 *cm* diameter and *ca.* 15 *cm* long, and oriented while they were still attached to the rock by marking the orientation of the *x* and *z* axis of the core (Appendix B).

Two techniques were used indistinctly to keep the orientation of collected oriented samples. The first consist to obtain the orientation (strike and dip) of one of the faces of the block plus an arrow indicating the direction of the north. The second technique is to draw two horizontal lines on two faces of the rock block plus an arrow indicating the direction of the north (Fig. 4.3). Special care was taken with samples which produced a deflection of the compass. In that case, second technique was preferred but orientation of the north was measured away from the rock.

4.2. Laboratory work

After fieldwork campaigns, stress analysis, isolation of RM vectors, thermomagnetic

experiments and anisotropy of magnetic susceptibility analysis (Appendix A, B, C, D) were carried out. These analyses lead to the determination of stress fields, rotational patterns, determination of ferromagnetic mineral phase, and magnetic sedimentary fabrics respectively.

Stress fields responsible for the generation of brittle structures in the southern and eastern parts of the Taitao ophiolite were calculated by means of the *multi-inverse* method (Appendix A). Processing of the data was kindly done by Dr. Yamaji. Results of the processed data were interpreted in this study.

Oriented samples were re-oriented and drilled at University of Tsukuba using a fix driller with a 30 *mm* outer diameter and 22 *mm* inner diameter perforation tube with synthetic diamond in its edge (Photo 7). After, cores were extracted cut into standard size paleomagnetic specimens (cylinders of rock of about 2.2 *cm* high and 2.2 *cm* diameter). More than 1000 specimens were obtained and properly labeled. Obtained specimens were used to determine characteristics RM vectors. In addition, AMS fabrics were determined for clastic samples of MVU.

Several representative samples per lithology were selected to determine their Curie temperatures and therefore ferromagnetic mineral phase. Samples were crashed using a manual agate mortar and an automatic spin agate mortar at the University of Tsukuba. Grain size was about or less than 1 *mm* diameter and the quantity used in the laboratory experiments was less than 5 *mg* per analyzed sample.

In order to obtain complete demagnetization paths, which provided with an easy method to isolate RM vectors, two techniques were used in a pilot analysis phase: (1) thermal and (2) alternating field demagnetization (Appendix B). These analyses were carried out at the Geological Service of Japan. Thermal demagnetization was done using a thermal demagnetizer oven model MMTD-18 manufactured by *Magnetic Measurement Inc* (Appendix E) (Photo 8) which can handle and demagnetize simultaneously up to 18 standard size paleomagnetic specimens. Samples are heated with a user-defined rate up to a user-defined peak temperature with a maximum peak of *ca.* 700°*C*. After each demagnetization step, the orientation of the RM

vector was measured using the SQUID (see further).

Alternating field demagnetization was performed using a pass-through cryogenic magnetometer model 2G-760, manufactured by *2G Enterprises*, with a in-line SQUID (Superconducting QUantum Interference Device) connected to it (manufactured by *Applied Physics Systems*) (Photo 9, Appendix E). The so-called alternating demagnetization device (2G-760+SQUID) can reach a peak demagnetization field of 80 *mT*. Fully-computer controlled, it can be set up to demagnetize simultaneously up to 8 specimens in user-defined steps.

Approximately 20 to 25 specimens per lithology were selected as pilot samples, corresponding to sister specimens (consecutive specimens). Both sister specimens were fully demagnetized; one using thermal demagnetization and the other using alternating field demagnetization. Demagnetization steps used during the pilot phase were each 50°C, from room temperature up to 700°C for thermal demagnetization; and 2.5 *mT* (from 0 to 20 *mT*), 5.0 *mT* (from 20 to 70 *mT*) and 2.5 *mT* (from 70 to 80 *mT*) for alternating field demagnetization. Isolated RM vectors from demagnetization paths were then compared using Fisher (1953) statistics (Appendix B).

Demagnetization paths and RM vectors for sister samples have similar orientations, being statistically undistinguishable in more than 90% of the analyzed pilot samples. Due to these similarities, only alternating field demagnetization was used for the rest of the samples (using demagnetization steps of 5.0 *mT* from 0 to 80 *mT*).

Orientation of the high-stability component(s) was calculated using the "*principal component analysis*" (Kirschvink, 1980; Appendix B). Isolation of the high-stability RM vector(s) and their associated error allowed the rejection or acceptance of specimens for a further paleomagnetic analysis. After rejection or acceptance of specimens was completed, mean orientations by site were calculated using statistical procedures. Used statistics correspond to the elliptical analog of the Fisher (1953) statistics, the Kent (1982) statistics (Appendix B). Reduction of the Kent (1982) to Fisher (1953) statistics occurred in about 50% of the analyzed sites. After statistical

procedure was applied, orientation of the mean RM vector and its associated error were obtained and their values allowed the rejection of acceptance of data at site level.

Thermomagnetic experiments data was used to determine the Curie temperature of each analyzed lithology. Data was obtained from powder samples using a KappaBridge susceptibility meter with a variation temperature furnace apparatus model CS-3 attached to it, both manufactured by *Agico Company* (Photo 10; Appendix E). The KappaBridge and furnace apparatus measures bulk susceptibility during temperature variation from room temperature (*ca.* 20°C) up to ca. 700°C. Measurement of bulk susceptibility is done during the heating and during the cooling of the sample. The differential method proposed by Tauxe (1998) (Appendix C) was applied to the thermomagnetic data in order to obtain representative Curie temperatures from each curve. Individual results per lithology were averaged and related errors were calculated using a Normal standard deviation procedure.

Magnetic susceptibility (Appendix D), including intensity and its anisotropy, was measured using the KappaBridge susceptibility meter (Photo 10) (Appendix E) and specific software packs provided by *Agico Company* at the Geological Service of Japan.

Chapter 5: Stress Fields

Brittle fault-slip data from the plutonic units was used to determine the stress field conditions imposed by the repeated subduction of the CR system that affected the Taitao ophiolite during and after the obduction process. Stress fields applied by each one of the subducting plates (Nazca and Antarctic) have different stress ratios due to their different subducting angles, velocity and direction (e.g. Cande and Leslie, 1986; Yañez and Cembrano, 2000). However, the resultant applied stress field has been constant in its direction but not in its stress ratio during, at least, 6 My time. Then, it is expected that structures generated by these stress fields inside and in the border the ophiolite recorded the change in stress field conditions. The "*multi-inverse*" method (Appendix A) was applied to the collected fault-slip data (N=53; Fig. 5.1) to obtain the orientation and characteristics of the involved heterogeneous stress fields.

5.1. Obtained data

Fault-slip data was collected in the inner and outer parts of the ophiolite, specifically in the plutonic units and along the major lineament of the area, the Bahía Barrientos bay (Fig. 5.1a). Other sections of the ophiolite were avoided in order to collect only data from those structures related to the ophiolite obduction and not those possible preserved structures developed during the generation of the ophiolite in the spreading center. Faults developed in the bimodal dike complex and the volcani-clastic units could be product of extension during the ophiolite generation at the spreading ridge, as structures observed in Hess Deep ridge (e.g. Hurst et al., 1994). These structures could have been preserved during the ophiolite obduction, similar to the spreading ridge structures reported in the Troodos ophiolite (Moores and Vine, 1971; Varga and Moores, 1985; Dilek et al., 1990) and others. Layer-parallel faults developed in the gabbro section could also be primary deformation structures generated during extension at the spreading

ridge, similar to those reported in the East Pacific ridge (Varga et al., 2004). Faults developed in the ultramafic mega-xenoliths founded in the gabbro unit were also excluded, since they may not preserve their original orientation.

Although the multi-inverse method does not need a priori division of the data, collected data was divided based on the locality that they were developed. Thus, two main set of faults were defined: (1) faults in the plutonic units and (2) faults in the eastern margin of the ophiolite (Bahía Barrientos).

5.1.1. Faults developed in the plutonic units

The contacts between the ultramafic and gabbro units show the development of strike-slip and thrust fault-planes (Photo 11). Also, fault-planes with similar movements were founded in the interior of each section, especially in the ultramafic unit. As mentioned before, two main sets of brittle fault-planes were observed in these units: one striking EW and other striking NE (Fig. 5.1b). Crosscutting relations between them are difficult to precise, making difficult to establish any temporal relation between these two sets. Such complex crosscutting relations suggest that any fault subset was probably acting synchronous with other (possible defined) subset. Thus, it is possible that these fault set recorded more than one stress field (heterogeneous). With no more *a priori* subdivision criteria any possible defined subset will include some fault data belonging to another (possible defined) subset (e.g. Fry, 1999). This fault-slip data was labeled "inner" and includes 38 faults (Fig. 5.1b).

5.1.2. Faults developed in Bahía Barrientos

The major lineament in the Taitao area, namely Bahía Barrientos Fault Zone (BBFZ) (Fig. 1.5), trends NNE-SSW and is located between Taitao and Tres Montes peninsulas. This fault

zone is composed by several small brittle fault planes (up to 3x3 m^2 in area) with a general NNW-SSE to NE-SW trend and dipping SE-ward. The BBFZ is believed to play a major role in the obduction and accommodation processes of the Taitao ophiolite (Veloso, 2001).

In the eastern border of the BBFZ outcrops of Cabo Raper pluton (south), ultramafic, gabbro, Oxxean Tres Montes sedimentary sequence (e.g. Nelson et al., 1993), and CMU deposits (north) are founded. In the opposite western border, outcrops of the LCMC and CMU deposits (Fig. 1.5) were observed.

In the eastern border, from Cabo Raper until almost Seno Hopper and in Punta Obstrucción, several small fault-planes (Fig. 5.1c), affecting mainly CMU deposits but also small ultramafic and gabbro outcrops (Photo 12), were observed. Fault-planes present a main strike-slip movement with minor and small dip-slip movements.

In this set it was possible to distinguish two subsets: one striking NNW-SSE (including strike-slip and dip-slip faults) and other striking ENE-WSW (including only strike-slip faults). No crosscutting relations were observed between these two subsets; further so, no subdivision of this data set was made. A total 15 fault-planes with the complete information were collected. This set of fault was labeled "outer".

5.2. Results of the multi-inverse method

The multi-inverse method (Appendix A) was applied to three fault-slip data sets: (1) the complete fault-slip data, labeled "all" (Fig. 5.1a), (b) "inner" set of faults (Fig. 5.1b) and (c) "outer" set of faults (Fig. 5.1c). Analysis of the "all" fault-slip data set seeks to validate and confirm the subdivision of the data into "inner" and "outer" sets. If all faults in the peninsula were product of a constant stress fields, then, such stress fields should be also obtained without any arbitrary division of the data (e.g. Fry, 1999; Yamaji, 2000, 2003). Optimum parameters used in the analysis are: (1) group parameter, k=5 and (2) enhancing parameter, e=11 (Yamaji, A.,

written communication).

5.2.1. Recognition of heterogeneous stress fields

Applying the method to the set "all" (Fig. 5.1a) two main clusters solutions in the σ_1 stereogram and other two in the σ_3 stereogram were obtained (Fig. 5.2a). A close analysis of both stereonets reveals the presence of a third solution. These solutions were labeled "A", "B" and "C". All obtained solutions have a stress ratio ranging between 0.1 and 0.7 (Table 2), differing only in the orientation of the compressional and extensional principal stress axes. Compressional axes for "A" and "B" solutions are EW and NNE-SSW trending and horizontal while extensional axes are vertically oriented, namely these solutions are reverse faulting regimes. In contrast, solution "C" has a NS trending compressional axis and an EW trending extensional axis, both horizontal (Fig. 5.2a); thus "C" solution corresponds to a strike-slip regime.

Only two cluster solutions were obtained in the analysis of the "inner" fault set. Orientation of both compressional and extensional axes and stress ratio values are easily correlated with "A" and "B" solutions (Table 2) previously obtained (Fig. 5.2b). Thus, "inner" fault set recorded only the reverse stress regimes "A" and "B". Analysis of the "outer" fault set reveals the presence of a main cluster solution and two minor ones (Fig. 5.2c). Main cluster has a stress ratio ranging from 0.1 to 0.5 with a nearly horizontal EW trending compressional axis and a horizontal NS trending extensional axis, corresponding to a strike-slip regime. This solution is similar to the "C" solution obtained in the analysis of the "all" fault set (Fig. 5.2a).

Other two solutions, labeled "D" and "E", have stress ratios between 0.2 and 0.6 ("D") and between 0.7 and 0.8 ("E"). Compressional axes are closely oriented, trending mostly WNW-ESE. However, "D" compressional axis is nearly horizontal while that of "E" plunges about 20°. Similarly, extensional axes for both solutions are nearly NE-ward oriented; with "D" extensional axis plunging about 30° and that of "E" plunging about 50° (Fig. 5.2c). These solutions were not

obtained previously. However, the restricted stress ratio of the "E" solution and the similar orientation of these two solutions with those obtained for the "C" solution suggests that division of the data into sets (inner and outer) enhances the resolution of the applied method. This is a proof of that identification of heterogeneous stress does not depend on the division of the data.

5.2.2. Real and artifacts solutions

The analysis of the data as a whole and the analysis of the subdivided data give some insights of (possible) real and artifact solutions. If same solutions are obtained with or without subdivision (A, B and C), such solutions are most probably real and reflect the stress field which originated the faults under analysis. In contrast, solutions which are dependant of the subdivision of the data (D and E) are most probably artifacts or enhancement in resolution of a particular solution. Therefore these later solutions do not reflect a real stress field state past or present.

Stress ratio for the solution "C" is between 0.1 and 0.6, value which includes that of the "D" solution (between 0.2 and 0.6) and roughly that of the "E" solution (between 0.6 and 0.7) (Table 2, Fig. 36). "C" and "D" compressional axes are similarly oriented, differing only in their inclination by *ca.* 20° and their strike by *ca.* 10°. Orientations of extensional axes are also similar for these two solutions, both been roughly EW trending; "C" extensional axis is located near the horizontal while that of "D" has an inclination of about 20°. It seems that "D" solution is about 20° clockwise rotated with respect to "C" solution about a slightly E-ward inclined rotational axis. Thus, "D" solution is most probably a local solution which was obscured in the analysis of the "all" fault set.

In contrast, the stress ratio obtained for "E" solution is off-limits of that of the "C" solution. Moreover, the orientations of both compressional and extensional axes are significantly displaced with respect to those of the "C" solution (Fig. 5.2). Then, "E" solution is most probably an artifact of the calculation and does not reflect any stress field.

Chapter 6: Paleomagnetism

In order to determine the tectonic and deformational history experienced by the Taitao ophiolite oriented samples from: (1) ultramafic rocks, (2) gabbros, (3) bimodal dike complexes and (4) volcani-clastic units were collected at 38 sites including more than 500 specimens (Fig. 6.1). Samples were demagnetized by means of AFD and ThD techniques in order to obtain their characteristics RM vectors (Appendix B; e.g. Kirschvink, 1980). From the orientations of within-site RM vectors, the orientations of mean RM vectors were calculated using Kent (1982) statistics. Orientation of mean RM vectors and related structures (foliation, compositional layers, bedding, etc) were then restored to the orientation of the expected GAD, obtaining the orientation of inclined rotational axes and untilting parameters (Appendix B) which aid to unveil the obduction processes experienced by the Taitao ophiolite.

6.1. Characteristics of isolated RM vectors

Reliable RM vectors were grouped in two groups depending on their demagnetization paths characteristics. Samples collected from volcani-clastic bimodal dike complex units yielded univectorial demagnetizations paths. In contrast, samples from the plutonic units yielded multivectorial demagnetization paths.

6.1.1. Univectorial demagnetization paths

These demagnetization paths show no affection of secondary magnetizations; although, small imprints of viscous remanent magnetization (VRM, Appendix B) were commonly observed. VRM was successfully removed after 10-15 *mT*, during AFD, and the remaining RM vector

corresponded to a single direction (univectorial) (Fig. 6.2).

a. Volcani-clastic deposits of the MVU and CMU units

Clastic sediments of the MVU were sampled at 7 sites (S1 to S4, S8, M2 and M3, Fig. 6.1., Table 3) and include 85 paleomagnetic specimens from sandstones and mudstones. Sites S5 to S7 and M1 (not shown in Fig. 6.1) were rejected, either because of large "*maximum angular deviation*" (MAD, e.g. Kirschvink, 1980) values or insufficient number of specimens (Appendix B). Reliable RM vectors for sandstones sites are all normal polarity while those of mudstones sites display both normal and reverse polarities (Fig. 6.3a). Normal polarity vectors have all NW to NNE-ward azimuths while reverse ones have SW-ward azimuths, being nearly antiparallel. However, they do not pass a reversal test and they were classified as R- (e.g. McFadden and McElhinny, 1990; Appendix B). Orientation of calculated mean RM vectors compared with the orientation of the expected GAD suggests a counterclockwise rotation of the majority of these sites, although small clockwise rotations were observed at two sites.

Pillow lavas and lava flows from the MVU were sampled at 6 sites (L1 to L7 in Fig. 6.1, Table 3), including 97 specimens. Sites correspond to 4 lava flows and 2 pillow lavas. Obtained reliable RM vectors from these sites are all normal polarity with NW-ward azimuths (Fig. 6.3b). Orientation of mean RM vectors compared to that of the expected GAD suggest that pillow lavas and lava flow deposits of the MVU were affected by counterclockwise rotations, similar to clastic deposits.

Feeder dikes of the MVU were sampled at 4 sites (D1 to D4 in Fig. 6.1), including 55 specimens in total. Additionally, three extra sites were sampled but these were rejected due to their large MAD values. RM vectors, at sites D1 to D4, are normal polarity, and inclined mostly NW to NNW-ward with exception of those from site D1 which are NNE-ward inclined (Fig. 6.3c). These orientations, as the rest of those of the MVU, suggest a counterclockwise rotation when compared with the orientation of the expected GAD. However, at site D1 a possible small

clockwise rotation at site D1 was observed.

Due to the scarcity of good outcrops at the Estero Lobos area (Fig. 1.5), only 1 reliable site of pillow lava was sampled from the CMU (labeled L7). Obtained RM vectors at this site are reverse polarity (Fig. 6.3b) with SW-ward azimuths and unusually low inclinations (almost horizontal). As previous sites ("S", "M" and L1 to L6 sites), the orientation of mean RM vectors compared with that of the expected GAD suggest a counterclockwise rotation. A point that should be kept on mind is that most of the CMU deposits are strongly affected by the dextral movement of the BBFZ. Thus, it is possible that the inferred rotation resulted from either the movement of the BBFZ or the counterclockwise rotation of the ophiolite (see further).

b. Bimodal dike complex unit

The ECDC intensively sampled, collecting a total of 185 specimens. However, only 127 specimens yielded RM vectors with reliable MAD. All obtained RM vectors from EDC were grouped in one site (labeled D5 in Fig. 6.1, Table 3) due to their small differences in orientation (Fig. 6.3d). All these RM vectors are normal polarity and most of them are SE to S-ward inclined (only few are SSW-ward inclined). The orientations of these RM vectors, compared to that of the expected GAD, suggest that this portion of the dike complex experienced a counterclockwise rotation about a nearly horizontal rotational axis. This is similar to the (possible) rotations observed in the MVU and CMU.

The MRDC was sampled at 5 sites (D6 to D10 in Fig. 6.1, Table 3); including 64 specimens (all with reliable MAD values) (Fig. 6.2e). Isolated RM vectors show both normal and reverse polarities; normal ones were obtained from northern sites (D6 to D8) and reverse ones in the southern sites (D9 and D10) near to the contact with the gabbro unit (Fig. 6.3d). Normal polarity vectors are N to W-ward inclined, varying from almost vertical to almost horizontal, while reverse ones are SE-ward inclined between ca. 30° and almost horizontal (Fig. 6.3d). Again, the orientations of RM vectors suggest a counterclockwise rotation of this part of the dike complex,

with a possible larger and increasing rotational amount towards south of the area.

c. Dike complex–Gabbro contact at Caleta Mitford-Rees

At the contact between the bimodal dike complex and the gabbro units at Caleta Mitford-Rees (Fig. 6.1) 2 sites were sampled, compromising 30 specimens. However, only one of these sites is statistically reliable (Appendix B), which was labeled G2 (Fig. 6.1) and it includes 18 specimens (Table 3). RM vectors isolated for this site are all reverse polarity, inclined approximately 20° SW-ward. The only exception is a nearly horizontal RM vector which has a normal polarity but close enough to the rest of the data (Fig. 6.3e). At this site, orientation of the RM vectors suggests, again, a counterclockwise rotation.

6.1.2. Multivectorial demagnetization paths

Unlike sites of the volcani-clastic and bimodal dike units, those of the plutonic units commonly display two stages of magnetization (multivectorial), associated with the low and high coercivity portions of the demagnetization paths. A third magnetization component was sometimes observed, which corresponded to a VRM successfully removed with after 5 to 10 *mT*. Isolated RM vectors were labeled "-young" (low coercivity) and "-old" (high coercivity); the first isolated between 0 *mT* (or after VRM removal) and ca. 30-40 *mT*, and the other after a demagnetization field of ca. 30-40 *mT*.

a. Ultramafic section

Taking into consideration that ultramafic rock outcrops are disrupted and not continuously connected, sampled sites were grouped according to the block they belong. These blocks were labeled ultramafic south, central and north (Fig. 6.1). Southern block is corresponds to ultramafic rock outcropping near the contact with the Cabo Raper pluton, central block is located in the

central-southeastern part of the ophiolite while northern block is in the central-northwestern part (Fig. 6.1), these last two included into the gabbro unit. The main purpose of this grouping is to explore the possibility of different tectonic histories for each one of them. All together the ultramafic section was sampled at 10 sites (sites labeled "P" in Fig. 6.1), including 105 specimens. However, only 7 sites are statistically reliable: 3 in the south (P1 to P3, 41 specimens), 2 in the central (P4 and P5, 20 specimens) and 2 in the north (P6 and P7, 28 specimens) blocks.

From all ultramafic sites, only two of them, sites P3 and P6, yielded univectorial demagnetization paths. Isolated RM vectors from site P3 were considered "young" due to their similar orientation with those obtained from the MVU, CMU and dike complex units; while isolated RM vectors from site P6 were considered "old" due to the similar orientation with those from site P7, both located in the north ultramafic block (Fig. 6.3f,g, 6.5a,b).

"Young" RM vectors from sites of the ultramafic south block (P1 to P3) are reverse polarity as well as those from site P7 in the north block, whereas those from sites in the ultramafic central block (P5 and P6) are normal polarity (Fig. 6.5a). In contrast, isolated "old" RM vectors of south and central ultramafic blocks are reverse polarity while those from the north block are normal polarity (Table 4). In general, both "young" and "old" RM vectors have widely scattered orientations with respect to each other (Fig. 6.5a, b), with shallow inclinations except for that of site P2.

These widely scattered orientations, both normal and reverse polarities, suggest that these blocks underwent complex folding. However, orientations of "young" RM vectors, compared to that of the expected GAD, suggest that counterclockwise rotation affected these blocks in addition to folding. This counterclockwise rotation seems reasonable since it has been detected in the rest of the rocks units of the ophiolite (MVU, CMU and dike complex). Thus, orientations of "old" RM vectors must be corrected by restoring "young" RM vectors to the orientation of the expected GAD by calculating both folding and rotational patterns.

b. Gabbro section

This rock unit was sampled at 12 sites but only 7 of them yielded reliable data (sites G3, G5-G8, G11 and G12 in Fig. 6.1) which include 100 specimens. Majority of these specimens yielded multivectorial demagnetization paths in which two distinct RM vectors were isolated from the low and high coercitivity portions. Similar to ultramafic rock sites, isolated RM vectors were labeled "young" (low coercivity) and "old" (high coercivity). Also, in few samples a VRM component was observed and easily removed with a peak field of 10 *mT* (Fig. 6.6).

Reliable "Young" RM vectors were isolated at 4 sites (G5, G6, G11 and G12 in Fig. 6.1) while reliable "old" ones were isolated at all sites except for site G12 (Table 4). Sites with G3, G7 and G8 yielded "young" RM vectors but these are statistically unreliable due to their large associated MAD values.

"Young" RM vectors are both normal and reverse polarities (Fig. 6.7a) with scattered SE-ward and NE-ward inclinations. In particular, normal polarity vectors have very shallow inclinations, similar to the ultramafic section. The orientations of "young" RM vectors suggest a counterclockwise rotation for the gabbro section, similar to that observed in all the other rock units of the ophiolite. However, the common presence of fold in this unit suggests that young RM vectors may have being re-oriented. Even more widely distributed than "young" RM vectors are "old" RM vectors (Fig. 6.7b), showing both reverse and normal polarities with usually steepest inclinations, similar to ultramafic "old" RM vectors. As for "old" RM vectors for the ultramafic unit, "old" RM vectors obtained from gabbro need to be corrected using folding and rotational patterns inferred from the correction of "young" RM vectors.

6.2. Statistical distributions of RM vectors

Within-site RM vectors (from all ophiolite units) show differences either in declination or inclination, displaying elliptical rather than circular distributions (Fig. 6.3). Thus, orientation of

within-site RM vectors and 95% confidence intervals were calculated using Kent (1982) statistics instead of the classically used Fisher (1953) statistics. Notice that if vectors are circularly distributed, Kent (1982) statistics are instantly reduced to Fisher (1953) statistics (Appendix B).

From the analyzed data, approximately 52% of the sites are elliptically distributed. However, remarkable differences can be observed within each rock unit. RM vectors from the northern part of the ophiolite – dike complex and volcani-clastic units – yielded elliptical distributions at *ca.* 66.6% of the sites. Similar situation was observed on "young" RM vectors of the plutonic units, which are elliptically distributed at ca. 71.4% and 100% of the ultramafic rock and gabbro sites respectively. In contrast, "old" RM vectors from the plutonic units are mostly circularly distributed; 60% and 66.6% of ultramafic rocks and gabbro sites respectively (Table 3, 5).

This distribution patterns suggest that the volcani-clastic and dike complex units rotated about inclined axes. The plutonic units seem to have rotated twice, both about inclined axes but the old rotational axis seems to be more stable than the young one.

According to MacDonald (1980) and Weinberger et al. (1995), the presence of arcuate distributions is a good proxy indicator of tectonic rotations about non-horizontal, non-vertical (i.e. inclined) rotational axes. Thus, rotational axes in the further analysis were calculated using a rotational procedure modified from that proposed by Weinberger et al. (1995) (Appendix B). However, a single rotational axis at a single site does not provide with an accurate rotational axis for the rock unit under analysis (MacDonald, 1980; Weinberger et al., 1995). Calculated rotational axes at each site (within-site) were treated as directions in order to calculate a mean rotational axis for the unit (between-sites) and its related confidence interval by means of Kent (1982) statistics. The associated mean rotational amount (θ) and the related error (θ_{dev}) were calculated assuming that individual amounts of rotations (within-site) are normally distributed.

6.3. Rotational axes for volcani-clastic and dike complex units

6.3.1. Individual and mean rotational axes

a. Volcani-clastic deposits (MVU and CMU)

Individual rotational axes calculated for each of the sampled sites of the MVU are inclined towards both east and west directions (Fig. 6.8, Table 6). W-ward inclined axes have usually steepest inclinations than E-ward inclined axes, which inclinations ranges from nearly horizontal to nearly vertical. Counterclockwise rotational amounts are associated to E-ward inclined axes while, in contrast, clockwise ones are associated to W-ward inclined axes. Amounts of rotation are as large as 87° and 48° for counterclockwise and clockwise rotations, respectively (Table 6).

The three clockwise rotational axes for the MVU subunits were only calculated for two sites in Caleta Monona area (clastic sediments) and one in the Estero Cono area (feeder dikes). Inclination of these axes is more or less stable about 65° W-ward. In contrast, inclination of counterclockwise rotational axes largely varies, apparently defining three different groups from east to west. This variation was also observed in the rotational amounts associated to each site (Fig. 6.9); rotational amounts systematically increase, either within each group or between them, from easternmost to westernmost sites of the MVU.

The mean rotational axis for the whole MVU inclines ENE-ward approximately 65° (Table 7). However, three different rotational axes were calculated instead due to the observed differences in rotational amounts of individual rotational axes mentioned above. These rotational axes also inclined E-ward (Fig. 6.8) and they show increasing amounts of rotation, from 14° to 55°, towards westernmost sites of MVU. Their mean orientations and their confidence intervals are usually overlapped between them and with the mean rotational axis calculated for the whole MVU. This, together with statistical F-test, indicate that they are statistically undistinguishable, suggesting that they represent variations of a similarly oriented rotational axis.

The rotational axis calculated for the CMU deposits is, as for those of MVU, E-ward inclined and with an associated rotational amount of approximately 95° (Table 6). Since only one site was sampled on the CMU, this rotational axis was taken as the mean rotational; although, it may not represent the rotational pattern experienced by this unit. However, its orientation is similar to that obtained for east and central groups of the MVU and other units (Fig. 6.8).

b. Bimodal dike complex (ECDC and MRDC)

The rotational axis obtained for the only sampled site at ECDC is inclined approximately 45° E-ward. This axis has a counterclockwise rotational amount associated (Table 6, Fig. 6.8). This rotational axis was taken as the mean rotational axis for this part of the dike complex.

From sites at the MRDC counterclockwise and clockwise rotational axes were calculated. Counterclockwise axes incline, as usual, E-ward approximately 60° while the only clockwise axis has an almost horizontal inclination. Same as for MVU, amount of rotation of individual axes seems to increase S-ward. However, no groups or systematic variations were observed.

The mean rotational axis calculated for MRDC inclines E-ward and an associated rotational amount of approximately 35° (Fig. 6.8, Table 7). Such amount of rotational is larger than that calculated for the whole MVU, but similar (within errors) to that of the westernmost group identified on the MVU.

Mean rotational axes for both part of the dike complex are neither overlapped nor included into each other. This suggests that they represent different rotational axes, suggesting that these two parts of the dike complex evolved tectonically different.

6.3.2. Restoration of related structures

After mean rotational parameters were established, related structures – clastic beddings and dike orientations – were restored to their "original" position before rotation, i.e. to the time of

RM acquisition (Appendix B).

Clastic beddings were restored using the three rotational axes calculated for each group of the MVU. After restoration, orientations of clastic beddings do not change significantly, becoming a NNW-facing slope (Fig. 6.10a). Inclinations become shallower except for site S4 with an unusual inclination of ca. 48°. Despite this site, inclinations become systematically shallower towards westernmost sites, reaching an almost horizontal inclination at site S8.

Pillow lavas and lava flows of the MVU were also corrected according to the defined groups of the MVU. After restoration, their orientations become scatter forming, roughly, a NW to N-ward facing slope. Again, orientation of lava flow in the westernmost site (L3) becomes nearly horizontal (Fig. 6.10b). Most of the restored orientations have nearly EW-trending strikes, subparallel to the Estero Cono lineament (Fig. 6.1).

The insitu NW-SE and NNE-SSW striking orientation of feeder dikes of the MVU changes to a nearly NW-SE and NE-SW trending orientations after restoration (Fig. 6.10c). The NW-SE trending orientation is subparallel to the main Estero Cono lineament, while the NE-SW trending one is nearly perpendicular to it. This suggests that a fissure system, with a NW-SE trending, facilitated the intrusion of these dikes in the MVU.

The only site of pillow lava of CMU becomes a gentle SE-facing slope, with a shallow inclination angle of ca. 16° (Fig. 6.10d). This result is opposite, in orientation, to that obtained for the MVU deposits.

Since the orientation of the calculated rotational axis for the ECDC is near to that of the pole of the dikes, the restoration does not change significantly the orientation of this part of the dike complex which remains with mostly NE-SW trending strikes (Fig. 6.10e). In contrast, MRDC change its orientation significantly, from a nearly NW-SE trending orientation to a nearly NS-trending orientation (Fig. 6.10f). The orientations of both dike complexes are nearly subparallel, and no so far oriented to that of the CR system.

Of special importance is the orientation of the contact between the dike complex and the

gabbro units. After correction, the orientation of this contact becomes to a nearly NS strike with an inclination of ca. 80° (Fig. 6.10f). The strike of the contact is similar to the orientation of the Chile-Peru trench but the inclination is far larger than that of the subducting plates.

6.4. Fold test and rotational axes for multivectorial sites

6.4.1. "Young" folding and rotation

The orientations of compositional layering in gabbro and foliation in ultramafic rocks at sampled sites indicate, with some exceptions, that these units were roughly cylindrically folded about a shallowly E-ward axis. Thus, a fold test (Appendix B) was performed separately on "young" RM vectors of both gabbro and ultramafic (south, central and north) units using the strikes of compositional layering and foliation respectively.

For the gabbro unit, optimum unfolding percentage (associated with maximum eigenvalues; e.g. Tauxe, 1998) was obtained when compositional gabbro layers were folded back approximately 55% (Fig. 6.11a). In contrast, optimum unfolding percentages for each one of the ultramafic blocks were obtained when foliation was folded back ca. 75% (south block) and ca. 70% (central block) (Fig. 6.11b). Unfolding percentage for the northern ultramafic block could not be calculated since the two sampled sites on this block have associated similarly oriented foliations. Unfolding percentages correspond to an average unfolding of ca. 35° for the gabbro unit and ca. 43° for the ultramafic unit. This may indicate that the gabbro unit behaved slightly more rigid than the ultramafic rocks and that these rocks underwent open folding during the acquisition of young RM vectors.

However, the unfolding procedure only narrowed the range of widely scattered "young" RM vectors only a little (Fig. 6.5, 6.7), with their orientations still differing from that of the expected GAD. Thus, further calculations were carried out by assuming that the large and remaining

portion of the deformation in the plutonic units was accommodated through rotation.

Individual rotational axes for both ultramafic and gabbro units, labeled Rot-1, are mostly NE-ward inclined, from nearly vertical to nearly horizontal, and with counterclockwise associated rotational amounts (Table 8, 9). These orientations are similar to those of the rotational axes obtained for volcani-clastic and dike complex units. Associated rotational amounts seem to vary with the inclination of the axis; larger rotational amounts are associated to declinations of ca. 70° (Fig. 6.12a). However, no clear spatial variation between sampled sites could be established.

Orientation of mean rotational axes for both the gabbro and the ultramafic units incline E-ward (Fig. 6.12b), having EW-trending confidence intervals associated (ellipses) (Table 10). These confidence intervals are overlapped, both including the mean orientation of the other, indicating that they are statistically undistinguishable. Thus, these units rotated counterclockwise about the same rotational axis. Associated rotational amounts are large compared to that obtained for volcani-clastic and dike complex units, reaching amounts of ca. 90°. However, mean rotational amounts between these units are different; the gabbro unit recorded nearly 20° more counterclockwise rotation than the ultramafic unit (Table 11). Such difference supports the argument resulted from the unfolding analysis; that is, the ultramafic unit accommodated an important portion of the total deformation through folding, in addition to rotation, compared to that accommodated by the gabbro unit.

6.4.2. "Old" folding and rotation

"Old" RM vectors from the plutonic units were also corrected using the unfolding percentages and rotational amounts previously determined. After these corrections, "old" RM vectors change to normal polarity but still they are widely scattered in a steronet projection (Fig. 6.5, 6.7). Since previous unfolding percentages were only 55% and ca. 70% for gabbro and ultramafic rocks units, respectively, a second unfolding procedure (labeled Fold-2) was carried

out assuming that they were cylindrically folded.

In this analysis no optimum unfolding percentages of statistically significance were calculated (Fig. 6.13). Unfolding curves for each ultramafic rock block are inconsistent between them; 160% for north and south blocks and -30% for central block. Although north and south have same unfolding percentages, unfolding curves increase continuously with larger unfolding percentages. For this analysis, foliation was used as a reference frame. However, old RM vectors must be acquired before the development of pervasive foliation observed in the ultramafic rocks. Such pervasive foliation erased any primary structures that could be used as a reference frame. Thus, unfolding percentages obtained for the ultramafic blocks most probably do not represent any real tectonic event, and further (possible) rotational axes were not calculated.

For the analysis of the gabbro unit an optimum unfolding percentage of ca. -55% was calculated (Fig. 6.13). However, concentration of the unfolding histogram is not statistically significant and unfolding curve systematically decreases with increasing amounts of unfolding. Thus, further rotational axes were calculated assuming two possibilities, that: (1) the remaining deformation after Fold-2 was accommodated through rotation or (2) the whole deformation recorded in old RM vectors was accommodated through rotation or non-cylindrical folding (i.e. Fold-2 is false).

Rotational axes, calculated assuming that Fold-2 was positive (labeled Rot-2+), are mostly NW-ward inclined with steep inclinations. Similarly, rotational axes calculated assuming that Fold-2 was negative (labeled Rot-2-) are mostly NW-ward inclined, although some exceptions with east and west-ward inclined axes were obtained (Fig. 6.12a). Mostly clockwise rotations took place about either Rot-2+ or Rot-2-axes.

Mean rotational axes are both (Rot2+ and Rot-2-) similarly NW-ward inclined. However, their associated confidence intervals differ significantly; circularly for Rot-2+ and EW-trending elliptical for Rot-2- (Fig. 6.12b). Rotational amounts are as large as 90° clockwise, pattern not previously obtained from other units. Differences in rotational amount between these two

possibilities are not larger than 10° of clockwise rotation.

6.4.3. Restoration of related structures

Related structures, compositional layering in gabbro and foliation in ultramafic rocks, were restored to their "original" orientation before folding and rotational events, i.e. at the time of RM acquisition; similar to the restoration of volcani-clastic and dike complex units.

Restored orientations of foliation in ultramafic rocks, by using Fold-1 parameters, become nearly horizontal, with shallow scattered inclinations (Fig. 6.14). In contrast, the insitu S-SE-ward dipping compositional layers change to stable SSE-ward dippings of ca. 30°, yielding common S-ward younging directions (Fig. 6.15). These orientations of both foliation and compositional layering change after corrected by using Rot-1 parameters. Foliations become with stable SE to SW-ward dippings, with shallow inclinations on south block and steep ones in north and central blocks (Fig. 6.14). The S-ward younging direction of compositional layers of gabbro does not change after Rot-1 correction. However, their inclinations become scattered towards S and W directions, with dips as low as 20° and as much as 90° (Fig. 6.15).

The orientations of both foliation and compositional layers previously corrected above were used as a starting point for the further analysis. Assuming that part of the deformation was accommodated by the plutonic units by folding (Fold-2+). Corrected orientations of foliation become scattered, with nearly horizontal and nearly vertical orientations and, usually, NE-SW or EW-trending directions (Fig. 6.14) depending on the analyzed ultramafic block. For compositional layers, several overturned layers with incongruent younging directions were obtained (Fig. 6.15). These orientations change drastically for both structures after correction using Rot-2+ axes. Foliations become nearly perpendicular or nearly horizontally oriented while orientations of compositional layering becomes highly scattered with opposite and incongruent younging directions (Fig. 6.14, 6.15). Thus, Fold-2+ and Rot-2+ parameters were rejected

leading to assume that all the deformation recorded on "old" RM vectors from the plutonic units was accommodated through rotation only.

Corrected orientations of foliation (by using only Rot-2- parameters) become similar to those obtained above, i.e. scattered and with EW and NE-SW trending directions (Fig. 6.14). However, and as mentioned before, these corrected orientations may have not tectonic validation since "old" RM vectors and developed foliation may not provide with a reliable reference frame for corrections. Completely different is the case of corrected (using Rot-2- parameters) orientations of compositional layers in gabbro. After this correction, inclinations of compositional layers become stable toward SE-ward direction, with roughly decreasing amounts of inclination towards SE-ward sites. Also, younging directions are in agreement with compositional layers orientations, becoming younger towards SE-ward direction as well (Fig. 6.15).

Chapter 7: Ferromagnetic phase

Characteristic Curie temperatures, and associated errors, were determined for several rock units through thermomagnetic experiments and the "*differential method*" (e.g. Tauxe, 1998; Appendix C). Obtained heating ($T_{c\text{-}heat}$) and cooling ($T_{c\text{-}cool}$) characteristics Curie temperatures were used to determine the ferromagnetic phase involved in both the anisotropy of magnetic susceptibility (see further) and the RM signals.

All thermomagnetic curves of MVU samples – including clastic sediments, pillow lavas, lava flows and feeder dikes – as well as those from dike complex, gabbro and ultramafic rocks show abrupt decays between 550°C and 600°C for both heating and cooling phases (Fig. 7.1). This suggests the contribution of magnetite (Fe_3O_4) to the magnetic signals (e.g. Dunlop and Özdemir, 1997).

Calculated temperatures roughly agree with the observed decays. Average Curie temperatures are strikingly close to the 580°C for all lithologies, with the only exception of pillow lavas and feeder dikes of MVU, which yielded slightly lower temperatures of approximately 550°C (Table 12). However, obtained temperatures still suggest the contribution of magnetite to the magnetic signal (e.g. Dunlop and Özdemir, 1997).

Unusual Curie temperatures of 330° (obtained from one clastic and one dike complex samples) and 200°C were also calculated. The first suggests the contribution of greigite (Fe_3S_4) and/or pyrrothite ($Fe_{1-x}S$) (e.g. Dekkers, 1989; Roberts, 1995), while the second the contribution of TM60 (Titanomagnetite 60; $Fe_{2.4}Ti_{0.6}O_4$) and/or goethite (FeO(OH)) (e.g. Dunlop and Özdemir, 1997). However, related heating curves yielded only temperatures nearby 580°C, indicating that these may be noise included in the thermomagnetic data (Appendix C).

Unusual temperatures of between 200° and 480°C were also obtained from samples of the plutonic units. In the heating runs, two individual temperatures of 486°C and 225°C were obtained from two gabbro samples. The first is intermediate between pyrrothite/greigite and

magnetite while the second is intermediate between pyrrothite/greigite and goethite (e.g. Dekkers, 1989; Roberts, 1995; Dunlop and Özdemir, 1997). Since both unusual temperatures were obtained in two isolated samples, they most probably are only artifacts of the calculation, i.e. amplified noise (e.g. Tauxe, 1998).

Chapter 8: Sedimentary AMS fabrics

In order to determine weather the clastic sediments of the MVU were normally deposited in an oceanic environment or they provenance is the continent, the AMS fabrics of conglomerates (4 sites), sandstones (7 sites) and mudstones (3 sites) were determined (Fig. 8.1). Pillow lavas and lava flows that bound the sediments show evidences of intrusion in shallow water conditions (e.g. Nelson et al., 1993; Lagabrielle et al., 1994, 2000; Guivel et al., 1996, 1999), suggesting that they were erupted close or in their actual location. Main NW-ward paleocurrent directions of sedimentary transport were determined by Nelson et al. (1993) based on the orientations of sedimentary structures – such as ripple marks, convolute folds, etc – present in these deposits.

Expected AMS fabrics are different depending on the type of sediment; sandstone and mudstone are expected to display fabric patterns typical of those of deposition, compaction and/or relative weak flows (e.g. King, 1955, Granar, 1958; Hrouda, 1982, Tarling and Hrouda, 1993); while conglomerate are expected to display fabrics typical of turbiditic currents (e.g. Tarling and Hrouda, 1993) (Appendix D).

8.1. AMS fabrics shapes

Bulk intensities range from 10^{-4} to 10^{-2} [SI] (Fig. 8.2a), which suggests the contribution of strong ferromagnetic minerals, such as magnetite, haemo-ilmenite and/or hematite to the susceptibility fabrics (e.g. Tarling and Hrouda, 1993). Higher bulk susceptibilities were obtained from sandstones while lower ones were from conglomerates. Thus, sandstones and conglomerates can be easily distinguished from each other using this parameter. In contrast, mudstones samples yielded K_{bulk} values intermediate between conglomerates and sandstones.

Analyzed conglomerates samples display nearly isotropic fabrics, accounted by both L vs. F and P' parameters (Appendix D; Fig. 8.2b), suggesting that they were deposited by strong

velocity (chaotic) current flows (e.g. Tarling and Hrouda, 1993). In contrast, sandstones display mostly oblate fabrics (Fig. 8.2c). This suggests that sandstones were deposited under the influence of medium or weak velocity currents. Only exceptions are sites S1 and S5 which display slight prolate fabrics. These later sites are stratigraphically on top of conglomerates layers, which suggest a reduction in velocity of the chaotic flow that deposited the conglomerates. Similarly, mudstones display strong oblate fabrics (Fig. 8.2d), which suggest deposition and/or compaction under the influence of very weak or null velocity flows.

Thus, a velocity reduction pattern is accounted by the different AMS fabric shapes, from conglomerates to mudstones. The fact that the grain size, in the whole clastic sequence, reduces constantly upsequence and W-ward suggest that sediments were deposited by a current flow originated in the easternmost edge of Estero Cono, and not in a mid-oceanic ridge environment.

8.2. Paleocurrent directions

Although different AMS fabrics pattern were obtained (Fig. 8.1), paleocurrent directions were inferred from the orientation of the principal AMS axes, K_{max}, K_{int} and K_{min} (Appendix D), and from their relative orientation with respect to the bedding plane in the case of sandstones and mudstones (Appendix D). In addition, the relative orientations of these axes give information about the nature of the transporting flow, similar to the AMS fabric shapes.

The orientation of the principal AMS axes of conglomerates is consistent from site to site, displaying a good concentration of K_{max} axes and randomly distributed, along a great circle, K_{int} and K_{min} axes (Fig. 8.1). These fabric patterns resemble those of a turbiditic flow and/or chaotic and strong velocity currents (e.g. Ellwood and Ledbetter, 1977; Tarling and Hrouda, 1993). Two different K_{max} concentration patterns were observed: (1) near the bedding strike in sites C2 and C3, and (2) near the bedding dipdirection at site C1 (Fig. 8.1). After bedding orientations were restored to the horizontal, paleocurrent directions were determined by the trending of the K_{int}-

K_{min} plane (Appendix D). Thus, from site C1 a NE-SW trending paleocurrent direction was inferred whereas for sites C2 and C3 a NNW-SSE to NW-SE paleocurrent direction was inferred (Fig. 8.3). The first direction is parallel to the Caleta Monona lineament while the second is parallel to the main trend of Estero Cono (Fig. 8.1).

Sandstones and mudstone fabrics, mostly oblate, display a good concentration of each of their principal AMS axes; namely these fabrics are triaxial (Fig. 8.1). In general, K_{min} axes are nearly vertically oriented and K_{max} and K_{int} axes are located near the horizontal plane (after correction of the bedding to the horizontal). This pattern suggests deposition/compaction processes under the influence of low, weak (sandstones) or null (mudstones) velocity currents (e.g. Hrouda, 1982; Tarling and Hrouda, 1993). Paleocurrent directions were inferred from the difference in orientation between K_{min} axes and the bedding pole (Appendix D). However, two sites (S5 and S7 in Cono Island; Fig. 8.1) display fabrics that resemble those of conglomerates, and related paleocurrent directions (defined by the K_{int}-K_{min} plane) were also considered in the analysis.

In general, NW to W-ward paleocurrent directions were inferred (Fig. 8.3). Sites located in the westernmost part of the clastic sequence (sites S1-S3) yielded NW-ward paleocurrent whereas those in the easternmost part yielded mostly W-ward (mudstones) or null (sites S8) paleocurrent directions. Sites located in the middle part of the sequence (S4 to S7) yielded scattered paleocurrent direction mostly trending NW-SE or NE-ward paleocurrent directions (Table 13). Although paleocurrent directions are slightly scattered, they agree with those reported by Nelson et al. (1993).

Inferred paleocurrent directions seem to be roughly clustered about both NW-SE trending and W-ward directions. However, counterclockwise rotations inferred from paleomagnetic analyses indicated that these paleocurrents directions should be corrected (Fig. 6.8). Paleocurrent directions were corrected site by site due to the presence of counterclockwise and clockwise rotations and different amounts of rotation from site to site. Unfortunately, not all analyzed sites have information about the involved rotations. In such cases, the rotational axis and associated

amount of rotation of the closest site was used to correct the paleocurrent direction. After correction, paleocurrent directions become even better clustered in a NW-ward direction, subparallel to the main Estero Cono lineament (Fig. 8.4), whereas minor NS and EW trending paleocurrent directions become subparallel to the Caleta Monona lineament (i.e. NNE-SSW trending and E-ward).

8.3. Depositional slope

The distribution of the principal AMS axes and their orientation with respect to the bedding plane can give more information, besides paleocurrent directions, about the depositional slope and the sedimentary processes involved. AMS fabrics from westernmost sandstones sites (S1-S3) commonly exhibit their K_{max} axes located near the bedding strike (Fig. 8.1) and the K_{max}-K_{int} plane forming and angle less than 10° with the bedding plane. This suggest that sandstones, at these sites, were deposited in a NW-facing slope in which prolate-like particles rolled down the slope arranging their long axes perpendicular to the slope direction (e.g. Tarling and Hrouda, 1993). Similar pattern was observed at sites M1 and M2, in where the K_{max}-K_{int} plane forms an angle less than 5° with the bedding plane. As before, this suggest that the depositional surface was facing NW to W-ward. At the westernmost site, S8, K_{max} axes are not oriented close to the bedding strike; however, K_{min} axes have nearly the same orientation as the bedding pole, indicating that deposition occurred in a nearly horizontal surface and perhaps under the influence of a very weak SE-ward paleocurrent.

This "*original*" bedding orientation – NW-facing and becoming shallower in inclination towards westernmost sites – was previously determined, independently, through the paleomagnetic analysis and the paleomagnetic restoration of these deposits (Fig. 6.8).

Chapter 9: Discussion

9.1. Stress fields

9.1.1. Ophiolite obduction and development of brittle faulting

Fault-slip data analyses, by means of the multi-inverse method, were carried out on data collected from the plutonic units and from the eastern margin of the ophiolite. The majority of collected fault-slip data indicates the development of inverse and strike slip faults (Fig. 5.1), generated and/or activated by a compressional stress state (transtensional and/or transpressional) rather than an extensional one. However, compression induced over ophiolite only occurred during and after the obduction and not in the mid-oceanic ridge where extensional stresses are present. Several causes may have produced compression over the ophiolite, and therefore the development of brittle faulting, like for example: (1) emplacement of plutonic bodies in the northern and southern margins of the ophiolite or (2) the continuous subduction of the Nazca-Antarctic plate system, and the CR system, offshore the Taitao peninsula (Fig. 3.3).

According to Yañez and Cembrano (2000) and Yañez et al. (2002) the subduction of a bathymetric anomaly, such as the CR system, results in contrasting stress fields, transpressional north of the CTJ and transtensional south of it. Since the CTJ migrated north and southward offshore the Taitao peninsula (Fig. 3.3), it is expected that the change in stress field conditions was recorded by the brittle faults present in the ophiolite. Thus, and following Nelson et al. (1993), brittle deformation of the ophiolite occurred during the obduction and/or during subsequent uplift of the ophiolite.

Analyses of the fault-slip data revealed three (five) stress fields that affected the ophiolite. Their orientations and characteristics indicate multi-deformation phases, recorded in the plutonic units (A and B solutions) and in the eastern margin of the ophiolite (C solution) (Fig. 5.2).

9.1.2. Development of brittle faulting in the plutonic units

In the plutonic units two stress fields were identified (labeled "A" and "B"; Fig. 5.2). Both solutions correspond to inverse stress fields with vertical extensional axes, differing in their stress ratios (0.1 to 0.7 for "A" and 0.2 to 0.6 for "B" solutions) and in the orientation of their compressional axes. Stress ratio values are in the range of transpressional stress field (0.1-0.5) but slightly included in the transtensional one (0.5-0.7). This wide variation in stress ratios of both solutions can be easily explained by involving the subduction of the Nazca-Antarctic plate system offshore of the Taitao area. This subduction induced alternating and contrasting stress field (transpressional and transtensional) offshore of the Taitao area (e.g. Yañez and Cembrano, 2000; Yañez et al., 2002).

The average convergence vector for the Nazca-Antarctic plate system had had an E-ward direction for the last ca. 10 My time without experienced important changes in orientation (e.g. Cande and Leslie, 1986). The E-ward convergence direction of the subducting oceanic plates is similar in orientation to the compressional axis of the "A" solution (Fig. 2.3, 5.2). Due to these similar orientations and the expected stress ratio variation mentioned above, the "A" stress field solution is interpreted to be the result of the convergence and subduction of the current oceanic plate system offshore the Taitao peninsula (Fig. 9.1).

In contrast, the compressional axis for the "B" solution is oriented approximately 60° counterclockwise rotated with respect to both the average Nazca-Antarctic convergence vector and the compressional axis for the "A" solution. Then, what resulted in the "B" stress field? Is it the result of the emplacement of plutonic bodies NNE and SSW (Fig. 1.5) of the ophiolite? Or the compressional stress induced in the forearc region changed from NNE-SSW-ward to EW-ward? Or the stress field "B" was generated similarly as the "A" stress field but it was counterclockwise rotated?

The emplacement of these plutonic bodies may have resulted in NE-SW-ward compression

over the ophiolite, with extensional axis vertically oriented. Such configuration agrees with the orientation of compressional and extensional axes for the "B" solution. However, this emplacement-induced stress field must have a restricted stress ratio value, most likely near pure axial compression, but "B" solution has a wide variation in its stress ratio value (0.2 to 0.6) not indicative of a pure compressional state.

The convergence vector of the Nazca-Antarctic plate system has experience no significant change for, at least, the last 10 My time (Cande and Leslie, 1986; Forsythe and Prior, 1992; Lagabrielle et al., 2000), remaining E-ward. Since fission track data indicates that uplifting, and probably obduction too, started approximately 6 My ago (Table 1), it is not likely that the induced stress field over the ophiolite changed for the last 6 My.

The obduction of the ophiolite cannot be explained by the simple incorporation of a block into the forearc. It is more likely that the different blocks experienced rotations during the obduction process, similar to that reported for the Oman Ophiolite (e.g. Thomas et al., 1988). The dextral BBFZ seems had played an important role during the obduction, resulting in a counterclockwise rotation of the ophiolite (Fig. 9.1b). This counterclockwise rotation was also independently identified through the paleomagnetic analyses. Then the "B" stress field is interpreted as the result of the subduction of the Nazca-Antarctic plate system offshore the Taitao area, similar to the "A" stress field solution, but the recorded compressional axis was counterclockwise rotated due to the similar rotation of the ophiolite.

Crosscutting relationships between fault-planes suggest a synchronous activity of the two identified sets of brittle faults. Rotation of the ophiolite resulted in the rotation of early-generated structures in the plutonic unit. Rotated structures were no longer able to absorb the deformation induced by the oceanic plate system subduction. As a result, new fault planes were generated to absorb the still induced compression. However, rotation of the ophiolite was a steady-state process, and some early-generated faults were still active during the generation of the new faults. This produced the observed dual crosscutting relationships observed between both fault sets.

9.1.3. Development of brittle faulting near the BBFZ

Analyses of the fault-slip data from the eastern margin of the ophiolite, one main and two minor solutions were obtained (labeled "C", "D" and "E"; Fig. 5.2). Orientation of compressional axes is roughly EW trending while that of the extensional axes varies from NS to NE-ward directions. Stress ratio values are as widely distributed as for solutions obtained from the faults in the plutonic units ("A" and "B"), ranging between 0.1 and 0.6 for "C", 0.2 and 0.6 for "D" and between 0.7 and 0.8 for "E".

For the main "C" solution, orientation of compressional axis is similar to that of the "A" stress field and to the average Nazca-Antarctic convergence vector. In contrast, the orientation of the extensional axis is nearly NS-trending. Stress ratio values are also similar to that of the "A" stress field, but more restricted to a compressional stress state (Fig. 5.2). Nevertheless, they agree with the expected variation in stress ratios induced by the repeated subduction of the CR system offshore the Taitao area (Fig. 3.5).

Partition of deformation (e.g. Passchier and Trouw, 1996; Cembrano et al., 2000) is a common feature in modern and ancient orogens, especially in the Andes belt where non-orthogonal acting stresses, over the overriding plate, become separated into compressional, near the trench, and strike-slip, far from the trench (e.g. Fitch, 1972; Bruhn et al., 2004) (Fig. 3.1). Then, the homogeneous stress field induced in the Taitao area divided into two components, which share a common direction for the compressional axis. As mentioned before, deformation in the plutonic unit has mainly inverse characteristics whereas that nearby the BBFZ has strike-slip characteristics. Since the convergence vector of the plates system is slightly oblique to the South American plate margin, right-lateral strike-slip displacements could be expected, with some minor vertical movements (normal or inverse), due to local accommodations of the deformation in the distal area from the plate convergence zone (e.g. Fitch, 1972). Thus, the "C" stress field solution is interpreted as the result of the partition of the deformation induced by the

subducting plates offshore the Taitao area.

The orientation of the principal stress axes for the "D" solution do not coincide neither with any of the previous identified stress fields nor with the convergence vector of the Nazca-Antarctic plate system. However, the orientations of these stress axes are not far from those of "C" stress field. Moreover, the observed stress ratio variation for the "D" solution is included in the wide range of stress ratio for the "C" stress field (Fig. 5.2), and the "D" solution is only accounted when the fault-slip data is divided. This suggests that the "D" solution is most probably an artifact of the calculation or a local solution of the BBFZ or a sub-solution of the "C" stress field due to an improvement in resolution of the multi-inverse method.

If "D" is an artifact of the calculation, then a restricted stress ratio value should be expected and randomly oriented axes. The orientation of the compressional axes for the "C" and "D" solution differ approximately 10°-15°, which is acceptable if some local accommodations occurred during the deformation (e.g. Lavenu et al., 1995). Then, the "D" solution is interpreted as a local solution of the "C" stress field, most probably as the result of small accommodations of the BBFZ.

In contrast, the orientation of the compressional axis for the "E" solution roughly coincides with the convergence direction of the Nazca-Antarctic plate system. However, the orientation of the extensional axis is far from any other identified solution. The stress ratio values for this solution are restricted to a compressional stress state and it does not coincide with any expected values. Thus, the "E" solution is interpreted as an artifact of the calculation.

9.1.4. Time-dynamic evolution of the stress field

Due to the lack of crosscutting relationships between inner and outer brittle fault sets, it is difficult to deduce temporality between the identified stress fields. Even more complex is to establish the temporality between faults in the plutonic units due to double crosscutting

relationships (Fig. 5.1). The "A" and "C" (plus "D") identified stress fields are easily correlated with the geodynamic framework of the Taitao area. In contrast, the "B" stress field is counterclockwise rotated with respect to the induced stress field in the Taitao area. If the principal stress axes of the "B" stress field are clockwise rotated, then they become similarly oriented as those of the "A" stress field. This suggests that the "B" stress field must be older than the "A" stress field.

The compressional axis of the "C" (and "D") stress field coincides with that of the "A" stress field and with the convergence vector of the subducting plates. However, due to the lack of crosscutting relations between faults developed in the plutonic units and those developed in the eastern margin of the ophiolite no temporal relationship can be established between "A" (or "B") and "C" stress fields. Nevertheless, induced stress field (resulted from the non-orthogonal subduction of the oceanic plates system) must have divided into its compressional ("A" or "B") and strike-slip ("C") components, acting near and far from the trench respectively (e.g. Fitch, 1972).

Thus, "B" and "C" stress fields were most probably synchronous, in where the compressional component resulted in the generation of inverse-like structures in the plutonic units whereas the strike-slip component resulted in the development of the BBFZ. Later on, the ophiolite rotated counterclockwise and with it the structures generated by the "B" stress field. Since the stress field induced over the Taitao area did not change, the "A" stress field was recorded by the newly generated structures in the plutonic units, while the "C" stress field was still being recorded by the faults of the BBFZ (Fig. 9.1).

9.2 Ferromagnetic phase and acquisition of RM vectors

Curie temperatures calculated from ultramafic and gabbro samples are close to the 580°C expected from the contribution of magnetite crystals (e.g. Dunlop and Özdemir, 1997). These

crystals must have formed during the cooling of these rocks as they were pushed away from the spreading center axis. Ultramafic and gabbro units were under high temperatures nearby the CR system, but temperature decreased rapidly as the oceanic crust moved away from the spreading center axis. Thus, it is most likely that magnetization (observed as old RM vectors in the demagnetization paths) of both units is primary and it was acquired after the oceanic crust moved away from the spreading center axis.

The high thermal regime imposed over the Taitao area due to the subduction of the active CR system (e.g. Lagabrielle et al., 2000) was unable to reset the primary acquired magnetization (old RM vectors), and the primary acquired magnetization was only partially erased. The subduction of the active CR system not only resulted in an increase in the geothermal gradient but also must have resulted in the release of some fluids all over the Taitao area. These fluids could have produced a deuteric metasomatism of the magnetite crystals (e.g. Butler, 1992), allowing them to acquire a secondary chemical magnetization (seen as younger RM vectors).

Curie temperatures calculated for the dike complex, only obtained from MRDC dikes, yielded values of approximately 577.8°±2.8°C. This suggests that main carrier of the magnetization is magnetite. Since paleomagnetic analyses only yielded one consistent RM vector, in addition to a VRM component (noise) recorded recently, suggests that the observed high stability RM vectors corresponds to a primary thermal magnetization. However, since the dike complex is part of the ophiolite, its magnetite crystals should carry the same amount of information those crystals in the plutonic units. The similar orientations of "young" RM vectors from the plutonic units and the high-stability RM vectors from the dike complex unit suggest that magnetite crystals in the dike complex were either remagnetized or formed synchronously or after the plutonic units acquired their secondary magnetization. The high supply of fluids in the upper part of the oceanic crust was able to change the primary mineral association due to a deuteric metasomatism (e.g. Butler, 1992). Primary magnetite crystals were destroyed and new magnetite crystals were formed at the time that secondary magnetization was acquired in the plutonic units.

Average Curie temperature calculated from clastic sedimentary samples is 577.3°±3.0°C which implies that the magnetic signals were carried mainly by magnetite (e.g. Dunlop and Özdemir, 1997). Since stable within site RM vectors were obtained, crystals must have formed during diagenesis processes, produced by the precipitation of magnetic minerals (chemical magnetization), or eroded from detrital sources (detrital magnetization) (e.g. Butler, 1992). The impossibility to obtain reliable RM vectors from conglomerate samples suggest that magnetization is detrital, but the stable RM vectors obtained from sandstones samples suggest that magnetization is chemical. This apparent contradiction can be solved by knowing the size of the magnetite crystals. RM vectors in multi-domain (MD) size magnetite crystals are commonly unstable due to the presence of different magnetic domains in each crystal (e.g. Butler et al., 1992), but those carried by single-domain (SD) or pseudo-single-domain (PSD) are stable. This suggests that magnetization in clastic sediments is chemical, acquired by MD magnetite crystals in conglomerates and by PSD and/or SD magnetite crystals in sandstones and mudstones.

Another characteristic of magnetite crystals is their dual AMS characteristics depending on their size. MD and PSD crystals display "*normal*" AMS fabrics (where AMS axes correspond one by one to the petrofabric axes) while SD crystals display "*reverse*" AMS fabrics (Rochette et al., 1992). AMS fabrics obtained from clastic sediments are close to expected from normal sedimentary fabrics, suggesting that magnetite crystals are in the MD or PSD size range. This, together with the nature of magnetization, suggests that magnetite crystals are perhaps in the PSD size state. However, more analyses are necessary to establish the true nature of these crystals.

Obtained Curie temperatures of 546.4°±36.6°C from volcanic deposits of the MVU are slightly lower than those obtained from clastic sediments, but within the large associated errors the 580°C temperature expected from the contribution of magnetite is included (e.g. Dunlop and Özdemir, 1997). The slightly lower Curie temperatures are perhaps the result of a slightly higher Ti content in the magnetite crystals. Acquisition of RM vectors must have occurred during the

cooling of these rocks, which is very fast due to a quenching effect produced by the surrounding water in where they extrude. Thus, RM vectors are considered to be the result of a primary thermally acquired magnetization.

9.3. Rotation and deformation patterns

The previous identified counterclockwise rotation of the plutonic units, through stress field analyses, is not enough to establish an accurate rotational, neither deformational, pattern for the whole ophiolite. No information about the rotational and deformational pattern of the dike complex and volcani-clastic units is available through the stress field analyses. Thus, paleomagnetic analyses were carried out on each of the rock units (Fig. 1.5, 6.1) to determine the rotational and deformational patterns of these units. Similar counterclockwise rotations about similarly E-ward oriented axes (Fig. 9.2) were identified from each of the rock units in addition to a clockwise rotation, about a NW-ward axis, only identified in the plutonic units. These later rotation seems to be synchronous with folding of these units.

9.3.1. Time of magnetic acquisition and rotational events

Several chronological constraints for the clastic sediments, submarine lavas and gabbro units are currently available (Fig. 3.8, Table 1), but these ages can not be directly correlated with the identified rotational and folding events. Volcani-clastic units (MVU and CMU) age ages between 5 and 2 Ma. Since isolated RM vectors from these units are primary and only one rotation was identified, then isolated RM vectors must have being acquired shortly after the formation of these rocks, i.e. ca. 5 Ma, Thus, the identified rotational event must have started about 5 My ago and the estimated degree of rotation presents a full-record of cumulative rotations.

An age of approximately 13 Ma (K/Ar, whole rock; Bourgois et al., 1993) is available for the

gabbro unit. However, this age is perhaps overestimated due to excess of Ar in the sample (Orihashi, Y., personal communication), providing only with a maximum age for the generation of the ophiolite at the CR spreading center. Another set of ages of approximately 6 Ma (K/Ar, hornblende and Fission track analyses; LeMoigne, 1994, this study) provides with a cooling age for the gabbro unit and therefore with an age close to the uplift, and perhaps rotation and deformation, for the plutonic units. Since the orientation of the "young" rotational axes obtained for the plutonic units can be easily correlated with those obtained for the dike complex and MVU units (with a maximum age of approximately 5 Ma), "young" RM vectors must have being acquired during, or shortly after, the uplift event. Since rotational amounts calculated for the plutonic units are far larger than those for the dike complex and MVU units, the "young" counterclockwise rotation must have started shortly before the rotation identified in the MVU, i.e. after 6 Ma.

Since "young" RM vectors were acquired after "old" RM vectors the clockwise rotation inferred from these later ones must have ceased slightly before 6 Ma. An older age limit for this rotation is not possible to constrain, since the ca. 13 Ma age is probably not representative for the plutonic units and does not provide with an age for the acquisition of "old" RM vectors.

9.3.2. Tectonic evolution of volcani-clastic deposits

From volcani-clastic deposits of the MVU one stable mean RM vectors was obtained at each analyzed site. The observed distribution of calculated rotational axes and the W-ward increasing of associated rotational amounts defined three different groups in the area (Fig. 6.9). The orientation of the calculated rotational axes for the MVU is similar, and statistically undistinguishable, to those calculated for the plutonic units. Therefore, the counterclockwise rotation identified in the MVU was associated to the "young" counterclockwise rotation identified in the plutonic units.

Using the available ages for these volcani-clastic deposits, calculated rotational amounts and assuming that rotations have being steady-state, rotational rates of ca. 6.4°/My, ca. 5.8°/My and ca. 12.1°/Ma for the eastern, central and western groups of the MVU were calculated, respectively (Table 14). Although these ages and rotational amounts can not be fully correlated to each other, it seems that westernmost deposits rotated faster then easternmost ones.

The distribution of individual rotational axes at each site, the orientations of mean rotational axes for each defined group and the associated elliptical confidence intervals, suggest that rotation of these deposits was controlled by the movement of a NW-SE trending strike-slip developed in the bottom of the Estero Cono area. The common presence of normal faults, especially in the westernmost part of Estero Cono, suggests that the strike-slip fault has an increasing extensional component W-ward, adopting a negative flower structure (e.g. Suppe, 1985) (Fig. 9.3).

The "young" counterclockwise rotation of the plutonic units and dike complex generated tectonic gaps between these units and the metamorphic basement (Fig. 9.4a); weaken the forearc crust north and east of the plutonic units. Newly generated volcanic products extruded through this weaken forearc areas (e.g. Guivel et al., 1993; Lagabrielle et al., 2000), perhaps through a fisural NW-SE trending system generated by the activity of the strike-slip fault in the area. Clastic sediments, eroded from eastern detrital sources, were also deposited in these tectonic gaps, as AMS analyses showed (see further). The newly extruded and deposited MVU also rotated with the rest of the ophiolite units, but recording only the later portion of the counterclockwise rotation.

The different group rotations identified on the MVU and the differences in rotational amounts can be explained through a "migrating pivot" model (Fig. 9.4b). In this model, newly extruded volcanic products in the westernmost edge of Estero Cono underwent counterclockwise rotation about a slightly E-ward inclined rotational axis. As counterclockwise rotation continued, the rotational axis (or pivot) migrated towards east to a second rotational axis. The first rotational

axis was then abandoned, and rotation of both the newly generated block and the old one occurred about the second rotational axis. This resulted in a re-orientation of the first rotational axis; more inclined towards east. Furthermore, this process repeated and the rotational axis migrated, again, E-ward to a third rotational axis. Again, rotation of the whole western part and the newly generated block occurred about this third rotational axis, and as a result the second rotational axis inclined more E-ward (Fig. 9.4b).

The reconstruction of the rotated block using the "*migrating pivot*" model is able to reproduce the coastal shape of the southern shore of Estero Cono, with its different inlets such as Caleta Monona, Caleta Pascuas and Caleta Gallegos (Fig. 8.1). The migration of this rotational axis, or pivot, is perhaps a consequence of the development of the strike-slip fault in the Estero Cono area induced by the E-ward migration of the deformation resulted from the generation of an asthenospheric window beneath the Taitao area (Fig. 9.5) (e.g. Guivel et al., 2003). This fault opened as scissors towards east, allowing the rotation of the different blocks.

A different rotational pattern was identified for CMU deposits. The orientation of the mean rotational axis is similar that of the "young" rotation in the plutonic units. However, the calculated rotational amount is far larger than that calculated for MVU, and only comparable to that calculated for the plutonic units. The local geodynamic environment of the CMU is slightly different from the rest of the peninsula; in this area the major NNE-SSW trending BBFZ affected the CMU most probably rotating it counterclockwise.

Using the orientation of the rotational axis and the associated rotational amount the "*original*" configuration of the CMU at the time of deposition was calculated to elongate nearly EW, subparallel to the transform faults that separate the segments of the CR system (Fig. 3.2). This may imply that the CMU deposited near or in a transform fault valley. This is not contradictory to the petrochemical characteristics; Guivel et al. (1999) suggested that volcanic deposits of the CMU were generated from MORB-like (Mid-Oceanic Ridge Basalts) magmas with little or no contamination of continental material. However, this reconstruction deduced from a single site

analysis may not be reliable.

9.3.3. Tectonic evolution of the bimodal dike complex

This analysis was carried out from isolated RM vectors isolated at both, MRDC and ECDC, expositions of the dike complex (Fig. 1.5, 6.1). At these two localities only one RM vector was obtained from each site. The orientation of the calculated mean rotational axis for the MRDC is similar, and statistically undistinguishable, from those calculated for the MVU and the "young" rotation of the plutonic units. Thus, the registered rotation was associated to the "young" counterclockwise rotation that affected the whole ophiolite. In contrast, the orientation of the rotational axes calculated for the ECDC is far from any other calculated rotational axis. However, the associated rotational amount is comparable to that of the MRDC (Table 7), suggesting that both complexes underwent similar rotation but about differently oriented axes.

The "original" orientation of both dike complexes was calculated using the mean rotational axes and associated amounts of rotation (Fig. 6.10). After restoration, strikes of dikes in ECDC do not change significantly, but dikes become more vertical with a NNE-SSW-ward strike and dipping towards west and east. Similarly, dikes in the MRDC become NS-trending and dipping towards both east and west direction (Fig. 6.10) after the restoration. These orientations agree with those proposed for dike intrusion in an oceanic ridge environment (e.g. Borradaile, 2001) and with natural observations in Hess Deep in the East Pacific Rise (e.g. Hurst et al., 1994; Varga et al., 2004). There, dikes intrude nearly vertical dipping towards both sides of the main intrusion orientation.

These restorations suggest that the main trends of the MRDC and the ECDC were subparallel and therefore that they were probably continuous or, at least, subparallel. The problem at this point is that the petrological associations of both dike complexes are different. However, and according to Guivel et al. (1999) the petrological compositions of bimodal dike complex is

highly variable. This may explain petrological differences within the same dike complex.

The orientation of the restored dike complex does not fit that of the CR system; instead they are rotated clockwise about 10°-20°. Deflection, or rotation, in the trending of the dike complex can be the result of dragging forces nearby the transform faults that separate the segments of the CR system. Here, the dike complex rotates about a vertical (?) axis due to the movement of the transform fault, becoming little by little parallel to it, as in the case of the dike complex of the Troodos ophiolite in Cyprus (Gass et al., 1994; Borradaile, 2001).

9.3.4. Tectonic evolution of the plutonic units

a. Folding and "young" rotation

In the gabbro unit, optimum unfolding percentage of 55% restores the compositional layers to their "*original*" orientation before the folding event, which are S-to-SE-ward dipping directions (with no overturned layers). Also, all restored "young" RM vectors become reverse polarity (Fig. 6.15), indicating that magnetization was acquired during the folding of compositional layering in a period of reverse magnetic field. However, unfolding procedure did not restore the orientation of young RM vectors to the expected GAD orientation, and mean RM vectors are still scattered when plotted in a steronet (Fig. 6.15).

A similar folding pattern was observed in the ultramafic unit, with an optimum unfolding percentage varying between 70% and 75%, depending on the analyzed block (Fig. 6.11). Unfolding restoration reoriented ultramafic foliation to an almost horizontal position, dipping slightly towards NE direction. "Young" RM vectors were not corrected to the orientation of the expected GAD by the unfolding procedure, and they remain widely scatter in a stereonet projection (Fig. 6.14).

Assuming that the rest of the deformation was absorbed through rotation of both units, large counterclockwise rotations about similarly NE-ward inclined axes were calculated for both units

(Fig. 6.12). These axes are statistically undistinguishable, suggesting that rotation of both units occurred about the same NE-ward inclined axis. This large rotation is comparable with those (about vertical axes) identified on accreted crustal blocks and other ophiolites during their obduction into active tectonic settings; such as New Zealand, the Eastern Mediterranean Massif and the Oman ophiolites (e.g. Gattacceca and Speranza, 2002; Lamb, 1988; Thomas et al., 1988).

Calculated amounts of rotation differ between these two units, affecting more the gabbro than the ultramafic unit, with a difference of ca. 20°. Assuming that rotation of these units was a steady-state process, a rotational rate of ca. 14°/My was calculated (Table 14). On the contrary, folding affected more the ultramafic than the gabbro unit, with a difference of ca. 20% shortening. These differences indicate that the young deformation of the plutonic units was a synchronous combination of folding and rotation rather than separate and discrete events on time.

Differences in amount of rotation and unfolding percentages can be attributed to differences in mechanical behavior (competence, ductility, etc) of these rocks (e.g. Wilks and Carter, 1990; Turcotte and Schubert, 1982). Ultramafic rocks are more viscous than gabbro, and they tend to absorb the deformation through ductile structures rather than brittle ones. Thus, the observed differences were most probably because the ultramafic unit absorbed a larger portion of the deformation through folding and flexural slip along foliations rather than rotation, perhaps as a result of a extra pure shear strain induced by the rotation of the gabbro unit.

Folding occurs under ductile conditions whereas brittle faulting occurs under brittle conditions. Stress analyses of the plutonic units indicate that they experienced a counterclockwise rotation of about 60° (although no information about the orientation of the rotational axis could be obtained from that analysis) under brittle conditions. This "brittle" rotation accounts for *ca.* 64% and 78% of the rotation experienced by the ultramafic and gabbro unit respectively. Thus, ca. 36% (gabbro) and 22% (ultramafic) of the rotations most probably occurred under ductile conditions together with the folding event.

b. Old rotation

A second unfolding analysis of the plutonic units yielded no optimum unfolding percentage (Fig. 6.13) and therefore it was assumed that the whole deformation recorded by "old" RM vectors was absorbed through rotation. Also, the probably post-obduction foliation developed in the ultramafic unit was not used in the analysis, leading any further analysis restricted to the gabbro unit solely.

Large clockwise rotations, of approximately 90°, were necessary to restore the orientations of the widely scattered "old" RM vectors (which were corrected previously together with "young" RM vectors) to the orientation of the expected GAD. The orientation of the calculated mean rotational axis, for this "old" event, is NW-ward inclined; contrary to the NE to E-ward inclined axes calculated for the "young" counterclockwise rotation identified in all the ophiolite units (Fig. 9.2).

Assuming that compositional layers of gabbro formed in a high temperature magma chamber before they cooled down their Curie temperature (ca. 580°C), they were restored to their "original" orientation. Restoration of compositional layers was previously carried out by using rotational (counterclockwise) and folding patterns calculated from the orientation of "young" RM vectors. After the "young" restoration, "old" RM vectors are still scattered over a stereonet and their orientations do not coincide with that of the expected GAD. By using the rotational axes obtained from "old" RM vectors, orientations of compositional layers of gabbro become with an almost steady orientation, with nearly NE-SW trending strikes, and with congruent upward younging directions (Fig. 6.15).

After these restorations, folding and both rotations, the steepest compositional layers are located in the westernmost part of the gabbro unit. Restored compositional layers turn gradually to shallower inclinations towards E-to-SE directions, reaching nearly 60° E-ward dipping nearby the easternmost edge of the unit. This suggests that the paleo-magma chamber, developed at the CR spreading system, had an asymmetrical "*mushroom*" shape (Fig. 9.6), in where steepest

compositional layers were located nearby the spreading center axis. Steepest inclination of compositional layers was the result of deflection produced by the uplift of the mantle beneath them at the spreading axis. This setting agrees with mid-oceanic magma chambers proposed by Nicolas (1995) and Nicolas et al. (1993), where compositional layers become more horizontal as they are pushed away from the spreading center by the uprising of the mantle at the spreading center axis.

9.4 AMS fabrics of clastic deposits of the MVU

9.4.1. Paleocurrent directions and depositional slope characteristics

AMS fabrics from clastic sediments of the MVU (Fig. 8.1) were determined in order to estimate paleocurrent directions and velocities as well as slope or depositional surface. AMS fabrics yielded two distinct patterns; observed in conglomerates and in sandstones and mudstones deposits.

Conglomerate AMS fabrics resemble those of turbiditic, high current and chaotic velocity flows while that of sandstones and mudstones resembles those of deposition and/or compaction under the influence of medium (sandstones) to weak (mudstones) velocity currents (e.g. King, 1955; Granar, 1958; Tarling and Hrouda, 1993). However, AMS fabrics from sandstones located nearby or between conglomerate deposits resemble a mix of the two identified patterns. Thus, a systematic reduction of the flow velocity was identified from western to easternmost sites (or upsequence); high-velocity fabrics at basal sites (conglomerates and coarse-grained sandstones) which evolved towards low-velocity to sedimentation/compaction fabrics (fine-grained sandstones and mudstones) W-ward.

According to Nelson et al. (1993), the whole clastic sequence of MVU corresponds to prograding sediments progressively deposited into deepest portions of a basin as they are

transporter away from the source. The depositional and transport environment that Nelson et al. (1993) describes is essentially a turbidite deposit, in which coarse-grained particles are deposited in the proximal part of the flow, by strong velocity currents, while fine-grained particles are deposited in the distal portions, by medium to weak velocity flows.

The a-priori NW to W-ward inferred paleocurrent (Fig. 8.4), based on AMS fabrics, agrees with the general paleocurrent direction proposed by Nelson et al. (1993), based on the orientation of sedimentary structures and the assumption that no rotations occurred. Secondary NE-SW trending and ENE-ward paleocurrent were also inferred from the AMS fabrics (Table 13), which are subparallel to the secondary Caleta Monona lineament in the area (Fig. 8.1).

The identification of rotations, mostly counterclockwise, in the Estero Cono area allowed the correction of these paleocurrent directions. The scatter main NW to W-ward paleocurrent changed to a better clustered NW-ward direction after the correction, whereas minor paleocurrent directions change to NNE-SSW trending and E-ward directions, still subparallel to the Caleta Monona lineament (Fig. 9.7a).

AMS analyses also suggests that the original depositional surface was a NW to W-facing slope (i.e. towards the Pacific Ocean), rather than horizontal surface. This inclination of the depositional surface was decreasing towards the same direction, until it become more or less horizontal near Caleta Pascuas (Fig. 9.7b). Similarly, Correction of bedding attitudes by means of rotational axes, suggest that sandstones and mudstones were deposited in W-facing slopes. The Westernmost analyzed site (S8) the inclination of the slope was virtually horizontal. Thus, the decrease in slope inclination was confirmed by the paleomagnetic analyses independently.

9.4.2. Triggering causes of turbiditic flow

The generation of the turbidite flows which transported clastic sediments towards NW direction, were induced by instabilities in the slope, most probably resulted from changes in

angle of the slope and/or earthquakes activity. AMS and paleomagnetic analyses indicate that the slope of the depositional surface decreased in angle W to NW-ward directions, reaching probably more than 20° in its steepest easternmost portion. Earthquakes are a common feature in the Pacific Rim, mainly triggered by subduction of the Nazca plate. In the Estero Cono area earthquakes must have been absorbed by the transpressional strike-slip fault zone. Movements of this fault resulted in a loose of the slope stability, triggering the flow of sediments down the slope (Fig. 9.7b).

9.5. Generation and original location of the Taitao ophiolite

From numerous studies of modern oceanic crust and ancient ophiolite sequences it has been established that ophiolites originally correspond to a vertical pseudo-stratified sequence with nearly horizontal contacts between its units (e.g. Moores, 1982; Nicolas, 1995; among many others) (Fig. 1.1). However, the different units of the Taitao ophiolite are tilted *ca.* 90° (Nelson et al., 1993; this study). Under the assumption that the contact between ultramafic and gabbro sections (Moho discontinuity) was originally horizontal, after the "old" rotational event it becomes roughly E-ward inclined *ca.* 30°. This restored Moho orientation coincides with the subduction vergence of the down-going Nazca-Antarctic plate system beneath the South American plate. However, the calculated dipping angle can not be correlated with the Nazca-Antarctic subduction angle, since nowadays there is no constrains about it in the CTJ area.

According to "*collisional*" ophiolite models (e.g. Nicolas and LePichon, 1980; Moores, 1982, Wakabayashi and Dilek, 2004) and numerical studies (van den Beukel, 1990), obduction takes place due to a break-up of the young subducting oceanic plate into tectonic slices under the toe of the continental plate, during which the ophiolite becomes part of the continental crust. Following the obduction model proposed by van den Beukel (1990) (Fig. 9.8) and restorations of the gabbro magna chamber (this study), the Taitao ophiolite originally should have belonged to

the Nazca plate. However, Wakabayashi and Dilek (2004) argue that an obducted piece of oceanic lithosphere should belong to the ocean-ward side of the spreading ridge, since this one lacks of the slab-pull force when it is subducted.

Chapter 10: Conclusions

Determination of stress field together with rock magnetic analyses allows the characterization of the complex tectonic history experienced by the Taitao ophiolite. This is closely linked to the spatio-temporal evolution of the CR system for the last ca. 10 Ma. The CR system collided with the western margin of the South American plate at least 3 consecutive times offshore of the Taitao area. These collisions were the result of the repeated north and south-ward migration of the CTJ (Fig. 3.3), and they provided with the necessary conditions for the obduction of (a probably highly buoyant) piece of oceanic lithosphere onto the continental margin.

The tectonic history of the Taitao ophiolite can be roughly divided into two phases; one pre- and early obduction phase, which occurred before 6 Ma ago, and a late obduction phase that took place after 6 Ma. During the first phase, the Taitao ophiolite was generated during normal spreading at the landward-side (Nazca plate) of the CR system (Fig. 10.1a). Shortly after the ophiolite was displaced westward of the spreading ridge it cooled down enough to acquire a stable remanent magnetization. These magnetizations recorded the orientation of the GAD at that time. Paleomagnetic analyses showed that orientation of these RM vectors ("old" RM vectors) do not coincide with the orientation of the expected GAD, indicating that some tectonic rotation/tilting affected the ophiolite before and/or during the obduction. Calculated rotational axes for the plutonic units (ultramafic and gabbro), using "old" RM vectors, indicate that the plutonic units underwent clockwise rotation about a NW-ward steeply inclined axis (Fig. 9.2, 10.1b, c). This rotation affected the ophiolite before 6 Ma, ending by the time that the ophiolite was incorporated, as tectonic slides, to the forearc of the Aysén region (e.g. van den Beukel, 1990; Wakabayashi and Dilek, 2004) (Fig. 10.1c, 10.2a).

In the second phase (after the ophiolite was attached to the forearc), magnetite crystals present in the plutonic units acquired a second magnetization (added to the previous older one), which recorded the orientation of the GAD at that time, i.e. about 6 Ma. This magnetization was

most probably acquired due to an increase of the geothermal gradient in the area resulted by the subsequent subduction of active spreading centers of the CR system beneath the Taitao area (e.g. De Long, 1979; Lagabrielle et al., 2000) (Fig. 3.5). During this time the bimodal dike complex unit acquired a stable RM (primary).

As fission track data showed, the uplift of the Taitao ophiolite started *ca.* 6 Ma ago due to the continuous subduction of the Nazca-Antarctic plate system. This subduction imposed W-ward compression over the ophiolite which resulted in the deformation of the plutonic units through folding and counterclockwise rotation. During this stage, the plutonic units acquired a second magnetization ("young" RM vectors) while the dike complex unit acquired its primary magnetization.

Paleomagnetic data indicate that ophiolite units were counterclockwise rotated about NE-to-E-ward inclined axes (Fig. 9.2). However, during early stages of rotation, folding affected the plutonic units synchronously with the counterclockwise rotation (Fig. 10.2b). Folding was more pronounced in the ultramafic (*ca.* 70%) than in the gabbro (*ca.* 50%) units but, on the contrary, counterclockwise rotation was more pronounced in the gabbro than in the ultramafic units. These differences were the result of the different rheological responses of the ultramafic and gabbro units to the deformation (e.g. Turcotte and Schubert, 1982; Wilks and Carter, 1990).

As ductile conditions ceased and brittle deformation started to be the main mechanism to absorb the imposed deformation, dip-slip faults were generated in the ophiolite while a dextral fault zone was developed in the eastern margin of it in the contact with the basement (Bahía Barrientos Fault Zone; BBFZ). These faults were developed as a result of the non-orthogonal stress field applied over the ophiolite. The stress field divided into its compressional and strike-slip components which were identified in the stress analyses. Compressional component ("B" stress field, Fig. 9.1a) generated thrust faults which disrupted both the gabbro and the ultramafic units (the later disrupted into, at least, three blocks) whereas strike-slip component ("C" stress field, Fig. 9.1) affected the eastern edge of the ophiolite.

As the ophiolite continued its counterclockwise rotation, early generated thrust faults inside the ophiolite were also rotated. These rotated structures were no longer able to absorb the compressional deformation induced by the subduction of the plates system due to their new orientation. As a result, new structures were generated in the plutonic units, recording the still acting compressional stress field (A stress field, Fig. 9.1). In the eastern margin of the ophiolite, the strike-slip (C stress, Fig. 9.1) component continued its activity throughout the obduction process. Counterclockwise rotation of the plutonic units under brittle conditions was about 60°.

Counterclockwise rotation accommodated most of the deformation of the ophiolite. The dextral movement of the BBFZ rotated the plutonic units at an approximate rate of 14.2°/My for the last *ca.* 6 My. During this rotation, the bimodal dike complex was disrupted into, at least, two major blocks; the ECDC and the MRDC, observed at Estero Cono and Caleta Mitford-Rees respectively (Fig. 1.5; 10.2b). The ECDC block did not changed its orientation significantly during the rotation, but the MRDC block rotated about 34.9°. This resulted in the almost perpendicular trending orientations of these two dike complexes observed today. Paleomagnetic restorations of the trending orientations of both dike complexes showed that they were originally subparallel, with a nearly NS-trending orientation. Such orientation was probably the result of dike intrusion along fissure system nearby one of the transform faults that separate the different segments of the CR system. The activity of this fracture zone deflected the normal N10°W fracture system expected due to the extension of the CR system.

The major accommodation of the ophiolite into the forearc through the counterclockwise rotation generated tectonic gaps between it and the basement (Fig. 9.4a). These gaps were filled by submarine lavas and volcani-clastic deposits erupted through the thinned continental crust (Guivel et al., 1996; Lagabrielle et al., 2000), resulted from the generation of the gaps, along the northern and eastern contacts between the ophiolite and the metamorphic basement.

AMS fabrics obtained from clastic sediments of the MVU indicate that they were transported by turbiditic currents generated most probably at the northeastern part of the peninsula due to the

slope instability. Such instabilities were built up by the movement of a normal-dextral fault zone during the counterclockwise rotation of the ophiolite body (Fig. 9.3). Turbiditic current flowed towards the Pacific Ocean (NW-ward) followed the preexistent depression along Estero Cono and left the sediments in a W-to-NW facing slope which was becoming shallower in angle towards same direction (Fig. 9.7).

As volcanic products and clastic sediments filled the Estero Cono tectonic gap, they also recorded the rotation that affected them; which corresponded only to the later portion of the counterclockwise rotation that the plutonic units and dike complex underwent. Counterclockwise block rotation in the Estero Cono area occurred through three different stages, with the deformation migrating repeatedly E-ward (Fig. 9.4b). This migrating deformation disrupted the MVU into three different blocks, which separations can be observed on the coastal morphology of the area with its different inlets (or "Caletas").

Submarine lavas of the CMU in the Estero Lobos area (east tectonic gap; Fig. 9.4a) were also counterclockwise rotated. The amount of rotation recorded here is far larger than that calculated for the MVU, being approximately 95.8°. This large rotation is most probably the result of two factors, coupling between the CMU and the plutonic units during the counterclockwise rotation and the activity of the nearby BBFZ.

Calculated amounts of rotation for all the rock units indicate that they recorded progressively the counterclockwise rotation, as they were formed through time. Older units (ultramafic and gabbro) recorded the full amount of rotation while younger ones (dike complex and MVU) recorded only the last part of it. Calculated rates of rotation indicate that the rotational speed has been constantly decreasing for the last *ca.* 6 My time, suggesting that most probably accommodation of the ophiolite has reach an stable state and no further rotation of the ophiolite should be expected.

During this study, it has been show that the accretion of oceanic blocks into active continental margin is not a simple process. It is expected that the force (stress field) induced by the

continuously subducting plates is the responsible for rotation and internal deformation of these blocks before, during and after the obduction process. Several thrust and strike-slip fault zones are expected to develop inside and in the margins of these blocks due to the compression and strike-slip components of the imposed deformation. Such faults control the accommodation of the obducted blocks. Thus, a high seismic activity in the subduction zone should probably be expected, in where seismic faults release the accumulated stress built up by the subduction compression.

Tables

Table 1. Available ages for the Taitao ophiolite and surrounding intrusive units

Unit	Method	Age	Error	Reference
Gabbro	K/Ar (whole rock)	13.0	3.0	Bourgois et al., 1993
Gabbro	K/Ar (hb)	6.0	3.0	Le Moigne, 1994
Gabbro	U-Pb (FT-zr)	5.90	0.4	This study
Gabbro	U-Pb (FT-zr)	5.80	0.2	This study
MVU	K/Ar (whole rock)	4.60	1.0	Mpodozis et al., 1995
MVU	Nannofossil	2.30	1.3	Bourgois et al., 1993
CMU	K/Ar (whole rock)	3.00	1.4	Mpodozis et al., 1995
CMU	K/Ar (whole rock)	2.90	0.8	Mpodozis et al., 1995
CMU	K/Ar (whole rock)	3.70	0.6	Mpodozis et al., 1995
CMU	K/Ar (whole rock)	4.40	0.6	Mpodozis et al., 1995
CMU	K/Ar (whole rock)	2.50	1.3	Mpodozis et al., 1995
CMU	K/Ar (whole rock)	4.30	1.2	Mpodozis et al., 1995
Cabo Raper	K/Ar (bt)	3.60	0.6	Mpodozis et al., 1985
Cabo Raper	K/Ar (bt)	3.30	0.3	Mpodozis et al., 1985
Cabo Raper	K/Ar (hb)	4.10	2.4	Mpodozis et al., 1985
Cabo Raper	K/Ar (hb)	3.40	0.8	Mpodozis et al., 1985
Cabo Raper	Ar/Ar (bt)	5.10	0.6	Guivel et al., 1999
Cabo Raper	Ar/Ar (bt)	4.80	0.3	Guivel et al., 1999
Cabo Raper	U-Pb (zr)	3.90	0.1	Hervé et al., 2003
Cabo Raper	U-Pb (zr)	4.00	0.2	Hervé et al., 2003
Cabo Raper	U-Pb (FT-zr)	4.00	0.3	Hervé et al., 2003
Cabo Raper	U-Pb (FT-zr)	3.50	0.3	Hervé et al., 2003
Cabo Raper	U-Pb (FT-ap)	1.90	0.6	Hervé et al., 2003
Cabo Raper	U-Pb (FT-ap)	2.90	0.8	Hervé et al., 2003

Table 1, continued

Unit	Method	Age	Error	Reference
Seno Hoppner	K/Ar (bt)	5.50	0.4	Mpodozis et al., 1985
Seno Hoppner	K/Ar (bt)	5.20	0.3	Mpodozis et al., 1985
Seno Hoppner	Ar/Ar (bt)	5.90	0.5	Guivel et al., 1999
Seno Hoppner	Ar/Ar (k-feld)	6.90	1.0	Guivel et al., 1999
Estero Cono	U/Pb (FT-zr)	3.50	0.3	Hervé et al., 2003
Barrientos	U/Pb (FT-zr)	3.50	0.2	Hervé et al., 2003
Barrientos	U/Pb (FT-ap)	3.20	1.3	Hervé et al., 2003

*FT: Fission track, hb: hornblende, zr: zircon, bt: biotite, ap: apatite, k-feld: K-feldspar.

Table 2. Calculated stress fields for the plutonic units and the eastern margin of the ophiolite

Stress field	Stress ratio	Orientation of σ_1 axes	Orientation of σ_3 axes
A	0.1-0.7	EW	Vertical
B	0.2-0.6	NNE-SSW	Vertical
C	0.1-0.7	EW	NS
D	0.2-0.6	NNE-SSW (200)	WSW-ENE (200)
E	0.7-0.8	NE-SW (500)	WNW-ESE (300)

*A, B stress fields were calculated for the plutonic units while C, D and E stress fields were for the eastern margin of it (BBFZ).

Table 3. Fisher statistics for MVU, dike complexes and CMU sites (univectorial)

Site	Unit	N	Fisher analysis				
			κ	α95	dec	inc	Fisher?
s1	MVU (clastic)	15	198.0	2.7	9.4	-61.6	no
s2	MVU (clastic)	11	144.2	3.8	-26.0	-73.6	yes
s3	MVU (clastic)	10	202.8	3.4	48.5	-63.5	no
s4	MVU (clastic)	12	469.3	2.0	-19.6	-72.3	yes
s8	MVU (clastic)	13	355.0	2.2	-27.0	-37.6	yes
m2	MVU (clastic)	14	18.6	9.5	-27.3	-64.0	yes
m3	MVU (clastic)	0	31.9	8.7	139.6	40.4	no
d1	MVU (feeder)	16	176.1	2.8	17.6	-43.5	no
d2	MVU (feeder)	16	149.8	3.0	-52.6	-45.2	no
d3	MVU (feeder)	13	120.1	3.8	-4.3	-53.9	no
d4	MVU (feeder)	10	351.4	2.6	-13.6	-56.2	no
l1	MVU (pillow)	10	68.4	5.9	-46.1	-60.0	no
l2	MVU (pillow)	15	103.6	3.8	-7.7	-57.0	no
l3	MVU (pillow)	16	245.4	2.4	-19.6	-49.9	yes
l4	MVU (pillow)	16	354.4	2.0	-81.9	-32.3	no
l5	MVU (pillow)	16	74.3	4.3	-20.3	-32.9	no
l6	MVU (pillow)	16	400.5	1.8	-57.5	-35.1	yes
d5	ECDC	127	27.6	2.4	168.9	25.9	no
d6	MRDC	12	430.8	2.1	-8.8	-47.1	no
d7	MRDC	13	91.4	4.4	-65.8	-72.7	yes
d8	MRDC	12	102.9	4.3	6.9	-18.0	no

Table 3, continued

Site	Unit	N	Fisher analysis				
			κ	α95	dec	inc	Fisher?
d9	MRDC	15	52.5	5.3	134.4	0.2	no
d10	MRDC	12	395.1	2.2	130.2	34.1	yes
d11	Contact	18	70.6	4.1	140.1	21.0	no
l7	CMU	10	52.3	6.7	101.1	5.6	no

*Only sites with MAD values larger than 15 (reliable ones) are shown (see figure 6.1) (e.g. Kirschvink, 1980; Butler, 1992). κ is the Fisher (1953) precision parameter, α95 refer to the semi-angle of the 95% confidence interval (cone). Dec. and inc. refers to declination and inclination (in degrees) of the mean direction, respectively. Also, Kent (1982) test of Fisher (1953) distribution, indicating if the data is elliptically ("No"; e.g. Kent, 1982) or circularly ("Yes"; e.g. Fisher, 1953) distributed about the mean value.

Table 4. Fisher statistics for gabbro and ultramafic sites (multivectorial)

Site	RM vector	N	Fisher analysis				
			κ	α95	dec	inc	Fisher?
g5	young	11	349.5	2.4	141.4	25.5	yes
g6	young	15	21.3	8.5	39.1	55.2	yes
g11	young	11	305.6	2.6	75.5	-15.7	yes
g12	young	16	23.2	7.8	40.2	23.3	yes
g3	old	21	305.6	1.8	-66.5	11.0	no
g5	old	10	50.9	7.8	251.0	70.5	no
g6	old	16	261.3	2.3	49.0	-45.3	yes
g7	old	15	94.8	3.9	148.8	60.9	yes
g8	old	10	65.4	6.0	63.8	88.8	yes
g11	old	11	23.3	9.7	7.6	62.0	yes
p1	young	17	197.1	2.5	0.4	5.5	no
p2	young	10	33.6	8.4	27.4	81.3	yes
p4	young	10	20.4	11.0	204.7	-31.4	no
p5	young	10	186.0	3.7	312.0	-19.9	yes
p7	young	10	520.3	2.1	-85.8	-31.8	yes
p3	young	11	523.8	2.0	155.4	9.6	yes
p1	old	17	223.2	2.4	-28.5	55.4	no
p2	old	13	228.4	2.7	170.8	67.5	no
p4	old	10	37.2	8.0	284.4	46.2	yes
p5	old	10	55.3	6.6	-22.8	28.3	yes
p7	old	13	206.9	2.9	21.2	59.0	yes

Table 4, continued

Site	RM vector	N	Fisher analysis				
			κ	α95	dec	inc	Fisher?
p6	old	15	93.0	4.0	19.2	72.1	yes

*Only sites with MAD values larger than 15 are shown (e.g. Kirschvink, 1980; Butler, 1992). Parameters listed on table 3. "RM vector" refers to the portion of the demagnetization path: high (old) or low (young) coercivity.

Table 5. Kent statistics for non-Fisher distributed sites (see tables 3 and 4)

Site	Kent Analysis							
	Mean direction		95% confidence ellipse					
	dec	inc	η	η dec	η inc	ζ	ζ dec	ζ inc
s1	9.4	-61.6	1.8	59.9	19.0	3.2	322.6	20.3
s3	48.5	-63.5	1.2	353.4	15.9	4.1	89.6	20.6
m3	139.6	40.4	1.5	318.3	49.6	11.0	49.0	0.7
d1	17.6	-43.5	0.8	333.6	37.2	3.6	83.0	23.7
d2	307.4	-45.2	1.1	264.3	36.0	3.8	12.2	22.9
d3	355.7	-53.9	0.6	321.6	31.1	5.3	61.8	16.4
d4	346.4	-56.2	0.8	68.1	5.5	3.4	334.4	33.2
d5	168.9	25.9	2.0	57.9	36.5	2.5	285.3	42.5
d6	351.2	-47.1	1.2	263.9	2.5	2.4	356.2	42.8
d8	6.9	-18.0	3.1	80.1	41.7	4.6	294.4	42.8
d9	134.4	0.2	0.6	44.0	64.3	7.3	224.5	25.7
l1	313.9	-60.0	1.3	253.7	16.0	7.2	351.3	24.7
l2	352.3	-57.0	1.3	50.0	19.1	4.9	310.3	25.8
l4	278.1	-32.3	0.7	340.4	36.3	2.5	216.7	37.1
l5	339.7	-32.9	2.5	18.9	50.1	5.4	263.3	19.9
l7	101.1	5.6	1.1	6.0	42.4	8.8	197.1	47.1
g2	140.1	21.0	25.3	47.5	6.7	5.2	300.8	67.9
g3-old	293.5	11.0	0.8	26.2	13.7	2.3	166.0	72.3
g5-old	251.0	70.5	2.9	42.4	17.3	9.4	135.2	8.8
p1-young	0.4	5.5	1.9	257.9	66.1	2.8	92.8	23.2
p4-young	204.7	-31.4	4.9	223.7	57.1	13.8	120.0	8.7

Table 5, continued

Site	Kent Analysis							
	Mean direction		95% confidence ellipse					
	dec	inc	η	η dec	η inc	ζ	ζ dec	ζ inc
p1-old	331.5	55.4	1.3	109.4	27.1	2.9	210.0	19.8
p2-old	170.8	67.5	0.6	286.2	10.1	3.6	19.9	19.9

*η and ζ refer to the smallest and larger semi-angles, respectively, of the 95% confidence interval (ellipse) calculated by means of Kent (1982) statistics. η dec, η inc, ζ dec and ζ inc refer to the dec and inclination of the planes containing the semi-angles (see Tauxe, 1998).

Table 6. Orientation of rotational axes for MVU, dike complexes, contact and CMU sites

Site	Declination	Inclination	ψ
s1	274.7	70.1	-10.0
s2	257.0	71.5	27.4
s3	294.3	88.2	-48.5
s4	260.2	69.5	20.9
s8	76.5	43.8	38.3
m2	76.4	87.9	27.3
m3	69.8	57.7	47.0
l1	67.0	83.6	46.4
l2	86.2	43.8	11.1
l3	80.2	52.2	24.7
l4	49.1	65.9	87.1
l5	79.9	31.5	37.8
l6	61.3	61.0	64.2
l7	50.6	48.1	95.8
d1	278.8	38.9	-27.7
d2	63.7	68.5	56.0
d3	87.9	21.1	11.9
d4	83.2	57.0	16.2
d5	84.4	15.2	40.6
d6	85.6	26.0	19.9
d7	237.1	82.9	66.2
d8	273.5	7.9	-47.5
d9	67.2	31.4	77.8

Table 6, continued

Site	Declination	Inclination	ψ
d10	65.1	56.7	58.1
g2	70.1	40.2	58.7

*Site numbers in figure 6.1 and tables 3 and 4; ψ refers to the amount of rotation associated with the rotational axis. Notice that negative values of φ indicate clockwise rotations while positive ones indicate counterclockwise rotations.

Table 7. Orientations of mean rotational axes for MVU, CMU, dike complexes and contact

Unit	Mean direction		Kent statistics						ψ	ψ error
	Dec	Inc	α95/η	η dec	η inc	ζ	ζ dec	ζ inc		
MVU (1)	70.4	82.3	2.7	170.3	1.3	26.9	260.5	7.6	14.8	30.6
MVU (2)	78.6	54.6	16.0						27.0	30.0
MVU (3)	67.5	59.1	0.9	200.5	22.2	10.9	299.3	20.4	55.9	44.1
CMU	50.6	48.1							95.8	
ECDC	84.5	15.2							40.6	
MRDC	74.8	52.3	7.1	165.2	0.3	28.5	255.5	37.7	34.9	50.9
Contact	70.1	40.2							58.2	

*Numbers in brackets for the MVU refer to the different identified groups (see figure 6.9). Statistical parameters listed in table 5 and 6.

Table 8. Orientations of rotational axes for each site on each block of the ultramafic unit

Block	Site	RM vector	Dec	Inc	ψ	Notes
North	p6	young	47.1	66.4	90.8	
	p7	young	47.1	66.4	90.8	
	p6	old	16.6	85.9	146.9	Fold-2-
	p7	old	27.6	83.3	125.2	Fold-2-
	p6	old	80.0	36.0	33.4	Fold-2+
	p7	old	74.6	41.3	45.4	Fold-2+
Central	p4	young	10.4	57.2	162.5	
	p5	young	66.6	33.7	76.1	
	p4	old	33.8	67.8	116.5	Fold-2-
	p5	old	279.2	17.8	-55.5	Fold-2-
	p4	old	28.8	63.9	127.5	Fold-2+
	p5	old	280.4	31.4	-38.8	Fold-2+
South	p1	young	87.1	17.6	19.3	
	p2	young	58.3	80.5	64.1	
	p3	young	85.6	14.2	35.2	
	p1	old	90.0	2.9	55.1	Fold-2-
	p2	old	57.4	84.3	65.6	Fold-2-
	p1	old	90.0	4.0	58.1	Fold-2+
	p2	old	66.6	54.9	55.8	Fold-2+

*Dec and Inc refer to the declination and inclination of the mean rotational axis, "RM vector" is same as in table 4 and ψ to the amount of rotation associated. Notes: refers to the orientation of the rotational axis, for each site, after the second fold-test was considered positive (Fold-2+) or negative (Fold-2-) (see text for details).

Table 9. Orientations of mean rotational axes for the ultramafic unit

	Mean direction		Kent statistics						ψ	ψ error
	dec	inc	η	η dec	η inc	ζ	ζ dec	ζ inc		
After Fold-1	65.2	51.0	6.3	178.7	17.9	20.2	281.0	33.4	77.0	46.4
After Fold-2+	73.7	41.8	3.1	184.0	21.2	31.3	293.5	40.7	46.9	53.3
After Foldt-2-	58.1	75.4	5.4	177.3	7.2	20.3	269.0	12.6	75.6	73.4

*Statistical parameters listed in table 5.

Table 10. Orientations of rotational axes for gabbro sites

Site	RM vector	Dec	Inc	ψ	Notes
g5	young	72.5	26.1	71.2	
g6	young	223.6	88.9	92.8	
g7	young	68.8	43.7	58.7	
g11	young	37.5	59.4	113.2	
g12	young	23.1	69.5	136.4	
g3	old	307.9	53.6	-88.0	Fold-2-
g5	old	338.6	75.0	-138.4	Fold-2-
g6	old	333.2	68.9	-129.5	Fold-2-
g7	old	275.6	42.2	-16.6	Fold-2-
g8	old	92.6	17.2	-17.5	Fold-2-
g11	old	342.5	64.8	-148.1	Fold-2-
g3	old	311.2	51.7	-96.1	Fold-2+
g5	old	345.2	60.7	-154.0	Fold-2+
g6	old	335.3	74.2	-132.3	Fold-2+
g7	old	153.4	80.0	-127.4	Fold-2+
g8	old	0.3	86.1	179.3	Fold-2+
g11	old	346.9	68.2	-155.6	Fold-2+

*Parameters listed in table 8.

Table 11. Orientations of mean rotational axes for the gabbro unit

	Mean direction		Kent Statistics						ψ	ψ error
	dec	inc	α95/η	η dec	η inc	ζ	ζ dec	ζ inc		
Fold-1	57.6	59.4	6.2	163.5	9.2	19.8	258.6	28.9	94.5	31.4
Fold-2+	333.1	74.1	15.4						-81.0	129.4
Fold-2-	311.4	63.6	3.8	170.3	21.1	14.1	74.3	15.1	-89.7	59.9

*Parameters listed in table 5.

Table 12. Calculated average Curie temperatures

Unit	Heating phase		Cooling phase	
	Temperature	Error	Temperature	Error
MVU clastic sediments	577.3	3.5	577.3	2.9
MVU volcanics	525.0	13.3	567.8	41.7
MRDC	579.3	3.2	576.3	1.5
Ultramafic rocks	580.6	3.9	572.8	12.5
Gabbro	574.5	13.8	583.8	8.5

Table 13. Paleocurrent and depositional slope directions

Site	Paleocurrent Direction	Facing slope	Relative Velocity
C1	NE-SW	N/A	High
C2	NNW-SSE (NW-SE)	N/A	High
C3	NNW-SSE (NW-SE)	N/A	High
S1	NW-SE	NW	Medium (?)
S2	NNW	NNW	N/A
S3	NW-SE	NW	Medium (?)
S4	ENE	ENE	N/A
S5	NW	N/A	High-Medium
S6	NW	N/A	High-Medium
S7	N/A	SE	Null
S8	N/A	Horizontal	Null
M1	NW	NW	N/A
M2	W (ENE-WSW)	W	Low
M3	W	W	N/A

*N/A means "not applicable". Under "relative velocity" "high" refers to velocities larger than 1 cm/s, "medium" to velocities between 1 cm/s and 0.1 cm/s while "low" refers to those below 0.1 cm/s (e.g. King, 1955; Granar, 1958; Tarling and Hrouda, 1993). See figure 8.1 for site locations.

Table 14. Rotational rates for the "young" counterclockwise rotation

Unit	Rate	error
Plutonic units	14.2	6.4
MVU-group 1	6.4	13.2
MVU -group 2	5.8	6.5
MVU -group 3	12.1	9.5
CMU	28.6	

*Rates were calculated for rock units with geochronological and amount of rotation data only.

Figures

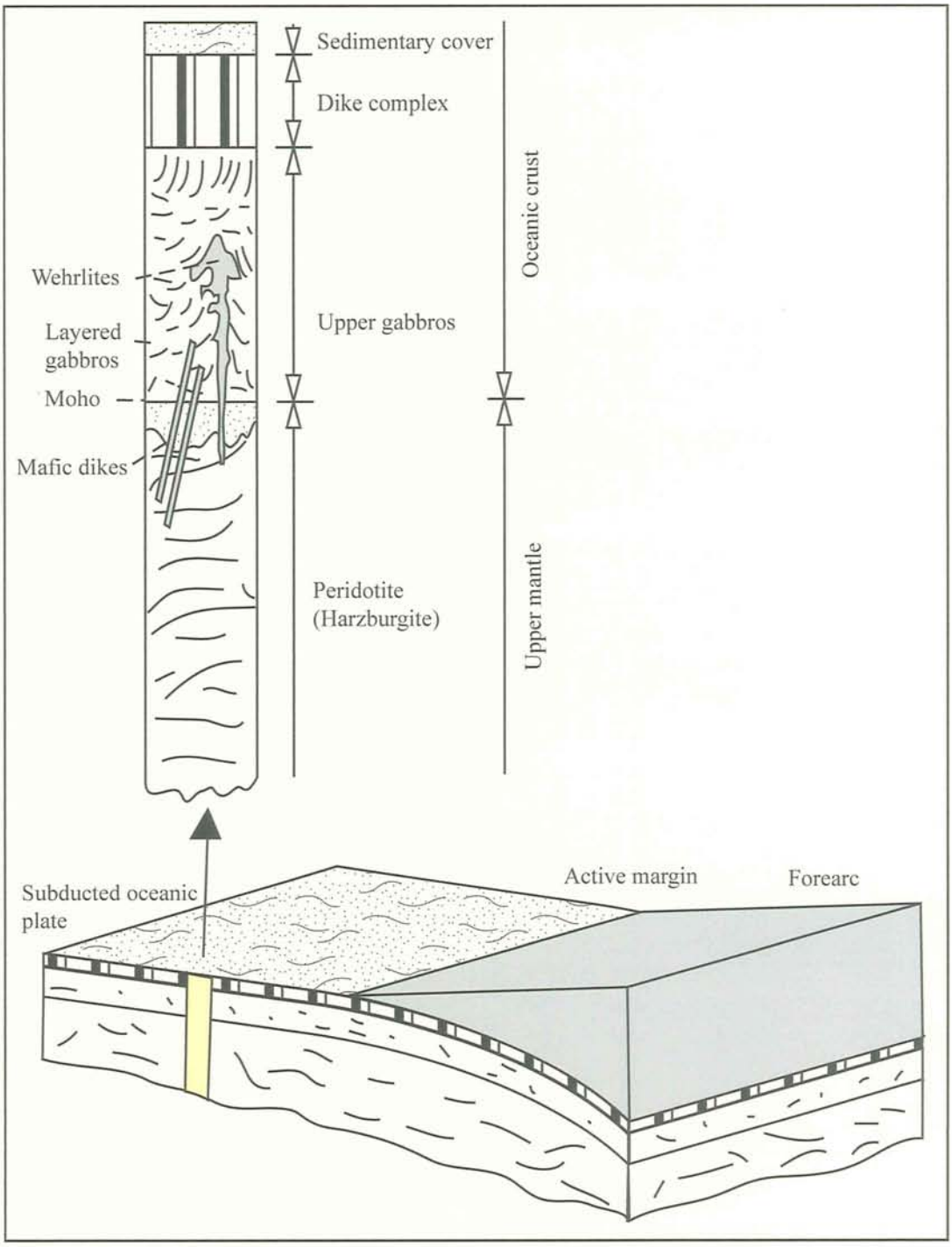

Figure 1.1. Schematic column of a "normal" ocean lithosphere (future ophiolite). From floor to top: (1) ultramafic rocks (harzburgites or lherzolites), (2) massive and layered gabbros, (3) dike complex and (4) pillow lavas, lava flows and sedimentary deposits. Adapted from Nicolas (1995).

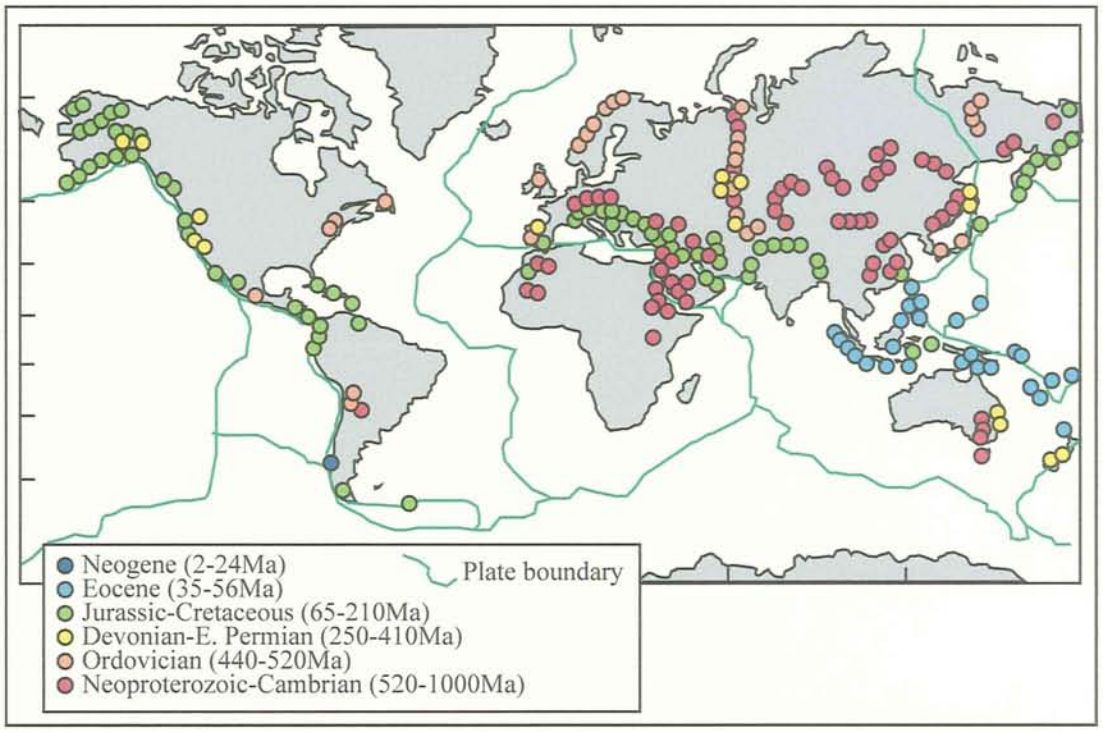

Figure 1.2. Worldwide map with the distribution of ophiolite belts, including major Neoproterozoic and Phanerozoic occurrences. Notice that ophiolites of several ages are represented in most orogenic belts. Modified from Vaughan and Scarrow (2003).

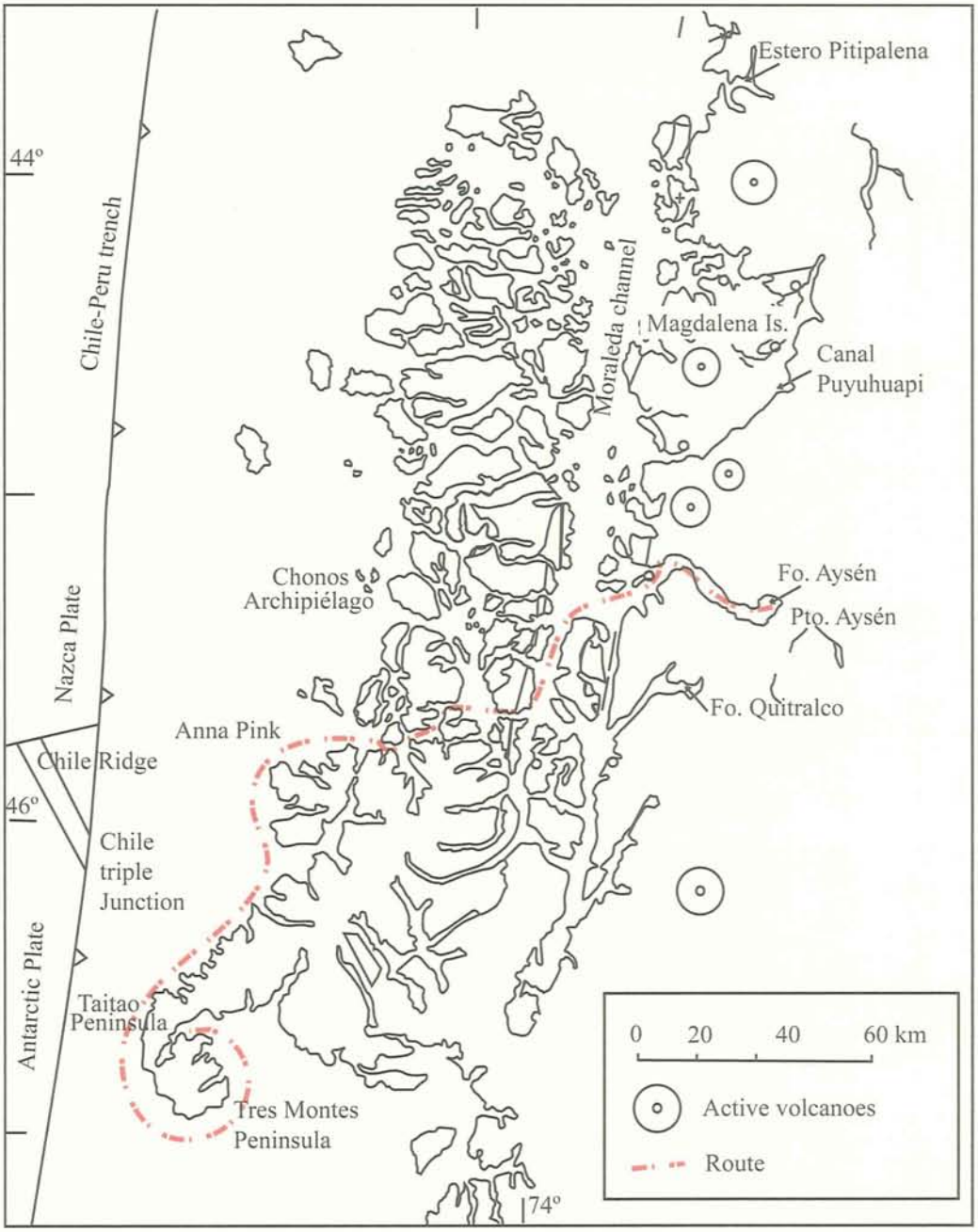

Figure 1.3. Coastline map of the Aysén region showing the most important localities in the area. The red line shows the route followed to approach the westernmost part of the Taitao peninsula during fieldwork expeditions.

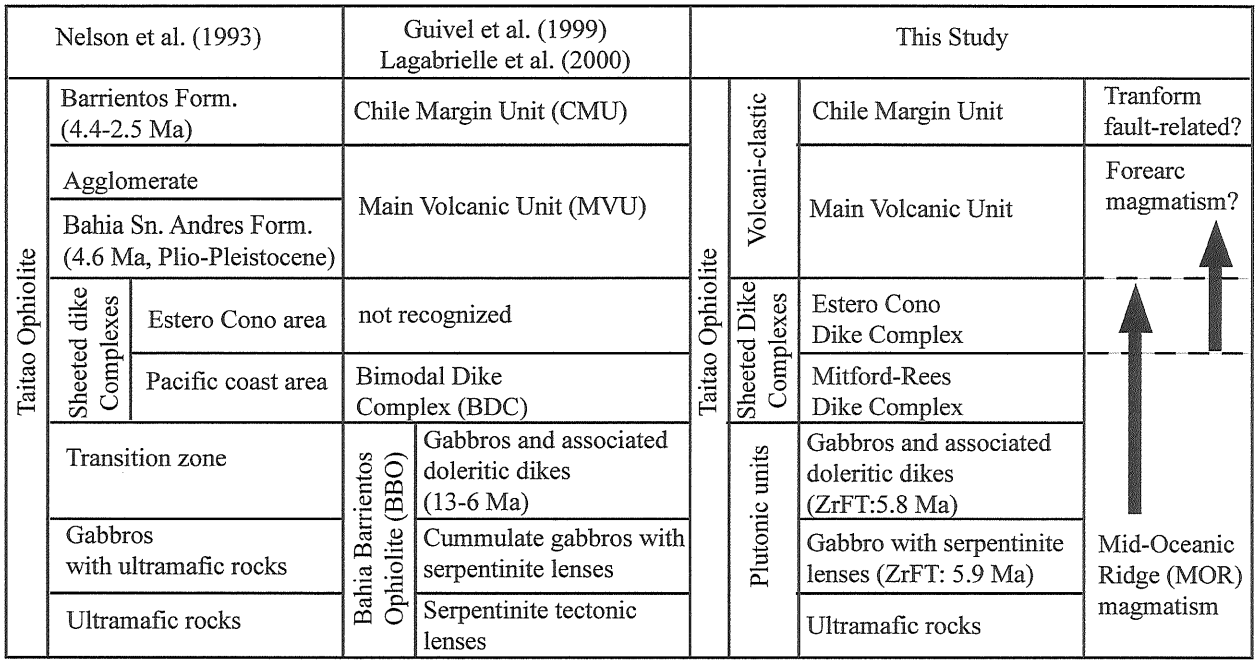

Fig. 1.4. Stratigraphy of the Taitao ophiolite and terminology used in this study

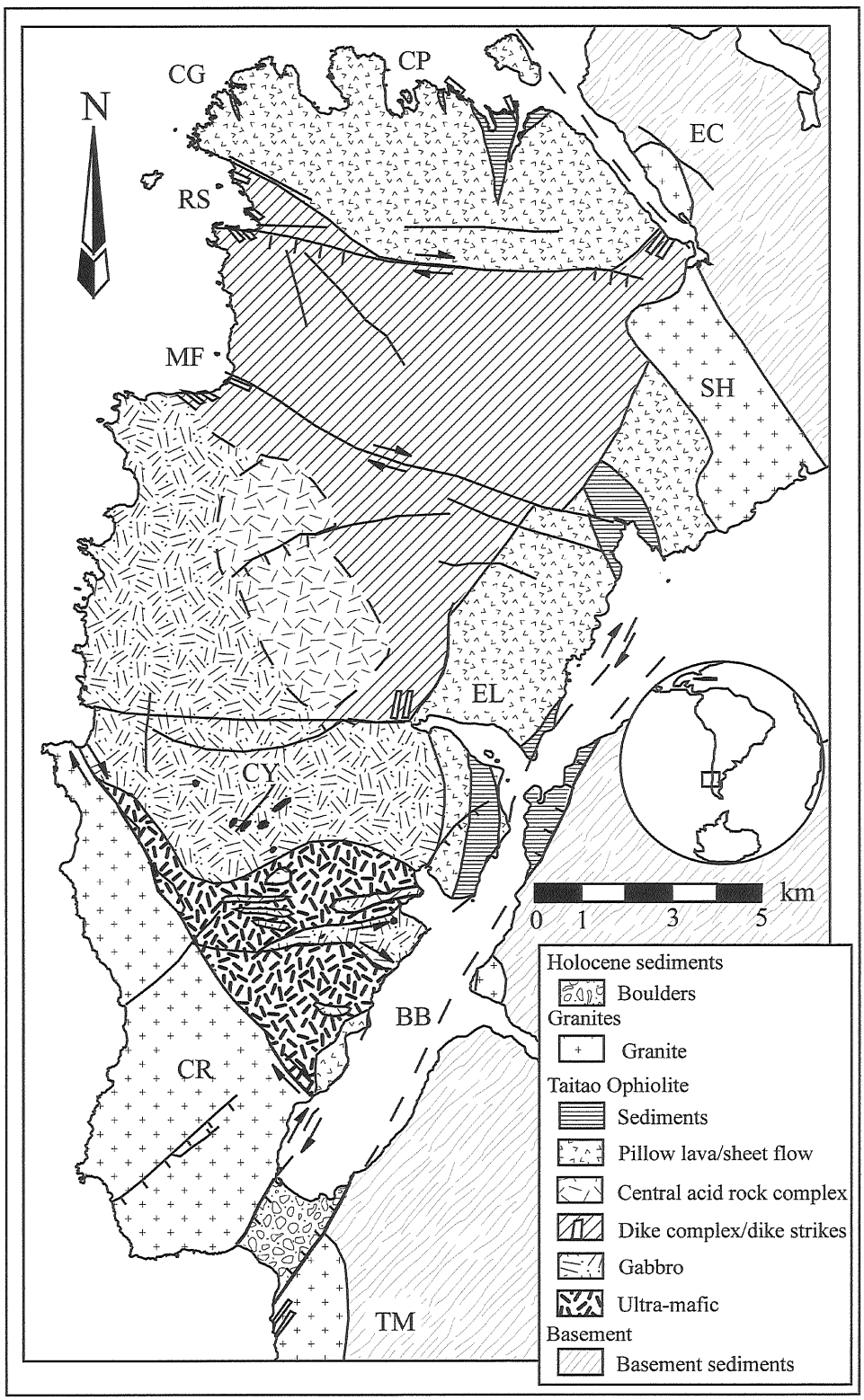

Figure 1.5. Geological map of the westernmost part of the Taitao peninsula. EC: Estero Cono, SH: Seno Hoppner, EL: Estero Lobos, BB: Bahía Barrientos, TM: Tres Montes, CR: Cabo Raper, CY: Cerro Yunques, MF: Caleta Mitford-Rees, RS: Caleta Rees, CG: Cabo Gallegos, CP: Caleta Pascuas.

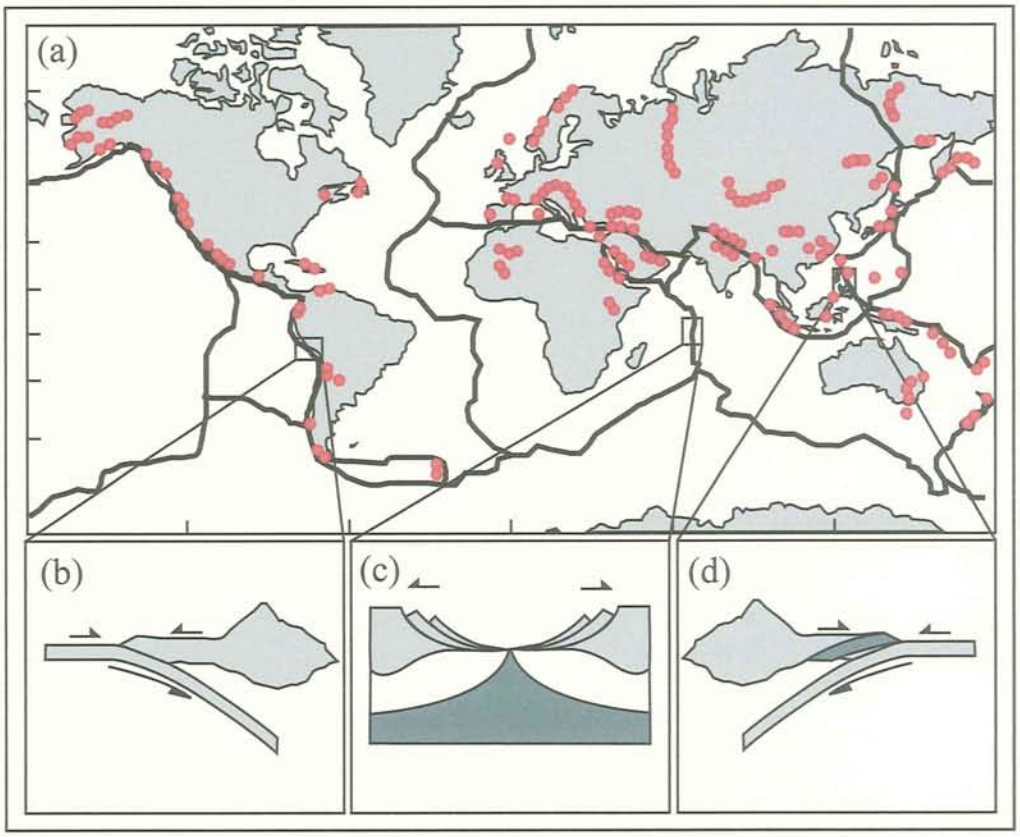

Figure 2.1. (a) Worldwide distribution of ophiolite belts (red circles) extracted from figure 1.2, (Modified from Vaughan and Scarrow, 2003). Black lines show the location of spreading ridges and active margins. (b) Diagram showing the subduction process at an active margin, (c) same as (b) showing the extension process at an oceanic spreading ridge, and (d) same as (b) showing obduction process at an active margin.

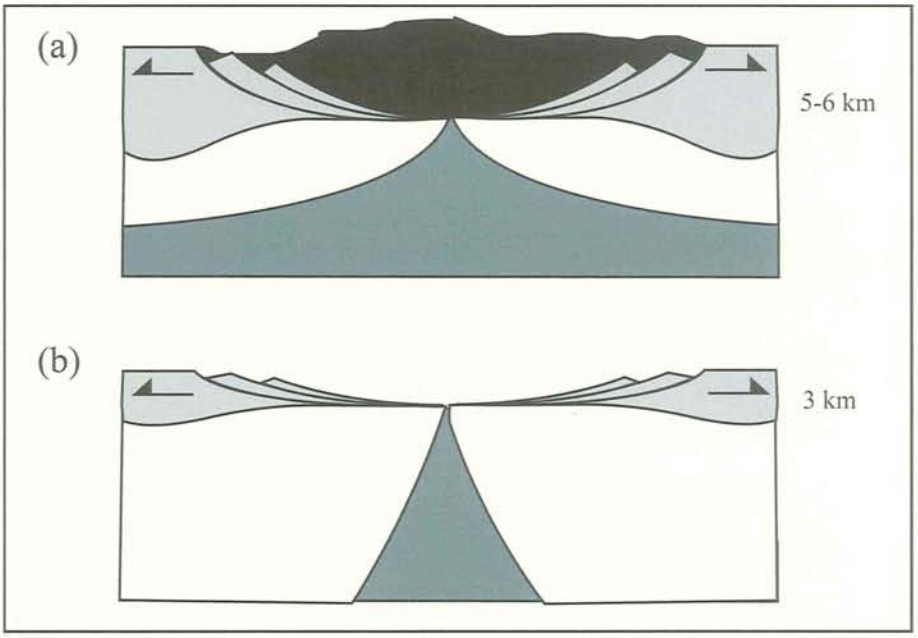

Figure 2.2. Types of oceanic lithosphere generated at different spreading rates: (a) fast (over 2 cm/yr of extension rate) and (b) slow (between 0.5 to 2 cm/yr) (Modified from Nicolas, 1995).

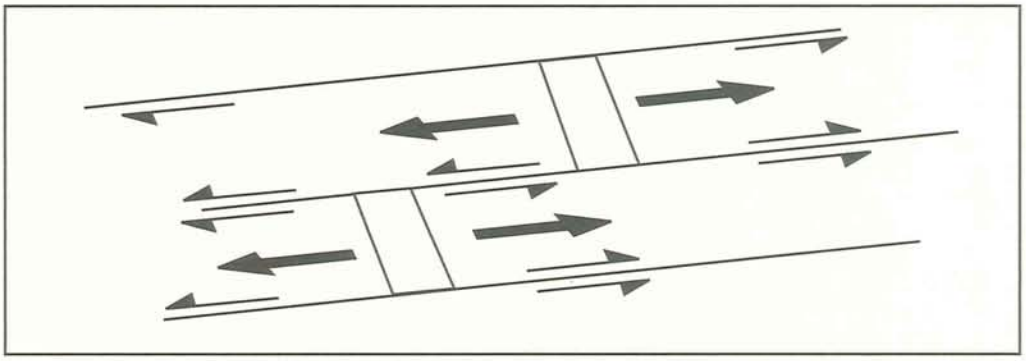

Figure 2.3. Schematic diagram showing the behavior of fracture zones in a spreading ridge system. Notice that in between spreading centers fracture zones have strike-slip movement while outside that area the movement becomes equal.

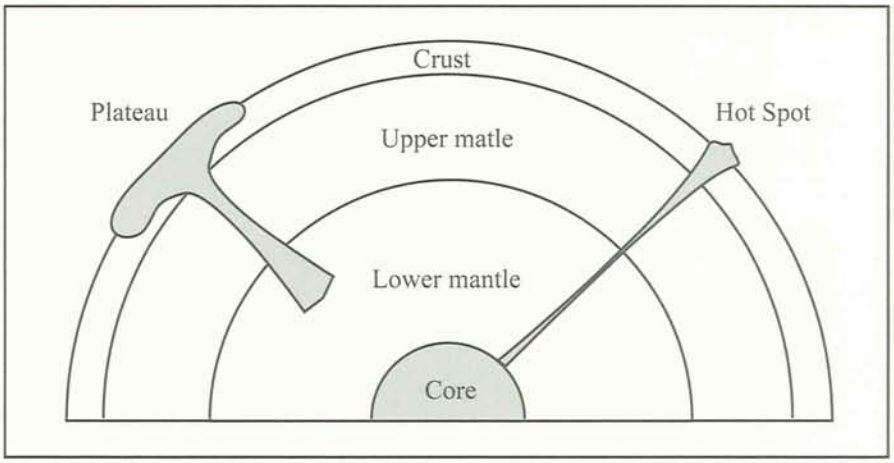

Figure 2.4. Location of the expected origin of hot spots and oceanic plateaus.

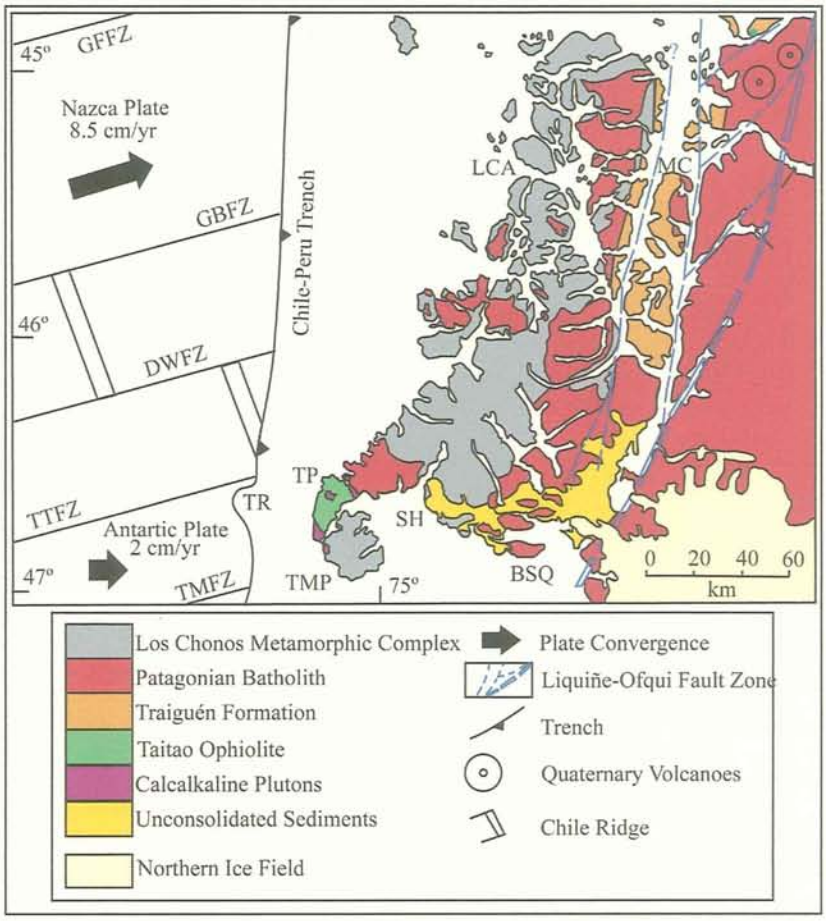

Figure 3.1. Regional geological map of the Aysén region. The convergence vector of each subducting plate is shown as a black arrow. GFFZ: Guafo F.Z., GBFZ: Guamblin F.Z., DWFZ: Darwin F.Z., TTFZ: Taitao F.Z., TMFZ: Tres Montes F.Z., CPT: Chile-Peru trench, LCA: Los Chonos archipelago, MC: Moraleda channel, TP: Taitao peninsula, TR: Taitao ridge, SH: Seno Holloway, TMP: Tres Montes peninsula, BSQ: Bahía San Quintín.

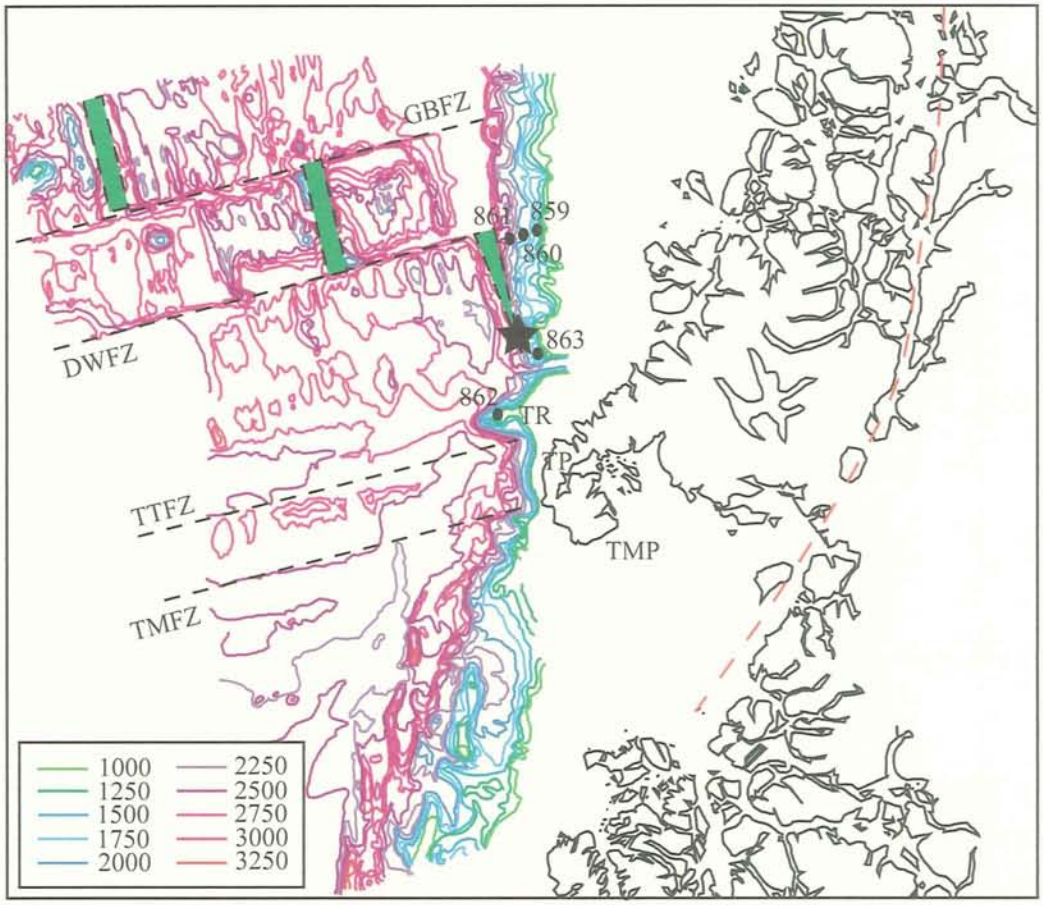

Figure 3.2. Simplified bathymetric map of the oceanic plates, Nazca and Antarctic, offshore Taitao peninsula (Adapted from Guivel et al., 1999). Names of locations are in figure 3.1. The star indicates the actual location of the CTJ and circles with numbers the location of holes drilled during ODP Leg 141 (Lewis et al., 1995).

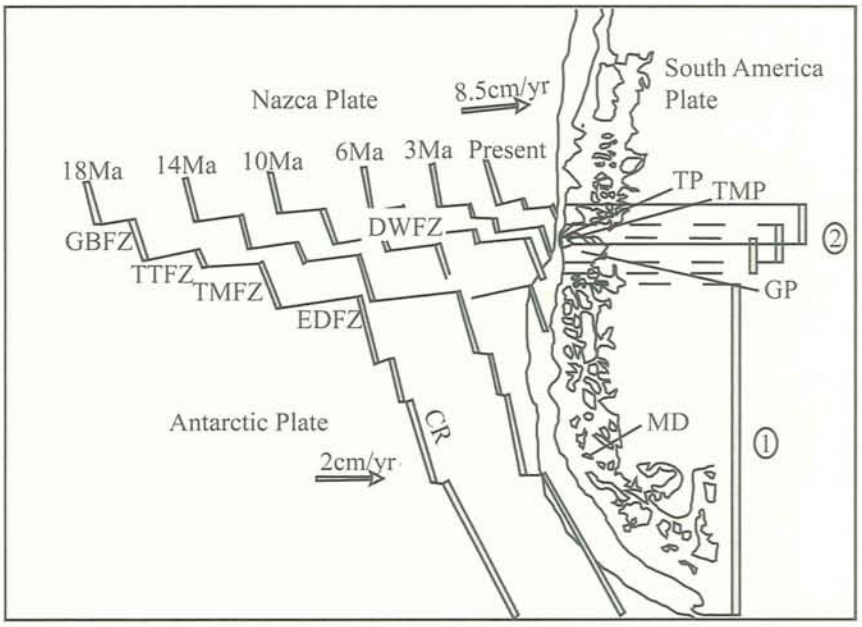

Figure 3.3. Evolution of the CR for the last 18 My time. Arrows indicate the convergence vector of each plate with respect to the fixed South American plate. Labeled circles at the right side indicate the collision locale of each one of the subducted segments of the CR system. Notice the strong overlap offshore the Taitao peninsula area (box 2). Names for localities are in figure 3.1, except for: GP: Golfo de Penas, CR: Chile ridge, MD: Madre de Dios archipelago. Adapted from Cande and Leslie (1986).

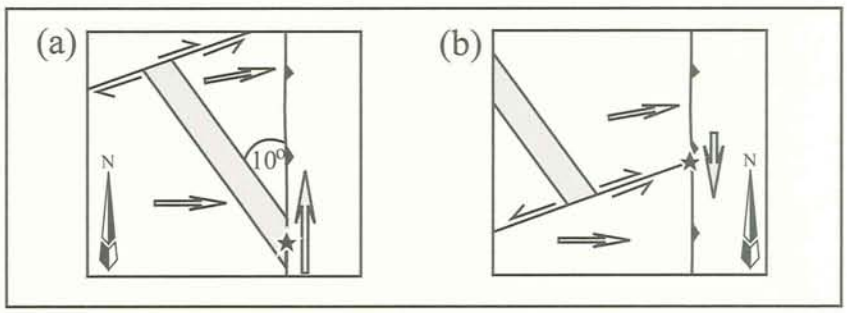

Figure 3.4. Evolution and migration of the CTJ through time. (a) Northward migration resulting from an TRT configuration of the CTJ and (b) southward migration due to a TFT configuration. The star indicates the position of the CTJ, while the gray arrow indicates the migrating direction of it. White arrows indicate the convergence vector of each subducting plate (see figure 3.3).

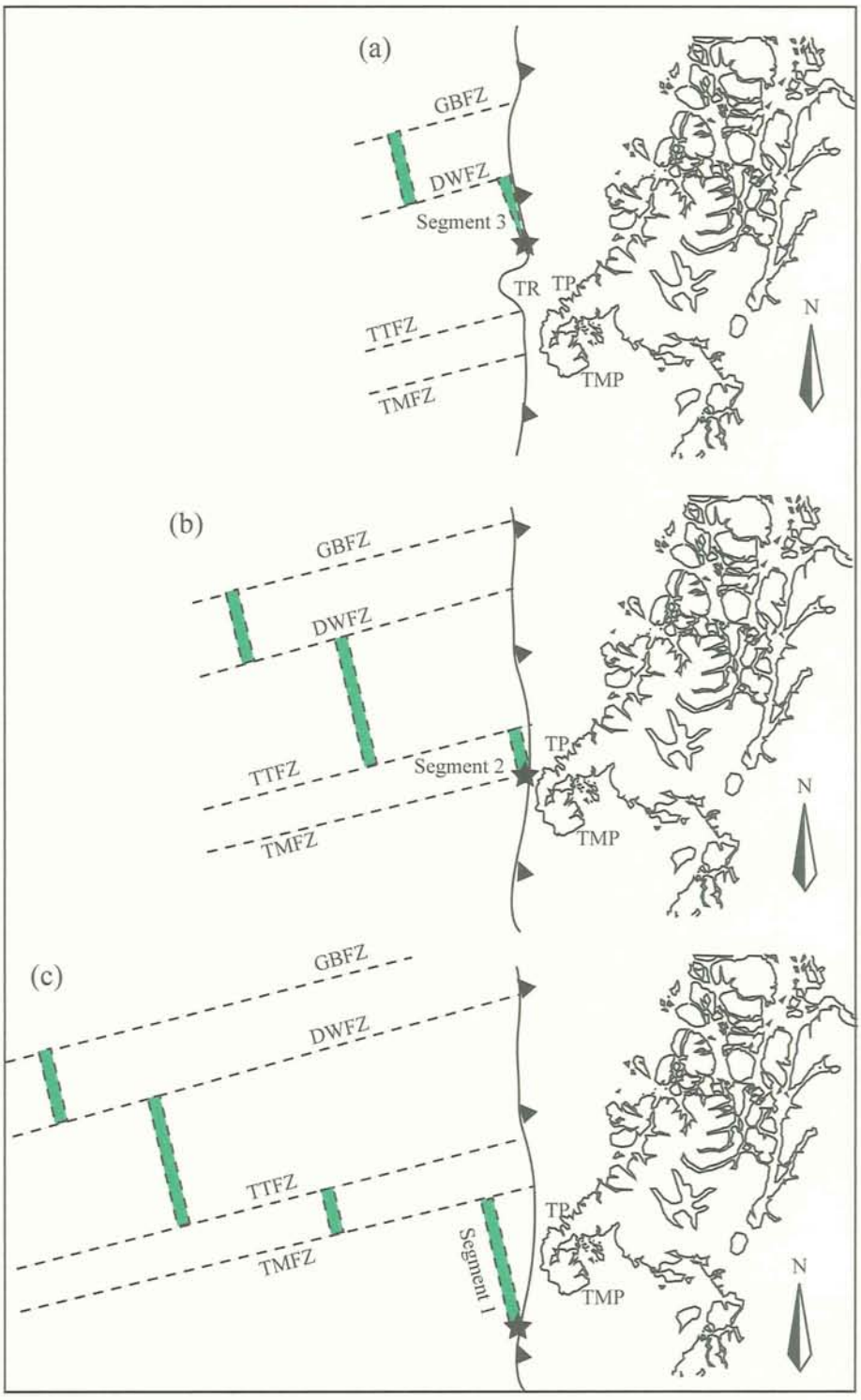

Figure 3.5. Close-up diagram of the evolution and collision of the CR segments offshore the Taitao peninsula area. (a) Collision of the segment 3 of the CR, about 0.3-0 Ma ago, in front of the northern end of the Taitao peninsula. (b) Collision of the segment 2 of the CR, about 3 Ma ago, in front of the coast of the Taitao peninsula. (c) Collision of the segment 1 of the CR, ca. 6 Ma ago, at the southern tip of the Taitao peninsula. Names of localities are on figure 3.1.

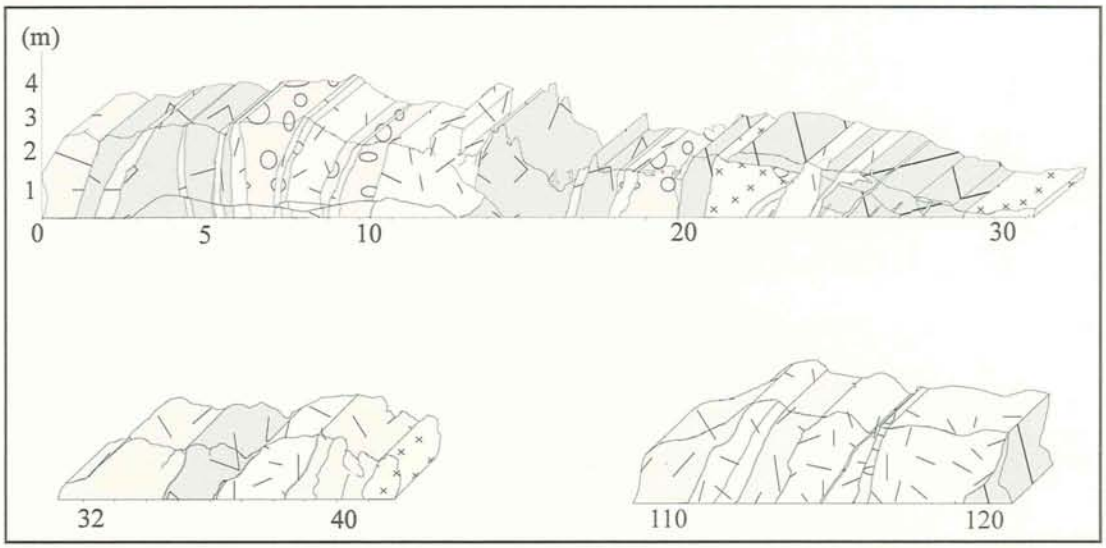

Figure 3.6. Sketch of the ECDC. The outcrop was divided into 3 subsections, separated by fault (?) (sections a and b) or cover by vegetation (sections b and c).

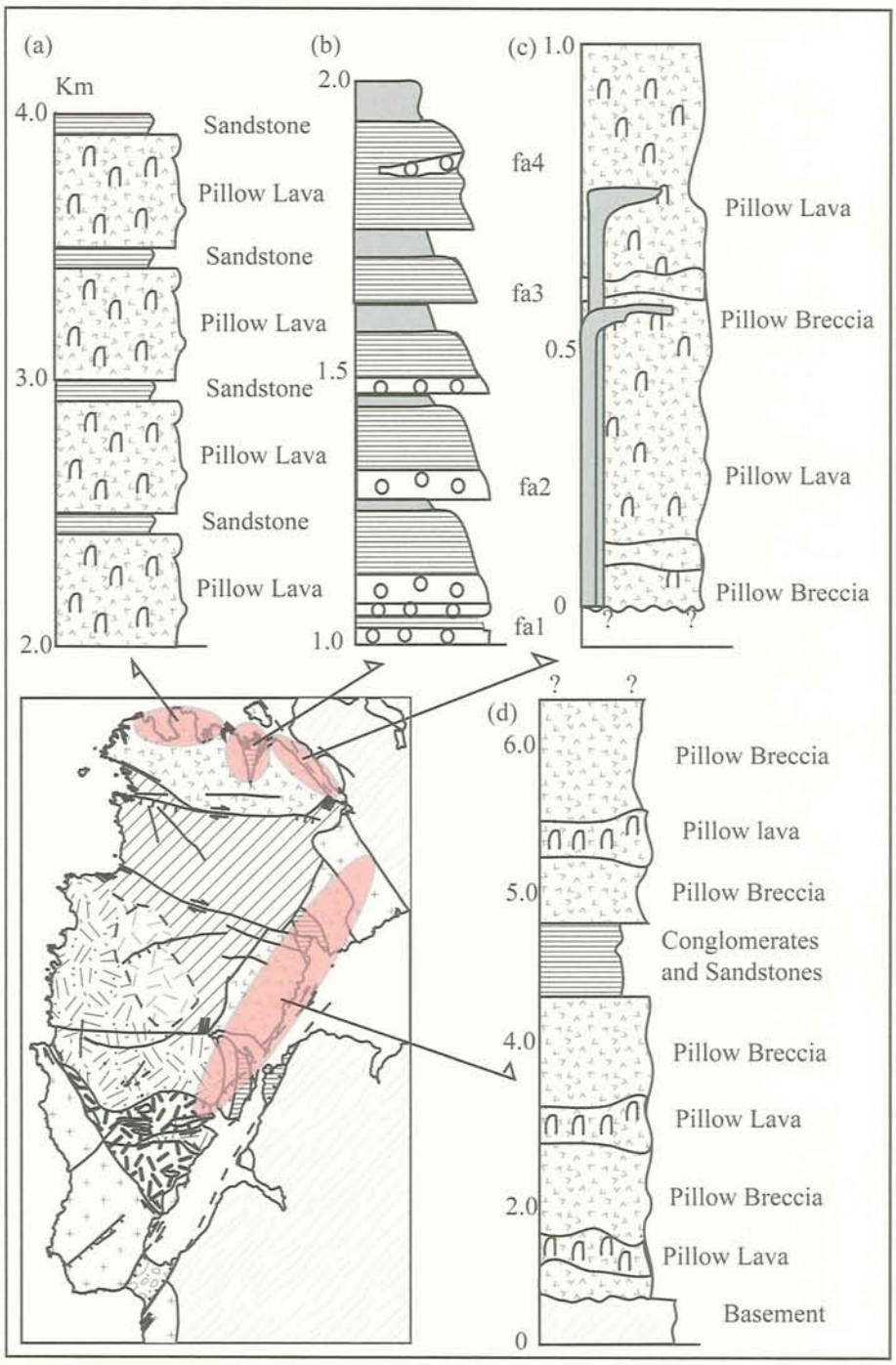

Figure 3.7. Generalized stratigraphic columns for the MVU and the CMU units (e.g. Guivel et al., 1996, 1999). (a) Upper volcani-sedimentary member, (b) middle sedimentary member and (c) lower volcanic member of MVU (e.g. Nelson et al., 1993); (d) CMU.

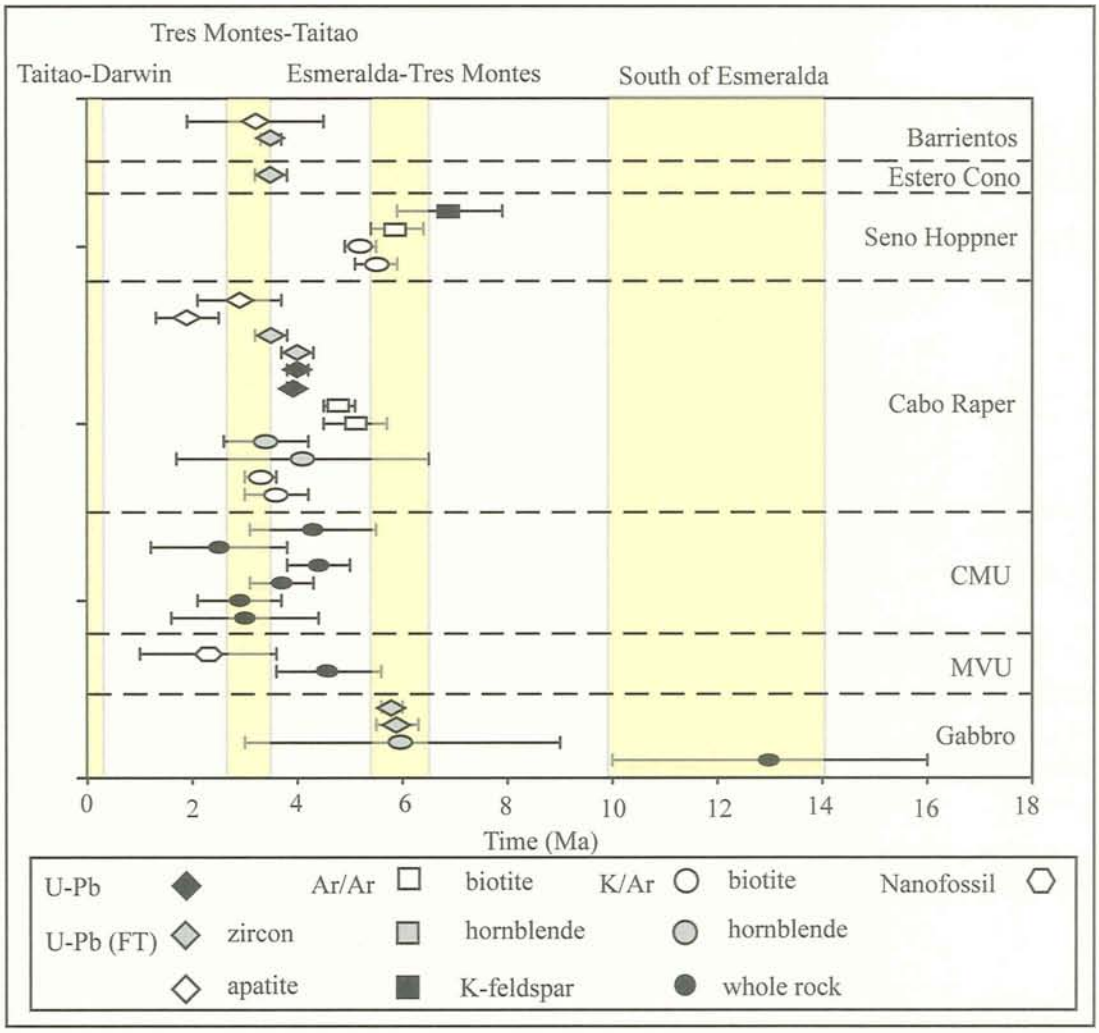

Figure 3.8. Available ages for the Taitao ophiolite and intrusive bodies. Yellow boxes indicate the collisional events of the CR system offshore the Taitao peninsula (indicated by the name of delimiting fracture zones).

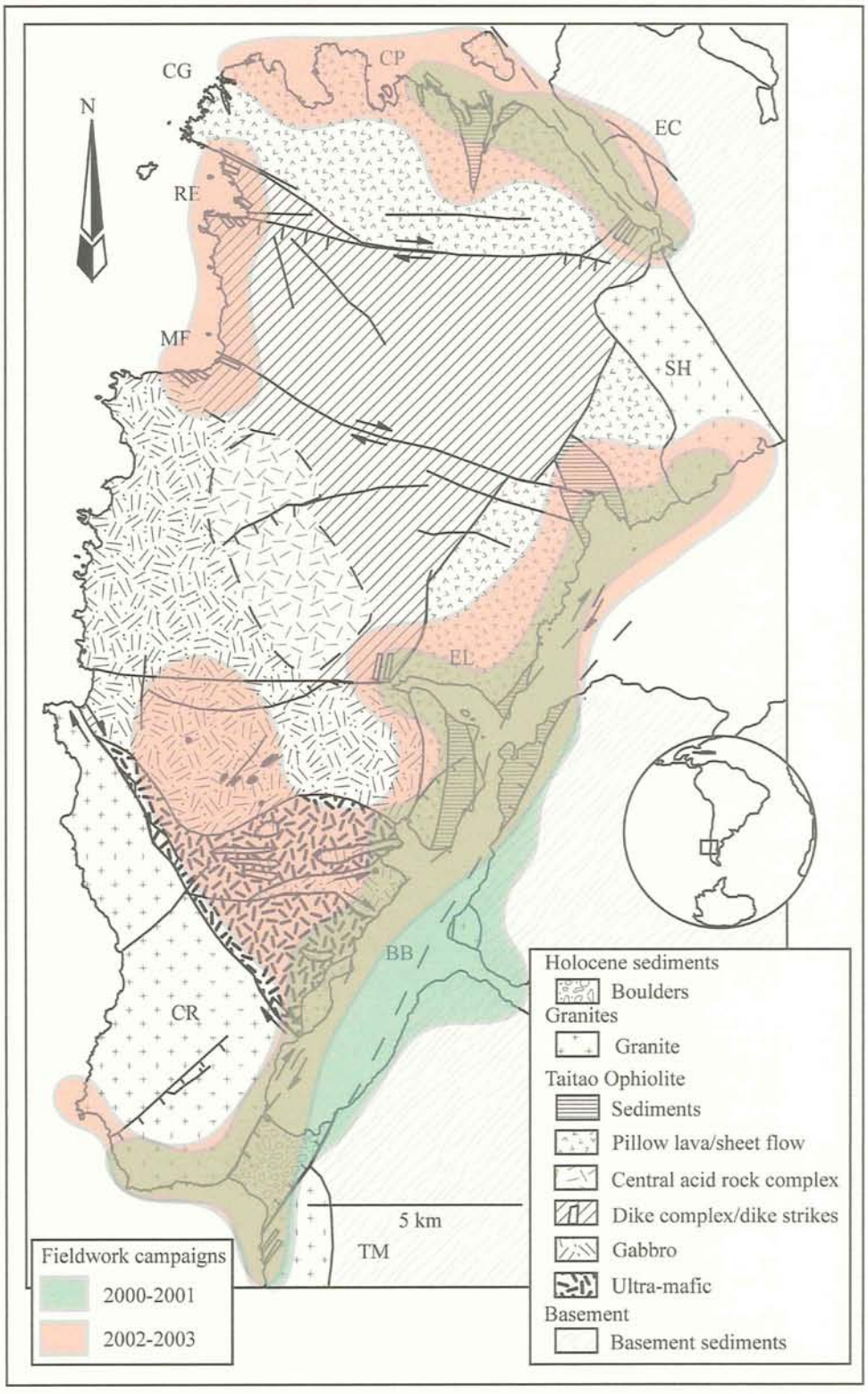

Figure 4.1. Geological map of the westernmost Taitao peninsula showing covered areas during fieldwork campaigns. Names for localities are in figure 1.5.

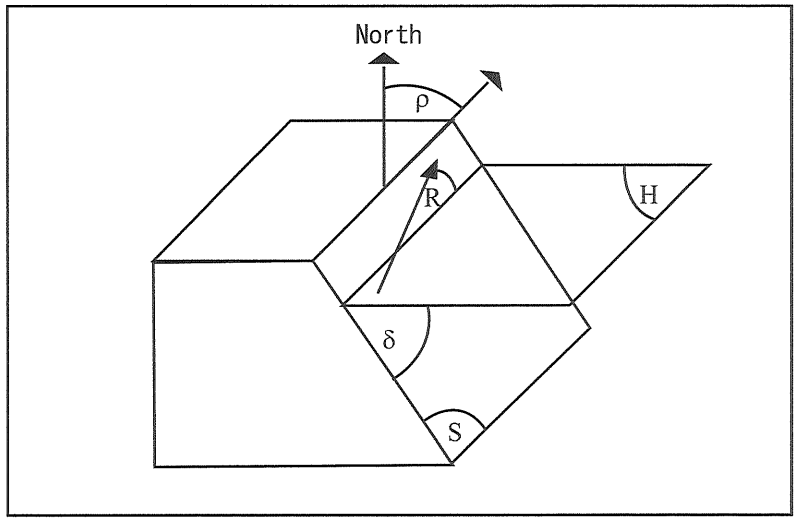

Figure 4.2. Geometric elements on a fault plane. Strike (ρ) is the angle between the surface and the north measured in the horizontal plane, dip (δ) is the angle between the horizontal plane and the surface measured in the vertical plane and pitch or rake (R) is the angle between the horizontal plane and the striae measured in the fault surface. H and S denote the horizontal and surface planes respectively.

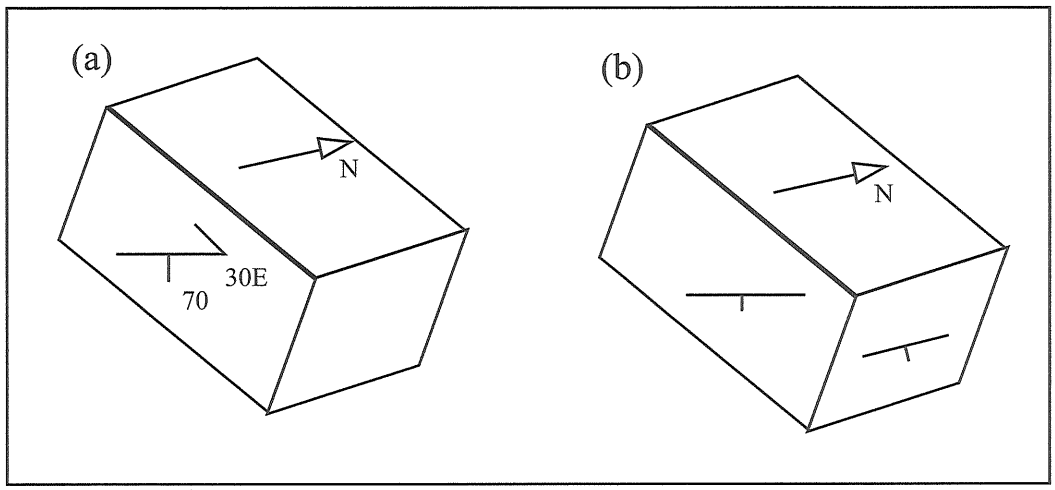

Figure 4.3. Block diagrams showing the orientation techniques of block samples used in fieldwork campaigns.

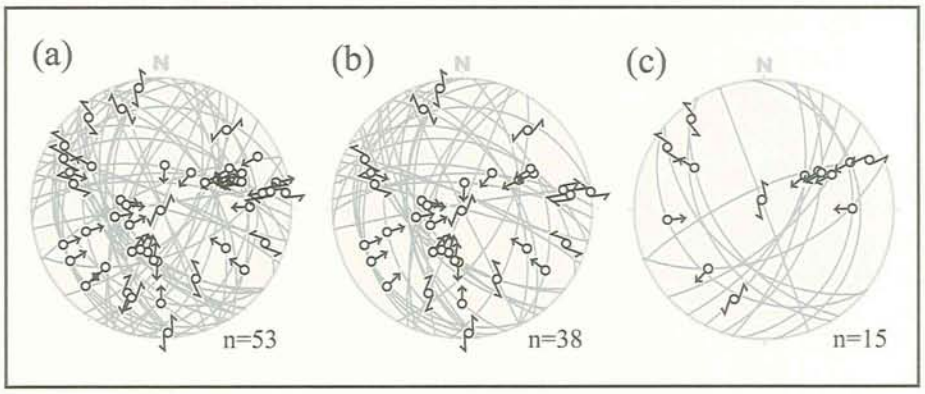

Figure 5.1. Lower hemisphere, equal area projections with the orientation and slip directions (arrows) of collected fault-slip data. (a) All data including: (b) fault-slip data from the plutonic units (ultramafic and gabbro) and (c) fault-slip data from BBFZ.

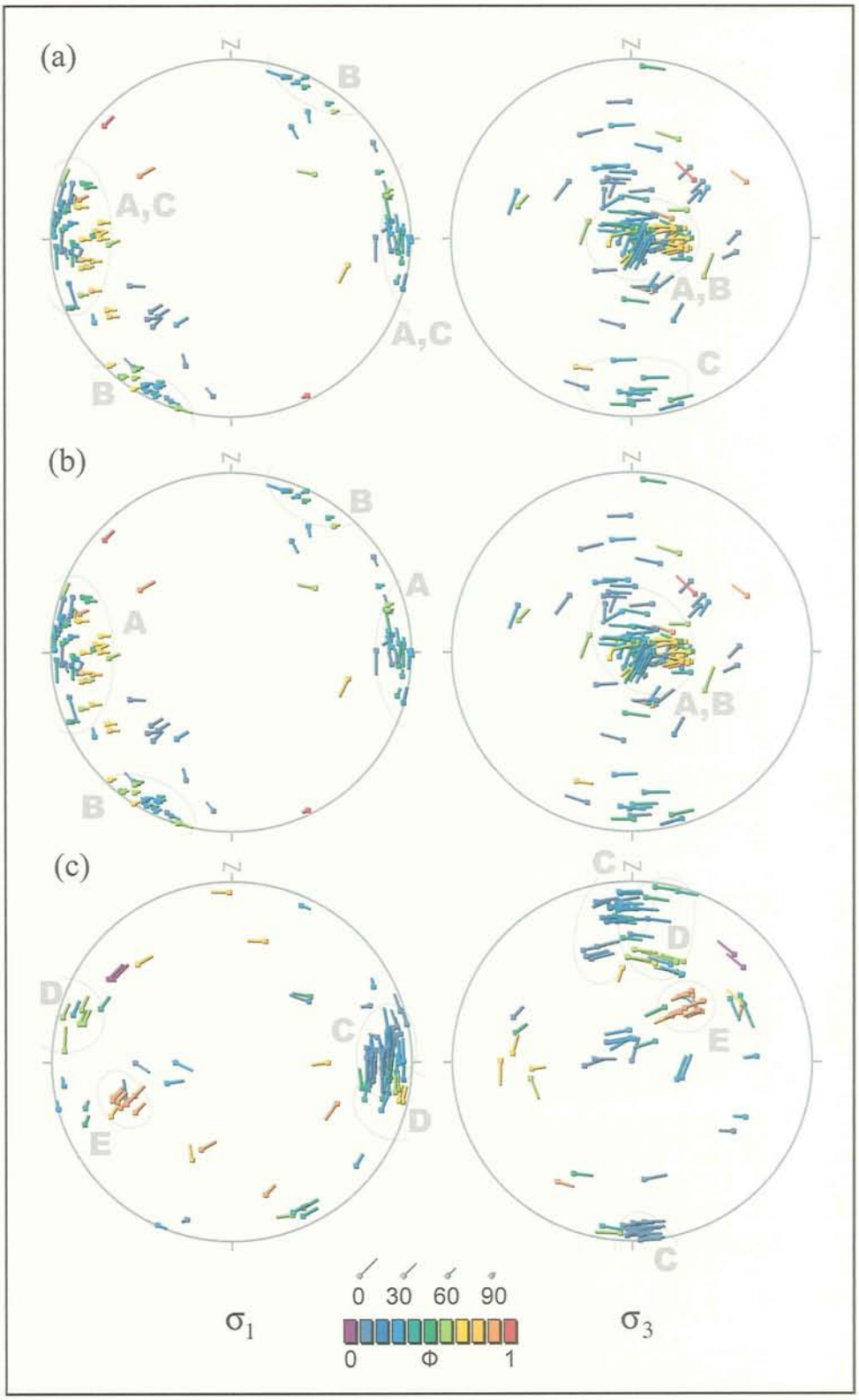

Figure 5.2. Equal-area, lower hemisphere projections with the orientation of compressional (left) and extensional (right) principal stress axes obtained for each analyzed set of fault. (a) "all" fault-slip set, (b) "inner" fault-slip set and (c) "outer" fault-slip set. See text and Appendix A for details. Figure courtesy of Dr. A. Yamaji (Kyoto University).

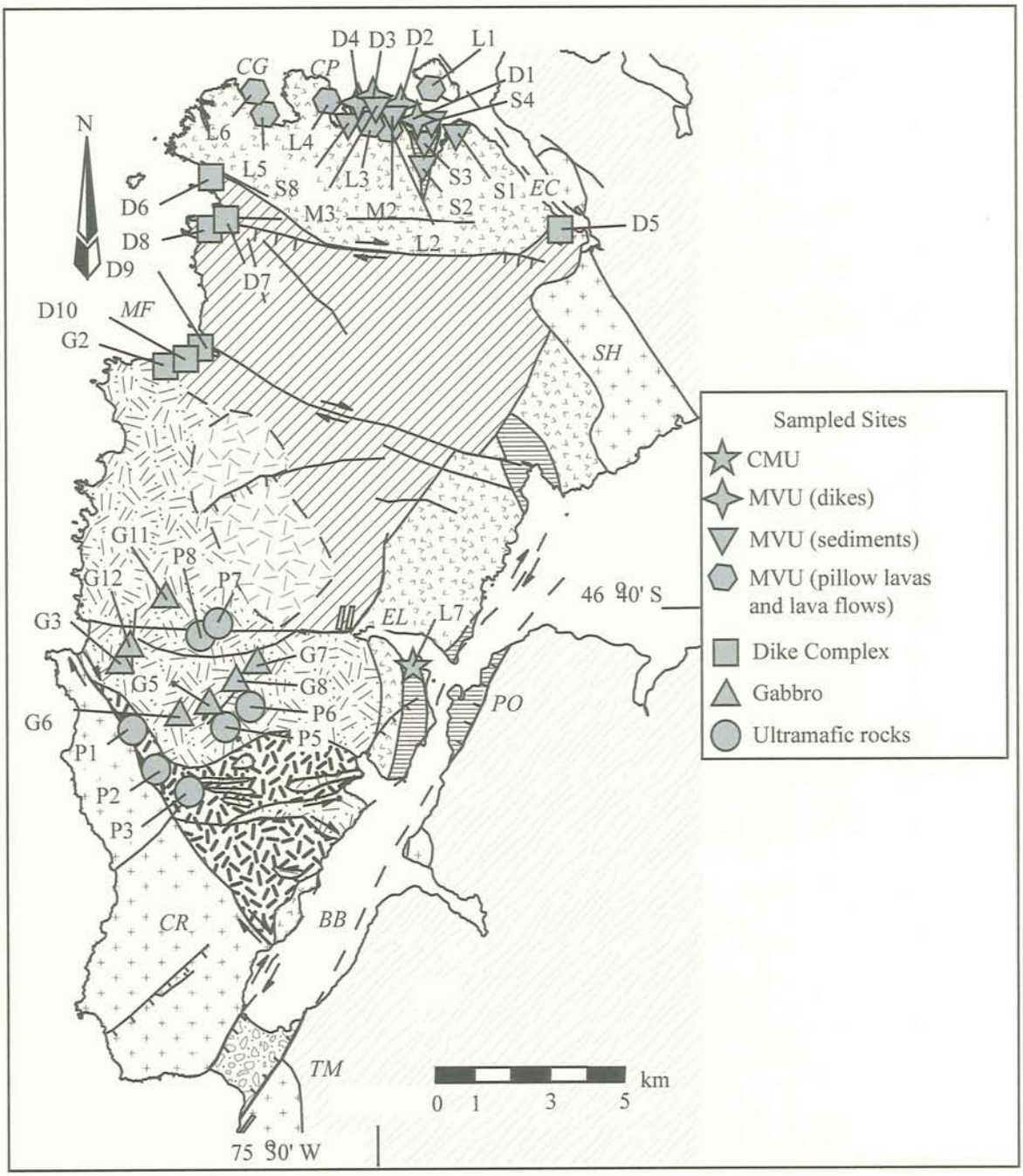

Figure 6.1. Geological map of the Taitao peninsula showing paleomagnetic sampling sites.

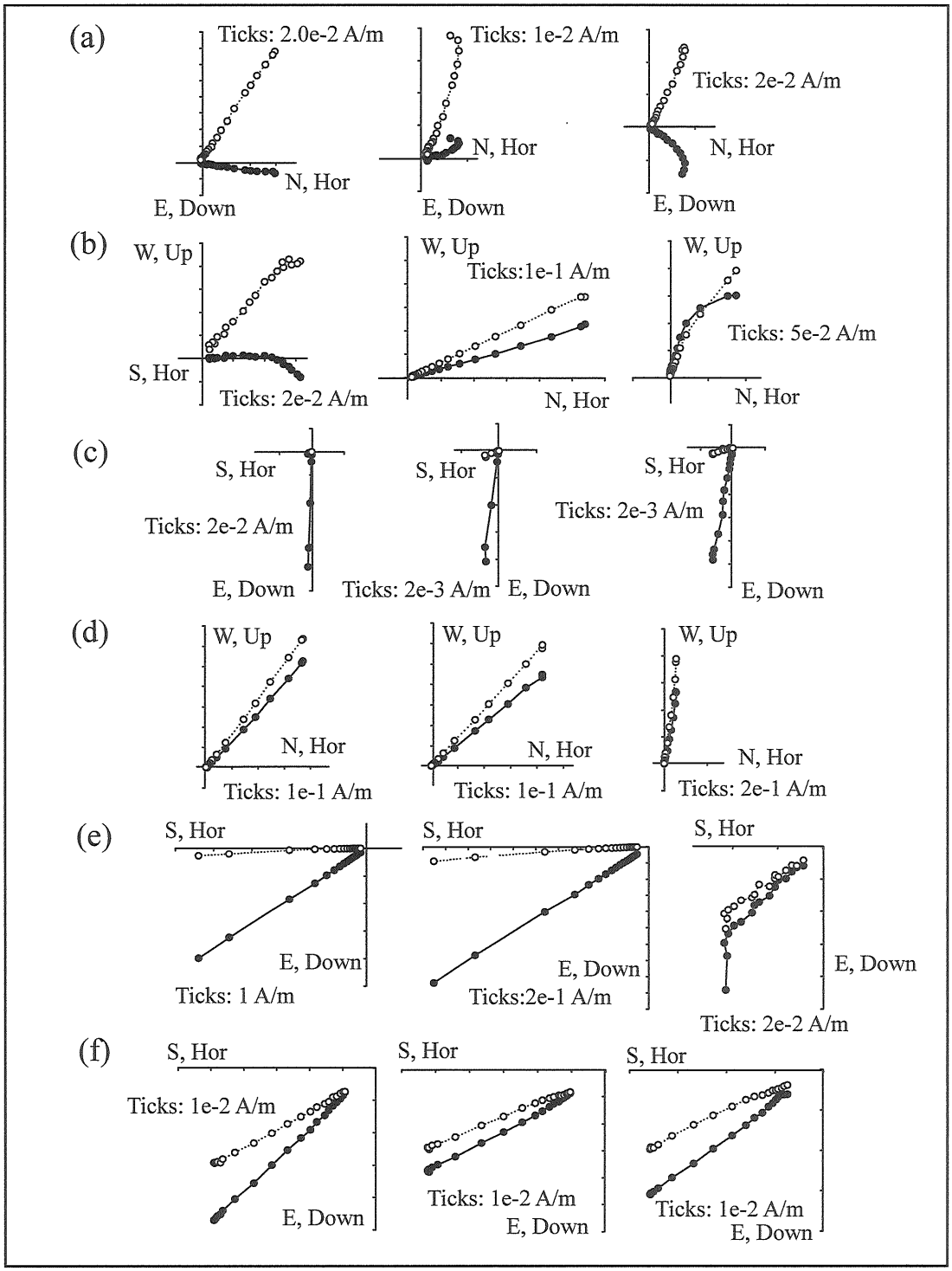

Figure 6.2. Selected univectorial demagnetization paths of: (a) clastic sediments of MVU, (b) pillow lavas and lava flows of MVU, (c) pillow lavas of CMU, (d) ECDC and dikes of MVU, (e) MRDC and (f) Contact between gabbro and dike complex units. Filled symbols are projections in the horizontal plane while open ones are in the vertical plane (see Appendix B for details).

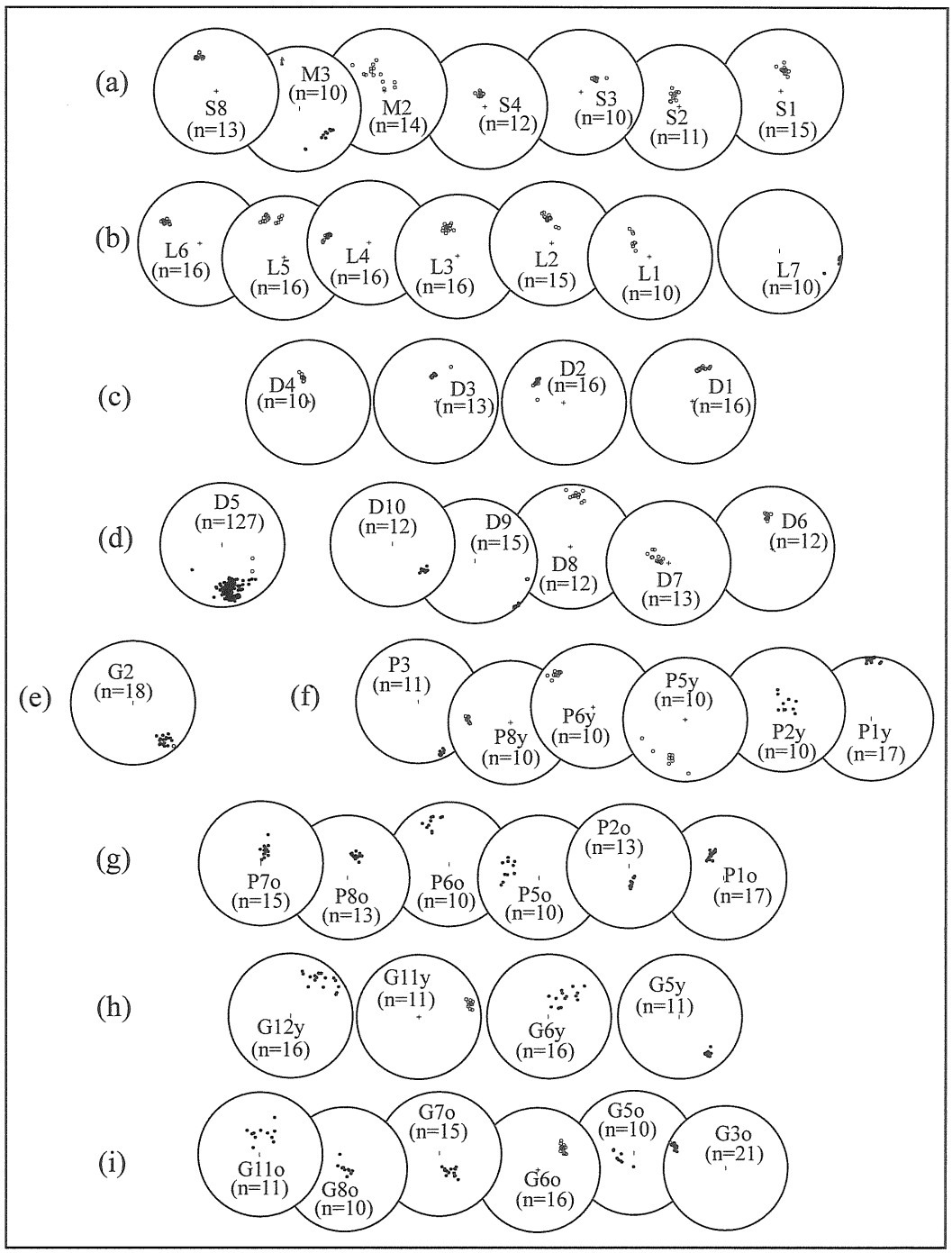

Figure 6.3. Lower (upper) hemisphere, equal area projections with the orientation of isolated RM vectors at each sampled site (see Fig. 6.1). (a) Clastic sediments of MVU, (b) Pillow lavas and Lavas flows of MVU (L1-L6) and of CMU (L7), (c) feeder dikes of MVU, (d) ECDC (D5) and MRDC (D6-D10), (e) contact between gabbro and dike complex, (f) "young" RM vectors of ultramafic rocks, (g) "old" RM vectors of ultramafic rocks, (h) "young" RM vectors of gabbro and (f) "old" RM of gabbro. Filled (open) symbols are projections in the lower (upper) hemisphere.

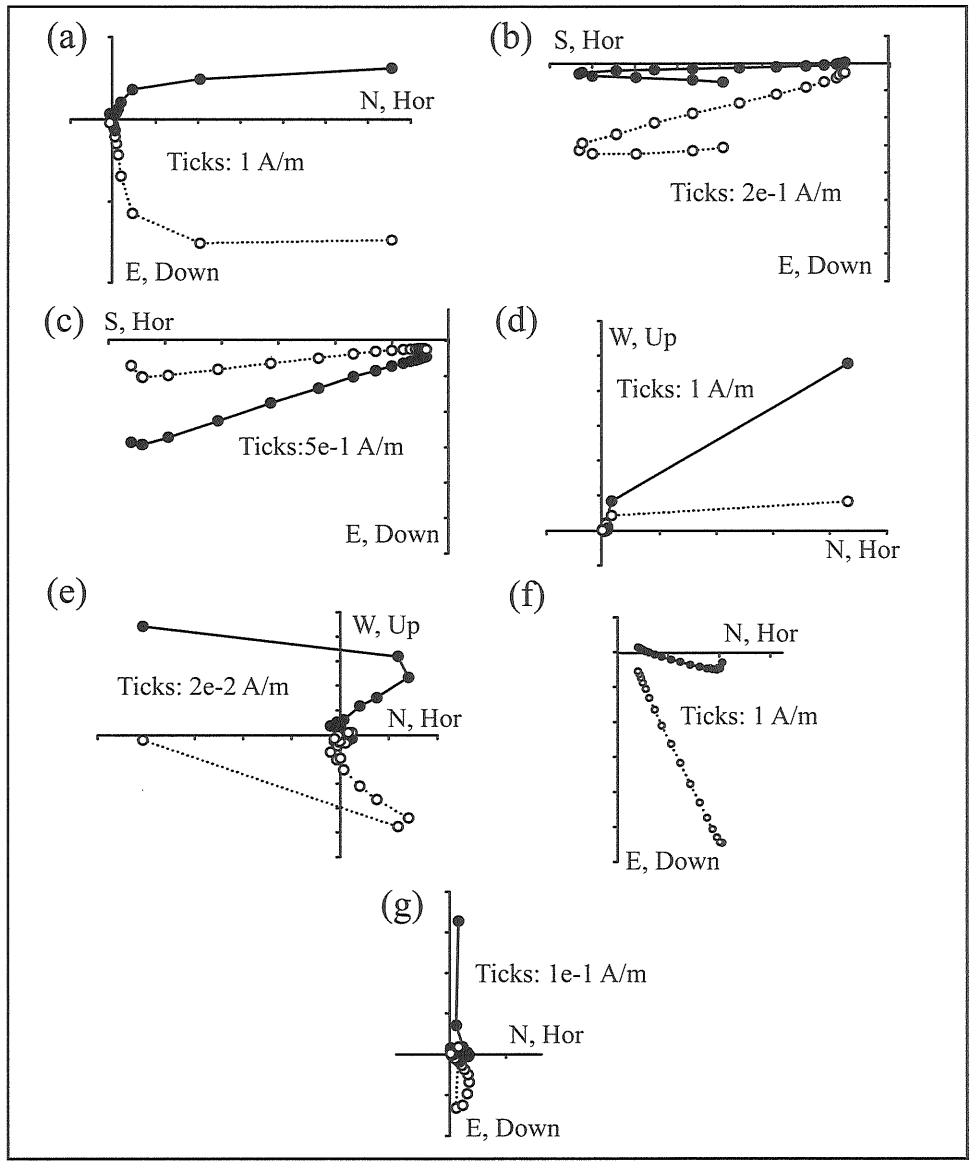

Figure 6.4. Selected multivectorial demagnetization paths of ultramafic rocks. Notice that most demagnetization paths show more than one magnetization component. Symbols in figure 6.2.

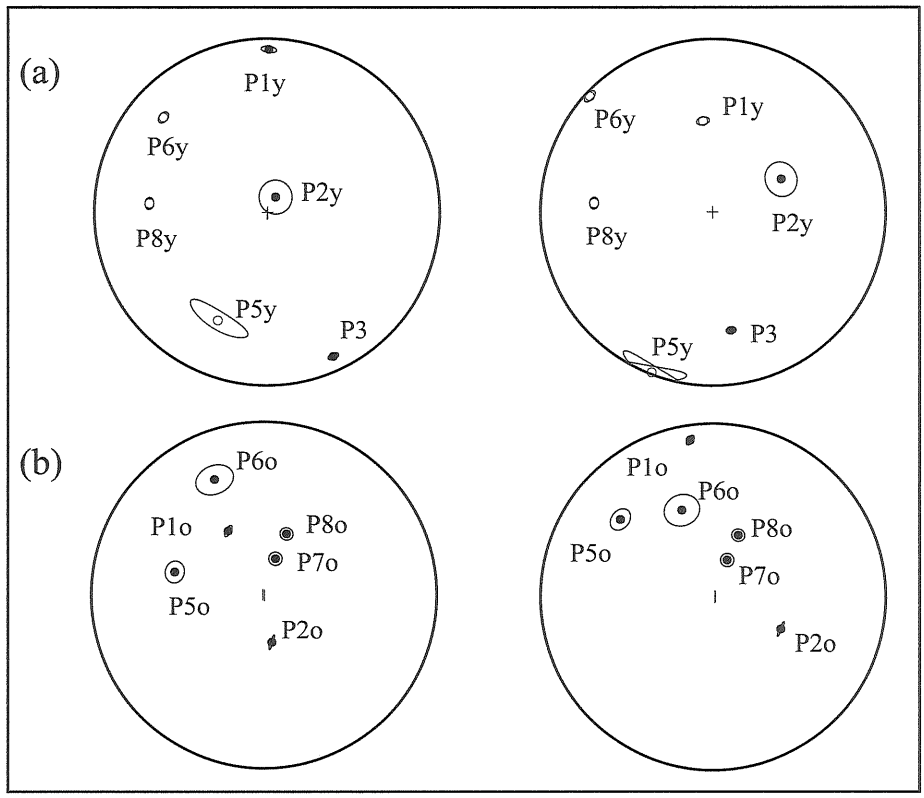

Figure 6.5. Lower (upper) hemisphere, equal area projections with the mean orientations of (a) "young" and (b) "old" RM vectors and associated confidence intervals for ultramafic rocks. Left side is insitu while right side is corrected after Fold-1. Symbols in figure 6.3.

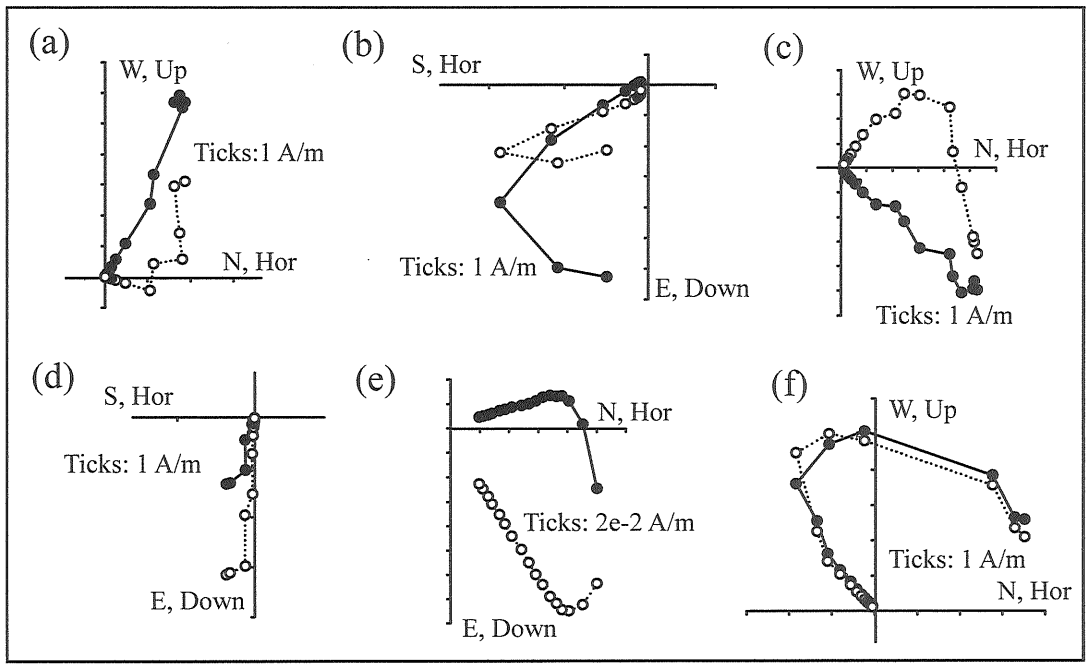

Figure 6.6. Selected multivectorial demagnetization paths of gabbro sites. Notice that most demagnetization paths show more than magnetization component. Symbols in figure 6.2.

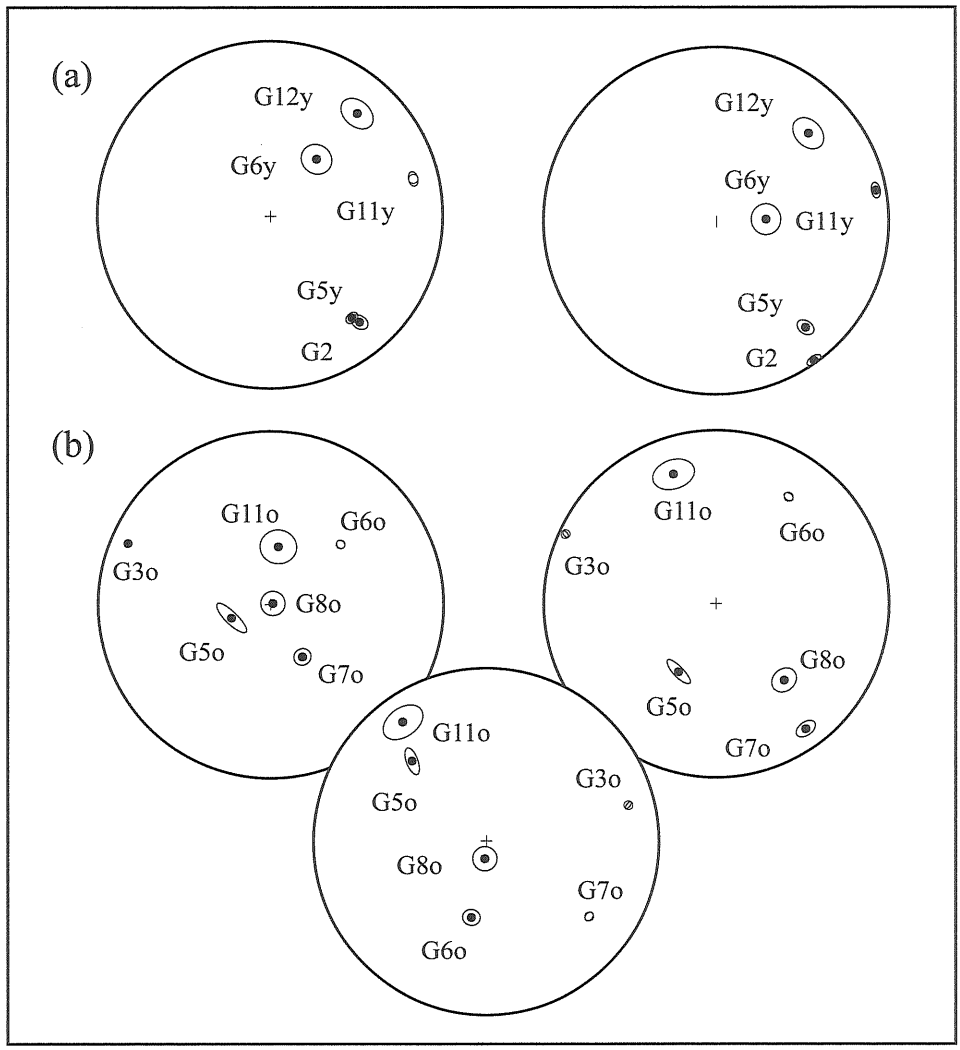

Figure 6.7. Lower (upper) hemisphere, equal area projections with the mean orientations and associated confidence intervals of (a) "young" (b) "old" RM vectors of gabbro. Left side is insitu orientations, right is after Fold-1 correction and down (in c) is after Rot-2- correction. Symbols in figure 6.2.

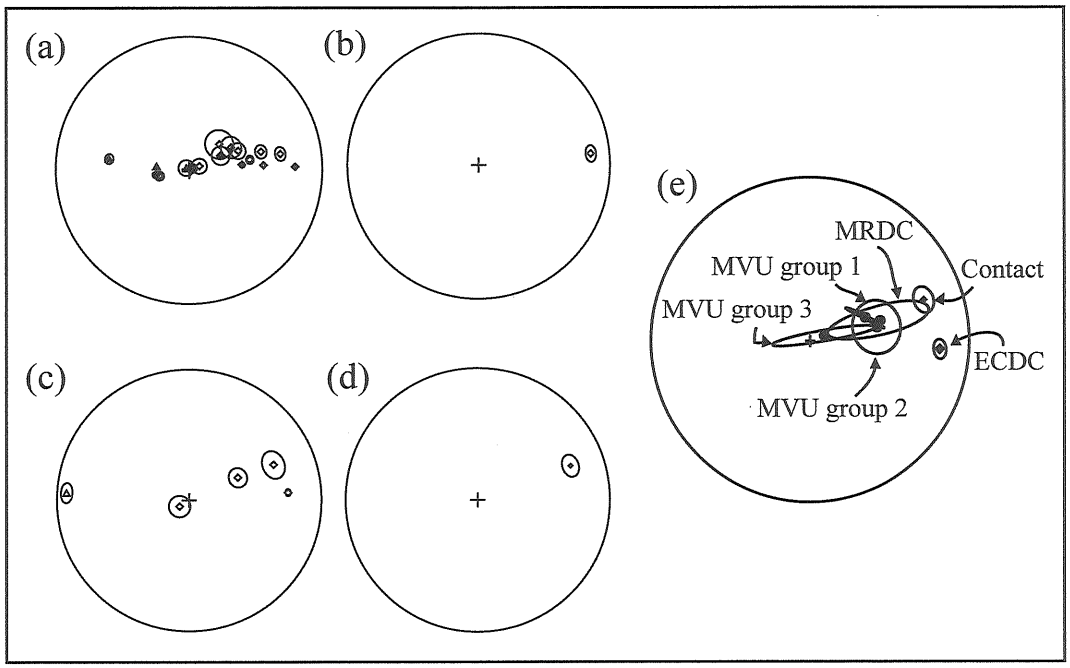

Figure 6.8. Lower hemisphere, equal area projections with the orientations of individual rotational axes for (a) MVU, (b) ECDC, (c) MRDC, (d) contact between gabbro and dike complex units; cones indicate 10% of the rotational amount for each axis. (e) Orientation of mean rotational axes and associated confidence intervals. Notice the strong overlap of the confidence intervals.

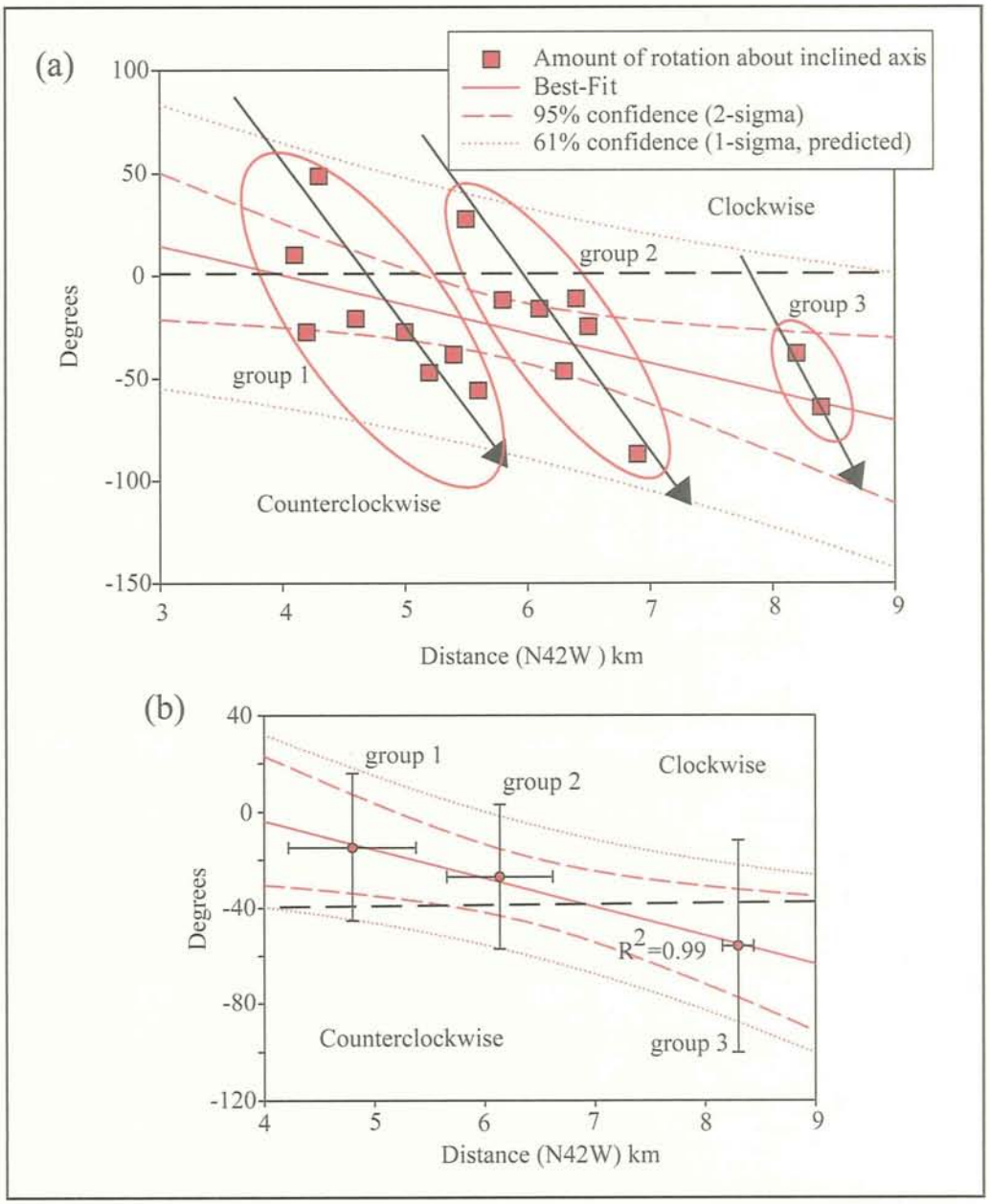

Figure 6.9. Rotational amounts about inclined axes vs. distance for MVU sites along the Estero Cono channel. (a) individual rotational amounts, (b) mean rotational amounts. Notice the three clearly identified groups. Distance is measured from the innermost part of Estero Cono (Fig. 6.1) in a straight $N42^0W$ line.

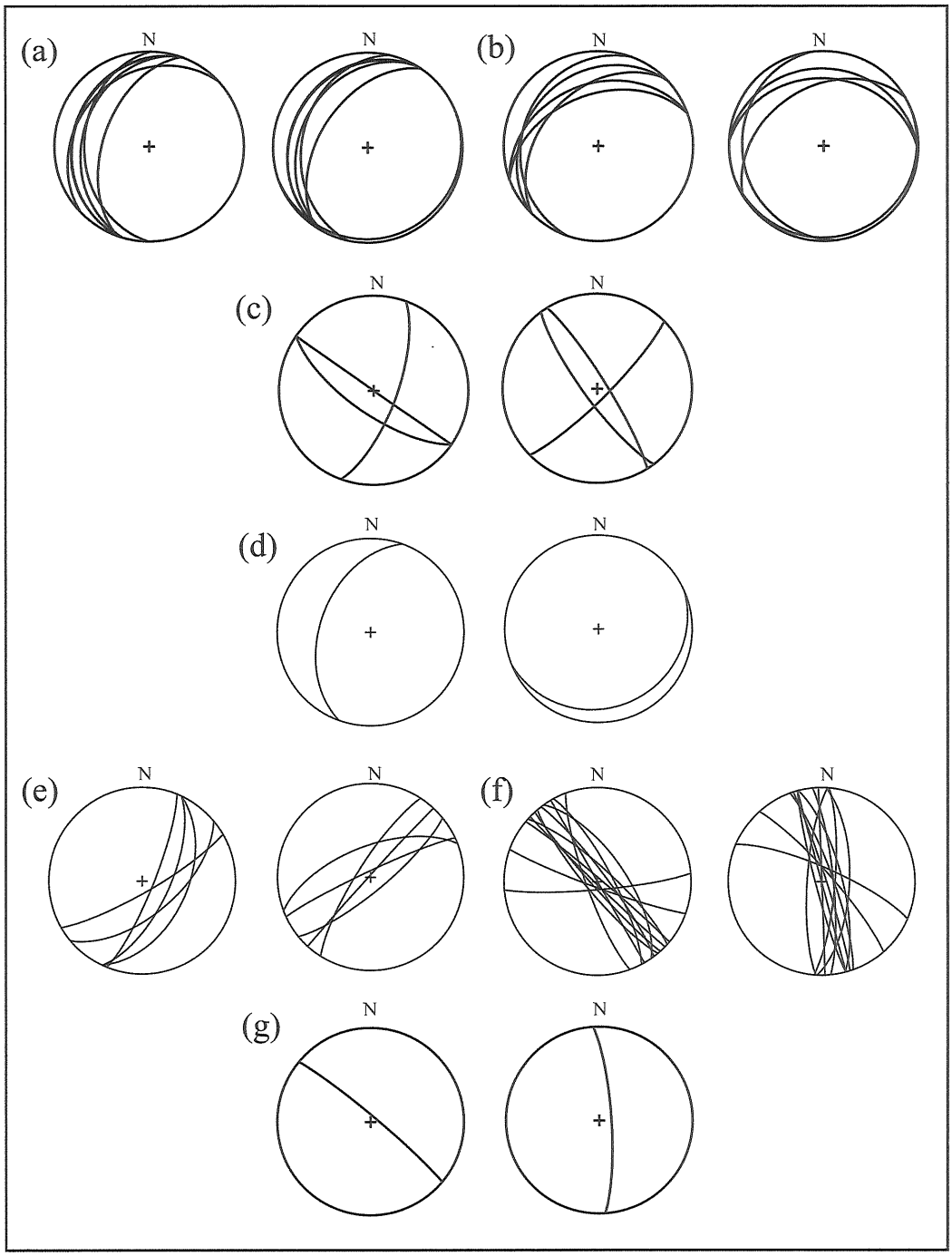

Figure 6.10. Lower hemisphere, equal area projection with the orientation of insitu (left) and restored (right) structures of MVU, CMU and dike complex units. (a) Clastic sediments of the MVU, (b) pillow lavas and lava flows of the MVU, (c) feeder dikes of the MVU, (d) pillow lava of the CMU, (e) ECDC, (f) MRDC and (g) contact between dike complex and gabbro units.

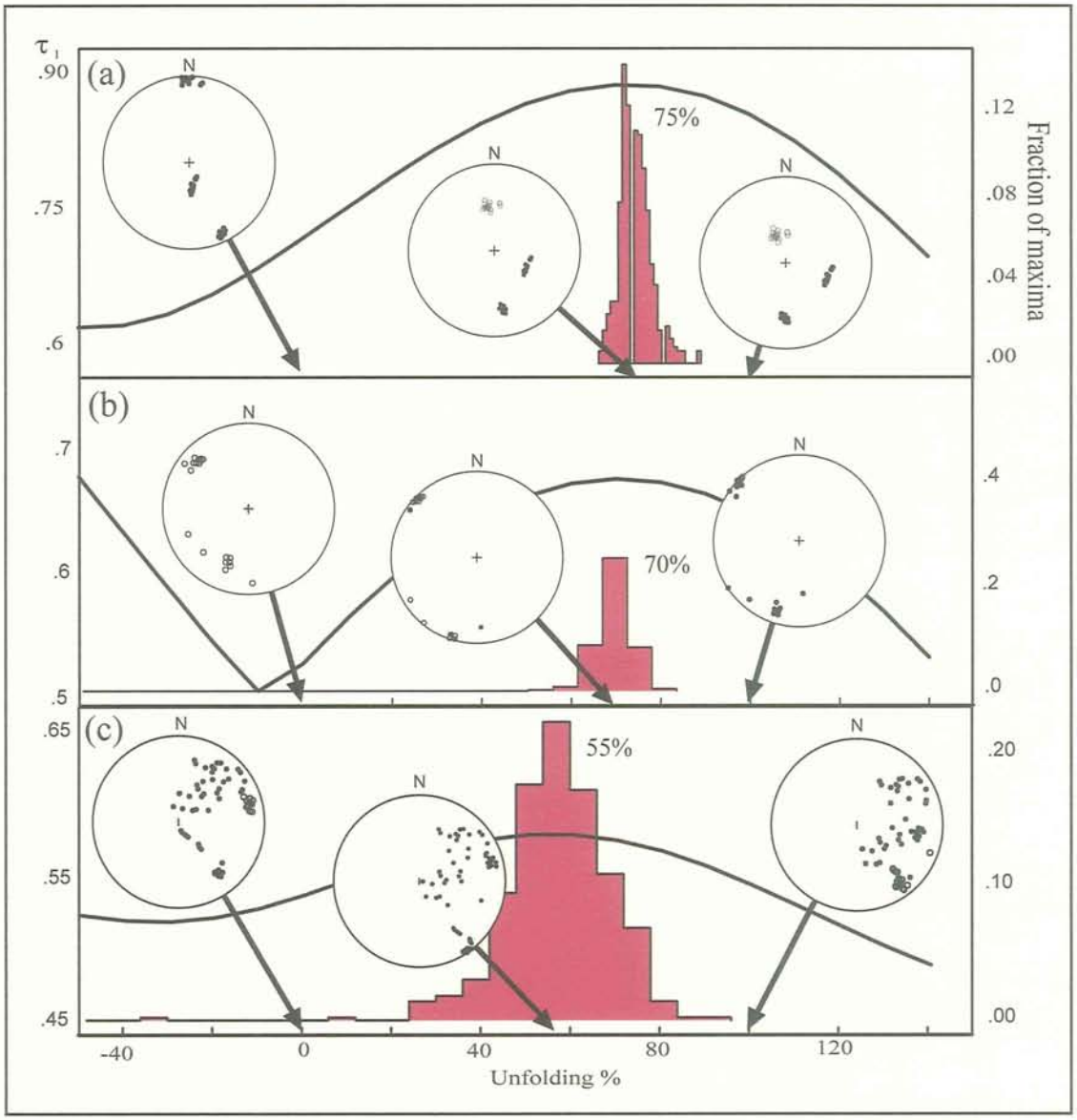

Fig. 6.11. Unfolding curves and histogram (see Tauxe, 1998) fold test analyses using "young" RM vectors and foliation in ultramafic (a) south and (b) central blocks, and (c) compositional layering in gabbro unit. Optimum percentages are indicated as well as the orientation of isolated RM vectors at 0%, 100% and optimum percentages.

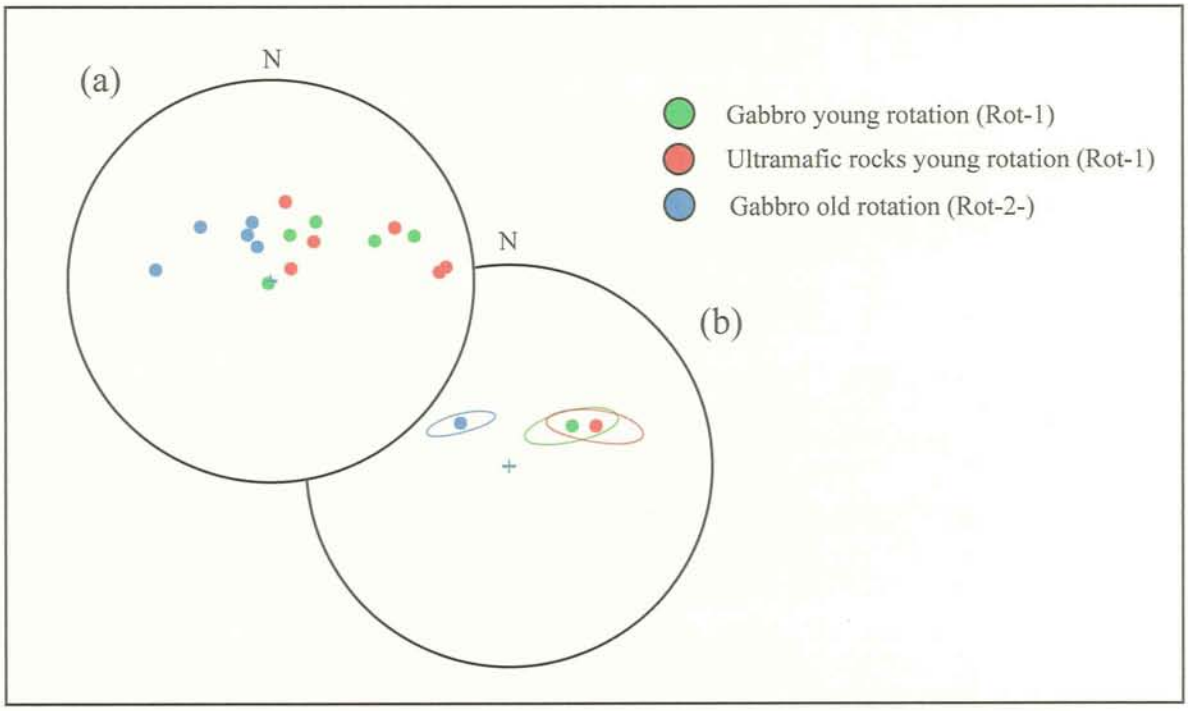

Figure 6.12. Lower hemisphere, equal area projections with the orientations, and associated confidence intervals, of (a) individual and (b) mean rotational axes for the plutonic units. Both "young" (Rot-1) and "old (Rot-2-) axes are plotted.

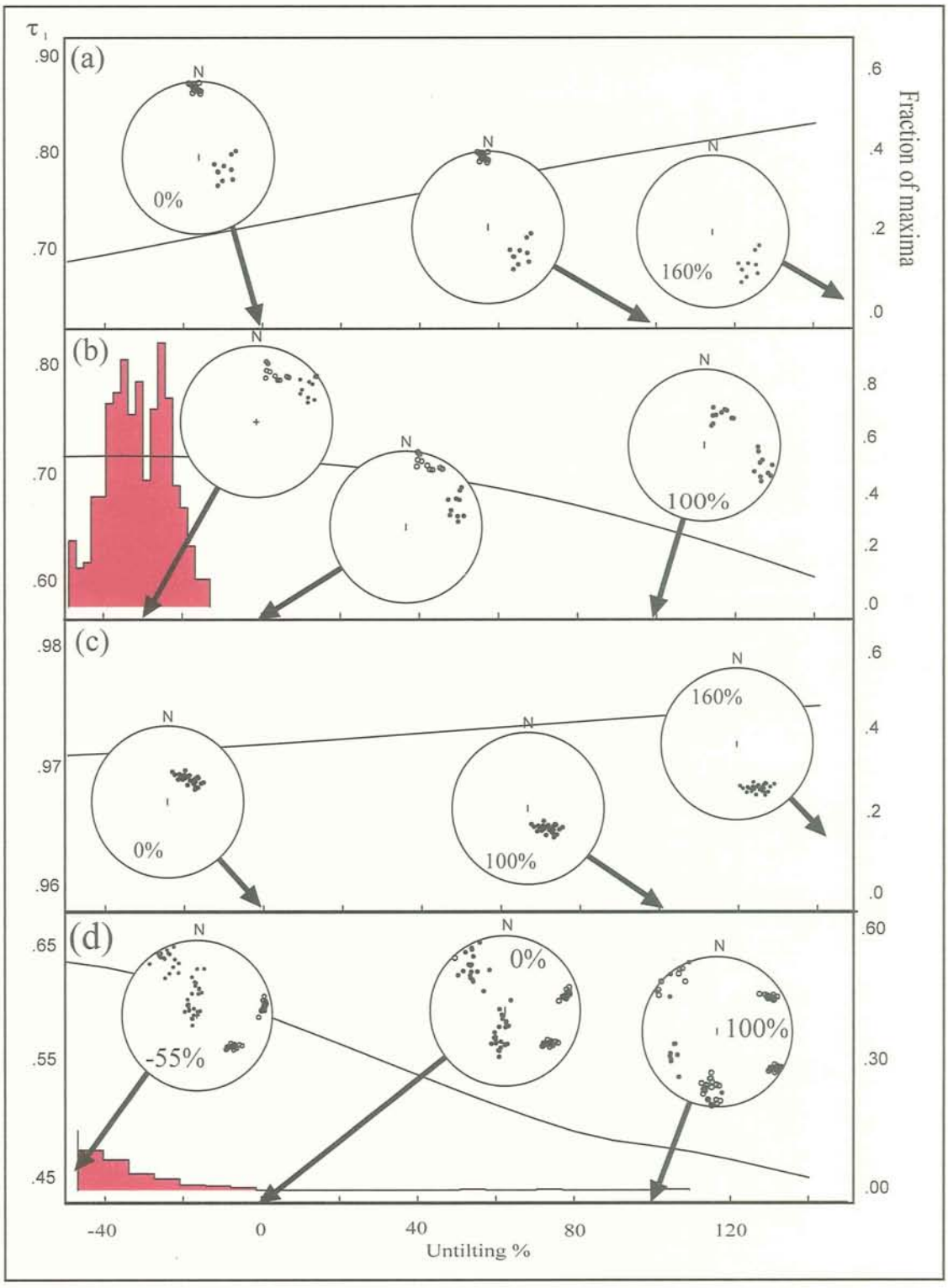

Figure 6.13. Unfolding curves and histogram (see Tauxe, 1998) fold test analyses of foliation in ultramafic (a) south, (b) central blocks and (c) north blocks, and (d) compositional layering gabbro unit using "old" RM vectors. Optimum percentages are indicated as well as the orientation of isolated RM vectors at 0%, 100% and optimum percentages.

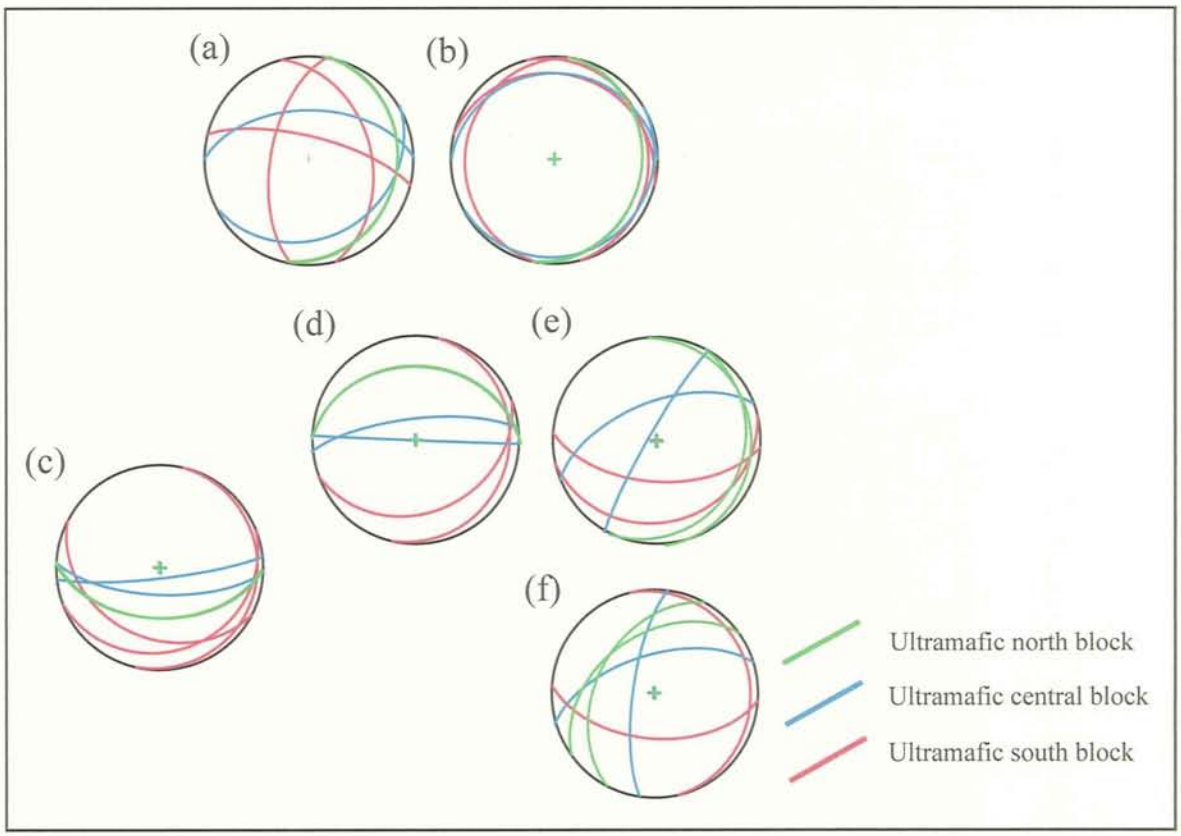

Figure 6.14. Lower hemisphere, equal area projections with the orientation of foliation in ultramafic blocks. (a) Measured insitu, (b) after Fold-1, (c) after Rot-1, (d) after Fold-2+, (e) after Rot-2+ and (f) after Rot-2- paleomagnetic corrections (see text for details).

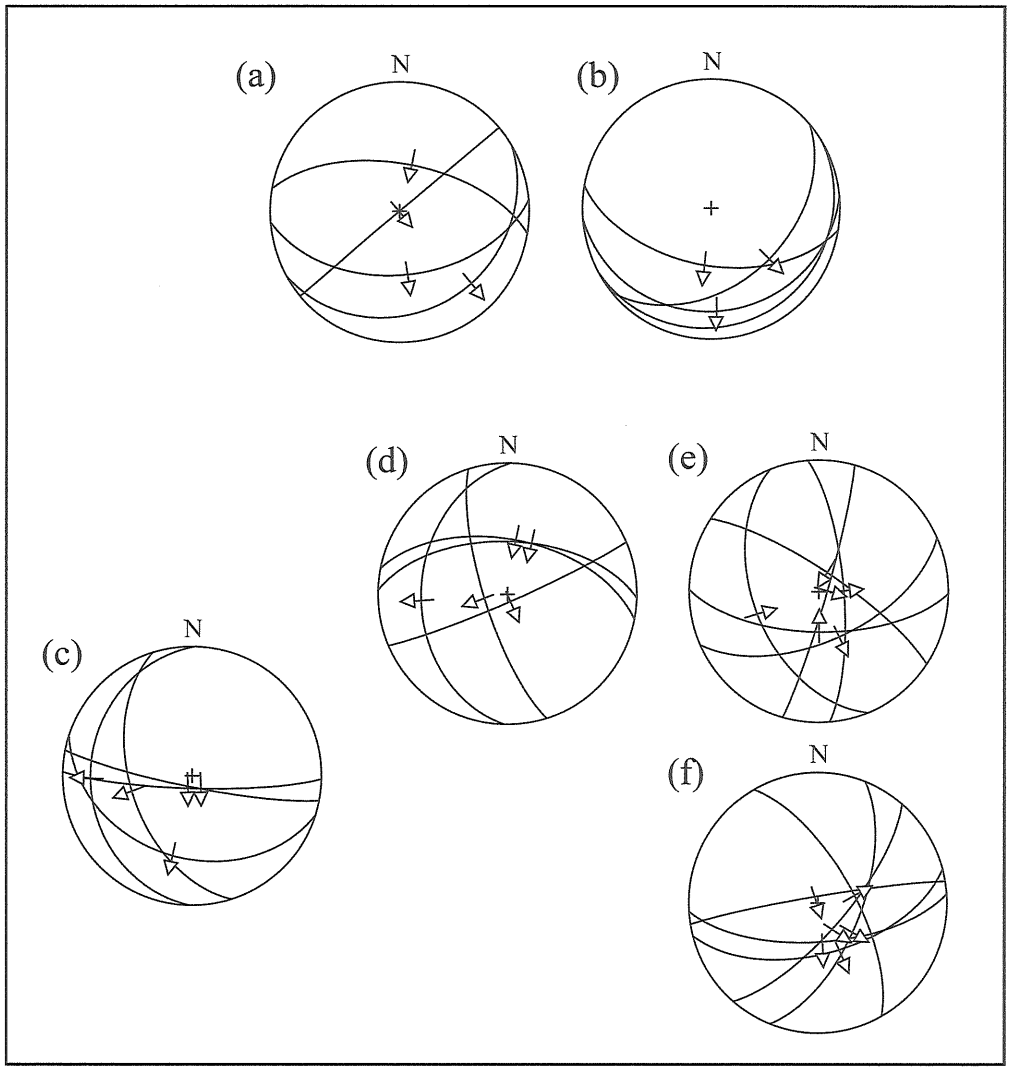

Figure 6.15. Lower hemisphere, equal area projections with the orientations of compositional layers of gabbro. (a) Measured insitu, (b) after Fold-1, (c) after Rot-1, (d) after Fold-2+, (e) after Rot-2+ and (f) after Rot-2- paleomagnetic corrections (see text for details). Arrows indicate younging direction of compositional layers.

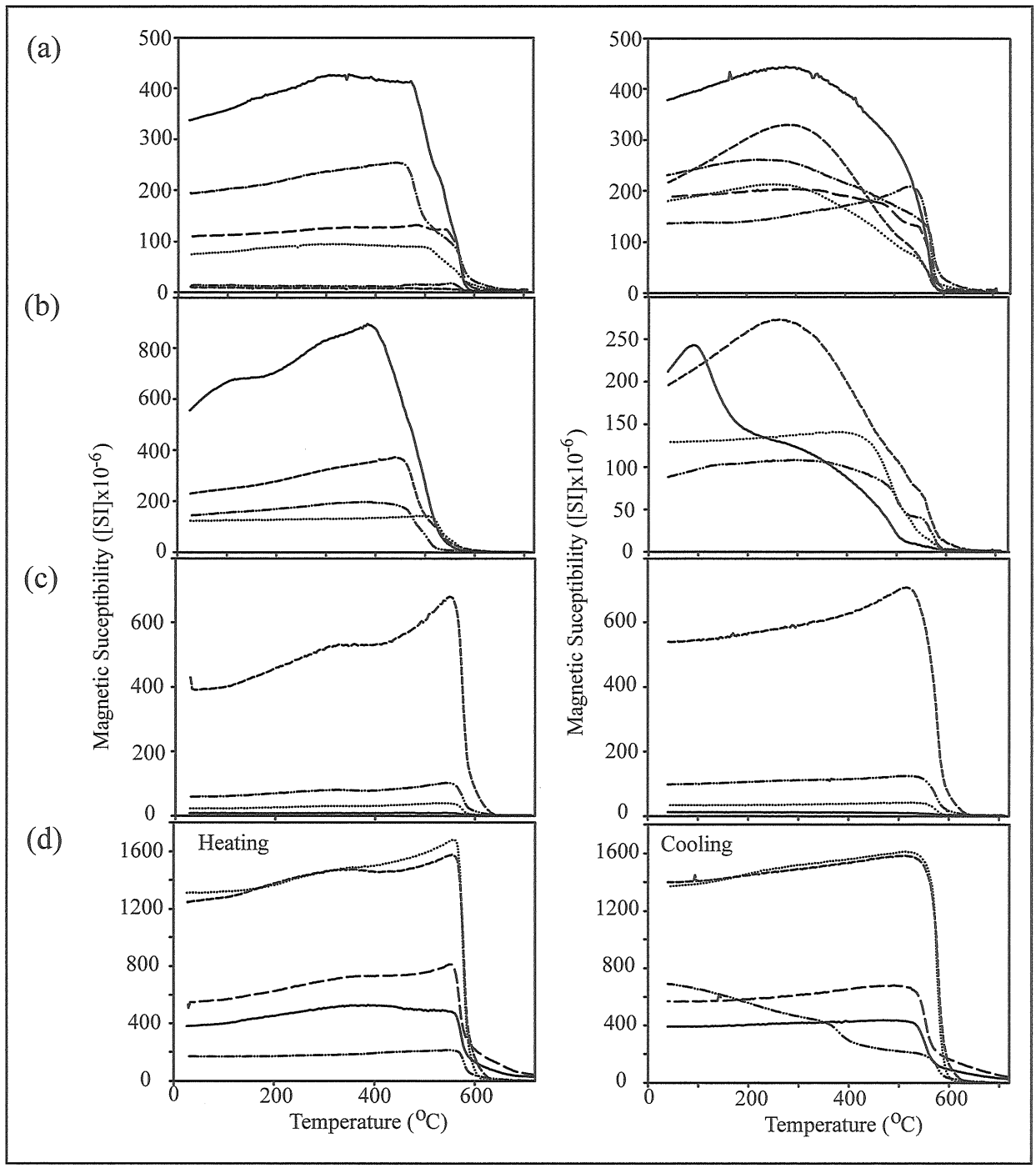

Figure 7.1. Heating (right) and cooling (left) thermomagnetic curves obtained from (a) clastic sediments of MVU, (b) pillow lavas and feeder dikes of MVU, (c) gabbro and (d) ultramafic rock samples. Notice the abrupt decay of all curves between 550^0 and 600^0

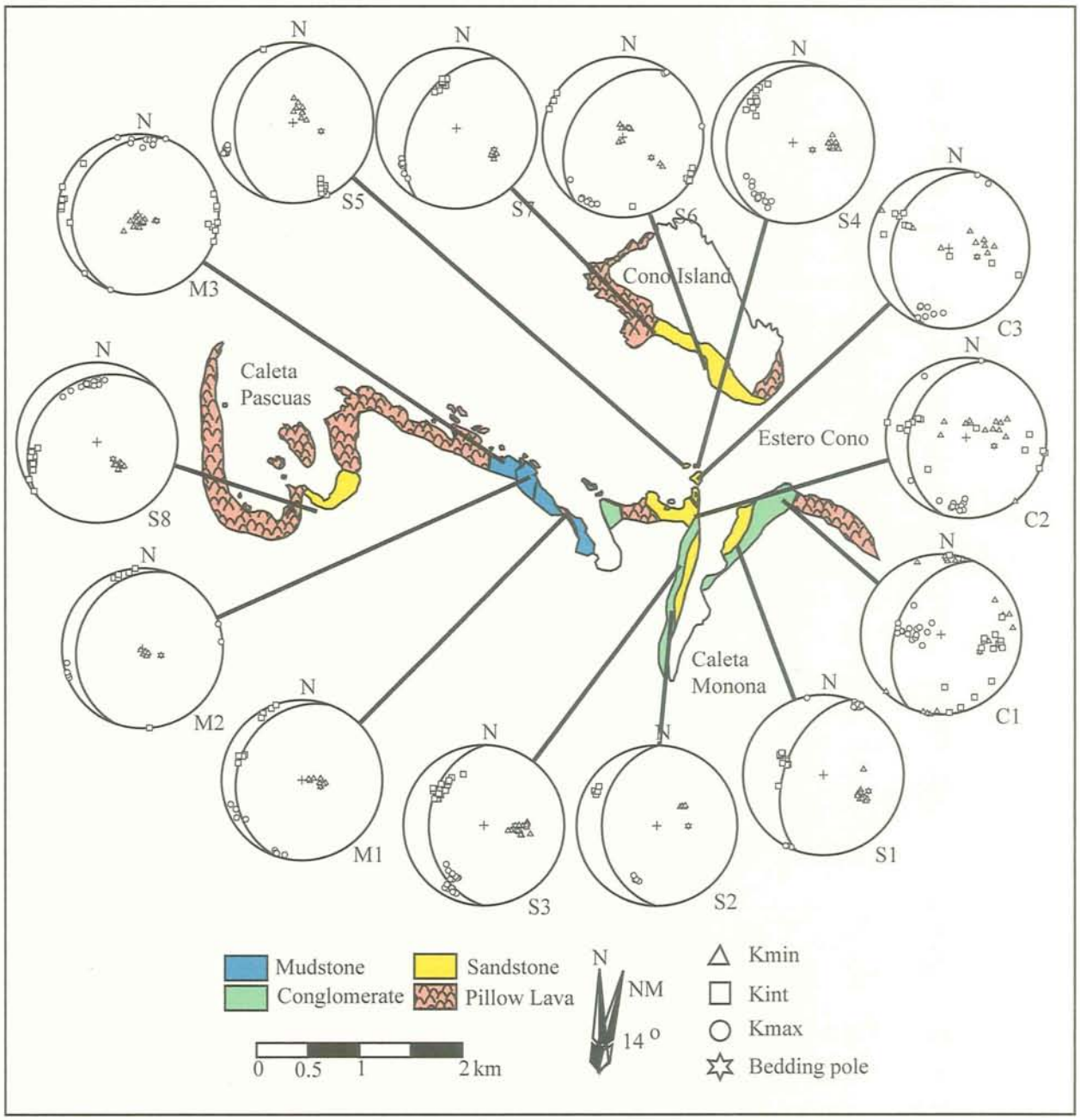

Figure 8.1. Simplified geological map of the coastal outcrops of the MVU in the Estero Cono area (see Fig. 1.5). Lower hemisphere, equal area projection with the orientation of the principal AMS axes (AMS fabric) at each sampled site (see text for details).

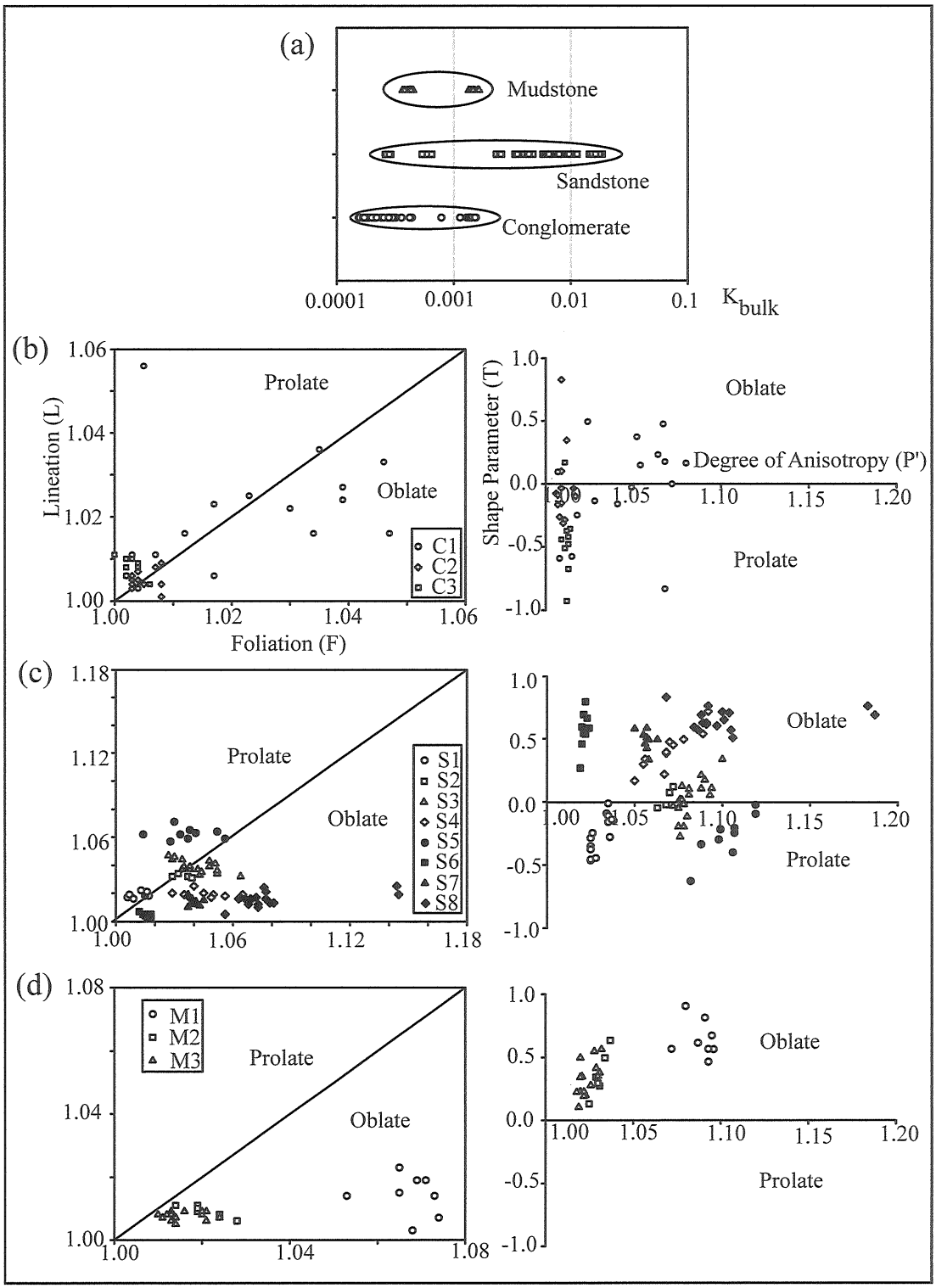

Figure 8.2. (a) AMS bulk intensities by lithology. Characterization of AMS fabric shapes by means of Lineation vs. Foliation plot (e.g. Balsley and Buddington, 1960; Stacey et al., 1960) (left side) and Shape parameter vs. Degree of Anisotropy plot (Jelinek, 1981) (right side) for: (b) conglomerates, (c) sandstones and (d) mudstones.

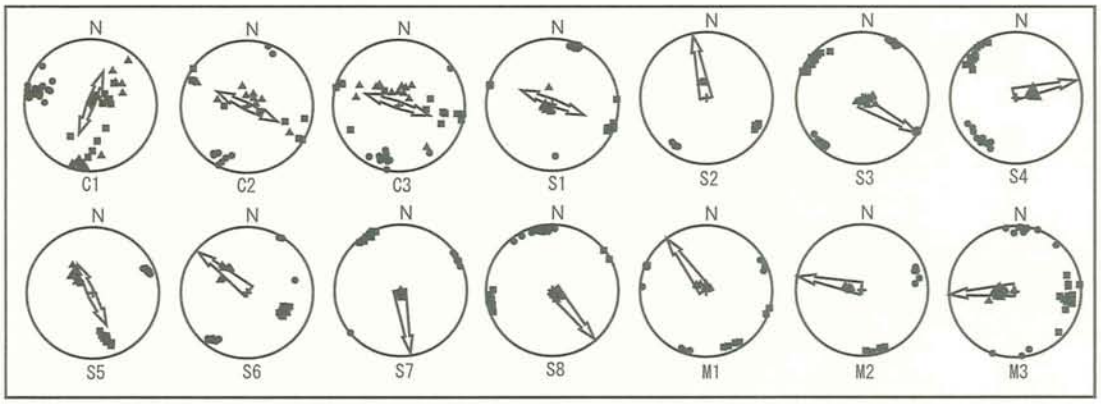

Figure 8.3. Lower hemisphere, equal area projection with the orientation of AMS axes after bedding correction (symbols in figure 8.1) and the inferred paleocurrent directions (arrows) at each sampled site.

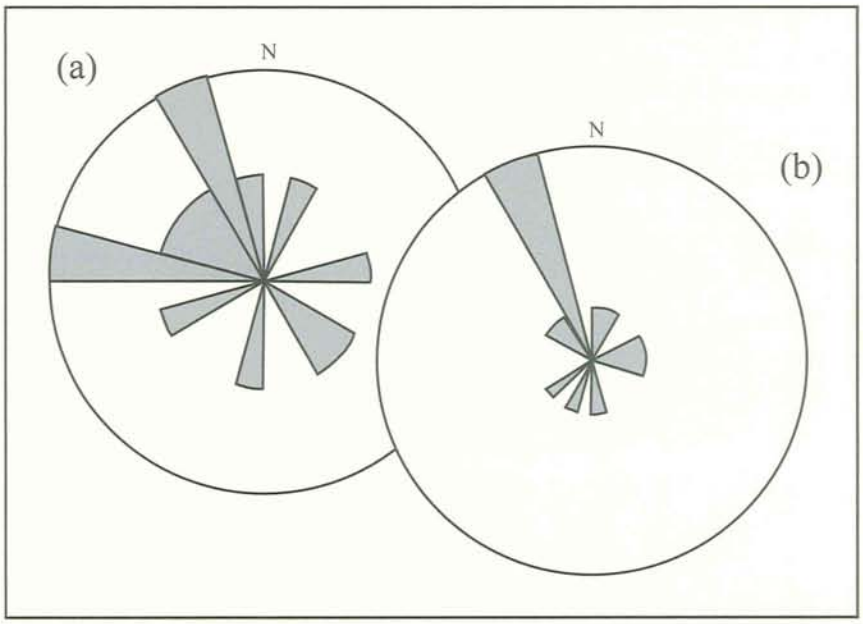

Figure 8.4. Polar plots with the azimuthal orientations of paleocurrent directions inferred from AMS analyses. (a) before and (b) after paleomagnetic correction.

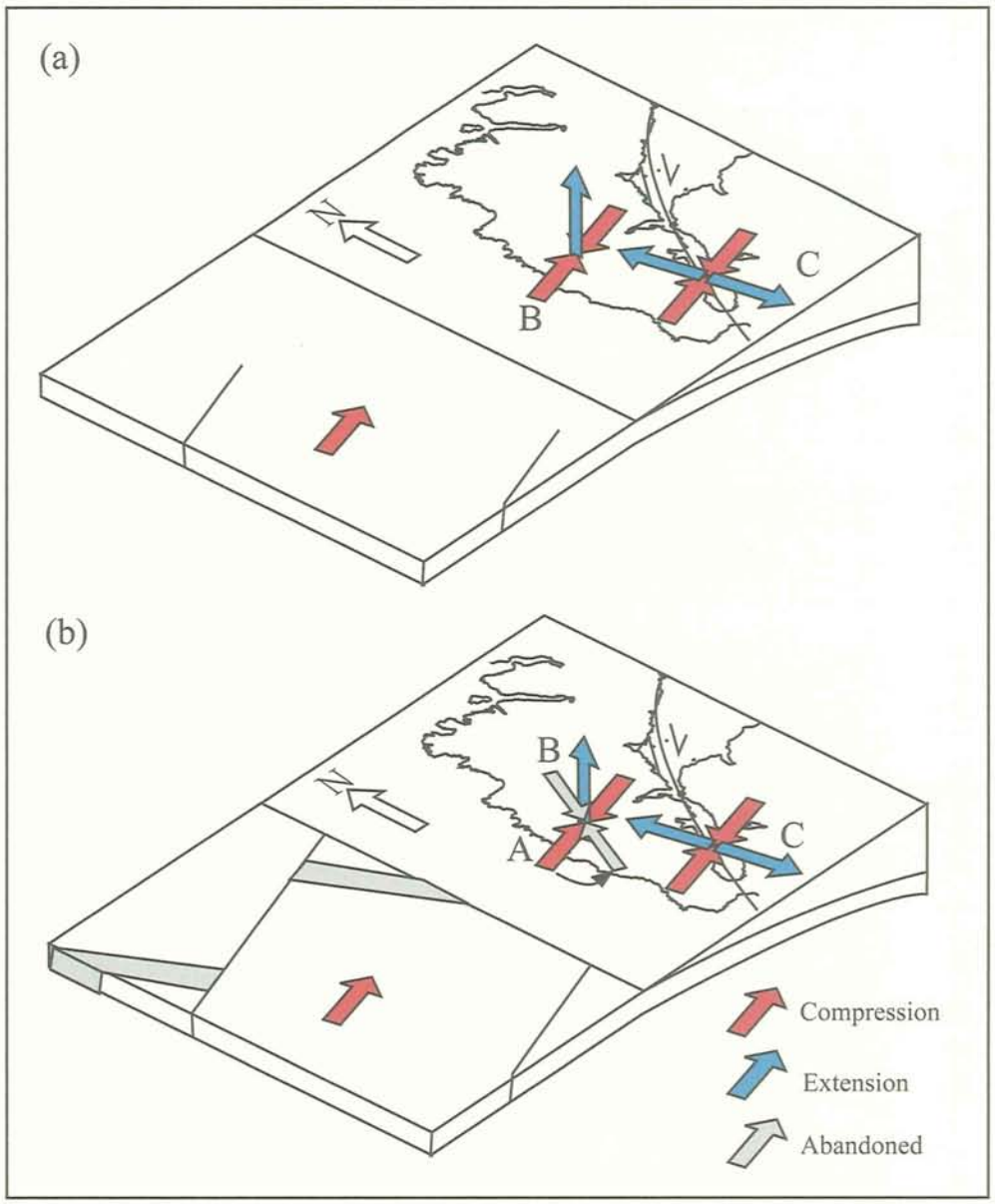

Figure 9.1. Block diagram showing the evolution of the stress fields recorded in the plutonic units and in the eastern margin of the ophiolite. (a) First obduction phase, before 6 Ma. The induced stress field divided into compressional ("B") and is strike-slip ("C") components acting in the interior and in the margin of the ophiolite respectively. (b) Second obduction phase in which the movement of the BBFZ, controlled by the "C" stress field, counterclockwise rotated the ophiolite about 60^0. Early generated structures, by "B" stress field, were abandoned and new ones were generated by the still acting compressional component ("A") induced by the subduction of the Nazca-Antarctic plates and the active CR systems offshore the Taitao area.

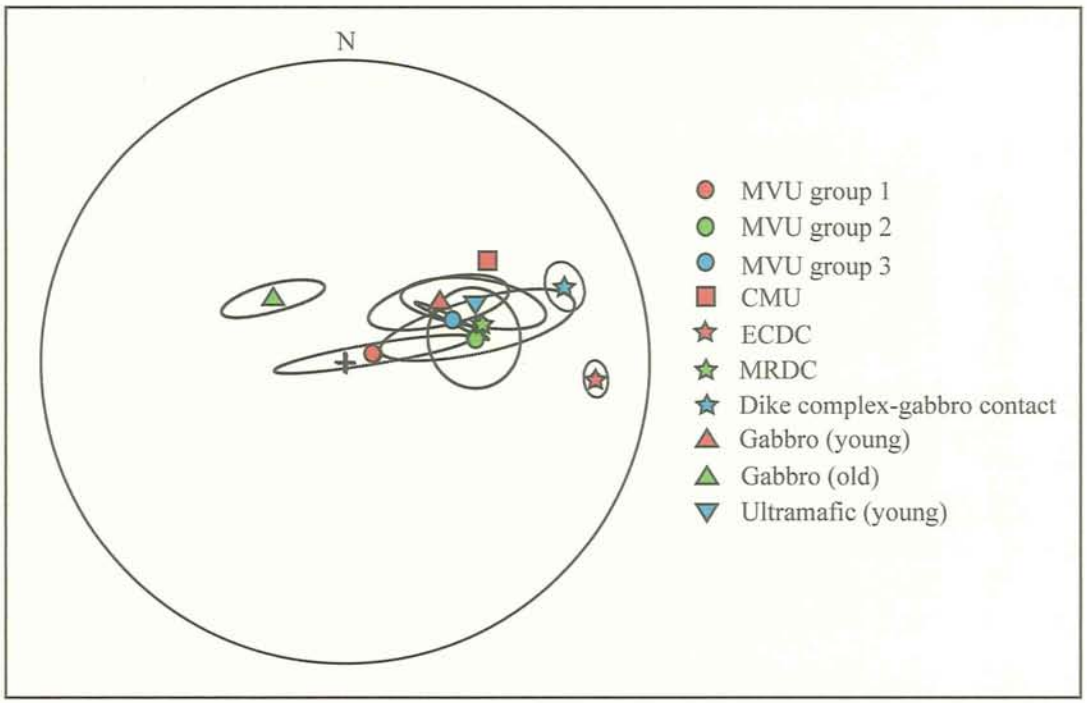

Figure 9.2. Lower Hemisphere, equal area projection with the orientation of all calculated mean rotational axes, including "old" and "young" rotations. Notice that the "old" rotational axis is NW-ward inclined while those of the young rotation are NE to E-ward inclined. Ellipses represent the 95% confidence interval for each mean rotational axis.

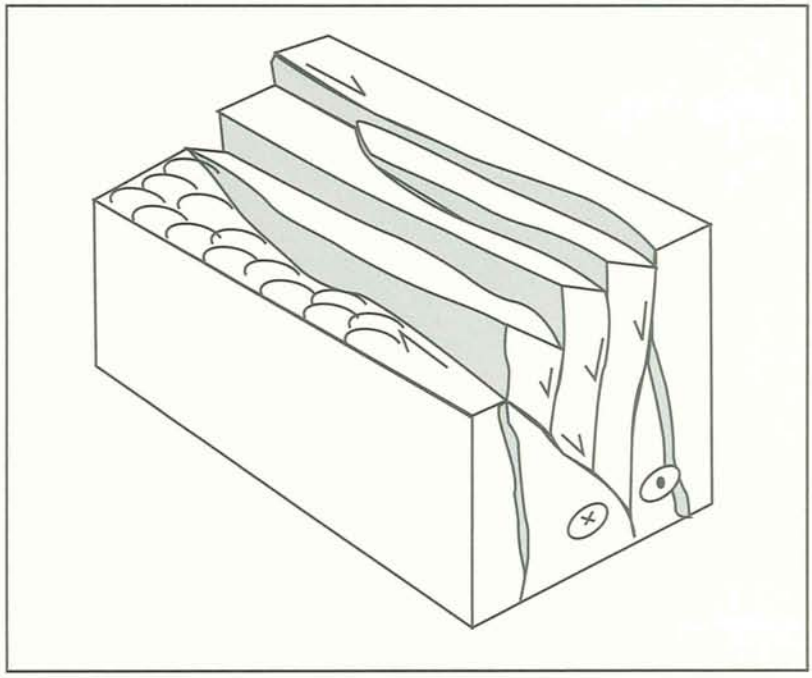

Figure 9.3. Block diagram illustrating the geometry of a negative flower structure controlled by the activity of a dextral-normal fault zone.

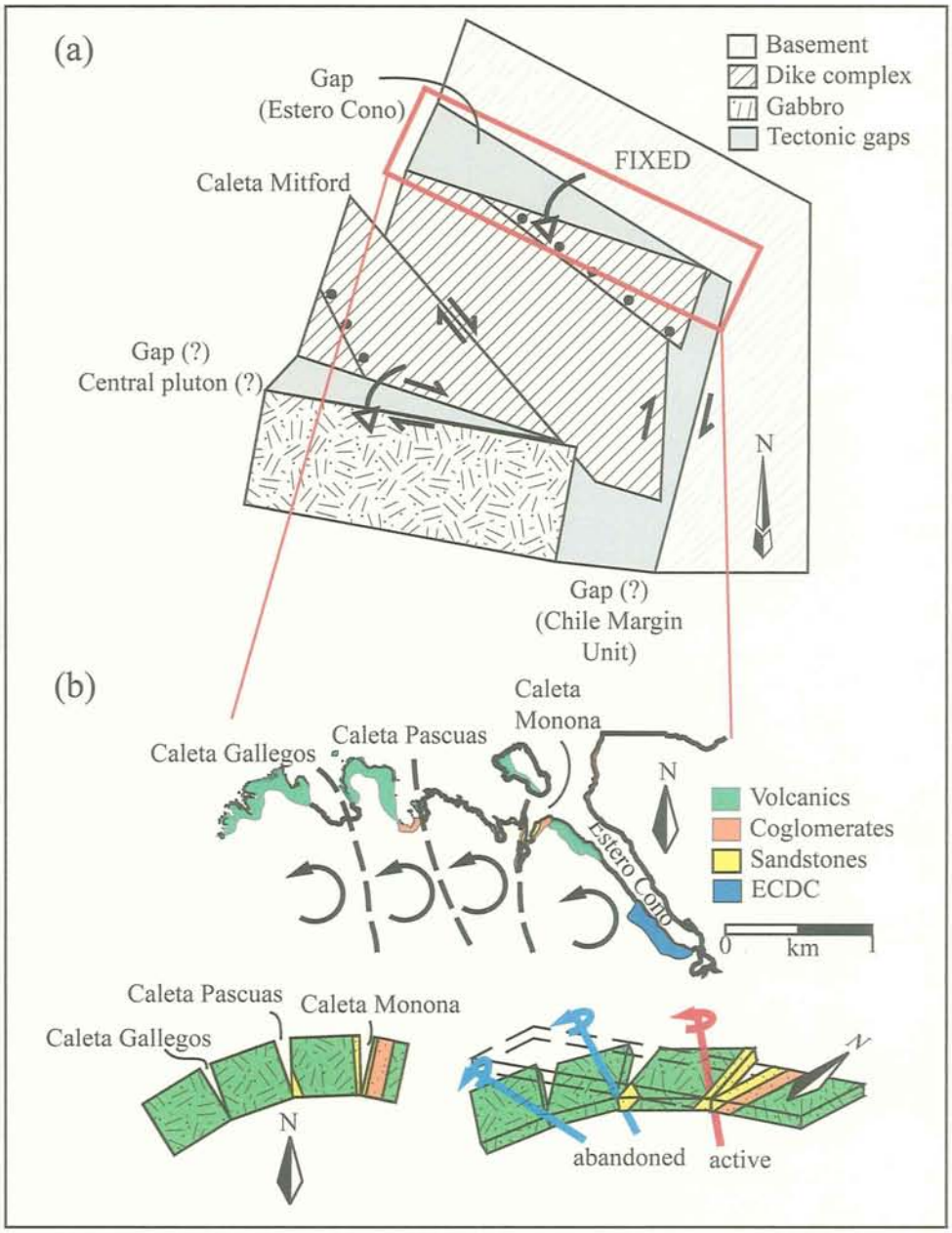

Figure 9.4. (a) Plan-view block diagram showing the rotation of the dike complex and gabbro units that resulted in the generation of several tectonic gaps to the north, east and center (?) of these units. (b) Coastal map of the Estero Cono (upper) showing the counterclockwise rotation of each of the MVU identified blocks; in plan-view (down-left) and in a 3D block model (down-right). Notice that blue rotational axes were abandoned and rotation of all the blocks occurred about the easternmost axis (red).

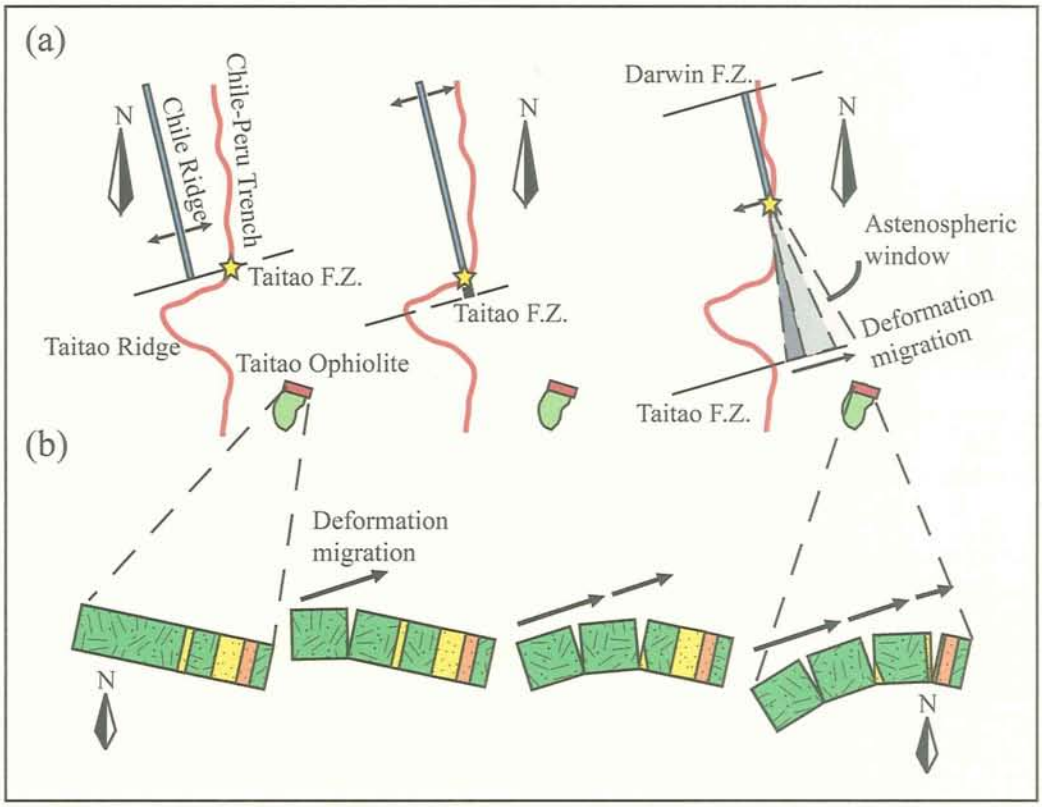

Figure 9.5. (a) Northward migration of the CTJ (star) due to the subduction of the CR system and the generation of an asthenospheric window beneath the Taitao area which opens progressively E-ward (figure after Guivel et al., 2003). (b) Same process resulted in the E-ward migration of the deformation identified in the Estero Cono area.

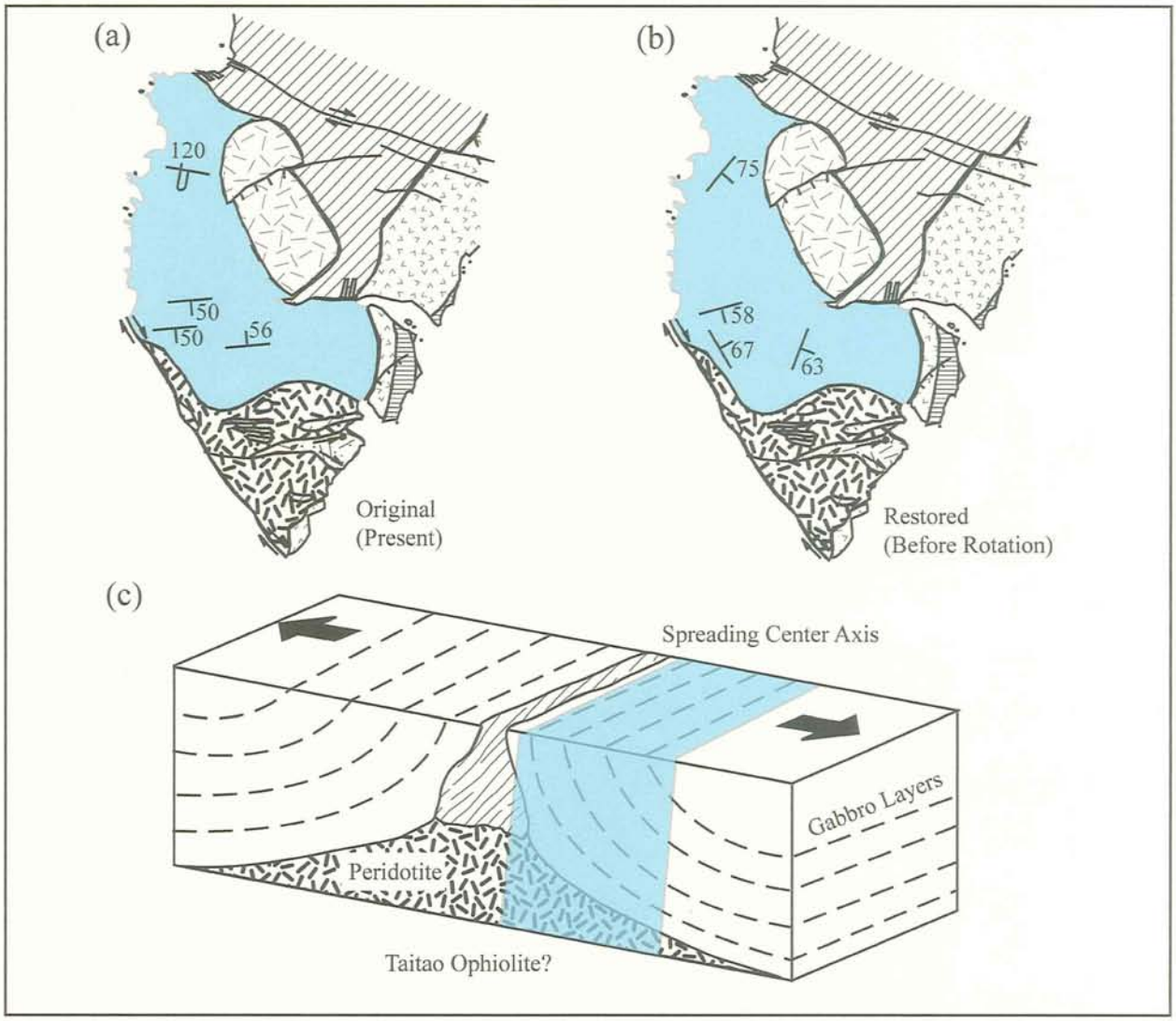

Figure 9.6. Restoration of gabbro compositional layers. Extracted geological map of the southern part of the Taitao ophiolite (Fig. 1.5) showing the orientation of (a) in situ and (b) restored compositional layers. (c) Block diagram showing the inferred shape of the gabbro magma chamber at the spreading ridge axis and the possible original location of the Taitao ophiolite with respect to the spreading axis.

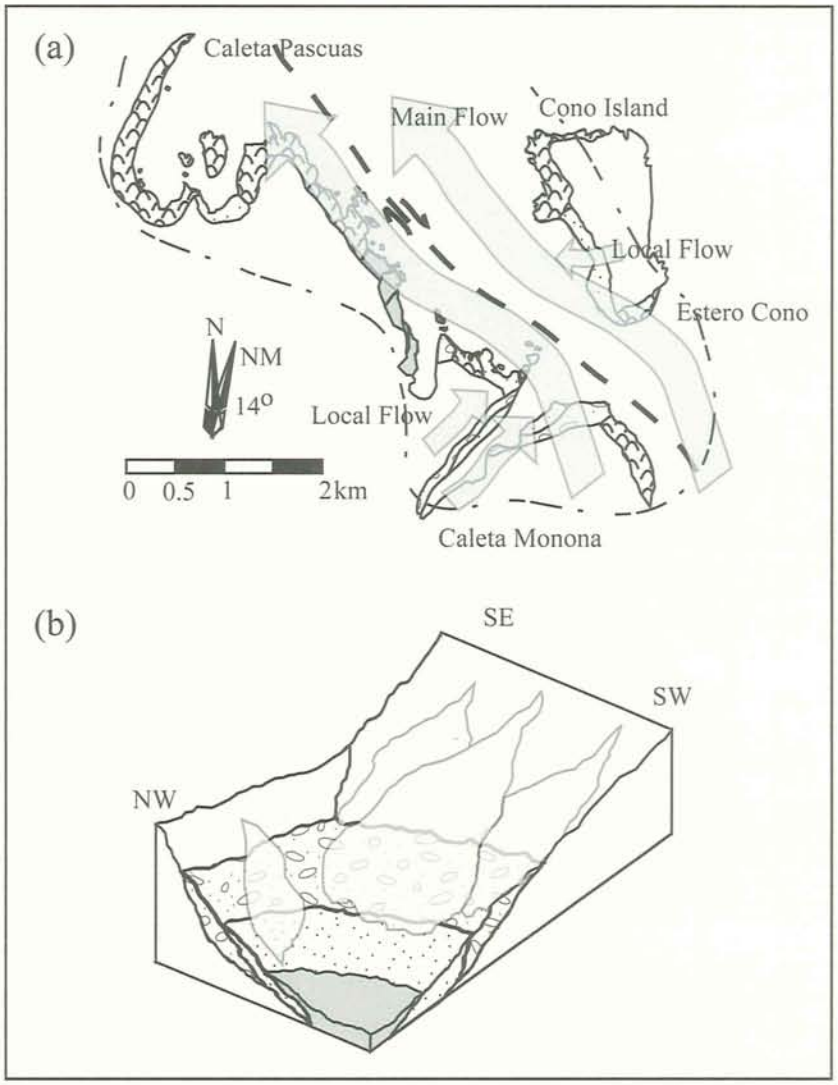

Figure 9.7. (a) Coastal map of the Estero Cono area showing the inferred paleocurrent pattern for the clastic sediments of the MVU. Notice that the main flow followed the Estero Cono lineament while minor flows followed the Caleta Monona lineament. Also, notice that the coastal line has being clockwise rotated (restored) using calculated mean rotational axes. (b) Block diagram illustrating the possible mechanism of generation, early flow and deposition of turbiditic flows in the Estero Cono area.

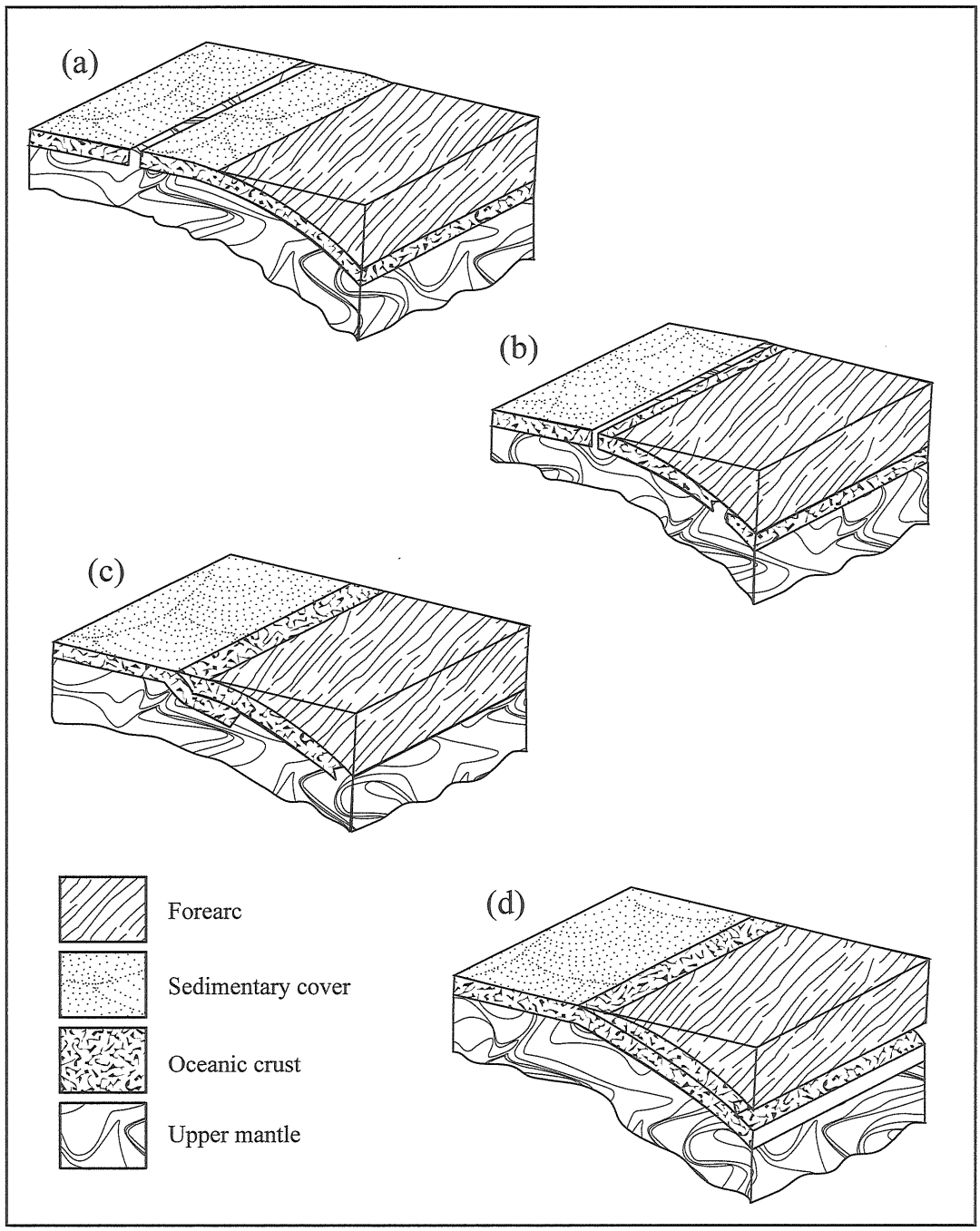

Figure 9.8. van den Beukel model (1990) for the incorporation of a piece of oceanic crust onto the forearc as a result of spreading ridge subduction. (a) Normal subduction prior to the break-up of the oceanic lithosphere and ophiolite obduction; (b) break-up of the oceanic lithosphere below the forearc region; (c) initiation of new subduction beneath the brake-up portion of the oceanic lithosphere which is now incorporated into the forearc; (d) Back to a normal subduction with the brake-up oceanic lithosphere incorporated into the forearc.

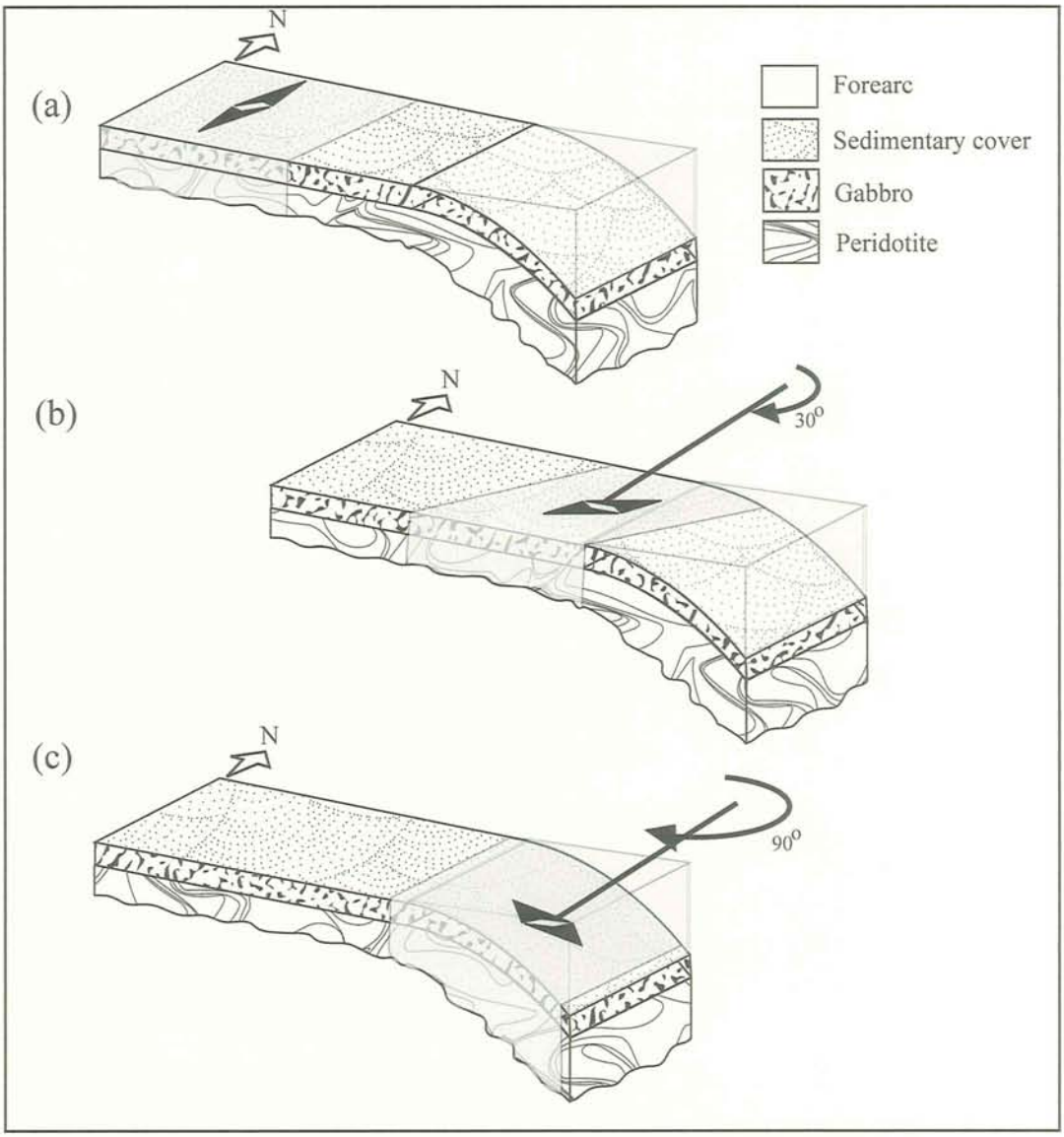

Figure 10.1. Block diagram showing the clockwise rotational event of the ophiolite (semi-transparent dark-gray block) divided into: (a) original orientation at the oceanic plate, (b) beginning of subduction and clockwise rotation and (c) subducted and clockwise rotated beneath the forearc (semi-transparent light-gray block). Double arrow on top of the block indicates the direction of the expected GAD acquire during the generation stage.

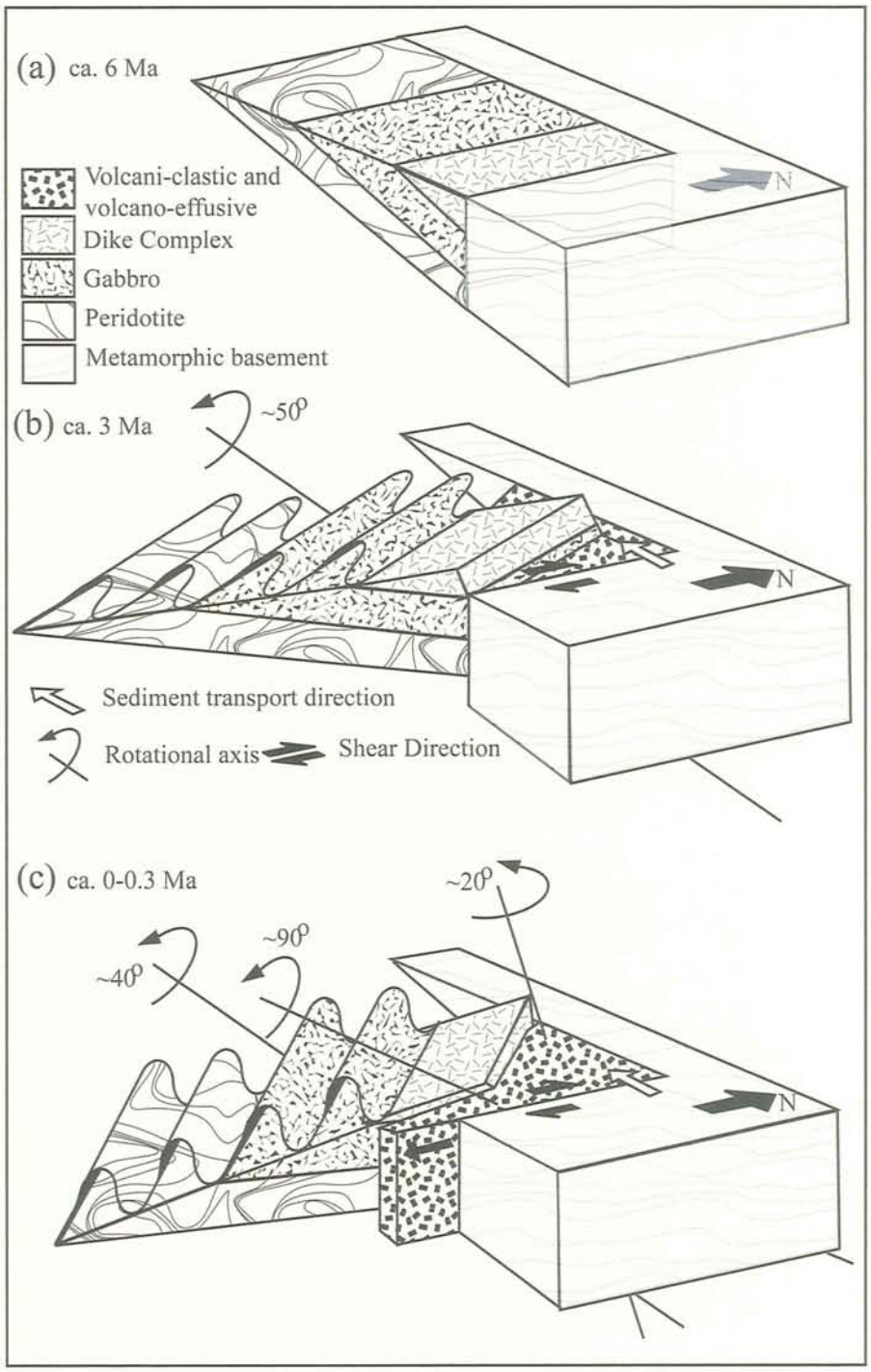

Figure 10.2. Block diagram showing the progressive counterclockwise rotational event. (a) Original orientation of the Taitao ophiolite after old rotation (see figure 10.1c). (b) Counterclockwise rotation of the ophiolite, which resulted in folding of the plutonic units and the generation of tectonic gaps east and northward of the ophiolite (see figure 9.4a) filled by volcani-clastic deposits. (c) Complete counterclockwise rotation of the ophiolite (actual disposition of the ophiolite).

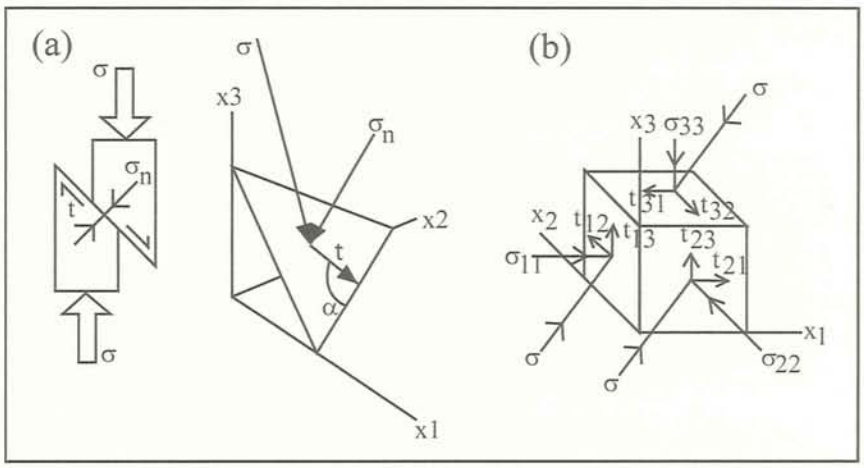

Figure A.1. Division of the stress field into vectorial (a) and tensorial (b) components. (a) right: Two dimensional model for division of a compressional vertical stress field; notice that the stress divides into its normal (σ_n) and shear (t) components; left: same as right side but in a 3-dimensional space, α is the angle between the horizontal plane and the shear. (b) Tensorial decomposition of the stress field (σ) in each one of the faces of the vanishing cube, x_i denotes the Cartesian coordinates.

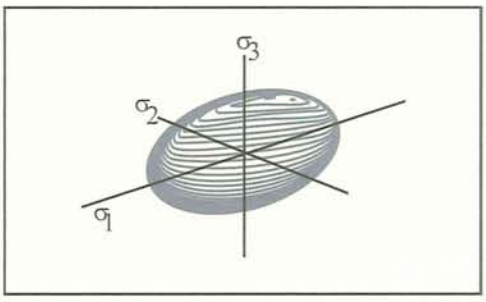

Figure A.2. Stress ellipsoid.

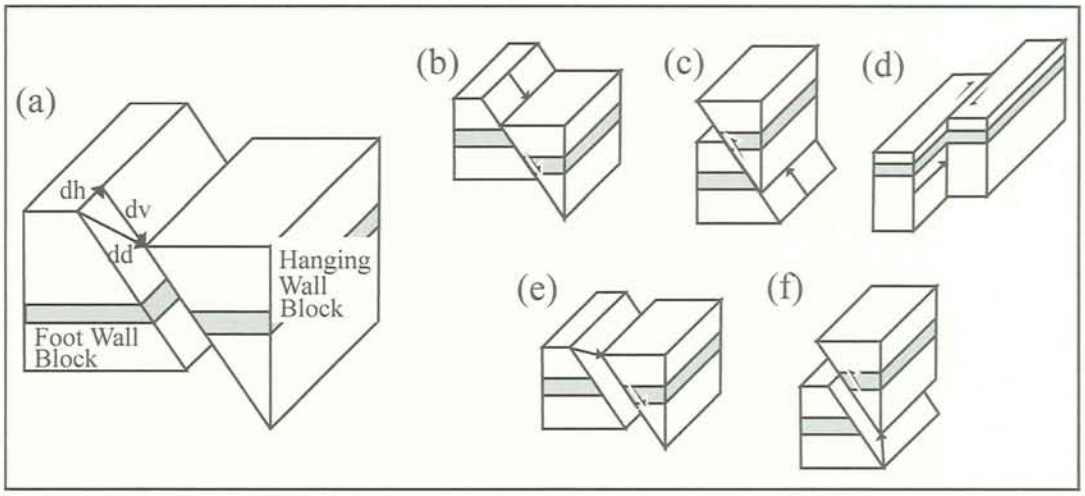

Figure A.3. (a) Geometric elements on a fault plane. Footwall and hanging wall blocks are indicated as well as movement vectors (dd, dh, dv) (see text for details). Block diagrams of: (b) normal fault, (c) reverse fault, (d) strike-slip fault, (e) normal-sinestral fault and (f) reverse-sinestral fault.

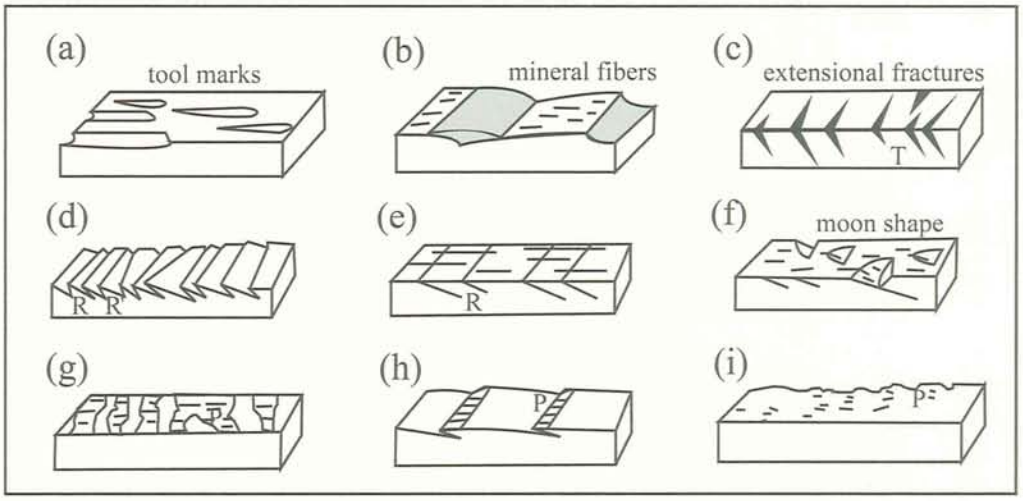

Figure A.4. Brittle kinematic indicators on a fault surface. (a) tool marks, (b) mineral fibers (slickenfibers), (c) extensional fractures. (d), (e) and (f) Secondary fractures of Petit (1987) criteria R; and (g), (h), (i) criteria P (see text for details). Modified from Petit (1987).

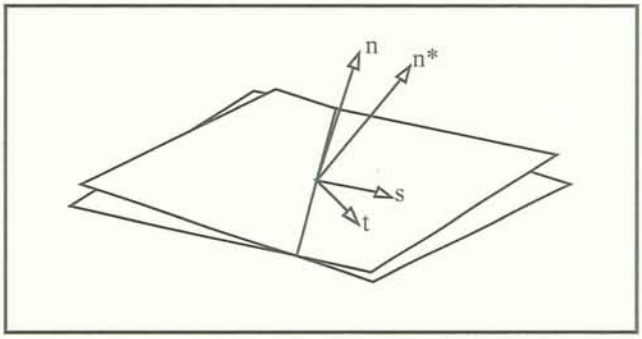

Figure A.5. Spatial orientation of planes using: (1) normal (n and n*) and (2) shear vectors (t and s)

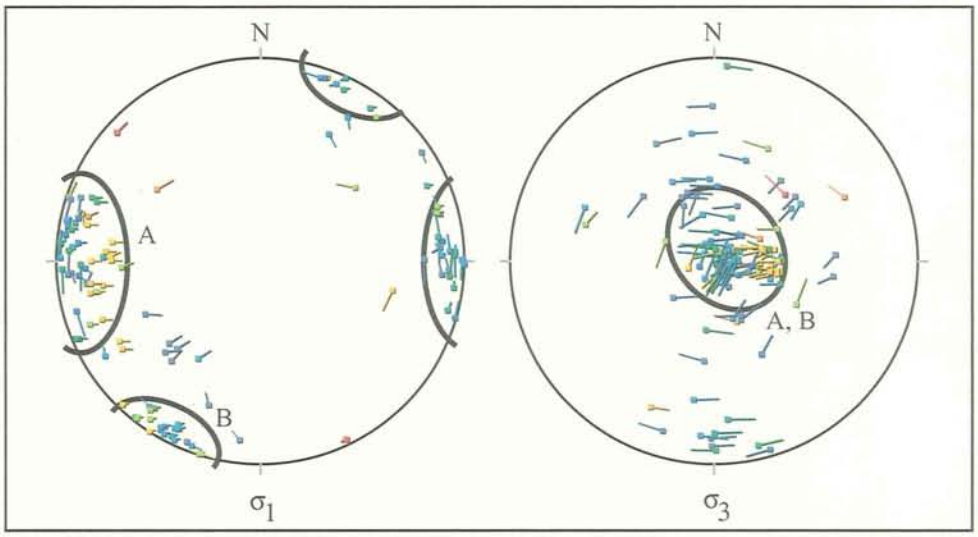

Figure A.6. Equal-area, lower hemisphere projections with the orientation of compressional (σ_1) and extensional (σ_2) principal stress axes obtained with the multi-inverse method (e.g. Yamaji, 2000). Color on symbols indicate stress ratio, varying between 1 (red) and 0 (blue). Parameters used in the analysis are k=5 and e=11. Data from Taitao ophiolite (this study).

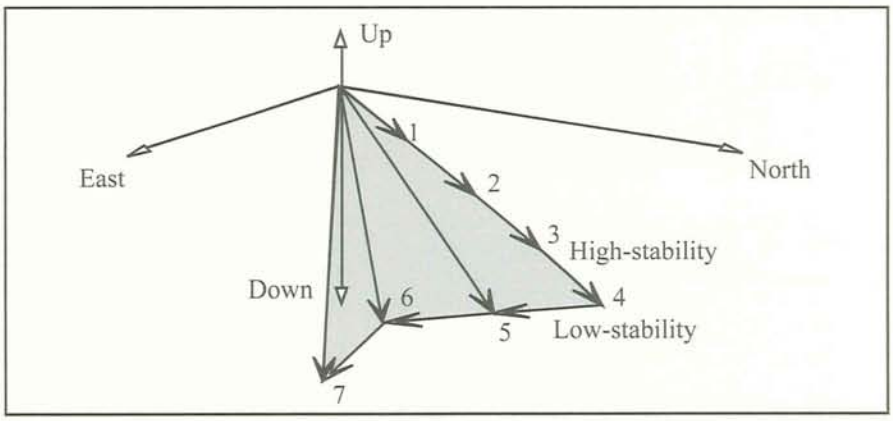

Figure B.1. Schematic 3D diagram showing a demagnetization path obtained from demagnetization process. Numbers indicate the progressive demagnetization step from 7 (NRM) to 1. From steps 7 to 4 a low-stability component was isolated, while from 4 to 1 a high-stability component was isolated. Vectors connecting the origin with each one of the steps correspond to the data given by the demagnetization process. Adapted from Butler (1992).

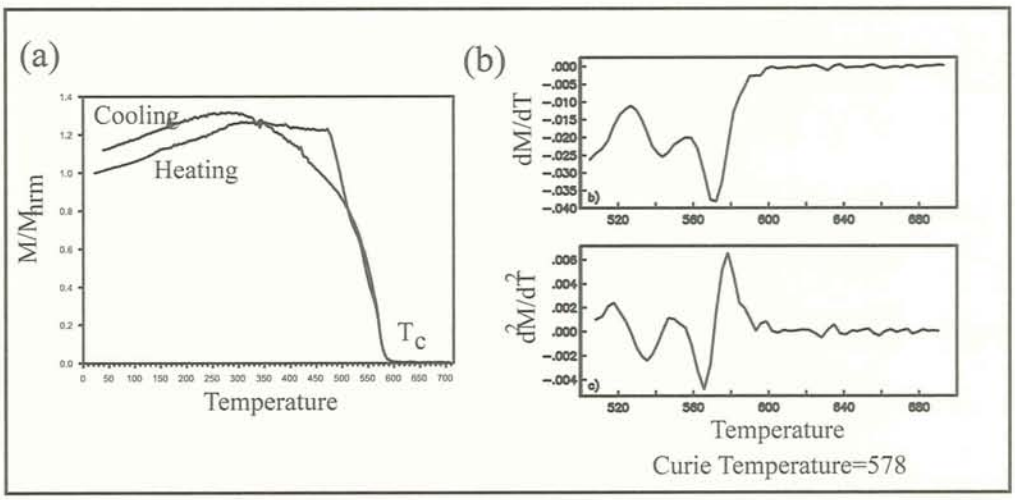

Figure B.2. (a) Normalized magnetic susceptibility intensity vs. temperature during heating and cooling of the sample, notice the fast decay of M/M_{NRM} near the 580^0C. Tc indicates the possible Curie temperature. (b) Differential method (e.g. Tauxe, 1998) applied to the data in (a); upper: $\partial M/\partial T$ curve, lower: $\partial 2M/\partial T2$ curve (see text for details). Analysis of the data was truncated between 500^0 and 700^0C in order to minimize possible noise. Notice that the peak of the second derivative, indicating a Curie temperature of 578^0C. Data from Taitao ophiolite, (this study).

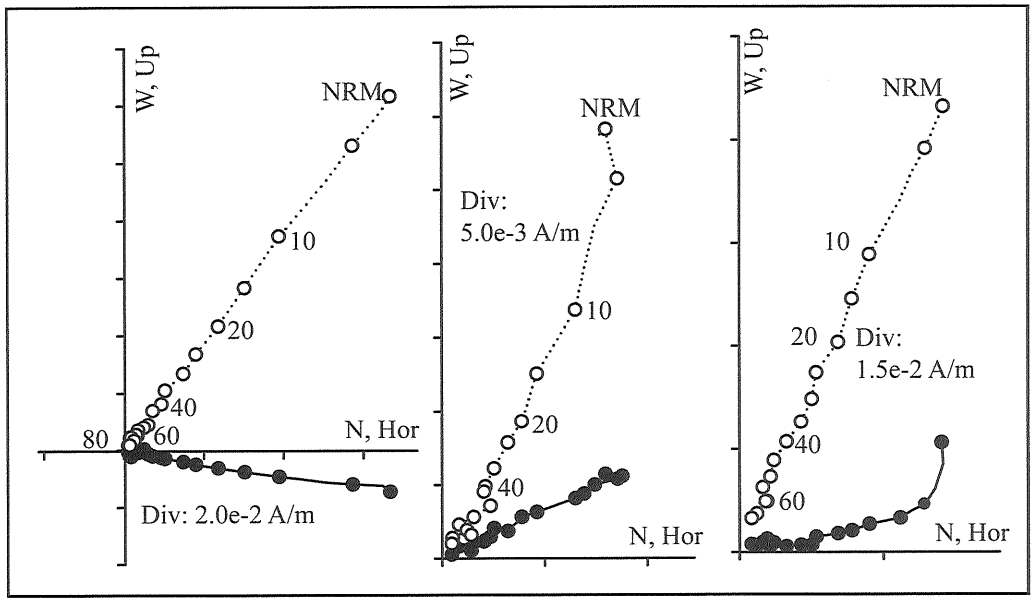

Figure B.3. Zijderveld (1967) diagrams of demagnetization data obtained by means of AFD. Notice that on each diagram axes are clearly labeled. Non-filled (filled) symbols are projections of end vector points in the north-down (north-east) planes. Numbers indicate the strength of the applied field during the AFD process in mT. Data from Taitao ophiolite (this study).

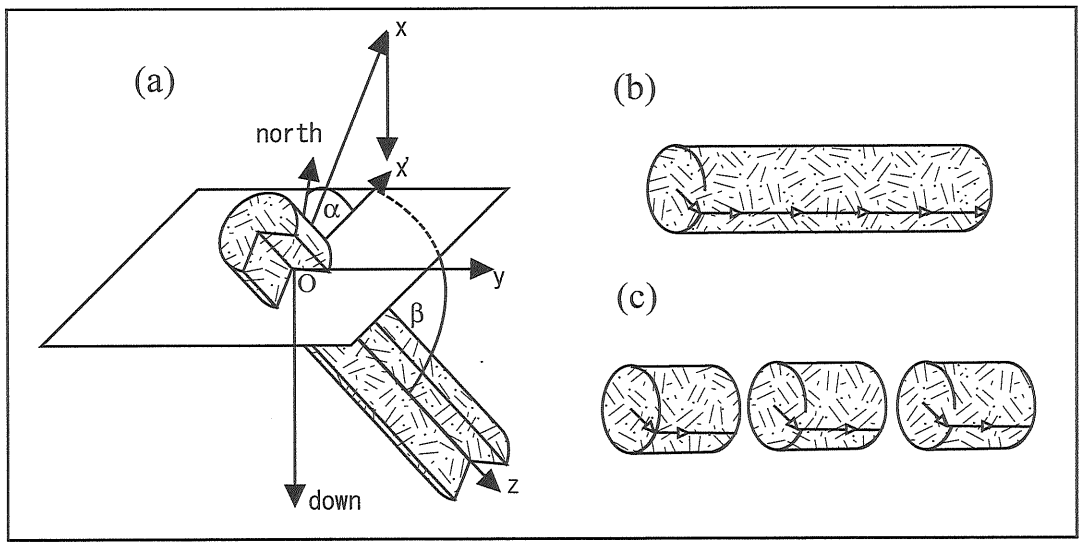

Figure B.4. Core sampling, orientation and specimen preparation. (a) Reference frame centered in the sampled core (α angle, between north and x' axis; β angle, between the plane and the z axis of the core). The coordinate system of the sample is defined as xyz; where x, z and down axes are in a vertical plane while y axis is in the horizontal plane. Adapted from Butler (1992). (b) Extracted core with an arrow on top indicating the x axis and another arrow in the side indicating the z axis. (c) Division of the core into specimens.

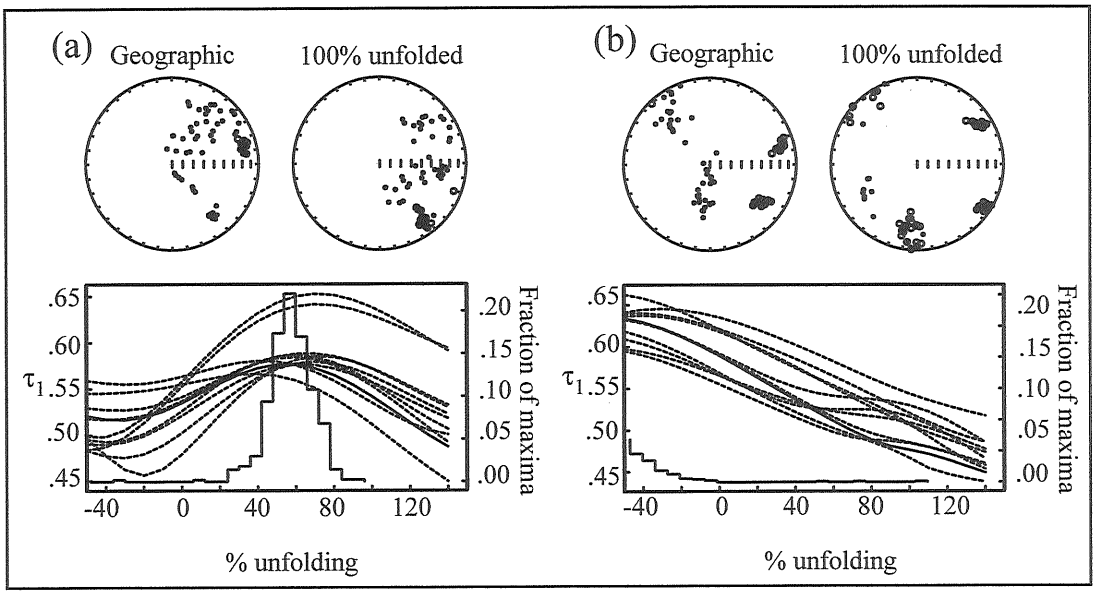

Figure B.5. Example of fold test procedure. On each sub-figure the upper part contains two equal-area, lower hemisphere projections with the insitu orientation of RM vectors (left side, up), and after 100% unfolding (right side, up). Also, histogram (lower par) with the frequency of τ_1 (largest eigenvector of the orientation matrix, equation [E.3.18]) during unfolding (filled line is the value of τ_1 during the unfolding while dashed lines indicates pseudo-sampling of the data) (e.g. Tauxe, 1998). (a) A positive fold test, notice the peak in the τ_1 curve and the peak in the histogram at ca. 55% of unfolding. (b) A negative fold test, in this case there is no clear concentration of the τ_1 histogram. Data from Taitao ophiolite (this study).

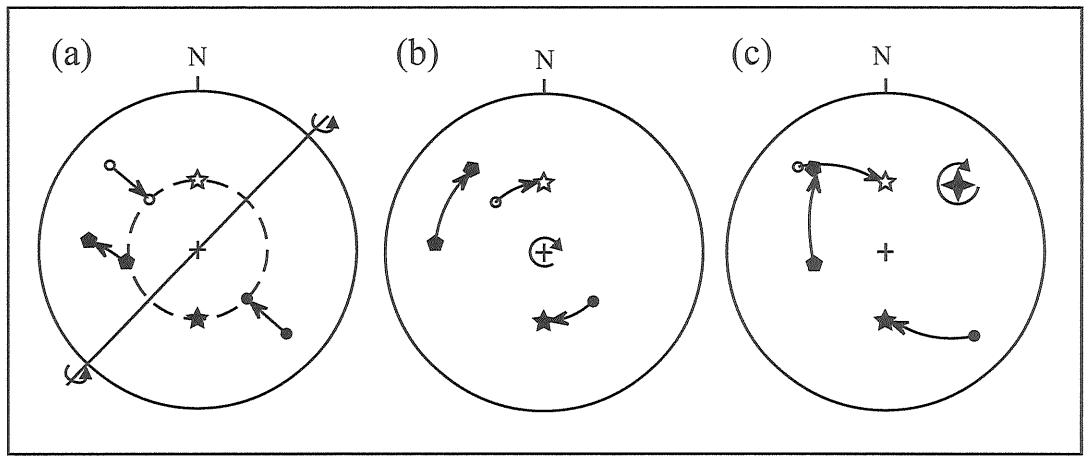

Figure B.6. Lower hemisphere (upper hemisphere), equal area projections with a graphical representation of the modified rotational process (after Weinberger et al., 1995). (a) Rotation about a horizontal axis perpendicular to the declination of the RM vector (circle). The dashed circle indicates all the orientations with inclination equal to the inclination of the expected GAD. (b) Rotation about a vertical axis; notice that after this rotation the orientation of the RM vector is the same as the orientation of the expected GAD. (c) Rotation about an inclined rotational axis (diamond); notice that is equivalent to (a) and (b) (see text for details). Filled (non-filled) symbols are projections into the lower (upper) hemisphere.

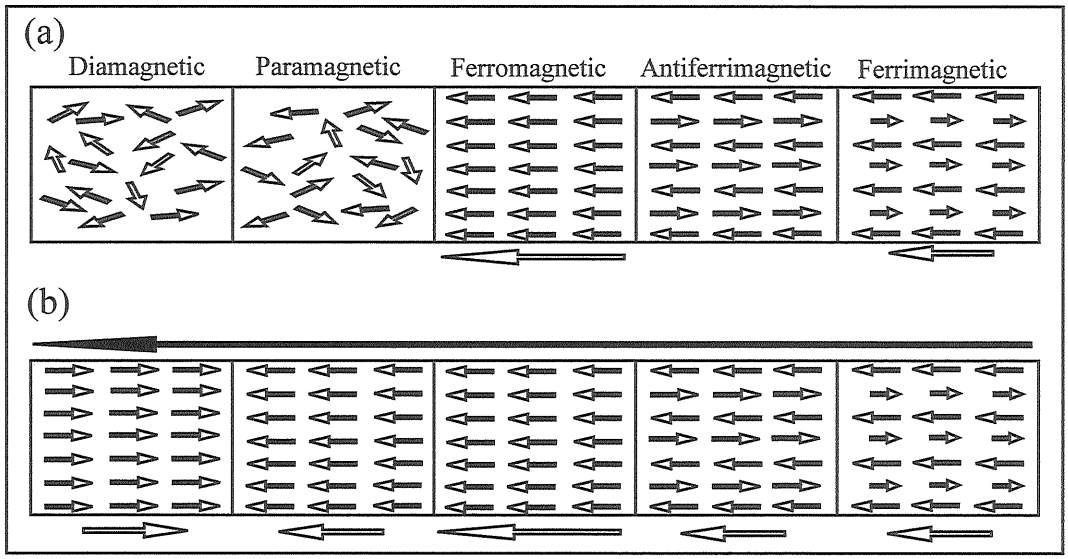

Figure C.1. Classification of magnetic minerals: (a) normal circumstances (applied field is 0) and (b) an external applied field (black arrow). Arrows in boxes represent the net magnetic moment of the particles; hollow arrows outside the boxes indicate the magnetic moment of the mineral when is under (a) normal circumstances or (b) under a certain external field.

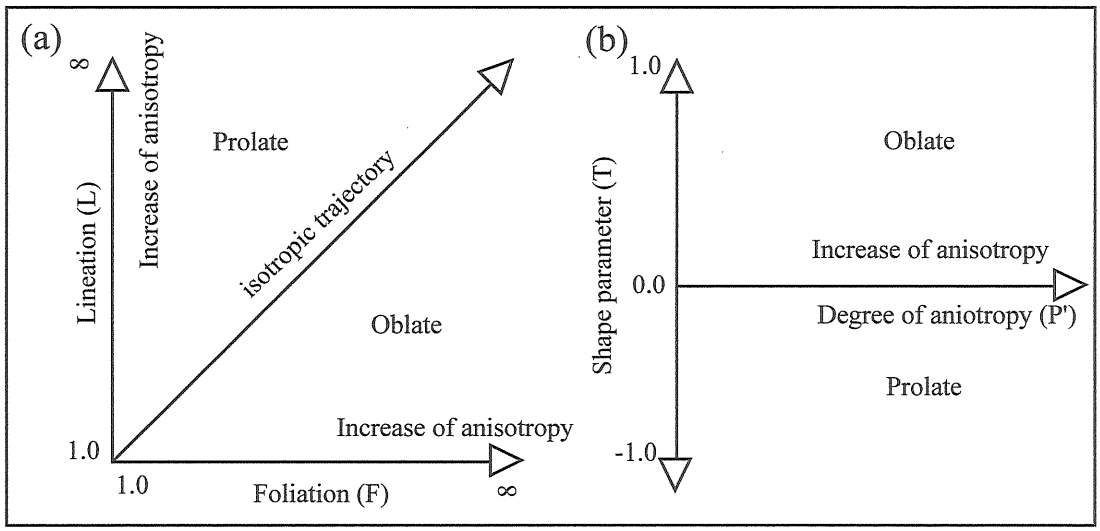

Figure D.1. Classification of the AMS fabric shape according to: (a) foliation (F) vs. lineation (L), and (b) Degree of anisotropy (P') vs. Shape parameter (T).

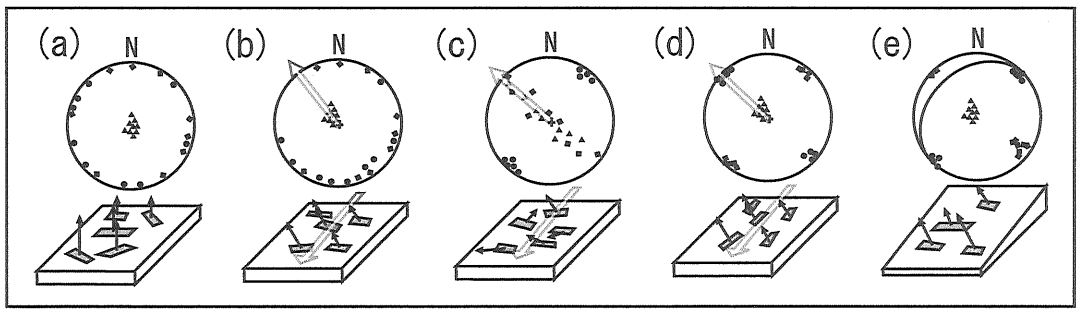

Figure D.2. Expected distribution of AMS axes of deposited sediments. On each sub-figure the upper part corresponds to a lower hemisphere, equal-area projection with the orientation of the different AMS axes; circles: K_{max}, squares: K_{int} and triangles: K_{min}. (a) Normal deposited sediments with no influence of currents or slope, (b) sediments deposited under the influence of a weak current, (c) under a high-velocity current, (d) under a low-velocity current, and (e) sediments deposited in a slope with no current influence.

Photos

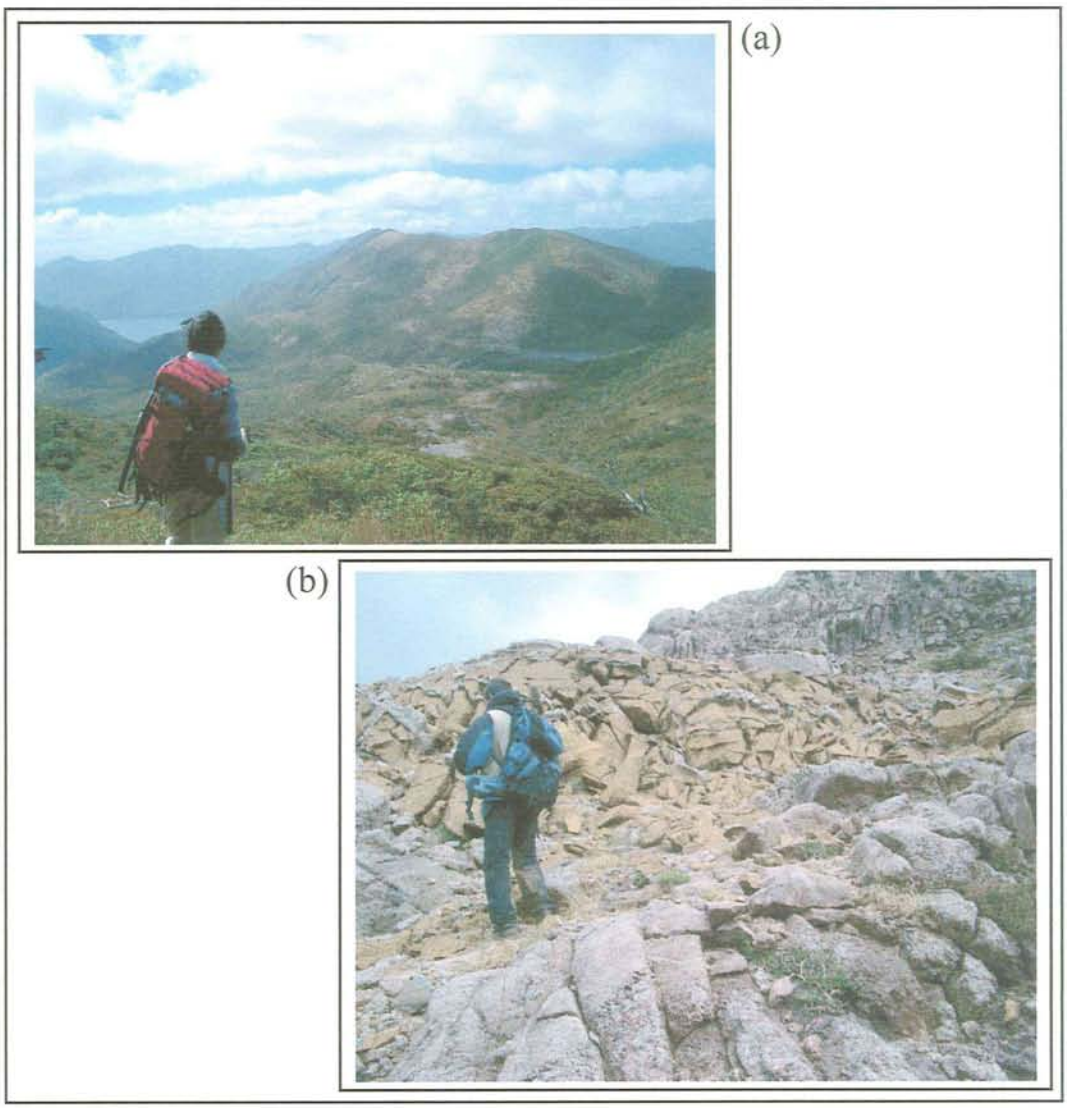

Photo 1. Examples of ultramafic rock outcrops in the southern part of the Taitao ophiolite. (a) Ultramafic rock outcrops in top of the hills, picture taken looking towards south; (b) ultramafic megaxenolith founded in the gabbro unit; notice the intense intrusion of stockwork gabbroic dikes.

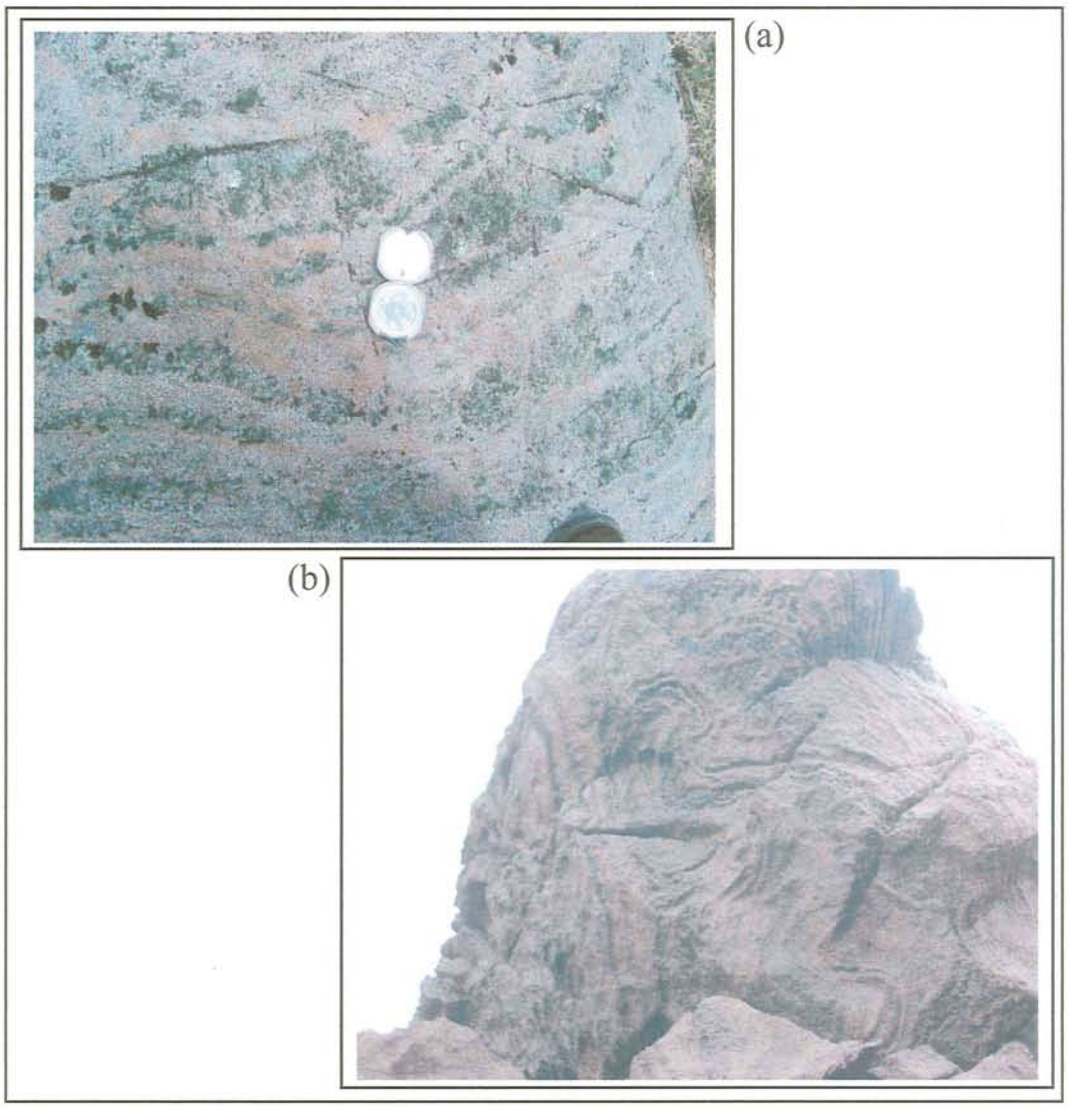

Photo 2. Gabbro outcrops. (a) Compositional layers in gabbro, notice the pyroxene-rich (dark area) and plagioclase-rich (light-area) sub-layers defining either folding and/or slumping characteristics. (b) Intense folding of gabbro compositional layers; notice the strong deformation.

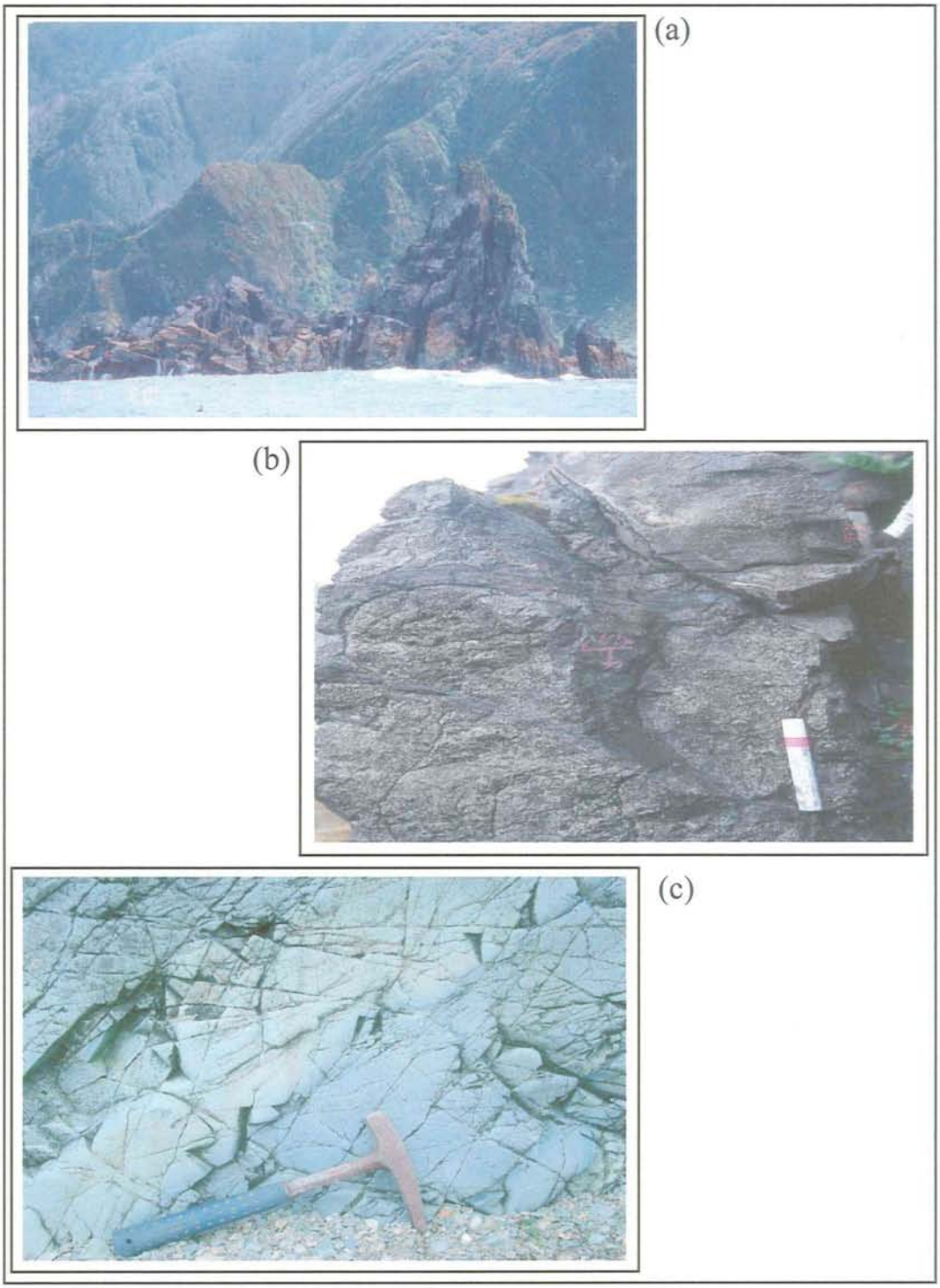

Photo 3. Bimodal dike complex outcrops at Caleta Mitford-Rees (a, b) and Estero Cono (c). (a) Dikes of the MRDC with nearly vertical orientations; (b) shallow dike intrusion in submarine (?) conditions. (c) Intrusion of dikes into dikes at the ECDC; notice the light-gray dike intruding into a dark-gray dike, and their chilled-margin. Photos (a) and (b) courtesy of Mr. R. Endo (University of Tsukuba).

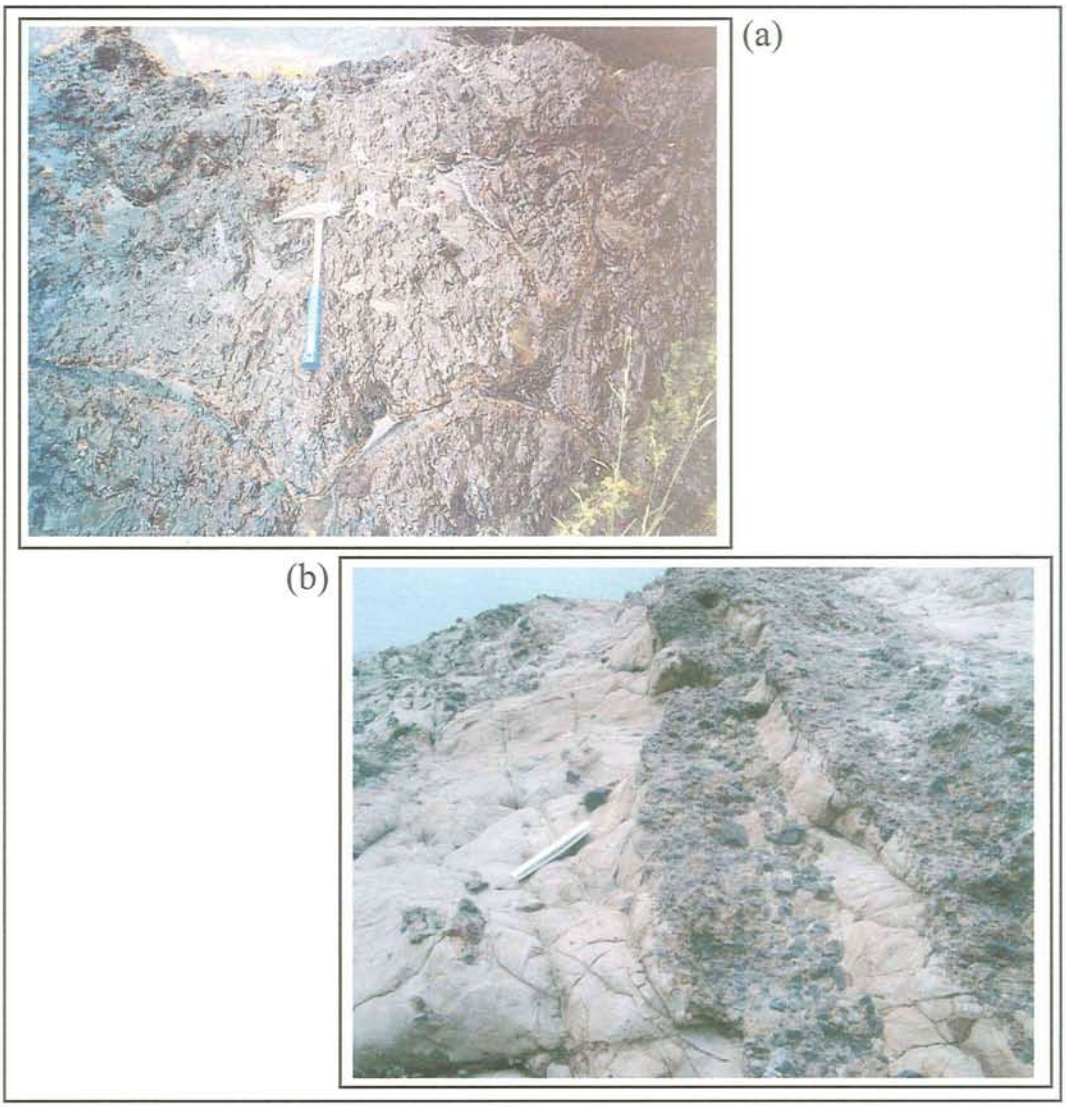

Photo 4. Outcrops of the CMU in Bahía Barrientos area (see figure 1.5). (a) Pillow lava deposits located in the northern part of Bahía Barrientos; notice the well-development of bottom and top indicators. (b) Rhythmic deposits of sandstones (light) and conglomerates (dark) belonging to the clastic sequence of the CMU in "*Islote Amarillo*".

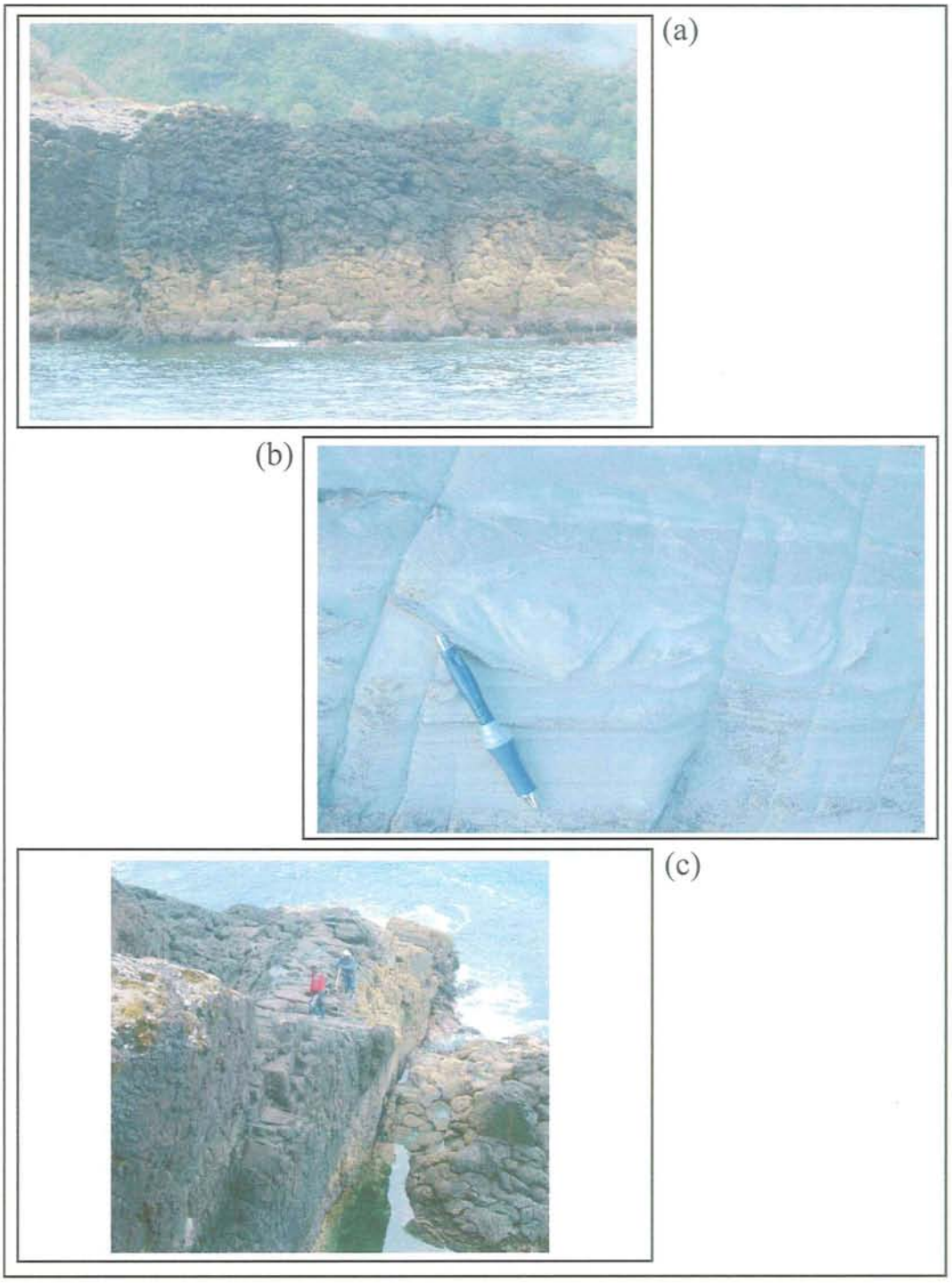

Photo 5. Outcrops of the MVU in the Estero Cono area. (a) Thick deposits of pillow lavas nearly horizontally oriented; (b) fine-to-very fine grain sandstones of the clastic sequence of the MVU located in the westernmost part of Estero Cono, notice the abundance of sedimentary structures. (c) Feeder (?) basaltic dike intruding volcanic-clastic strata of the MVU at Caleta Pascuas.

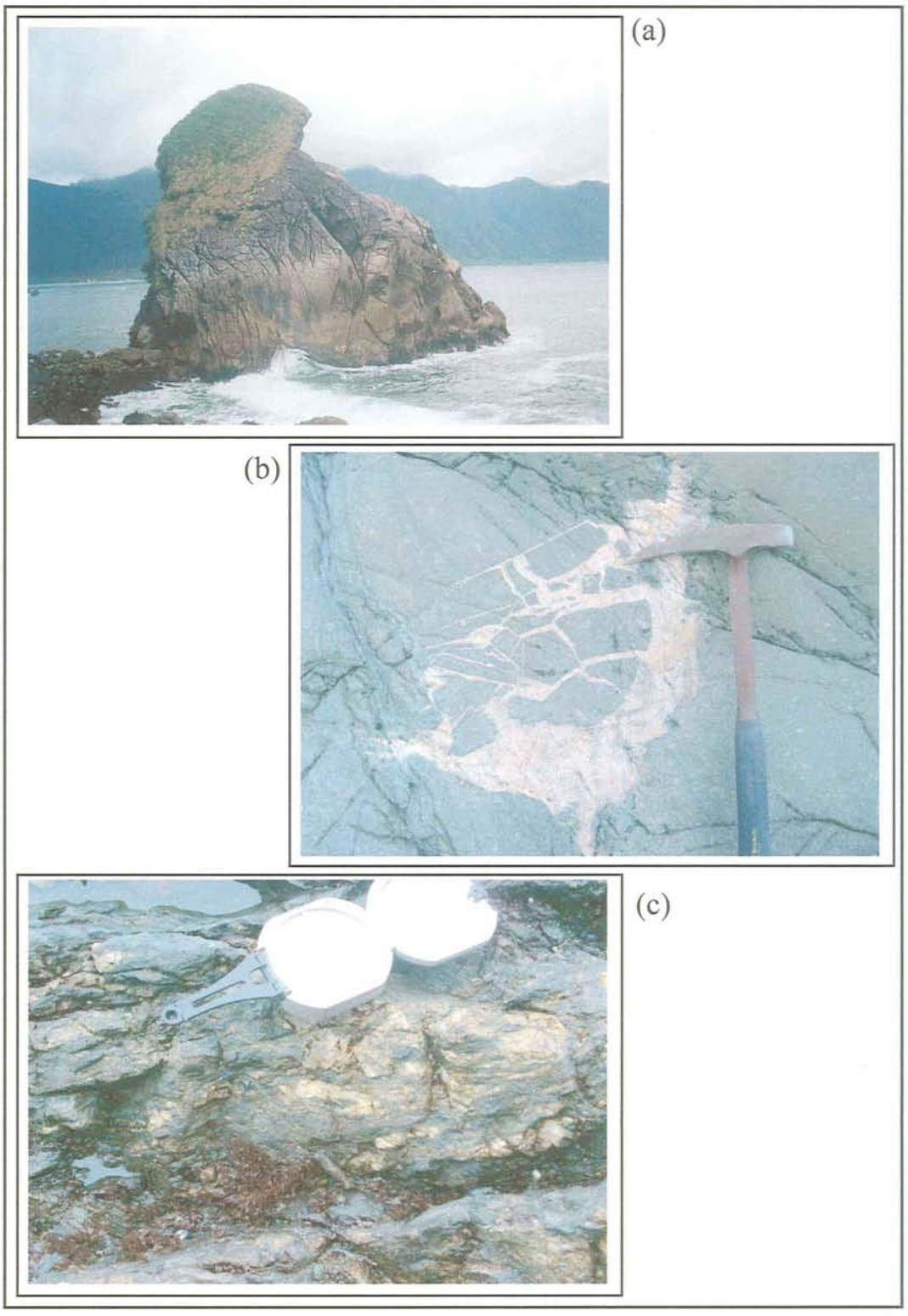

Photo 6. Outcrops of rocks units surrounding the ophiolite. (a) Cabo Raper pluton located southward of the ophiolite. (b) Tres Montes pluton located in the SW part of Tres Montes peninsula; here evidence of hydraulic faulting was observed. (c) Clastic (?) Hornfels developed in the metamorphic basement, located in the northward of the mentioned pluton.

Photo 7. Driller machine at the University of Tsukuba used to prepare paleomagnetic cores.

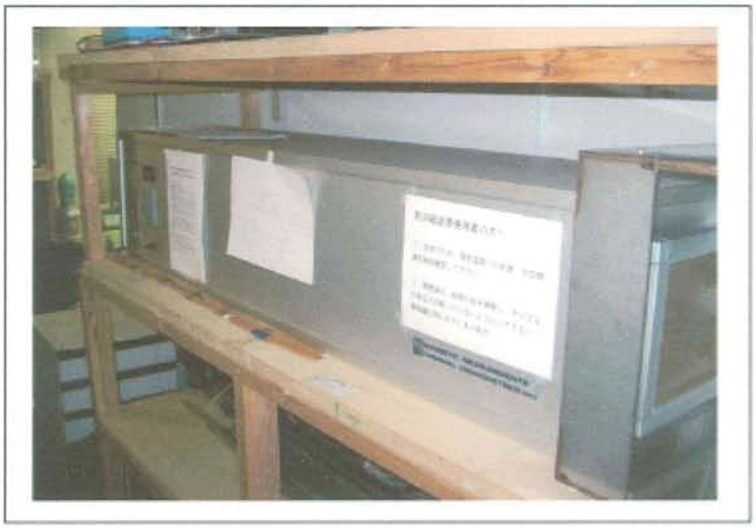

Photo 8. Thermal demagnetizer oven model MMTD-18, at the Geological Service of Japan, used for thermal demagnetization analyses.

Photo 9. AFD Laboratory used for alternating field demagnetization analyses. Up: AFD demagnetizer unit model 2G-760, down: SQUID model 581DC.

Photo 10. Laboratory of Magnetic Susceptibility used for AMS and thermomagnetic analyses. From left to right: KappaBridge pick-up unit model KLY-3, KappaBridge susceptibility meter model KLY-3S, Temperature control unit model CS-3 and computer control center.

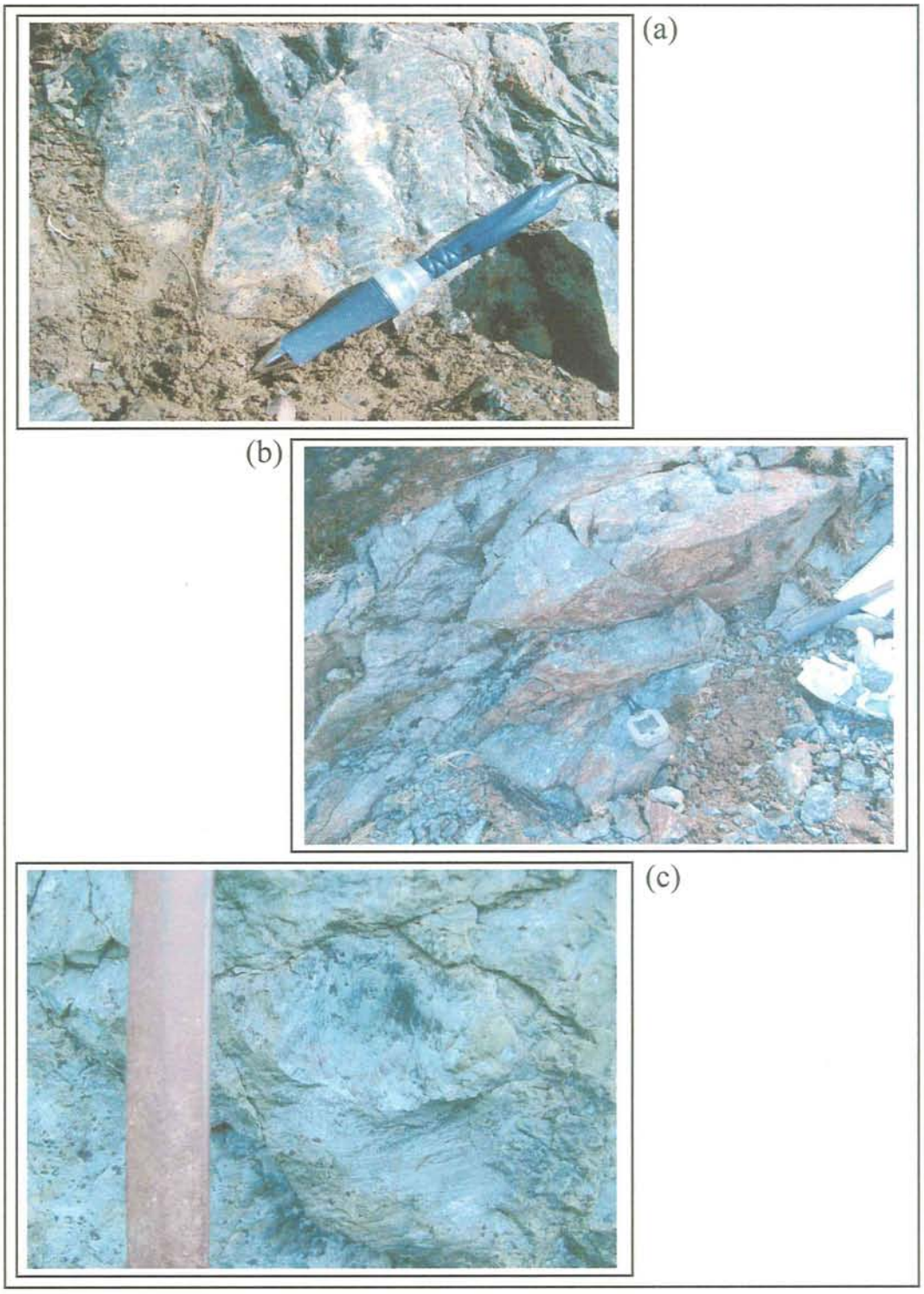

Photo 11. Fault-planes developed in the plutonic units. (a) Ultramafic rocks, (b) contact between ultramafic and gabbro units, and (c) ultramafic rocks. Notice that in (c) two sets of slickenlines can be observed.

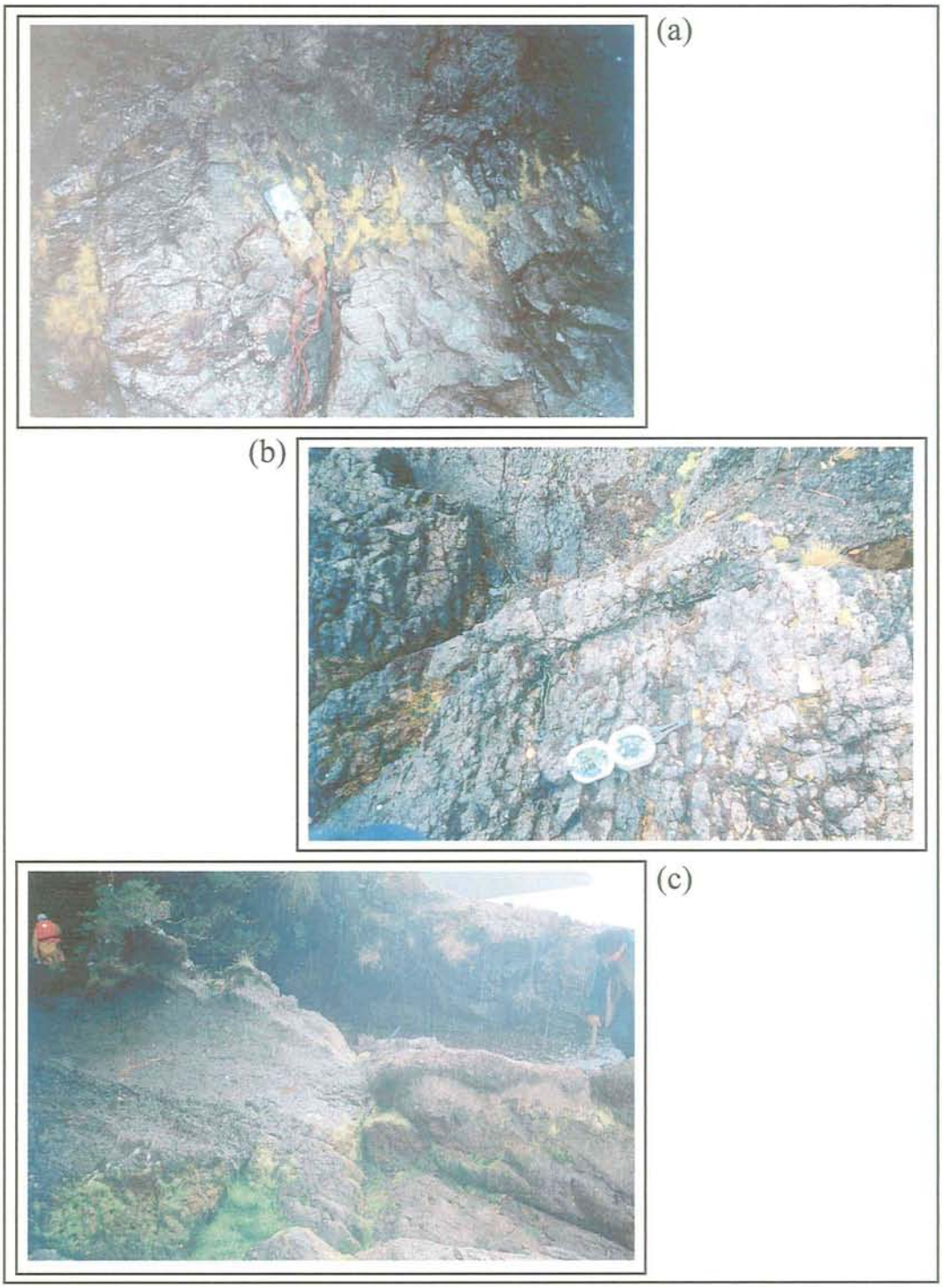

Photo 12. Fault-planes developed in the eastern margin of the ophiolite (BBFZ). (a) Slickenlines developed in gabbro, (b) fault-plane developed in pillow breccias of the CMU, and (c) fault-plane developed in clastic sediments of the CMU. In the last photo, notice the displacement of the sedimentary bedding (conglomerate, dark layer).

Acknowledgements

Fieldwork campaigns and research facilities were supported by the grant -in-aid of the Science Research Project N° 13373004 financed by the Ministry of Education, Sports, Science and Technology of Japan (Monbukagakusho). University facilities were also supported by the Ministry of Education, Sports, Science and Technology of Japan by means of Government scholarship granted to the author.

Thanks to Dr. R. Anma (University of Tsukuba) for his guidance, uncountable discussions and corrections of this work; to Dr. T. Yamazaki (Geological Survey of Japan) for granting unconditional access to all rock magnetic laboratories at the Geological Survey of Japan; and to the Dr. Y. Yamamoto (Geological Survey of Japan) for his help during pilot phases of rock magnetic analyses. Especial thanks to Dr. A. Yamaji (Kyoto University) for processing of fault-slip data by means of the "*multi-inverse*" method as well as for suggestions and discussions regarding this especial topic.

Thanks to Drs. Y. Kaneko (Yokohama National University), M. Terabayashi (Kagawa University), T. Otha and T. Komiya (Tokyo Institute of Technology), S. Kagashima (Yamagata University), Miss C. Herrera (University of Chile), Mrs. M. Schilling (University of Chile), I. Katayama, S. Yamamoto, T. Shibuya, Y. Con (Tokyo University) and R. Endo (University of Tsukuba) which assisted with field data collection during fieldwork campaigns during the months of December and January of both 2000-2001 and 2002-2003.

Very special thanks to the crew of the R/V Petrel for their professional work and cooperation during fieldwork campaigns. Thanks also to CONAF (Corporación Nacional Forestal) Aysén for giving all possible facilities for the realization of fieldwork campaigns.

And at last, but not least, to Miss K. Barrameda who helped in innumerable ways for the final realization of this work; and Mr. R. Endo for his help during the entire project.

To all of them, and many others… thanks.

References

Abdeldayem, A., Yamazaki, T. and Ikahara, K. 1999. Magnetic susceptibility anisotropy and remanecence of some deep-sea sediments of the Tokai Basin. *In*: Yuasa, M. (Ed), Marine geological investigations of the Tokai offshore area. Geological Survey of Japan, Japan, pp. 127-146.

Allen, M., Nelson, E., Elthon, D. and Forsythe, R. 1991. Geochemical indicators of depleted and enriched sources for sheeted dikes of the Taitao Ophiolite, Southern Chile. VI Con. Geol. Ch. (resúmenes expandidos), pp 615.

Angelier, J., 1994, Fault slip analysis and paleostress reconstruction, in Hancock, P., ed., Continental deformation, Pergamon press, p. 53-100.

Angelier, J. and Goguel, J. (1979). Sur une méthode simple de détermination des axes principaux des contraintes pur une population de failles. Comptes Rendus de L'Academie des Sciences. Paris, France. D 288, pp 307-310.

Bangs, N., Cande, S., Lewis, S. and Miller, J. 1992. Structural framework of the Chile margin at the Chile Ridge collision zone. In: Proceedings of the Ocean Drilling Program, Initial reports, edited by Behrmann, J., Lewis, S., Musgrave, R., et al. vol 141, pp 11-21.

Balsley, J. and Buddington, A. 1960. Magnetic susceptibility anisotropy and fabrics of some Adirondack granites and orthogneisses. American Journal Science, 258A, pp. 6-20.

Behrmann, J., Lewis, S., Musgrave, R., et al. 1992. Proceedings of the Ocean Drilling Program, initial reports, 141: College station, TX (Ocean Drilling Program).

Bingham, C. 1964. Distributions on the sphere and on the projective plane. [PhD Thesis], Yale University, USA.

Borradaile, G. 2001. Paleomagnetic vectors and tilted dikes. Tectonophysics, 333, pp 417-426.

Bourgois, J., Lagabrielle, Y., Le Moigne, J., Urbina, O., Janin, M-Ch. and Beuzart, P. 1993. Preliminary results of a field study of the Taitao ophiolite (southern Chile): Implications for

the evolution of the Chile triple junction, Ofioliti, 18(2), p. 113-129.

Bourgois, J., Martin, H., Lagabrielle, Y., Le Moigne, J. and Frutos Jara, J. 1996. Subduction erosion related to spreading-ridge subduction: Taitao peninsula, Geology, 24 (8), p. 723-726.

Brown, D., Spadea, P. and Anma, R. 2000. Preface: Processes of arc-continent collision. Tectonophysics, 325, pp vii-viii.

Bruhn, R., Pavlis, T., Plafker, G. and Serpa, L. 2004. Deformation during terrane accretion in the Saint Elias orogen, Alaska. Geological Society of America Bulletin, Vol. 116 (7/8), pp 771-778.

Bryan, P. and Cherkis, N. 1995. The Bahía seamounts: Test of a hotspot model and a preliminary South American late cretaceous to tertiary apparent polar wander path. Tectonophysics, 241, pp 317-340.

van den Beukel, J. 1990. Breakup of young oceanic lithosphere in the upper part of a subduction zone: Implications for the emplacement of ophiolites. Tectonics, 9 (4), pp 825-844.

Butler, R. 1992. Paleomagnetism: Magnetic domains to geologic terranes. Blackwell Scientific Publications, Boston, USA. 238p.

Callot, J., Geoffroy, L., Aubourg, C., Pozzi, J. and Mege, D. 2001. Magma flow direction of shallow dikes from the East Greenland margin inferred from magnetic fabric studies. Tectonophysics, 335, pp. 313-329.

Callot, J. and Guichet, X. 2003. Rock texture and magnetic lineation in dikes: a simple analytical model. Tectonophysics, 366, pp. 207-222.

Campbell, I. and Griffits, R. 1992. The changing nature of mantle hotspots through time: implications for the chemical evolution of the mantle. Journal of Geology, 92, pp 497-523.

Cande, S., Herron, E. and Hall, B. 1982. The early Cenozoic tectonic history of the southeast Pacific, Earth Planetary Sciences Letters, 57, p. 63-74.

Cande, S and Leslie, B. 1986. Late Cenozoic tectonics of southern Chile trench, Journal of Geophysical Research, 91 (B1), p. 471-496.

Cande, S., Leslie, R., Parra, J. and Hobart, M. 1987. Interaction between the Chile ridge and Chile trench: geophysical and geothermal evidence. Journal of Geophysical Research, 92, pp 495-520.

Carey, M. and Brunier, M., 1974, Analyse théorique et numérique d'un modèle mécanique élémentaire appliqué a l'étude d'une population de failles, Comptes Rendus de L'Academie des Sciences. Paris, France. D269, p. 891-894.

Cembrano, J., Schermer, E., Lavenu, A. and Sanhueza, A. (2000). Contrasting nature of deformation along an intra-arc shear zone, the Liquiñe-Ofqui fault zone, southern Chilean Andes. Tectonophysics, 319, pp 129 – 149.

Chan, L. 1988. Apparent tectonics rotations, declination anomaly equations, and declination anomaly chart. Journal of Geophysical Research, 93, pp 12151-12158.

Condie, K. 1997. Plate tectonics and crustal evolution. Butterworth-Heinemann, Oxford, 288p.

Coffin, M. and Eldholm, O. 1994. Large igneous provinces: crustal structure, dimensions, and external consequences. Review of Geophysics, 32, pp 1-36.

Cox, A. and Doell, R. 1960. Review of paleomagnetism. Bulletin of the Geological Society of America, 71, pp 645-768.

Cox, A. and Hart, R. 1986. Plate tectonics: How it works. Blackwell Scientific Publications, Boston, USA. 392 p.

Davidson, J., Mpodozis, C., Godoy, E., Hervé, F., Pankhurst, R. and Brook, M. 1987. Late Paleozoic accretionary complexes on the Gondwana margin of southern Chile: Evidences from the Chonos Archipiélago. In: Gondwana six, structure, tectonic and geophysics American geophysical union, McKenzie, G (ed.). Geophysical monograph, 40, pp 221-227.

De Long, S., Schwarz, W. and Anderson, R. 1979. Thermal effects of ridge subduction. Earth and Planetary Sciences Letters, 44, pp 239-246.

DeMets, C., Gordon, R., Argus, D. and Stein, S. 1994. Effects on Recent Revisions to the Geomagnetic Reversal Time Scale on Estimates of Current Plate Motions. Geophysical

Research Letters, 21 (20), 2191-2194.

Dekkers, M. 1989. Magnetic properties of natural pyrrothite. II. High and low temperature behaviors of Jrs and TRM as a function of grain size. Physics and Earth Planetary Interiors, 57, pp 266-283.

Didenko, A. and Forsythe, R. 1995. Petromagnetic study of igneous rocks of the Taitao ridge, Chile Triple junction, Site 862. In: Lewis, S., Behrmann, J., Musgrave, R. and Cande, S. (Eds.), Proceedings of the Ocean Drilling Project, scientific results, Leg 141: College station, TX (Ocean Drilling Project), pp 51-57.

Dilek, Y., Thy, P., Moores, E. and Ramsden, T. 1990. Tectonic evolution of the Troodos ophiolite within the Thetyan framework. Tectonics, 9 (4), pp 811-823.

Doblas, M., 1998, Slickenside kinematic indicators, Tectonophysics, n. 295, p. 187-197.

Dunlop, D. and Özdemir, Ö. 1997. Rock magnetism: Fundamentals and Frontiers. Cambridge University Press, Cambridge. 573 p.

Ellwood, B. and Ledbetter, M. 1977. Antarctic bottom water fluctuations in the Vema channel: effects of velocity changes on particle alignment and size. Earth planetary science letters, 35, pp 189-198.

Ellwood, B and Ledbetter, M. 1979. Paleocurrent indicators in deep-sea sediment. Science, 203, pp 1335-1337.

Ellwood, B., Ledbetter, M. and Johnson, D. 1979. Sedimentary fabric: a tool to delineate a high-velocity zone within a deep Western Indian Ocean bottom current. Marine Geology, 33, pp M51-M55.

Ellwood, B. 1980. Application of the anisotropy of magnetic susceptibility method as an indicator of bottom-water flow direction. Marine Geology, 34, pp M83-M90.

Fisher, R. 1953. Dispersion on a sphere. Proceedings of the Royal Society of London, Series A, 217, pp.295-305.

Fisher, R. 1984. Submarine volcanic rocks. In: Marginal basin geology, volcanic and associated

sedimentary and tectonic processes in modern and ancient marginal basins, Kokelar, B. and Howells, M (Eds.). Geological Society Special Publication N^0 16. pp. 5-27.

Fitch, T. 1972. Plate convergence, transcurrent faults, and internal deformation adjacent to Southeast Asia and Western Pacific. Journal of Geophysical Research, Vol. 77 (23), pp 4432-4460.

Flinn, D. 1962. On unfolding during three-dimensional progressive deformation. Geological Society of London Quaternary Journal, 118, pp 385-433.

Forsythe, R., and Nelson, E. 1985. Geological manifestations of the ridge collision: Evidence from the Golfo de Penas-Taitao Basin, southern Chile, Tectonophysics, 4 (5), p. 447-495.

Forsythe, R., Nelson, E., Carr, M., Keading, M., Hervé, M., Mpodozis, C., Soffia, J. and Harambour, S. 1986. Pliocene near-trench magmatism in southern Chile: A possible manifestation of the ridge collision. Geology, 14, pp 23-27.

Forsythe, R. and Prior, D. 1992. Cenozoic continental geology of South America and its relations to the evolution of the Chile triple junction, in Behrmann, J., Lewis, S., Musgrave, R., et al., eds., Proceedings of Ocean Drilling Program, initial reports, 141, p. 23-31.

Forsythe, R., Meen, J., Bender, J. and Elthon, D. 1995. Geochemical data on volcanic rocks and glasses recovered from site 862: Implications for the origin of the Taitao ridge, Chile Triple junction region. In: Lewis, S., Behrmann, J., Musgrave, R., and Cande, S (Eds.), Proceedings of the Ocean Drilling Program, scientific reports, 141. p. 331-348.

Forsythe, R. y Diemer, J. (2000). Neotectonics observations from the southern terminus of the Liquiñe-Ofqui fault, Itsmus of Ofqui. Actas IX Congreso Geológico Chileno, vol 2, pp. 205-209 (resúmenes expandidos).

Fry, N. 1999. Striated faults: visual appreciation of their constraint on possible paleostress tensors. Journal of Structural Geology, 21, pp 7-21.

Gass, I., MacLeod, C., Murton, B., Panayiotou, A., Simonian, K. and Xonophontos, C. 1994. The geology of southern Troodos transform fault zone. Cyprus geological survey department

memoir, N. 9, 218p.

Gattacacceca, J. and Speranza, F. 2002. Paleomagnetism of Jurassic to Miocene sediments from the Apenninic carbonate platform (southern Apennines, Italy): evidence for a 60^0 counterclockwise Miocene rotation. Earth and Planetary Science Letters, 201, pp 19-34.

Guivel, C., Lagabrielle, Y., Bourgois, J., Maury, R., Martin, H., Arnaud, N. and Cotton, J. 1996. Magmatic responses to active spreading ridge subduction: Multiple magma sources in the Taitao peninsula region (46°-47°, Chile Triple Junction), Third ISAG, St Malo (France), p. 575-578.

Guivel, C., Lagabrielle, Y., Bourgois, J., Maury, R., Fourcade, S., Martin, H. and Arnaud, N. 1999. New geochemical constraints for the origin of ridge-subduction-related plutonic and volcanic suites from the Chile triple junction (Taitao peninsula and Site 862, LEG ODP141 on the Taitao ridge), Tectonophysics, 311, p. 83-111.

Guivel, C., Lagabrielle, Y., Bourgois, J., Martin, H., Arnaud, N., Fourcade, S., Cotton, J. and Maury, R. 2003. Very shallow melting of oceanic crust during spreading ridge subduction: Origin of near-trench Quaternary volcanism at the Chile Triple Junction. Journal of Geophysical Research, 108 (B7), 2345, doi: 10.1029/2002JB002119, 2003.

Granar, L. 1958. Magnetic measurements on Swedish varved sediments. Arkiv Geofysik, 3, pp. 1-40.

Grommé, C., Wright, T. and Peak, D. 1969. Magnetic properties and oxidation of iron-titanium oxide minerals in Alae and Makaopulhi lava lakes, Hawaii. Journal of Geophysical Research, 74, pp. 5277-5293.

Hancock, P. (1985). Brittle microtectonics: principles and practice. Journal of structural Geology, 7, pp 437 – 457.

Hervé, M., Suárez, M. and Puig, A. 1984. The patagonian batholith S of Tierra del Fuego, Chile: Timing and tectonic implication. Journal of the Geological Society of London, 141, pp 909 – 917.

Hervé, F., Mpodozis, C., Nasi, C., Soffia, J., Forsythe, R. and Nelson, E. 1985. Magmatic effects of pliocene ridge subduction in the southern Chile Margin Triple junction: K-Ar geochronology. Comunicaciones, 35, pp. 109-112.

Hervé, F., Godoy, E., Garrido, I., Hormázabal, L., Brook, M., Pakhurst, R. and Vogel, S. 1988. Geocronología y condiciones de metamorfismo del complejo de subducción del archipiélago de los Chonos, V Congreso Geológico Chileno (expanded abstracts), v. II, p. E157-E173.

Hervé, M., Green, F. and Pankhurst, R. 1994. Metamorphosed fragments of oceanic crust in the upper Paleozoic Chonos accretionary complex, southern Chile. Journal of South American Earth Sciences, 7 (3/4), pp 263-270.

Hervé, F., Pankhurst, R., Drake, R. and Beck, M. 1995. Pillow lava metabasalts in a mid-Tertiary extensional basin adjacent to the Liquiñe-Ofqui fault zone: The Magdalena area, Aysén, Chile. Journal of South American Earth Sciences, 8(1), pp 33 – 46.

Hervé, F., Demant, A., Ramos, V., Pankhurst, R. and Suarez, M. 2000. The southern Andes. In: Cordani, U., Milani, E., Tomaz Filho, A. and Campos, D. (Eds). Tectonic evolution of South America. 31st International Geological Congress (Brazil), pp 605-634.

Hervé, F. Fanning, M., Thomson, S., Pankhurst, R., Anma, R., Veloso, A. and Herrera, C. 2003. SHRIMP U-Pb and FT pliocene ages of the near-trench granites in the Taitao peninsula, southern Chile, IV South American Symposium on Isotope Geology, Short Papers, v. 1, Salvador, Brazil, pp190-193.

Hrouda, F. 1982. Magnetic anisotropy of rocks and its applications in geology and geophysics. Geophysical Survey, 5, pp 37-82.

Hurst, S., Karson, J. and Verosub, K. 1994. Paleomagnetism of tilted dikes in fast spread oceanic crust exposed in the Hess Deep rift: Implications for spreading and rift propagation. Tectonics, 13 (4), pp 789-802.

Jelinek, V. 1981. Characterization of the magnetic fabric of rocks. Tectonophysics, 79, pp T63-T67.

Keading, M., Forsythe, R. and Nelson, E. 1990. Geochemistry of the Taitao ophiolite and near-trench intrusions from the Chile margin triple junction, Journal of South American Earth Sciences, 3 (4), p. 161-177.

Kearey, P. 2001. The new Penguin dictionary of Geology (second edition). Penguin Books. London, England. 327 p.

Kent, J. 1982. The Fisher-Binghman distribution on the sphere. Journal of Royal Statistical Society, B 44, pp. 71-80.

Kerr, A., Tarney, J., Nivia, A., Marriner, G. and Saunders, A. 1998. The internal structure of oceanic plateaus: Inferences from obducted cretaceous terranes in western Colombia and the Caribbean. Tectonophysics, 292, pp 173-188.

King, R. 1955. The remanent magnetism of artificially deposited sediments. Monographic Notes of the Royal Astronomical Society, 7, pp 115-134.

Kirschvink, J. 1980. The last-square line and plane and the analysis of paleomagnetic data. Geophysical Journal of the Astronomical Society, 62, pp. 699-718.

Kurnosov, V., Forsythe, R., Lindsley-Griffin, N., Zoloratev, G., Kashinzev, G., Eroshchev-Shak, V., Aratamonov, A and Chudaev, O. 1995. Comparison of the alteration and petrology of the Taitao ridge to the Taitao ophiolite, in: Lewis, S., Behrmann, J., Musgrave, R., and Cande, S (Eds.), Proceedings of the Ocean Drilling Program, scientific reports, 141. p. 349-360.

Lagabrielle, Y., Le Moigne, J., Maury, R., Cotton, J. and Bourgois, J. 1994. Volcanic record of the subduction of an active spreading ridge, Taitao peninsula (southern Chile), Geology, 22, p. 515-518.

Lagabrielle, Y., Guivel, C., Maury, R., Bourgois, J., Fourcade, S. and Martin, H. 2000. Magmatic-tectonic effects of high thermal regime at the site of active ridge subduction: The Chile triple junction model, Tectonophysics, 326, p. 255-268.

Lamb, S. 1988. Tectonic rotations about vertical axes during the last 4 Ma in part of the New Zealand plate-boundary zone. Journal of Structural Geology, 10 (8), pp 875-893.

Lavenu, A., Noblet, C. and Winter, Th. (1995). Neogene ongoing tectonics in the Southern Ecuadorian Andes: analysis of the evolution of the stress field. Journal of Structural Geology, 17, pp 47–58.

Lavenu, A. and Cembrano, J. (1999). Compressional- and transpressional-stress pattern for the pliocene and quaternary brittle deformation in fore arc and intra-arc zones (Andes of central and southern Chile). Journal of Structural Geology, 21, pp 1669 – 1691.

Le Moigne, J. 1994. Subduction d'une dorsale océanique active: géologie des ophiolites de Taitao (point triple du Chili) [Ph.D. thesis]: Brest, Université de Bretagne Occidentale, 160p.

Ledbetter, M. and Ellwood, B. 1980. Spatial and temporal changes in bottom-water velocity and direction from analysis of particle size and alignment in deep-sea sediments. Marine Geology, 38, pp 245-261.

LePichon, X., Franceteau, J. and Bonnin, J. 1973. Plate Tectonics. Elsevier. Amsterdam, Netherlands. 300 p.

LePichon, X. and Blanchet, R. 1978. Where are the passive margins of western Tethys Ocean?. Geology, 6, pp 597.

Lewis, S., Behrmann, J., Musgrave, R. and Cande, S. (Eds.). 1995. Proceedings of the Ocean Drilling Project, scientific results, 141:College station, TX (Ocean Drilling Project), 499p.

Liu, B., Saito, Y., Yamazaki, T., Abdeldayem, A., Oda, H., Hori, K and Zhao, Q. 2001. Paleocurrent analysis for late Pleistocene-Holocene incised-valley fill of the Yangtze delta, China by using anisotropy of magnetic susceptibility data. Marine Geology, 176, pp 175-189.

MacDonald, W. 1980. Net tectonic rotation, apparent tectonic rotation, and the structural tilt correction in paleomagnetic studies. Journal of Geophysical Research, 85 (B7), pp. 3659-3669.

Mahony, J., Storey, M., Duncan, R., Spencer, K. and Pringle, M. 1993. Geochemistry and age of the Ontgong Java plateau, *In*: Pringle, M., Sange, W., Sliter, W. and Stein, S (Eds.), The

Mesozoic Pacific: Geology, tectonics and volcanism. American Geophysical Monograph, 77, pp 233-261.

Martin, H. 1994. The Archaean grey gneisses and the genesis of continental crust. In: Archaean crustal evolution, Condie, X. (Ed.), Amsterdam, Netherlands, Elsevier, pp 205-259.

Martin, H. 1999. Adakitic magmas: Modern analogues of Archaean granitoids. Lithos, 46, pp 411-429.

McElhinny, M. 1964. Statistical significance of the fold test in paleomagnetism. Geophysical Journal of the Royal Astronomical Society, 8, pp 338-340.

McFadden, P. and McElhinny, M. 1990. Classification of the reversal test in paleomagnetism. Geophysical Journal International, 103, pp. 725-729.

McKenzie, D and Morgan, W. 1969. Evolution of triple junctions, Nature, 224, p. 125-133.

Menke, W., 1989, Geophysical data analysis: Discrete inverse theory. Academic Press. San Diego, USA.

Molnar, P. and Atwater, T. 1978. Interarc spreading and cordilleran tectonics as alternates related to the age of subducted oceanic lithosphere. Earth and Planetary Science Letters, 41, pp 330.

Moores, E. and Vine, F. 1971. The Troodos massif, Cyprus, and other ophiolites as oceanic crust: Evaluation and implications. Philosophical Transactions of the Royal Society of London A, 268, pp 443-466.

Moores, E. 1982. Origin and emplacement of ophiolites. Reviews of Geophysics and Space Physics, 20 (4), pp 735-760.

Morgan, W. 1978. Rodriguez, Darwin, Amsterdam..., a second type of hot spot island. Journal of Geophysical Research, 83, pp 5355-5360.

Mpodozis, C., Hervé, M., Nasi, C., Soffia, J., Forsythe, R. and Nelson, E. 1985. El magmatismo Plioceno de la península Tres Montes y su relación con la evolución del punto triple de Chile, Revista Geológica de Chile, 25-26, p. 13-28.

Munizaga, F. 1970. Informe preliminar sobre las edades radiométricas en la provincia de Aysén. Instituto de Investigaciones Geológicas (Chile). (Inédito), 14 p.

Murdie, R. and Russo, R. 1999. Seismic anisotropy in the region of the Chile margin triple junction. Journal of South American Sciences, 12, pp 261-270.

Nelson, E., Forsythe, R., Diemer, J., Allen, M. and Urbina, O. 1993. Taitao ophiolite: A ridge collision ophiolite in the forearc of southern Chile (46°S), Revista Geológica de Chile, 20, p. 137-166.

Neves, S., Araujo, A., Correia, P. and Mariano, G. 2003. Magnetic fabrics in the Cabanas granite (NE Brazil): Interplay between emplacement and regional fabrics in a dextral transpressive regimen. Journal of Structural Geology, 25, pp 441-453.

Nicolas, A. 1989. Structures of ophiolites and dynamics of oceanic lithosphere. Kluwer Academics Publishers, 367p. Dordrecht.

Nicolas, A. 1995. The mid-oceanic ridges: Mountains below sea level. Springer-Verlag, New York, USA. 200p

Nicolas, A. and LePichon, X. 1980. Thrusting of young lithosphere in subduction zones with special reference to structures in ophiolitic peridotites. Earth and Planetary Science Letters, 46, pp 397-406.

Nicolas, A., Freydier, Cl., Godart, M. and Vauchez, A. 1993. Magma chambers at oceanic ridges: How large? Geology, 21, pp 53-56.

Ortner, H., Reiter, F. and Acs, P. 2002. Easy handling of tectonic data: The programs TectonicsVB for Mac and TectonicsFP for Windows™. Computers & Geosciences, 28 (10), pp 1193-1200

Pankhurst, R., Weaver, S., Hervé, F. and Larrondo, P. 1999. Mesozoic-Cenozoic evolution of the north patagonian batholith in Aysén, Southern Chile. Journal of the Geological Society of London, 156, pp 673-694.

Pares, J., van der Pluijm, B. and Dinares-Turrell, J. 1999. Evolution of magnetic fabrics during

incipient deformation of mudrocks (Pyrenees, northern Spain), Tectonophysics, 307, pp 1-14.

Passchier, C and Trouw, R. 1996. Micro-tectonics. Springer-Verlag. Berlin, Germany. 289 p.

Petit, J., 1987, Criteria for the sense of movement on fault surfaces in brittle rocks, Journal of Structural Geology, 9, p. 597-608.

Piper, J., Elliot, M. and Kneller, B. 1996. Anisotropy of magnetic susceptibility in a Paleozoic flysch basin: the Windermere Supergroup, northern England, Sedimentary Geology, 106, pp 235-258.

Ramsay, J. 1961. The effects of folding upon the orientation of sedimentary structures. Journal of Geology, 69, pp 84-100.

Ramsay, J. 1967. Folding and fracturing of rock. McGraw-Hill. New York, USA. 568 p.

Rees, A. 1965. The use of anisotropy of magnetic susceptibility in the estimation of sedimentary fabric. Sedimentology, 4, pp 257-271.

Rees, A., von Rad, U. and Shepard, F. 1968. Magnetic fabrics of sediments from the La Jolla submarine canyon and fan, California. Marine Geology, 6, pp 145-178.

Roberts, A. 1995. Magnetic properties of sedimentary greigite (Fe_3S_4). Earth and Planetary Sciences Letters, 134, pp 227-236.

Rochette, P., Jackson, M. and Aubourg, C. 1992. Rock magnetism and the interpretation of anisotropy of magnetic susceptibility. Reviews of Geophysics, 30, pp. 209-226.

Schieber, J. and Ellwood, B. 1993. Determination of basin wide paleocurrent patterns in a shale succession from anisotropy of magnetic susceptibility (AMS): a case study of the mid-proterozoic Newland formation, Montana. Journal of Sedimentary Petrology, 63, pp 874-880.

Scheidegger, A. 1965. On the statistics of the orientation of bedding planes, grain axes, and similar sedimentological data. United States Geological Survey Prof Paper, 525-C, pp 164-167.

Sleep, N. 1997. Lateral flow and ponding of starting plume material. Journal of Geophysical Research, 102, pp 10001-10012.

Sperner, B., Ott, R. and Ratschbacher, L. (1993): Fault-striae analysis: a turbo pascal program package for graphical presentation and reduced stress-tensor calculation. Computer and Geosciences, 19(9), pp 1361-1388.

Stacey, F., Joplin, G and Lindsay, J. 1960. Magnetic anisotropy and fabric of some foliated rocks from SE Australia. Geophysics Pure Applied, 47, pp 30-40.

Suppe, J. 1985. Principles of structural geology. Prentice-Hall. New Jersey, USA. 537 p.

Taira, A. and Lienert, B. 1979. The comparative reliability of magnetic, photometric and microscopic methods of determining the orientations of sedimentary grains. Journal of Sedimentary Petrology, 49, pp 759-772.

Tarling, D. and Hrouda, F. 1993. The magnetic anisotropy of rocks. Chapman & Hall, London, 217 p.

Tauxe, L. 1998. Paleomagnetic principles and practice. Modern approach in geophysics. Kluwer Academic. Netherlands. 299 p.

Tauxe, L. and Watson, G. 1994. The fold test: an eigen analysis approach. Earth Planetary Sciences Letters, 122, pp 331-341.

Thomas, V., Pozzi, J. and Nicolas, 1988. A. Paleomagnetic results from Oman ophiolites related to their emplacement. Tectonophysics, 151, pp 297-321.

Turcotte, D. and Schubert, G. 1982. Geodynamics, applications of continuum physics to geological problems. John Wiley & Sons, New York, USA, 450p.

Vaughan, A. and Scarrow, J. 2003. Ophiolite obduction pulses as a proxy indicator of superplume events?. Earth and Planetary Sciences Letters, 213, pp 407-416.

Varga, R. and Moores, E. 1985. Spreading structure of the Troodos ophiolite, Cyprus. Geology, 13, pp 846-850.

Varga, R., Karson, J. and Gee, J. 2004. Paleomagnetic constraints on deformation models for uppermost oceanic crust exposed at the Hess Deep rift: Implications for axial processes at the east Pacific Rise. Journal of Geophysical Research, 109, B02104, doi:

10.1029/2003JB002486

Veloso, E. 2001. Condiciones de emplazamiento y deformación frágil de la ofiolita Taitao (46°42'Lat. S; 73°35' Long. W), Región de Aysén, Chile [Degree Thesis]: Santiago de Chile, Universidad de Chile, 100p.

Vogt, P. 1971. Asthenosphere motion recorded by the ocean floor south of Iceland. Earth and Planetary Science Letters, 13, pp 153-160.

Wakabayashi, J. and Dilek, Y. 2004. Ophiolite obduction and the Semail ophiolite: the behavior of the underlying margin. Geological Society of London Special Paper, 218, in press.

Watson, G. 1956. A test for randomness. Monograph notice to the Royal Astronomical Society, 7, pp 160-161.

Weinberger, R., Agnon, A., Ron, H. and Garfunkel, Z. 1995. Rotation about inclined axis: three dimensional matrices for reconstructing paleomagnetic and structural data. Journal of Structural Geology, 17 (6), pp. 777-782.

Wilks, K. and Carter, N. 1990. Rheology of some continental lower crustal rocks. Tectonophysics, 182, pp 57-77.

Yamaji, A., 2000, The multiple inverse method: A new technique to separate stresses from heterogeneous fault-slip data. Journal of Structural Geology, 22, p. 441-452.

Yamaji, A., 2003, Are the solutions of stress inversion correct? Visualization of their reliability and the separation of stresses from heterogeneous fault-slip data, Journal of Structural Geology, 25, p. 241-252.

Yañez, G. and Cembrano, J. 2000. Tectonics models for ridge collision at a continental plate boundary: The case of Juan Fernandez and Chile Rise, preliminary results. Actas IX Congreso Geológico Chileno (expanded abstracts), pp. 649-654.

Yañez, G., Cembrano, J., Pardo, M., Ranero, C. and Selles, D. 2002. The Challenger-Juan Fernandez-Maipo major tectonic transition of the Nazca-Andean subduction system at 33-34^{0}S: geodynamic evidence and implications. Journal of South American Earth Sciences, 15,

pp 23-38.

Zijderveld, J. 1967. A.C. demagnetization of rocks: Analysis of results. In: Collinson, D; Creer, K. and Runcorn, S. (Eds), Methods in paleomagnetism. Elsevier, Amsterdam. pp. 254-286.

Appendix

Appendix A: Stress fields

A.1. Basic concepts

A.1.1. Stress field definition

Stress corresponds to the force per unit area acting on a surface of a solid, such as an imaginary or real block, plus the equal and opposite reaction of the material (e.g. Kearey, 2001), been a mixture of physical (force) and geometrical (surface) quantities (e.g. Suppe, 1985). It has the same physical dimensions of pressure (N/m^2). Notice that forces can be represented as vectors, defined by size and direction, independent from the orientation of the surface where they act. However, related stress depends on the orientation of the surface and then it is only possible to define it at that surface (e.g. Passchier and Trouw, 1996).The stress field can be divided into its tangential (shear), and its normal component (Fig. A.1a).

As many others physical parameters, stress field can be fully described using tensor matrices. The stress tensor matrix has nine independent components, and its representation is given by:

$$T = \begin{bmatrix} \sigma_{11} & t_{12} & t_{13} \\ t_{21} & \sigma_{22} & t_{23} \\ t_{31} & t_{32} & \sigma_{33} \end{bmatrix} \begin{bmatrix} x_1 \\ x_2 \\ x_3 \end{bmatrix} \qquad [E.1]$$

Where T represents the applied stress field, σ_{ii} (with i=1 to 3) represents each one of the normal stresses while t_{ij} (i, j=1, 2, 3) are the shear stresses, both in each one of the faces of a vanishing cube (Fig. A.1b), and x_i is the unit vector of the Cartesian coordinate system.

In geological situations, stress fields are taken to be symmetrical and therefore only six independent components are needed. Of these, three components describe the "*principal stress values*" along "*principal stress axes*" in three orthogonal directions (resembling a certain coordinate system) while the other three components describe the spatial orientation of the

"*principal stress axes*" (e.g. Passchier and Trouw, 1996). The principal stress axes correspond to the intrinsic axes related to the stress field and surface. It is always possible to find a coordinate system in which the tensor matrix is diagonal, containing only the principal stress axes magnitude. Thus, the tensor matrix equation [E.1] becomes:

$$\begin{bmatrix} T_1 \\ T_2 \\ T_3 \end{bmatrix} = \begin{bmatrix} \sigma_1 & 0 & 0 \\ 0 & \sigma_2 & 0 \\ 0 & 0 & \sigma_3 \end{bmatrix} \begin{bmatrix} n_1 \\ n_2 \\ n_3 \end{bmatrix} \qquad [E.2]$$

Where T_i represent the force vector in the new coordinate system, σ_i represents the magnitude and orientation of the principal stress axis and n_i the vector normal to each surface where the principal stress axis is acting (i.e. the new coordinate system). In this orthogonal system there is no traction in the direction of the principal stress axes. Mathematically, the principal stress axes correspond to the eigenvectors of the tensor matrix T (equation [E.1]). The largest eigenvector correspond to the "*maximum*" (σ_1) stress axis describing the orientation of the "*maximum*" compressional axis; while the "*intermediate*" (σ_2) and "*minimum*" (σ_3) eigenvectors correspond to the "*intermediate*" and "*minimum*" compressional axes respectively. The relation between the principal stress axes is, by definition:

$$\sigma_1 \geq \sigma_2 \geq \sigma_3 \qquad [E.3]$$

Notice that in geological situations, σ_3 is usually considered as an extensional axis rather than compressional.

A.1.2. The stress ellipsoid

It corresponds to a graphical representation of each principal stress axis (Fig. A.2). Here, the major three axes of the ellipsoid correspond in magnitude and orientation to the principal stress axes. In this sense, a sphere represents an isotropic stress field ($\sigma_1=\sigma_2=\sigma_3$) whereas a general ellipsoid (where the three major axes are different from each other) represents a general triaxial stress field ($\sigma_1>\sigma_2>\sigma_3$). In a geological context, the orientation and shape of the stress ellipsoid is

used to represent the stress field related to the three major types of faults (normal, reverse and strike-slip).

A.1.3. The stress ratio

A useful parameter to describe a stress field acting on a rock mass is the "stress ratio" (φ) which is the relation between the principal stress axes defined by:

$$\varphi = \frac{\sigma_1 - \sigma_2}{\sigma_1 - \sigma_3} \qquad [E.4]$$

Where σ_i is the magnitude of the i-th principal stress axis. The stress ratio varies between 1 and 0, with 0 representing a uniaxial extension stress field state ($\sigma_1=\sigma_2$) and 1 a uniaxial compressional stress state ($\sigma_2=\sigma_3$). Intermediate values of φ represent triaxial stress field states ($\sigma_1>\sigma_2>\sigma_3$). The stress ratio is a mathematical aid to characterize the shape and size of the stress ellipsoid.

The stress ellipsoid is a complete characterization of the stress field while the stress ratio only carries information about the relative magnitudes between the principal stress axes. In practice, the stress ratio is preferred by many geologists due its easy implementation in any computer routine.

A.2. Indicators of stress fields rocks

A.2.1. Fault planes

A fault plane is any fracture in the rock mass which presents a measurable displacement across its surface (e.g. Suppe, 1985). Several geometrical elements can be defined on the fault (Fig. A.3a), such as: (1) hanging wall block (above the fault plane) and (2) footwall block (below

the fault plane).

The relative displacement between these two blocks is represented by the vector which merges two points which were together before the movement (dd in Fig. A.3a). This vector can be divided into two components, one across strike (in the horizontal plane, dh) and another across the dip of the fault surface (dv). According to the relative movement of the blocks, the fault plane can be classified as (e.g. Suppe, 1985):

- Normal: where the hanging wall block moves downward, in a vertical plane, with respect to its original position (Fig. A.3b). If the dip angle of the fault plane is less than 45^0 then the fault is called "lag". Notice that in a normal fault dh=0.
- Reverse: where the hanging wall block moves upward with respect to its original position (Fig. A.3c). If the angle is less than 45^0 then the fault plane is called "thrust". Notice that, as in a normal fault, dh=0
- Strike-slip: The relative movement of blocks occurs in a horizontal plane; therefore definition of hanging and footwall blocks is no longer valid. One of the blocks is displaced left (in which case the fault is called sinestral) or right (dextral) respect to the other (Fig. A.3d). Notice that in and strike-slip fault dv=0.

Real fault planes usually show both vertical ($dh \neq 0$) and horizontal ($dv \neq 0$) movements. Thus, fault planes are usually classified using two of the above terms (i.e. "normal-dextral"), where the first indicates the major or more characteristic movement (Fig. A.3e, f).

A.2.2. Brittle kinematic indicators

The relative movement on a fault plane is a product of the stress field induced over that surface. As the stress field is applied, traction over the fault surface is also applied (shear). This traction usually leaves marks in the fault plane surface which can be classified as:

- Tool marks (Hancock, 1985): produced by objects more resistant than the rock mass, the end

of the mark indicates the sense of movement (Fig. A.4a)

- Slickenfibers (Hancock 1985): Mineral fibers that grow in the irregularities of the fault plane and parallel to the movement of the fault (Fig. A.4b).
- Secondary fractures (Petit, 1987; Doblas, 1998): These correspond to minor fractures in the fault plane product of the movement, they can be divided into:
  1. T: secondary fractures are arranged "*en echelon*" with angles between 30^0 and 90^0 with respect to the main fault plane. The dip of the fracture indicates the movement direction of the missing block (Fig. A.4c).
  2. R: The fault surface is intersected by striated secondary fractures in a fixed pattern. They can present the same sense of movement than the fault plane (R) or opposite (R'). Intersection of R and R' fractures may produce "moon" shape structures (Fig. A.4d-f). Dip of R fractures indicates the movement direction of the missing block.
  3. P: The fault plane is always striated in a low penetrative way with secondary fractures having a low dipping angle, usually less than 10^0. P structures dip opposite to the direction of the missing block (Fig. A.4g-i).

From the spatial orientation of these marks, direction and sense of movement of the fault plane can be qualitatively established. This, together with the orientation of the fault plane, provides a complete characterization of the fault.

A.3. The inverse problem

In theory or in the laboratory, parameters like orientation and magnitude of the stress field are known and the work focus on obtaining the orientation of generated structures. In contrast, real fractures and fault planes are already generated (by some stress field) with their orientation known and easily measurable. Then, the problem is t find the stress field responsible for the generation of such fractures or fault planes. This mathematical problem is called "*inverse*

problem" (e.g. Carey and Brunier, 1974; Angelier and Gougel, 1979; Angelier, 1994).

To solve the inverse problem is necessary to assume that the orientation of the striae (or any other kinematic indicator) indicates the direction and sense of the shear stress which corresponds to a certain stress field tensor (Angelier, 1994). Then, an average common stress field tensor can be calculated for a certain population of faults.

Suppose that we have a number of N fault-slip data and all these faults slip under a common stress field T. If n_i denotes the normal vector of a fault plane (i=1,..., N), then the stress vector (υ_i) acting on the surface is:

$$\upsilon_i = Tn_i \qquad \text{[E.5]}$$

Subtracting the normal stress, the shear stress component t_i is obtained:

$$t_i = Tn_i - (n^T{}_i Tn_i)n_i \qquad \text{[E.6]}$$

Where the superscript "T" indicates the transpose of the matrix or vector. This later equation gives the orientation of the shear stress. However, this orientation (of the calculated shear stress) may not coincide with the orientation of the measured striae (real shear stress). The best-fitting stress tensor for a certain fault population can be obtained by minimizing:

$$T^* = \sum_{k=1}^{k} W_k (F_k)^2 \qquad \text{[E.7]}$$

Where T^* represents the best-fitting stress field tensor, W_k is the weight of the k-th fault-slip data and F_k is a function which denotes the difference between the calculated orientation of the shear (t) and the real orientation of the striae (s) (Angelier, 1994). Several forms and solutions had been proposed for F_k. All these solutions have shown a good consistency in the results and only differences in iteration times (e.g. Angelier, 1994).

Calculated errors between the orientations of t and s should not be the only ones considered to calculate the shear stress. Also, the difference between the real fault plane and the theoretical one should be considered. The orientation of a real fault plane can be completely characterized by a couple of vectors n and s (the first normal to the surface and the second parallel to the striae

orientation) (Fig. A.5); while a theoretical fault plane can be characterize by vectors n^* and t (similar to the previous one). In order to find the best-fitting stress field tensor for a certain fault population the difference between n^* and n must be consider as well as the difference between t and s (Angelier, 1994).

Since the calculation of the stress field tensor is performed in an ideal situation, some degree of tolerance must be allowed in the difference between t and s (or n^* and n). Several studies had proven that a *ca.* 20^0 tolerance is still valid (e.g. Lavenu et al., 1995; Lavenu and Cembrano, 1999; Cembrano et al., 2000; among others).

The calculation of stress fields by the present method is not straightforward by hand. However, several software packs have been developed to solve this problem; such as: (1) algorithm of Carey and Brunier (1974), (2) software TectonicsFP® (Ortner et al., 2002; Angelier and Gougel, 1979; Sperner, 1993) and others; providing a fast and easy way to determine the stress field tensor related to a certain population of faults. Differences between calculated and real orientations of the shear stresses can be easily accounted and the related stress field tensor can then be rejected or accepted.

In reality, a certain population of faults was probably generated by different stress fields acting synchronously or at different times (heterogeneous stress field). The previous method works well for homogeneous fault-slip data population, but it is unable to identified heterogeneous stress fields. Thus, certain division criteria are necessary to separate and filter the fault-slip data before applying the method. These criteria are usually ambiguous, making sometimes virtually impossible to separate and interpret identified stress fields.

A.4. The multi-inverse method (Yamaji, 2000, 2003)

In order to separate heterogeneous fault-skip data, Yamaji (2000) proposed a numerical method called "*multi-inverse*" method which is able to identify and separate heterogeneous stress

fields recorded on the fault-slip data without any previous knowledge of the data. The core of the method is akin to cluster analysis (Menke, 1989) which uses a sort of self-correlation of the data (Yamaji, 2000).

Suppose that we have N fault-slip data and no a priori knowledge of how many or what kind of stress fields are recorded on it. The problem is how to divide the fault-slip data into subsets that corresponds to stress fields that activated each subset (Yamaji, 2000). For this, the method separates a k-element subset from the N data. Thus, the number of subsets that can be obtained from the N fault-slip data is given by the binomial coefficient:

$$ {}_N C_k = \frac{N!}{k!(N-k)!} \qquad \text{[E.8]} $$

Where $N!$ stands for the factorial of N ($N!=N(N-1)(N-2)...(N-N+1)$). For each subset the inverse method is applied, obtaining a number of solutions equal to the number of analyzed subsets (Yamaji, 2000). Once the ${}_N C_k$ stress fields are obtained, their principal stress axes can be extracted. To have a visual aid of the obtained solutions a couple of stereonet projections are used, one with the orientation of the maximum stress axis and other with that of the minimum stress axis calculated for each stress field.

Since the number of obtained solutions can be quite large, it becomes necessary to investigate the density distribution of the solutions. Let m be the number of solutions at a certain grid point (i.e. with a certain general orientation) with $P(m)$ the frequency of those solutions. If d is the standard deviation of $P(m)$ then it is possible to define an "enhanced parameter" (e):

$$ e = \frac{m}{4d} \qquad \text{[E.9]} $$

If $e<1$ at certain grid point, no symbol is plotted. This relationship allows thinning out erroneous solutions and enhanced correct ones (Yamaji, 2000).

To have an easy way to visualize obtained stress fields, a special symbol is used in the stereonet representation. The orientation of the stress axis is color-coded, where the color indicates the stress ratio related to that solution. Also, an attached tail indicates the direction of

the complementary stress axis; i.e. if the maximum (minimum) stress axis is plotted, then the tail points in direction of the complementary minimum (maximum) stress axis. Stress fields solutions for the entire fault-slip data are seen as clusters with same color and with tails pointing to a common direction (Fig. A.6) (Yamaji, 2000, 2003).

Similar to the classical inverse method (Angelier, 1994), the multi-inverse method (Yamaji, 2000, 2003) provides with an easy way to calculate the responsible stress field which generated a certain population of faults. Certainly, the multi-inverse method is an upgrade of the classical inverse method, solving the main limitation of the later one.

The convergence of the obtained solutions is highly dependant on N (number of faults) and k (number of faults in each subset) (Yamaji, 2003). As the fault-slip data includes noise, usually because of inaccurate measurements of the fault plane and/or the direction of the striae, the calculation for a small number of faults (N) usually provides with incorrect solutions called "*artifacts*". Also, the choice of the parameter k is arbitrary, yet small values may yield erroneous and unstable solutions (artifacts) (Yamaji, 2000). The number of computations required increases with k in order of:

$$ {}_N C_k \propto N^k \qquad \text{[E.10]} $$

Where the symbol $\propto$ means "*proportional to*". Then, if $k \ll N$ a small value of k is preferable. Tests of the method with simulated and real data have shown that the optimal k value is between 3 and 5, depending on the fault-slip data and N (Yamaji, 2000, 2003).

Appendix B: Paleomagnetism

If a mineral or a mineral aggregate had recorded the magnetic field of the Earth, then is possible, with the aid of certain techniques, to extract this information. This provides with excellent data to determine the magnetic and tectonic history of the rock. By comparing the orientations of RM vectors with that expected to be the magnetic field at the acquisition time, it is possible to determine qualitatively the amount and sense of rotation of the site under analysis.

In order to have an accurate constraint of the magnetic and tectonic history of the rock, it is crucial to know the RM acquisition time. Since nowadays there is no available technique to obtain an exact age for the magnetization, indirect techniques must be used. A good age control of the rock and/or any other well age-constrained tectonic event is highly desirable. Indirect techniques are varied, but most commonly used are those which provide a direct relation between the RM acquisition time and a certain tectonic event, such as folding, tilting, metamorphism, etc.

B.1. Obtaining Paleomagnetic directions: magnetic cleaning methods

Since a rock or mineral aggregate contains (possibly) a series of magnetic fields recorded, it becomes necessary to isolate progressively the different recorded magnetic fields. Two techniques are briefly discussed here: (1) Alternating Field demagnetization (AFD) and (2) Thermal demagnetization (ThD). Both allow a controlled and partial removal of the RM, revealing the orientation and magnitude of the different RM vectors recorded in the rock.

The Alternating Field Demagnetization (AFD) technique is based in the spectra of different coercitivities of the ferromagnetic (*sensu lato*) minerals. By applying a continuous increasing magnetic field, it is possible to realign progressively the RM in a rock sample. The remaining, non-aligned magnetic field is measured, obtaining the orientation and intensity of RM at certain

coercitivity level. To force the RM to rotate over its energy barrier (i.e. to realign the RM) an external magnetic field must be applied which exceeds the energy barrier ΔE_m (e.g. Butler, 1992). From the theory of magnetism:

$$\Delta E_m = \frac{h_c j_s}{2} \qquad [E.11]$$

Where j_s is the intensity of the RM and h_c is the coercive force (e.g. Butler, 1992). The coercive force is a measure of the energy barrier to rotate j_s (the RM) and realign it in the direction of external applied field.

The fundamental AFD procedure is to expose the rock sample to an alternating magnetic field. The waveform of this field is a sinusoid with a linear decrease in magnitude with time. Applying a peak magnetic field H_{AF} to the sample, all magnetic particles with $h_c \leqq H_{AF}$ will become align with it. This field can be assigned arbitrarily (without loosing generality) with "up" direction. As the applied magnetic field reduces in intensity, the next field $H'_{AF} = H_{AF} - \Delta$ (Δ denotes a small difference) aligns all particles with $h_c \leqq H_{AF} - \Delta = H'_{AF}$ with an arbitrary "down" direction. In the next step, an external field $H''_{AF} = H'_{AF} - \Delta = H_{AF} - 2\Delta$ pointing "up", is applied and all particles with $h_c \leqq H''_{AF}$ become aligned with the external field H''_{AF}. The net result is that all particles with $H'_{AF} \leqq h_c \leqq H_{AF}$ are realigned pointing "up"; while particles with $H''_{AF} \leqq h_c \leqq H'_{AF}$ are realigned pointing "down". The total magnetic moment of particles in these two h_c intervals cancel each other. When the applied external field reaches 0, the magnetic moments of all particles with $h_c \leqq H_{AF}$ are destroyed and only the magnetic moments of the particles with $h_c > H_{AF}$ remain. The procedure to remove the magnetic moments with $h_c \leqq H_{AF}$ is called "AFD step". Performing a progressively increase of the peak H_{AF} in each AFD step (i.e. H_{AF} (step 1) $\leqq H_{AF}$ (step 2) $\leqq H_{AF}$ (step 3)... $\leqq H_{AF}$ (step N)) it is possible to obtain a progressive image of the RM recorded in the sample.

Different from the AFD procedure, the thermal demagnetization (ThD) relies on the basis on blocking temperatures. RM vectors acquire at temperatures below the blocking temperature are

stable, especially if temperature is decreasing (Butler, 1992). The procedure involves the heating of the sample to an elevated peak temperature (T_{demag}) below the blocking temperature of the constituent minerals. Further, the sample is cooled to room temperature (about 20^0C) in a null magnetic field. This heating causes that magnetic moments of all particles with $T_b \leqq T_{demag}$ are randomized, as with low h_c during AFD (Butler, 1992). Performing increases in T_{demag} temperature over different steps (as AFD steps) allows a complete isolation of the characteristic RM vectors.

B.2. Types of remanent magnetization

The net RM of a rock or a mineral aggregate present before any laboratory treatment is called "Natural Remanent Magnetization" (NRM) (e.g. Butler, 1992; Tauxe, 1998), and it depends on the geomagnetic field of the Earth and geological processes during the rock formation and evolution. NRM can be composed for more than one component, referred as primary and secondary. Secondary NRM components can be acquired subsequent to rock formation and can alter or obscure primary ones (Butler, 1992). These secondary components are added to the primary to produce the total NRM (Fig. B.1); there are four basic forms of secondary NRM: (1) viscous, (2) thermal, (3) chemical and, (4) light-induced magnetizations.

Viscous RM (VRM) results from the action of the geomagnetic field after the formation of the rock. From the paleomagnetic point of view, VRM is undesirable noise (Butler, 1992). However, it can be easily erased during the first steps of demagnetization. It can be recognized as an increase in the magnetization intensity respect to the NRM (Fig. B.2).

Thermal RM is the form of magnetization most commonly acquire by igneous rocks during cooling (e.g. Butler, 1992). As the temperature of the minerals in the rock decreases, minerals change theirs behaviors from paramagnetic to ferromagnetic (*sensu lato*), been able to acquire magnetization. The magnetic field of the Earth can then align the magnetic moment of the

minerals with blocking temperatures below the present temperature, similar to the ThD process in reverse. As the cooling temperature decreases, ferromagnetic (*sensu lato*) behavior of the minerals is stronger and acquired RM becomes stable and recorded into the mineral.

Chemical magnetization is acquired due to a chemical change in the magnetic minerals, as a result of alteration to ferromagnetic (*sensu lato*) minerals or precipitation of ferromagnetic minerals. As the chemical composition of the minerals changes to a ferromagnetic (*sensu lato*) behavior under temperatures below the blocking temperature, new magnetic minerals acquire a RM parallel to the applied magnetic field. If the temperature is below the blocking temperature the acquire magnetization will became stable, similar to the thermal RM.

Light-induced RM is a product of a short-term exposure of the magnetic minerals to a strong magnetic field at constant temperature. Lightning strikes apply a randomly oriented magnetic field of *ca.* 10 to 100 mT over an area of about 1 m around the impact point (Butler, 1992). As a result, the area around the striking point can be partially or completely remagnetized.

B.3. Isolation and display of RM vectors

In order to isolate the recorded characteristic RM, an exhaustive analysis of both the intensity decay vs. temperature (or alternating field) and the orientation of obtained RM vectors are necessary. The following procedure is done on data obtained from the magnetic cleaning procedure, which includes both the remaining RM intensity and the orientation of the related RM vector at each magnetic cleaning step (M_i).

In order to compare the demagnetization data from several samples from the same or different sites, it is necessary to normalize it. Thus, it is convenient to normalize the whole data from the sample against the NRM intensity:

$$(M_i)_n = \frac{M_i}{M_{NRM}} \qquad \text{[E.12]}$$

Where $(M_i)_n$ is the normalized RM intensity at the i-th step, M_i is the RM intensity at the i-th step and M_{NRM} is the RM intensity at the initial step.

Since normalization of RM intensities was done against M_{NRM}, the first value of the decay curve is always equal to 1. Any further increasing of the normalized RM intensity, i.e. $(M_i)_n>1$, indicates the possible presence of VRM (noise). After RM intensity curve has decay below 1, a high-stability component has been isolated. Such component can consists of more than one representative vector.

As the magnetic cleaning step becomes stronger (high temperatures or high h_c) it is common to observe a complete decay of the RM intensity to, or near, 0 (Fig. B.2a); this means that the sample has been completely demagnetized. The point where the magnetic intensity has decay to 0 can be interpreted as: (1) the maximum blocking temperature of the sample (on ThD analysis) or, (2) as the maximum coercive force present in the sample (on AFD analysis). This value can give a good constrain about the magnetic mineral phase which carries the RM vector.

Widely used in the paleomagnetic literature the Zijderveld (1967) end-vector diagram has the advantage of including information about both the direction and the intensity of the RM vector at each progressively cleaning step (Fig. B.3). The base of the M_i vector is placed at the origin of a coordinate system and its end is projected into two overlapped orthogonal planes. The length of the plotted vector is proportional to the intensity of the M_i vector projected onto that plane (Zijderveld, 1967; Butler, 1992). The two orthogonal planes used for the projection are the horizontal plane, north (x_1) and east (x_2), and the vertical plane, north (x_1) and down (x_3). The Cartesian coordinates of any vector in this space are given by:

$$x_{1i} = M_i \cos(I_i)\cos(D_i) \qquad [E.13]$$

$$x_{2i} = M_i \cos(I_i)\sin(D_i) \qquad [E.14]$$

$$x_{3i} = M_i \sin(I_i) \qquad [E.15]$$

Where M_i is the intensity of the RM vector, I_i is the inclination and D_i is the declination of the i-th cleaning step. The Zijderveld (1967) diagram is constructed by merging the end-point of each

RM vector. Since the diagram contains the information of both intensity and orientation of the RM vector, a more or less straight line on both projections (at same demagnetization levels) reveals the presence of a high-stability RM (Fig. B.3).

After recognition of possible high-stability components of the RM, the most accurate way to obtain the orientation of the characteristic RM vector is the "*principal component analysis*" (PCA) proposed by Kirschvink (1980). The best-fitting vector through a series of slightly scattered vectors corresponds to the minimum moment of inertia of the related covariance matrix (Kirschvink, 1980; Tauxe, 1998). The values of this matrix are the coordinates of the center of mass of the data (Scheidegger, 1965). Transforming the RM vector to Cartesian coordinates using equations [E.13] to [E.15], the center of mass of the involved vectors is given by:

$$\bar{x}_i = \frac{1}{N}\left(\sum_{j=1}^{N} x_{ij}\right); \forall i = 1,2,3 \qquad [E.16]$$

Where the subscript i (i=1, 2, 3) denotes the three Cartesian axes and N is the number of vectors involved. To transform the data to the new coordinate system (center of mass):

$$x'_{ij} = x_{ij} - \bar{x}_i, \forall i = 1,2,3 \qquad [E.17]$$

Then, the covariance matrix (C') for the demagnetization data is given by replacing the elements of the orientation matrix tensor with the elements obtained in [E.17]. Thus:

$$C' = \begin{bmatrix} \sum x'^{2}_{1i} & \sum x'_{1i}x'_{2i} & \sum x'_{1i}x'_{3i} \\ \sum x'_{1i}x'_{2i} & \sum x'^{2}_{2i} & \sum x'_{2i}x'_{3i} \\ \sum x'_{1i}x'_{3i} & \sum x'_{2i}x'_{3i} & \sum x'^{2}_{3i} \end{bmatrix} \qquad [E.18]$$

The eigenvectors of the matrix C' correspond to V_1, V_2, V_3 and the related eigenvalues are τ_1, τ_2, τ_3. The direction of V_1 is the direction in where the moment of inertia is least, representing the direction of the best-fitting vector for the data. Kirschvink (1980) introduced the so-called "*maximum angular deviation*" (MAD) as a precision parameter for this analysis. The standard deviation of each eigenvector of the matrix C' is given by:

$$\xi_i = \sqrt{\tau_i}; \forall i = 1,2,3 \qquad [E.19]$$

and the MAD is defined as:

$$MAD = \tan^{-1}\left(\frac{\sqrt{\xi_2^2 + \xi_3^2}}{\xi_1}\right) \qquad [E.20]$$

B.4. Statistical analysis of RM vectors

In order to characterize the RM vector at certain geographical location or rock type, it becomes necessary to have a mean orientation for it at the site. An error, usually associated with the mean direction, is statistically calculated as the interval containing at least 95% of the data. The following statistical techniques help to determine the orientation of the mean vector and the associated error.

B.4.1. The Fisher Distribution

This distribution is the spherical analog of the widely known Normal distribution. It is based on the assumption that the data is "*symmetrically and randomly distributed*" about certain mean direction. The Fisher (1953) density function is given by:

$$F_{Fisher} = \frac{\kappa}{4\pi \sinh(\kappa)} e^{\kappa \cos(\rho)} \qquad [E.21]$$

Where ρ is the angle between the true direction and the unit vector, κ is a precision parameter (such that $k \to \infty$, dispersion goes to 0), and *sinh* is the hyperbolic sine function. Notice that in this treatment intensity or length of the RM vector does not play any role and vectors are supposed to have unit length (Fisher, 1953; Tauxe, 1998).

In order to obtain the mean direction from a set of RM vectors they need to be converted to Cartesian coordinates. Using [E.13] to [E.15], the length of the sum vector (R) is given by:

$$R = \sum_{j=1}^{3}\left(\sum_{i=1}^{N} x_{ji}\right)^2 \qquad [E.22]$$

Where N is the number of RM vectors involved in the analysis. Thus, the Cartesian coordinates of the mean direction are given by:

$$\overline{x_1} = \frac{1}{R}\left(\sum_{i=1}^{N} x_{1i}\right); \overline{x_2} = \frac{1}{R}\left(\sum_{i=1}^{N} x_{2i}\right); \overline{x_3} = \frac{1}{R}\left(\sum_{i=1}^{N} x_{3i}\right) \qquad [E.23]$$

This coordinates can be re-converted to declination and inclination components using:

$$D = \tan^{-1}\left(\frac{\overline{x_2}}{\overline{x_1}}\right); I = \sin^{-1}\left(\overline{x_3}\right) \qquad [E.24]$$

the statistical precision parameter can be estimate by:

$$\kappa \cong k = \frac{N-1}{N-R} \qquad [E.25]$$

and the related confidence interval, i.e. the error associated, is calculated by:

$$\alpha_{(1-p)} = \cos^{-1}\left(1 - \frac{N-R}{R}\left(\left(\frac{1}{p}\right)^{\frac{1}{N-1}} - 1\right)\right) \qquad [E.26]$$

Where *1-p* indicates the probability level of confidence. This is usually 95% (p=0.05) and it is equivalent a two estimated standard errors from the mean (e.g. Butler, 1992).

B.4.2. The Kent Distribution

The problem with the Fisher (1953) distribution arises when the data is not "*symmetrically distributed*" around the mean direction; like for example in arcuate distributions (e.g. MacDonald, 1980). In this kind of unit vector distributions, where the scatter is mainly in declination but inclination remains more or less constant, the Fisher (1953) mean has an inclination steeper than the true inclination (MacDonald, 1980). The assumption that the data is Fisher (1953) distributed is not always true, leading sometimes to erroneous and inaccurate interpretations.

The Bingham (1964) distribution is the more general case of "*bi-modal, non-symmetrical and randomly distributed*" data. However, this distribution is difficult to handle, especially for further paleomagnetic procedures such fold tests, randomness test, etc (Tauxe, 1998). Let consider a simple case of the Bingham (1964) distribution where the data is "*symmetrically and elliptically distributed*" about a mean direction. The Kent (1982) density function is given by:

$$F_{Kent} = \frac{1}{c(\kappa,\beta)} e^{\kappa(\cos(\alpha)+\beta\sin^2(\alpha)\cos(2\rho)} \qquad [E.27]$$

Where α is the angle between a given direction and the true mean direction (estimated by the principal eigenvector V_1 of the orientation matrix C' on [E.18]), ρ is the angle in the plane perpendicular to the true mean direction (with ρ=0 parallel to the eigenvector V_2 of the matrix C' in that plane), κ is a precision parameter similar to the Fisher (1953) κ, and $c(\alpha, \beta)$ is a complex function of κ and β (Fisher et al., 1987). Notice that when β=0 this distribution reduces to the Fisher (1953) distribution (Tauxe, 1998).

To obtain the orientation of the mean direction it is necessary to express the data with a new set of coordinates, given by:

$$x'_i = \Gamma^T x_i, \forall i = 1,2,3 \qquad [E.28]$$

Where x_i are the cartesian coordinates of the RM vector and x'_i are the new coordinates of the vector. $\Gamma=(\gamma_1, \gamma_2, \gamma_3)$ is a matrix containing the constrained eigenvectors of C' [E.18] such as γ_1 is parallel to the Fisher (1953) mean of the data whereas γ_2 and γ_3 diagonalize C' as much as possible subject to being constrained to γ_1 (Kent, 1982; Tauxe, 1998). Then, the orientation of the Kent (1982) mean direction can be calculated using the values of x'_i on equations [E.23].

Since the data is elliptically distributed around the mean direction, the confidence interval is an ellipse about the mean, with its major (ζ) and minor (θ) semi-axis calculated as:

$$\zeta_{(1-p)} = \sin^{-1}\left(\frac{R\sqrt{\tau_2}}{\sqrt{-2N\ln(p)}}\right) \qquad [E.29]$$

$$\theta_{(1-p)} = \sin^{-1}\left(\frac{R\sqrt{\tau_3}}{\sqrt{-2N\ln(p)}}\right) \qquad [E.30]$$

Where τ_2 and τ_3 are the eigenvalues of V_2 and V_3 eigenvectors of the matrix C' respectively, R is the resultant length [E.22], N is the number of data involved and *(1-p)* is the confidence level (Tauxe, 1998). Since the confidence interval is an ellipse with different radius in different directions, it is also necessary to define the orientation of the planes that contain these semi-axes. The orientation of such planes is given by:

$$D_\zeta = \tan^{-1}\left(\frac{v_{22}}{v_{12}}\right), I_\zeta = \sin^{-1}(v_{32}) \qquad [E.31]$$

$$D_\theta = \tan^{-1}\left(\frac{v_{23}}{v_{13}}\right), I_\theta = \sin^{-1}(v_{33}) \qquad [E.32]$$

Where D and I are the declination and inclination of the pole of the plane containing the confident interval angle, and v_{ij} is the component of the x_i coordinate of the V_j eigenvector (Tauxe, 1998).

B.5. Statistical rejection of paleomagnetic data

Calculated RM vectors as well as mean RM vectors are statistical approximations for a certain value, both having errors related. Thus, it is necessary to define a criterion for the rejection of non-representative RM vectors and for mean RM vectors. Rejection can be divided into specimen and site levels.

A paleomagnetic specimen is a single oriented sample obtained from one core at one locality (Fig. B.4). One representative RM vector is obtained from each specimen by the PCA method (e.g. Kirschvink, 1980) and it has, therefore, an associated MAD value. There is no convention about a reliable MAD value; however, vectors fitted from PCA analysis that yield MAD$\geqq$15 are often consider ill defined and of questionable significance (e.g. Butler, 1992).

Once reliable RM vectors were filter by means of their MAD values, the next procedure is to obtain the orientation of the mean RM vector, its related confidence interval and precision parameter using Kent (1982) statistics (in the best case is reduced to Fisher (1953) statistics).

For a site in order to be statistically reliable it must verify the following conditions:

- The number of specimens with MAD<15 at the site must be larger or equal than 10 ($N \geqq 10$),
- The precision parameter κ (Fisher or Kent) must be larger than 10 ($\kappa \geqq 10$),
- The confidence interval, calculated by Fisher (1953) statistics, must be smaller than 10^0 ($\alpha_{95} \leqq 10^0$).

B.6. Paleomagnetic Tests

Obtained RM vectors from several sites can be compared in order to determine the magnetic acquisition time with respect to a certain tectonic event. For this, orientation of related structures at the sampled site – such as bedding, compositional layers, dike intrusion, foliation, etc – are necessary in addition to the orientation of the mean RM vector and its confidence interval.

The two most commonly used paleomagnetic test are briefly discussed: (1) the reversal test and (2) the fold (or bedding-tilt) test. These tests are used to determine: (1) whether two mean RM vector with opposite polarities were acquired consecutively and (2) if RM vectors were acquired before, during or after a folding or tilting event that affected the rock mass, respectively.

B.6.1. The reversal test

This paleomagnetic test seeks to answer if two sets of RM vectors, with different polarities, are 180^0 apart. In the case that the two polarities were acquire continuously (and no major block rotations had occurred) the means of each can not be distinguish at the 95% confidence limit (Watson, 1956; Butler, 1992; Tauxe, 1998). In such positive case, the test is label RT+. In

contrast, if means are distinguishable at the 95% confidence level the test is label RT- (Watson, 1956; McFadden and McElhinny, 1990). The choice of the 95% confidence level is not arbitrary since it is possible (and quite common) that RM vectors are contaminated with secondary components which had shift each mean, putting them not longer 180^0 apart (e.g. Cox and Doell, 1960; McFadden and McElhinny, 1990).

As noticed by McFadden and McElhinny (1990) the classification of the reversal test into positive or negative is not fully convenient, and it should be classified accordingly to the amount of information used in the test. In the McFadden and McElhinny (1990) fold test the procedure is to first to "flip" one of the polarity sets to the polarity of the other. The way to include the amount of information is the angle μ_c, which is the angle between the mean directions of the two sets at which the null hypothesis of a common mean direction would be rejected with 95% confidence. Given the observed dispersion of the two samples (McFadden and McElhinny, 1990), the critical angle μ_c is given by:

$$\mu_c = \cos^{-1}\left(1-\frac{(N-R_1-R_2)(R_1+R_2)}{R_1R_2}\left(\left(\frac{1}{p}\right)^{\frac{1}{N-2}}-1\right)\right) \qquad \text{[E.33]}$$

Where N is the number of RM vectors in both samples ($N=N_1+N_2$), R_i ($i=1,2$) is the resultant vector length (using [E.22]) for each one of the sets, and *(1-p)* is the confidence level (McFadden and McElhinny, 1990). If the angle μ_0 (real angle measured between the two means) exceeds μ_c then the reversal test is classified as RT-. If the angle μ_0 does not exceed the angle μ_c then the test is RT+, and further sub-classified according to the value of μ_c by using: (1) RTa if $\mu_c \leqq 5^0$, (2) RTb if $5^0 < \mu_c \leqq 10^0$, (3) RTc if $10^0 < \mu_c \leqq 20^0$, and (4) RTinter if $\mu_c > 20^0$ (McFadden and McElhinny, 1990).

B.6.2. The Fold Test

This paleomagnetic test seeks at which degree of folding (or tilting) the mean RM vectors at different sites are more tightly clustered by progressively restoring to the horizontal the orientation of the bedding and its related mean RM vectors. Restoration to the horizontal is carried by rotation of the data about a horizontal axis parallel to the strike of the related structure).

McElhinny (1964) proposed that the concentration of the data, using the Fisher (1953) precision parameter, could be calculated before and after restoring the bedding to the horizontal and that the ratio of the two values should be compared with those listed in statistical "F" tables. However, they are several problems with the McElhinny (1964) fold test; like that the geomagnetic field is not perfectly dipolar or that RM vectors were acquire sometime in between the original horizontal bedding orientation and the 100% folding (Tauxe and Watson, 1994; Tauxe, 1998).

To solve this problem Tauxe and Watson (1994) proposed an alternative approach using the orientation matrix (equation [E.18]). Here, polarity of RM vectors does not play any role and the tightness of grouping is reflected in the relative magnitudes of the principal eigenvalues (τ_i) of the matrix C'. As the data become more tightly grouped by the procedure, the variance along the principal axis (τ_1) grows and those along the other axes shrink (Tauxe and Watson, 1994; Tauxe, 1998). The optimal unfolding percentage is revealed by examination if the behavior of τ_1 during the procedure (Fig. B.5).

B.7. Inclined rotational axes

The fold test, yet powerful and widely used, relies on a questionable assumption: that tilting of the bedding strata (or mineral layering, foliation, etc) is a product of a rotation about a

horizontal axis parallel to the strike of the bedding. A more general case is to consider that rotation of the related structure occurred about an inclined rotational axis (e.g. Ramsay, 1961, 1967; MacDonald, 1980; Chan, 1988; Weinberger et al., 1995) and not necessarily parallel to any structure. Rotation about inclined axis occurs in complex fold structures, complex faulted structures, torsional motions on dipping fault planes, emplacement of coherent sedimentary slump blocks, etc (MacDonald, 1980).

Weinberger et al. (1995) proposed a procedure base on rotational matrices (e.g. LePichon et al., 1973; Cox and Hart, 1996) in order to find the orientation of the rotational axis which restore the bedding strata to the horizontal and the mean RM vector to the expected geomagnetic direction. The procedure is rather simple but relies on another questionable assumption: that bedding strata was "*originally*" horizontal. Examples of non-horizontal "*original*" orientations are: (1) sedimentary strata deposited in the proximal or medium portions of a slope, (2) orientation of poles of dikes in a spreading ridge, (3) mineral layering in plutonic bodies, etc.

To solve this, the "*modified rotational axis method*" is introduced here as a modification of the Weinberger et al. (1995) method. This modified method seeks the restoration of the orientation of the mean RM vector to the orientation of the expected geomagnetic axial dipole at the time of RM acquisition. Using the calculated rotational axis the related structure (bedding strata, mineral layering, etc) is restored to its "*original*" orientation. Although the inclined rotational axis can restore the RM vector to the expected original orientation, it does not provide with information about the finite rotations experienced by the rock mass but with the equivalent net tectonic rotation (e.g. LePichon, 1973; MacDonald, 1980; Weinberger et al., 1995).

B.7.1. The Geomagnetic Axial Dipole (GAD) orientation

In order to have a reference orientation to which mean RM vectors are compared, it is necessary to define the orientation of the magnetic north or geomagnetic field. The geomagnetic

axial dipole (GAD) field of the earth is generated by convection currents in the outer core of the planet, which produce a magnetic field similar to a gigantic bar magnet located in the center of it and aligned with the spin axis (e.g. Tauxe, 1998). The magnetic field depends on the radius of the Earth, the co-latitude and the longitude of the study area. The geographical components (north, east and down) of the orientation of the GAD are:

$$B_N = -\frac{1}{r}\frac{\partial P(r,\varsigma,\omega)}{\partial \varsigma}; B_E = -\frac{1}{r\sin\varsigma}\frac{\partial P(r,\varsigma,\omega)}{\partial \omega}; B_D = -\frac{\partial P(r,\varsigma,\omega)}{\partial r} \qquad \text{[E.34]}$$

Where $P(r, \varsigma, \omega)$ is a complicated formula which depends on the radius of the earth (r), the co-latitude (ς) and the longitude (ω) of the study area (see Tauxe, 1998, equation 1.8). The function $P(r, \varsigma, \omega)$ denotes the intensity of the GAD at certain location on the surface of the Earth. There are several empirical and theoretical methods to calculate the orientation and magnitude of the GAD. Some of these methods have been implemented on computer routines available on the Internet at the National Geophysical Data Center web page (*http://www.ngdc.noaa.gov*).

B.7.2. The rotational matrix and rotational procedure

The rotational matrix is a mathematical procedure which "*rotates*" the orientation of certain vector, with Cartesian coordinates (x_1, x_2, x_3), about a certain rotational axis defined by the vector $U=(U_1, U_2, U_3)$ and the rotational amount δ. As a result, the Cartesian coordinates of the rotated vector are (x''_1, x''_2, x''_3). The elements of the symmetric rotational matrix are defined by (e.g. LePichon, 1973; Cox and Hart, 1986):

$$S = \begin{bmatrix} s_{11} & s_{12} & s_{13} \\ s_{12} & s_{22} & s_{23} \\ s_{13} & s_{23} & s_{33} \end{bmatrix} \qquad \text{[E.35]}$$

with:

$$
\begin{aligned}
s_{11} &= U_1^2(1-\cos\delta)+\cos\delta;\\
s_{12} &= U_1U_2(1-\cos\delta)-U_3\cos\delta;\\
s_{13} &= U_1U_3(1-\cos\delta)+U_2\cos\delta;\\
s_{21} &= U_2U_1(1-\cos\delta)+U_3\cos\delta;\\
s_{22} &= U_2^2(1-\cos\delta)+\cos\delta;\\
s_{23} &= U_2U_3(1-\cos\delta)-U_1\cos\delta;\\
s_{31} &= U_3U_1(1-\cos\delta)-U_2\cos\delta;\\
s_{32} &= U_3U_2(1-\cos\delta)+U_3\cos\delta;\\
s_{33} &= U_3^2(1-\cos\delta)+\cos\delta
\end{aligned}
\qquad [E.36]
$$

In order to obtain the orientation of the inclined rotational axis which restores the orientation of the mean RM (vector with Cartesian coordinates (x_1, x_2, x_3), equations [E.13] to [E.15]), to the orientation of the expected GAD, two consecutive rotations must be perform. First, the orientation of the mean RM vector is rotated about a horizontal axis perpendicular to its declination (Fig. B.6a), such as the inclination of the mean RM vector (I_{rmv}) after the rotation is the same as that of the expected GAD (I_{EGAD}). Thus, inclination and declination of the horizontal rotational axis are given by:

$$I^h_{axis} = 0, D^h_{axis} = D_{rmv} - 90^0 \qquad [E.37]$$

Where the superscript h means "*horizontal*" and I and D refer to inclination and declination respectively. The Cartesian coordinates of the horizontal rotational axis, $U^h=(U^h_1, U^h_2, U^h_3)$, can then be obtained using [E.13] to [E.15]. Notice that $U^h_3=0$.

The amount of rotation through the horizontal axis is defined by:

$$\delta^h = I_{rmv} - I_{GAD} \qquad [E.38]$$

Using the horizontal axis $U^h=(U^h_1, U^h_2, U^h_3)$ and δ^h in the rotational matrix S (equations [E.35] and [E.36]), the horizontal rotational matrix S^h is fully defined. Then, the corrected orientation of the mean RM vector (x'_1, x'_2, x'_3) can be calculated by using the matrix notation:

$$
\begin{bmatrix} s^h_{11} & s^h_{12} & s^h_{13} \\ s^h_{12} & s^h_{22} & s^h_{21} \\ s^h_{13} & s^h_{21} & s^h_{33} \end{bmatrix}
\begin{pmatrix} x_1 \\ x_2 \\ x_3 \end{pmatrix} =
\begin{pmatrix} x'_1 \\ x'_2 \\ x'_3 \end{pmatrix}
\qquad [E.39]
$$

Where $x'=(x'_1, x'_2, x'_3)$ is the orientation of the mean RM vector after the rotation about the

horizontal rotational axis. Inclination (I'_{rmv}) and declination (D'_{rmv}) of the rotated mean RM vector can be obtained using equation [E.24]. After the new orientation of the mean RM vector has been obtained, a second rotation about a vertical rotational axis is performed (Fig. B.6b). Analog to the previous rotation, this second rotation starts from the corrected orientation of the mean RM vector (x'). The orientation of the vertical rotational axis is defined by:

$$I^v_{axis} = 90^0, D^v_{axis} = 0 \qquad [E.40]$$

Where the superscript "v" means "*vertical*". The Cartesian coordinates of the vertical rotational axis $U^v=(U^v_1, U^v_2, U^v_3)$ can be obtained using equations [E.13] to [E.15]. The rotational amount δ^v is defined so the declination of the rotated mean RM vector (D'_{rmv}) becomes equal to the declination of the expected GAD (D_{EGAD}):

$$\delta^v = D_{EGAD} - D'_{rmv} \qquad [E.41]$$

Notice that $D'_{rmv}=D_{rmv}$. In matrix notation, the vertical rotational matrix is given by S^v, where its elements had been calculated using the matrix S with $U^v=(U^v_1, U^v_2, U^v_3)$ and δ^v. The final orientation for the mean RM vector is given by:

$$\begin{bmatrix} s^v_{11} & s^v_{12} & s^v_{13} \\ s^v_{12} & s^v_{22} & s^v_{21} \\ s^v_{13} & s^v_{21} & s^v_{33} \end{bmatrix} \begin{pmatrix} x'_1 \\ x'_2 \\ x'_3 \end{pmatrix} = \begin{pmatrix} x''_1 \\ x''_2 \\ x''_3 \end{pmatrix} \qquad [E.42]$$

Where $x''=(x''_1, x''_2, x''_3)$ is the final orientation of the mean RM vector and it is equal to the orientation of the expected GAD.

In order to obtain the equivalent inclined rotational axis, which restores the mean RM vector to the orientation of the EGAD (Fig. B.6c), the matrix S^t is defined as the matrix product between S^h and S^v, by:

$$S^v x' = x'' \rightarrow S^v(S^h x) = x'' \rightarrow (S^v S^h)x = x'' \rightarrow S^t x = x'' \qquad [E.43]$$

Finally, the orientation of the related structure is corrected using this inclined rotational axis. The orientation of the related structure is defined by the inclination (I_{pole}) and declination (D_{pole}) of its pole (vector normal to the plane). The Cartesian coordinates of the pole $b=(b_1, b_2, b_3)$ are

obtained from its inclination (I_{pole}) and declination (D_{pole}) using equations [E.13] to [E.15]. Applying the obtained inclined rotational matrix S^t:

$$S^t b = b'' \qquad \text{[E.44]}$$

Thus, the final corrected orientation of the bedding strata (b'') is obtained. The inclination and declination of the rotated bedding strata can be obtain, as usual, using equation [E.24].

B.7.3. Orientation of the inclined rotational axis and its rotational amount

For the previous two consecutive rotations the orientation of the rotational axes and the amounts of rotation are known but for the combined inclined rotational axis these parameters are unknown. The Cartesian coordinates and rotational amount of the inclined rotational axis are the Eurelian elements of the matrix S^t, given by (e.g. LePichon, 1973; Weinberger et al., 1995):

$$\delta^t = \cos^{-1}\left(\frac{s_{11}^t + s_{22}^t + s_{33}^t - 1}{2}\right) \qquad \text{[E.45]}$$

$$U^t = (U_1^t, U_2^t, U_3^t) = \left(\frac{s_{32}^t - s_{23}^t}{2\sin(\delta^t)}, \frac{s_{13}^t - s_{31}^t}{2\sin(\delta^t)}, \frac{s_{21}^t - s_{12}^t}{2\sin(\delta^t)}\right) \qquad \text{[E.46]}$$

Notice that S^t is not symmetric although is the product of two symmetric matrices (S^v and S^h).

Appendix C: Blocking and Curie temperatures

C.1. Classification and characteristics of magnetic minerals

Since magnetic properties arise from the motion of electrically charged particles, any electron has a magnetization associated with its axial spin and with its orbital motion around the nucleus (Tarling and Hrouda, 1993). Then, any material or mineral has magnetic properties above 0^0K. When an external magnetic field is applied to an aggregate of minerals (rock), each one of the minerals behaves in different ways depending on its chemical composition, especially in the amount of metallic elements it contains.

Minerals can be classified in basis of their behavior under a certain externally induced magnetic field. In general, minerals are subdivided into the ones on which: (1) magnetization is lost as soon as the applied magnetic field is removed and (2) those which retain certain amount of magnetization after the external magnetic field is removed.

Diamagnetic and paramagnetic minerals correspond to those minerals in which the induced magnetization aligns (parallel or anti-parallel) with the applied field (H). If a mineral or substance has its electron shells complete, the electrons spins process and produce a magnetization in the opposite direction (anti-parallel, $-K$) to the external magnetic field in response. Minerals or substances which present this behavior are called "*diamagnetic*" (Fig. C.1). In contrast, all minerals, or substances, that have incomplete electron shells will produce a magnetization in the same direction (parallel, $+K$) to that of the external magnetic field (H) (Tarling and Hrouda, 1993; Butler, 1998) (Fig. C.1); these minerals are called paramagnetic.

Some few minerals or substances that have much stronger positive susceptibilities than paramagnetic minerals and also carry a strong RM are called, in general, ferromagnetic (*sensu lato*). These elements have a spontaneous magnetization, which is when electron spins are aligned even in absence of any external applied magnetic field.

If the electron spins of adjacent cations are directly coupled, exchange forcers act so that magnetic vectors all lie in the same direction (Fig. C.1); these types of minerals are called ferromagnetic (*sensu estricto*). However, if the electron spins of the cations are share via the electron shell of an intermediate anion, as in complex metallic compounds, the direction of the electron spins of the cations are reversed with respect to the anions, creating two opposite magnetized (but mixed) lattices in the mineral. The resultant magnetization depends on the difference of magnetization between the two lattices. Minerals or substances in which the two lattices are equally magnetized are called "*anti-ferromagnetic*" (Fig. C.1). In contrast, minerals in which there is a difference in the magnetization of the two lattices (providing with a net magnetization) are called "*ferrimagnetic*".

Superpara-magnetic minerals or substances are those in which in absence of an external magnetic field display magnetic moments which become rapidly randomized, but when the external field is applied their magnetic moments become rapidly aligned with it.

C.2. Blocking and Curie Temperatures

Magnetic remanecence is caused by strong interactions between neighboring spins in any ferromagnetic (*sensu lato*) material. The so-called exchange energy is minimized when spins are aligned parallel or antiparallel depending on the details of the crystal structure (Tauxe, 1998), but scatter in spin directions increases as temperature increases. Above certain temperature, depending on the composition of the mineral, cooperative spin behavior disappears and the material becomes paramagnetic (Butler, 1992; Tarling and Hrouda, 1993; Tauxe, 1998), i.e. alignment of the spins disappears as soon as the applied field is removed. The temperature where the mineral changes its behavior from ferromagnetic (*sensu lato*) to paramagnetic is known as the "blocking temperature". This is achieved when the mineral is no longer able to retain a stable RM. Similarly, the temperature at which a ferromagnetic (*sensu lato*) mineral can not retain any

induced magnetization is called "*Curie Temperature*". In practice, these two temperatures have nearly similar values.

Been a property of ferromagnetic (*sensu lato*) minerals, this temperature can be derived using the Curie's law of paramagnetism and the Weiss theory (Tauxe, 1998). Then, an expression which can be solved graphically or numerically to obtain it for a particular mineral is:

$$T_c = \frac{N m_b^2 \beta}{v k} \qquad \text{[E.47]}$$

Where T_c is the calculated blocking (or Curie) temperature, N is the total number of spin moments, m_b is the moment of unpaired spins, β is a constant of proportionality, v is the volume and k is a constant depending on the thermal energy of the spins (Tauxe, 1998).

In practice, the measure of this temperature is more straightforward and simply than measuring spins moments. From thermomagnetic experiments, Curie temperature can be easily determined from a visual inspection of the RM susceptibility during temperature variation (Fig. B.2a). Many methods have been proposed to obtain an accurate temperature value.

Magnetite and hematite crystals are maybe the most common opaque mineral phases in rocks, accounting for *ca.* 5% of the total amount (e.g. Tarling and Hrouda, 1993). These two minerals have ferromagnetic (*sensu lato*) properties and are the main carriers of RM. The Curie temperature for pure Magnetite is *ca.* 580^0C and for pure hematite is *ca.* 680^0C (e.g. Dunlop and Özdemir, 1997)

C.3. The "differential method" (Tauxe, 1998)

One of the first proposed methods to determine the Curie (or blocking) temperature was the "*intersecting tangents method*" (Grommé et al., 1969). The intersection of two tangents of the thermomagnetic curve near the temperature where the RM susceptibility, or intensity, decays to 0 indicates the searched value (Fig. B.2a). As pointed by Tauxe (1998) this method is easy to do it

by hand but is rather subjective and difficult to automate.

To solve this subjectivity, Tauxe (1998) proposed the "*differential method*", which seeks the maximum curvature in the thermomagnetic curve. The maximum peak in *F"(T)*, which corresponds to the second derivative of a function which denotes the thermomagnetic curve (*F(T)*, occurs at the maximum curvature of *F(T)* and represents the searched temperature value (Fig. B.2b)

The main disadvantage of the method is that noise is highly amplified during the differential procedure. To overcome this problem a filter can be applied over the data prior to the analysis or the method can be just applied to a certain interval of the thermomagnetic curve where the value of the blocking temperature is most probably located (Tauxe, 1998).

C.4. Acquisition and washout of the magnetic remanecence

Any ferromagnetic (*sensu lato*) mineral or substance can retain a RM and has magnetic susceptibility below its blocking temperature. Spins of ferromagnetic (*sensu lato*) minerals become align in the presence of a external (applied) magnetic field, but when this magnetic field is removed the alignment of the spins remains. Minerals are constantly under the magnetic field of the Earth, which is a very low external magnetic field. Spins of ferromagnetic (*sensu lato*) minerals become align with this magnetic field retaining "*in memory*" its orientation. As the mineral cools down below the blocking temperature, more spins become align with the applied (Earth) field. As a result, the RM is progressively recorded in a vectorial form (Fig. B.1).

If the tectonic block, containing the magnetic minerals, had no experience any change in its orientation, the recorded RM will be a single vector indicating the direction of the external magnetic (Earth) field. However, if the block experiences changes in its orientation (tectonic rotations) the recorded RM orientation will also rotate with it. During and after such rotation it is possible that the mineral continues recording the orientation of the magnetic field; in such a case,

the recorded field will be the vectorial sum of the present magnetic field and the previous magnetic field recorded (Fig. B.1). The magnetic field of the Earth changes trough time, both in polarity and in orientation near the geographic north (or south); phenomenon know as "*secular variation*" (e.g. Butler, 1992). As a result, ferromagnetic (*sensu lato*) minerals also record these variations.

RM vectors can also be erased (washout) from ferromagnetic (*sensu lato*) minerals. Suppose that we have a ferromagnetic (*sensu lato*) mineral with some RM recorded on it. If the mineral experiences a temperature increase (caused by an increase in the geothermal gradient, for example) over its blocking temperature, magnetic spins in the mineral become scatter and any previous alignment of them is lost. If the mineral experiences a further cooling below its blocking temperature, the recorded magnetic field is the one acquired after the temperature dropped below the blocking temperature.

Appendix D: Anisotropy of Magnetic Susceptibility (AMS)

The strength of the induced magnetization can be directly related to the strength of the applied field by a constant (K) by:

$$M \propto H \Rightarrow M = KH = K\frac{B}{\mu_0} \qquad [E.48]$$

Where M is the magnetic dipole moment per unit volume in *A/m*, H is the applied magnetic field strength in *A/m*, B is the magnetic field measured in *Tesla*, μ_0 is the permeability of the free space ($4\pi x10^{-7}$ *Henry/m*) and K is a non-dimensional constant called "*susceptibility*" (Tarling and Hrouda, 1993).

D.1. General characteristics of AMS fabrics

D.1.1. Bulk intensity and the AMS fabric

If an external magnetic field (H) is applied in several different directions over some mineral, then each direction has its own susceptibility constant (K_d). Since directions are in a three dimensional space, it is possible to define a tensor matrix containing information of the different susceptibilities on each one of the applied directions. This tensor matrix is called "*Anisotropy of Magnetic Susceptibility*" (AMS) and its eigenvectors correspond to the maximum (K_{max}), intermediate (K_{int}) and minimum (K_{min}) magnetic susceptibility axes, called "*principal susceptibility axes*", of the mineral.

The orientation of the AMS axes is controlled mainly by the preferred orientation of the crystallographic axes of the mineral, which also controls the shape of it (Rochette et al., 1992). Thus, mineral size also plays an important role in the orientation of the AMS axes. Large size minerals often show internal magnetic domains developed on each one of the mineral faces, with

different magnetization directions and orientation of their AMS axes.

The bulk susceptibility of a mineral aggregate (rock) is the sum of all the individual susceptibilities from each one of the minerals composing the aggregate. Since the orientation of the AMS axes depends on the orientation, shape and size of each one of the minerals in the aggregate, orientation of AMS axes provides an image of the "magnetic fabric" of the aggregate, rock or soft sediment (Hrouda, 1992; Tarling and Hrouda, 1993). In most cases, and depending of the minerals involved (see further), the magnetic fabric coincides with the petrographic fabric of the rock or soft sediment. Thus, the orientation of the AMS axes (hereafter called AMS fabric) is a one to one image of the petrographic fabric (Ledbetter and Ellwood, 1980; Rochette et al., 1992; Tarling and Hrouda, 1993; Schieber and Ellwood, 1993; Liu et al., 2001).

D.1.2. Shape of the AMS fabric

Using the orientation of the principal susceptibility axes it is possible to construct an ellipsoid which carries information about the magnitude and orientation of the AMS axes. However, it is more convenient to define some parameters in order to characterize the shape of this ellipsoid (and the shape of the AMS fabric). Several parameters had been defined in order to characterize the shape of the AMS ellipsoid, but the following four are the most representatives:

- Lineation (L) (Balsey and Buddington, 1960) and Foliation (F) (Stacey et al., 1960): These two parameters account for the degree of anisotropy of the AMS ellipsoid in a similar way to the Flinn (1962) diagram used to classify deformed objects (Fig. D.1a). In essence, this is a polar plot in which radial trajectories indicates an increasing in anisotropy (Tauxe et al, 1998). Notice that points over the line F=L indicates isotropic shapes but points located over (down) this line indicates cigar-like or prolate (dish-like or oblate) shapes. L and F parameters are defined as:

$$L = \frac{\tau_1}{\tau_2} \qquad [E.49]$$

$$F = \frac{\tau_2}{\tau_3} \qquad [E.50]$$

Where τ_i (i=1, 2, 3) is the i-th eigenvalue of the AMS tensor matrix

- Shape parameter (T) and the Corrected Anisotropy degree (P') (Jelinek, 1981): Different from the previous plot, the T vs. P' diagram is Cartesian in nature. Anisotropy increases along the horizontal axis while shape does in the vertical axis (Fig. D.1b). Notice that points plotted over the line T=0 have isotropic fabrics while points located in the region T>0 (T<0) have oblate (prolate) fabrics. T and P' are defined as:

$$T = \frac{(2\eta_2 - \eta_1 - \eta_3)}{(\eta_1 - \eta_3)} \qquad [E.51]$$

$$P' = e^{\sqrt{2(\eta_1-\bar{\eta})^2+(\eta_2-\bar{\eta})^2+(\eta_3-\bar{\eta})^2}} \qquad [E.52]$$

$$\text{with,} \quad \bar{\eta} = \frac{\eta_1 + \eta_2 + \eta_3}{3} \qquad [E.53]$$

Where η_i is the natural logarithm for the i-th eigenvalue (i=1, 2, 3) and e denotes the exponential function.

With these two diagrams it is possible to fully characterize the shape of the AMS fabric. These parameters, plus the orientation of the different principal susceptibility axes, characterize completely the AMS fabric shape (Rochette et al., 1992).

D.3. AMS fabric from sediments

A case of special interest is the AMS fabric of sedimentary rocks or soft sediments. These fabrics had been widely used to determine paleocurrent directions of flows as well as characteristics of the depositional surface (King, 1955; Granar, 1958; Ellwood and Ledbetter, 1977; Ledbetter and Ellwood, 1980; Ellwood, 1980; Schieber and Ellwood, 1993; Piper et al., 1996; Liu et al., 2001).

Under an undisrupted sedimentary environment, i.e. in absence of currents and in horizontal and flat depositional surface, magnetic minerals are deposited with their larger surfaces parallel to the depositional surface. Thus, the related AMS fabric has randomly oriented K_{max} and K_{int} axes in the horizontal plane (the depositional surface) while K_{min} axes are vertical (Fig. D.2a).

The direction and velocity of the depositional current is perhaps the most influent parameter which can disrupt the AMS fabric. Direction of the depositional current tends to imbricate the deposited minerals in the direction of the flow, tilting their shorter axis in that direction. The related AMS fabric takes the same orientation of the deposited minerals, having K_{min} axis tilted in the direction of the current (Fig. D.2b). The orientation of the two other axes varies depending if the current has a high (> 1 *cm/s*) or a medium to low (< 1 *cm/s*) velocity (King, 1955; Granar, 1958).

High velocity currents produce a roll of the magnetic minerals due to traction with the depositional surface (consider horizontal) and minerals become more stable with their long axes perpendicular to the current. The related AMS fabric has K_{min} and K_{int} axes randomly oriented in the direction of the current while K_{max} axis is perpendicular to it (Fig. D.2c). Usually, K_{min} axis lays no more than 20^0 away from the vertical, unless the velocity of the current is very strong, and more or less chaotic, like in the proximal part of a turbiditic flow (Granar, 1958; Tarling and Hrouda, 1993).

Medium to low velocity currents align the longest axis of the magnetic minerals parallel to the current. The related AMS fabric has K_{min} axis tilted from the vertical in the direction of the current, K_{max} axis is located in the direction of the current and K_{int} axis is perpendicular to it (Fig. D.2d). Additionally, the current produces an angle, hereafter called alpha (α), of less than 10^0 between the depositional surface and the AMS foliation plane (the best-fitting plane between K_{max} and K_{int} axes) (King, 1955).

The inclination of the depositional surface also produces a roll of the magnetic minerals down the slope due to gravitational forces (Tarling and Hrouda, 1993). Magnetic minerals become

more stable with their longest axes perpendicular to the slope or, which is the same, parallel to the strike of the depositional surface (King, 1955; Granar, 1958; Tarling and Hrouda, 1993). As in normal deposited sediment, minerals deposited in an inclined slope have randomly distributed their long and intermediate axis in the depositional surface plane (Tarling and Hrouda, 1993). As a consequence of the inclinational of the depositional surface, the long axes of the magnetic minerals are parallel to the strike of the surface. The related AMS fabric has K_{min} axes near the vertical and K_{max} and K_{int} axes distributed near the depositional surface plane. However, K_{max} axis is usually near the strike of the depositional surface (Fig. D.2e).

Most minerals have a one to one correspondence between crystallographic and principal susceptibility axes, but others have an inverse one. For example, tourmaline, cordierite and goethite display "*inverse*" AMS fabrics (i.e. crystallographic axes are in inverse relation with the principal susceptibility axes); while hematite and pyrrothite have "*normal*" ones (e.g. Rochette et al. 1992). Magnetite (Fe3O4), which is often the most common mineral which contributes to the AMS fabric, yields different AMS fabric depending on the shape and size of the individual grains (Rochette et al., 1992). Multi-domain (MD) magnetite crystals are large enough to contain several magnetic domains while pseudosingle-domain (PSD) and single-domain (SD) crystals are small enough to contain only one magnetic domain. MD and PSD magnetite crystals display "*normal*" AMS fabrics while SD displays "*inverse*" AMS fabric (Rochette et al., 1992).

Appendix E: Laboratory Technical Specifications

E.1. KappaBridge KLY-3S

E.1.1. General Overview

The KLY-3S Spinner Kappabridge is the most sensitive commercially available laboratory instruments for measuring anisotropy of magnetic susceptibility (AMS) as well as bulk susceptibility in weak variable magnetic fields. It consists of the pick-up unit and control unit connected with PC computer via RS-232C.

In principle the instrument represents a super-precise fully automatic inductivity bridge. It is equipped with automatic zeroing system (in both real and imaginary components) and automatic compensation of the thermal drift of the bridge unbalance as well as automatic switching of appropriate measuring range. The measuring coil is designed as 6th-order compensated solenoid with outstanding field homogeneity.

The digital part of the instrument is based on microelectronic components, with the microprocessor controlling all the Kappabridge functions. (Extract from AGICO manuals)

E.1.2. Technical specifications

- Operating frequency: 875 *Hz*
- Field intensity: 300 *A/m*
- Field homogeneity: 0.2 %
- Measuring range automatic: up to 0.2 [SI]
- Sensitivity (typical): (1) bulk: $3x10^{-8}$ [SI], (2) anisotropy: $2x10^{-8}$ [SI]

- Accuracy within one range: ± 0.1 %
- Accuracy f the absolute calibration: ± 0.3 %
- Pick-up coil inner diameter: 43 *mm*
- Power: 100, 120, 230 *V*; 50/60 *Hz*; 40*VA*
- Operating temperature range: +15 to $+35^0$ *C*
- Relative humidity: up to 80 %

E.2. KappaBridge variation temperature measure device cs-3

E.2.1. General Overview

The CS-3 Furnace Apparatus is designed for thermal treatment of a specimen and measurement of the temperature dependence of low-field susceptibility in weakly magnetic minerals, rocks and synthetic materials, in co-operation with the KLY- 3S Kappabridge.

The apparatus consists of a non-magnetic furnace with a special platinum temperature sensor, a temperature control unit and a cooling water reservoir. The specimen (up to $0.25cm^3$ in volume) is placed in a silica glass vessel, heated by a platinum wire, and the temperature is measured by the temperature sensor.

To perform the susceptibility measurement at a given temperature, the equipment automatically moves the furnace into and out of the pick-up coil of the KLY-3S Spinner Kappabridge. The quasi-continuous process of measurement is fully automated, being controlled by the Temperature Control Unit and PC computer.

The CS-3 apparatus includes a supplement which may be used to measure temperature variations of susceptibility in argon atmosphere, in order to prevent oxidation of measured specimen.

The temperature variation of susceptibility of the specimen is displayed continuously on the

monitor. The results are also written into a data file (in ASCII format) which can be (off line) interpreted and evaluated by included special software package CUREVAL.

The standard measured curve of temperature variation of susceptibility consists of about 500 to 700 pairs of susceptibility and temperature determinations. If a weakly magnetic specimen has been measured, the curve can be resolved into paramagnetic hyperbola and complex ferromagnetic curve. (Extract from AGICO manuals)

E.2.2. Technical specifications

- Nominal specimen volume: 0.25 cm3 (fragments or powder)
- Inner diameter of measuring vessel: 0.5 cm
- High temperature measurement: up to 700^0C
- Accuracy of temperature determination: $\pm 2^0$C
- Sensitivity to susceptibility changes: 1x10-7 (SI)
- Dimensions, Mass:
  - Temperature control unit: 26x16x25cm, 9 kg
  - Furnace with temperature sensor: 1 kg
  - Cooling water reservoir 50 l: 71x36x36 cm, 4 kg (empty

E.3. Thermal demagnetizer oven MMTD-18

E.3.1. General Overview

The MMTD-18 demagnetizer oven is designed to heat standard size paleomagnetic samples in temperatures steps reaching a maximum temperature peak. Temperature steps as well as maximum temperature peak can be set up by the user.

The MMTD-18 oven can hold and heat up to 18 standard size paleomagnetic samples.

Usually, samples are demagnetized in user-defined steps of *ca.* 50^0C up to a maximum peak temperature of 700^0C. (Extract from Magnetic Measurements Inc. manual).

E.3.2. Technical specifications

- Maximum temperature: 700^0C,
- Integrated D.C. coil for acquisition experiments of thermoremanent magnetization (TRM),
- Single chamber for heating and cooling,
- Programmable for heating and cooling sequences, 1 sample boat for 18 samples.

E.4. Alternating field demagnetizer, SQUID model 581

E.4.1. General Overview

The Model 581 system consists of the following components:

1. Model 581H SQUID Processor Electronics
2. Model 581S Control/Display Console
3. Model 581P Cryogenic Probe
4. Model 581SQ DC SQUID Sensor

The SQUID sensor is mounted in a protective fiberglass enclosure which is in turn mounted to a nonmagnetic printed circuit (PC) board. A step up transformer and miniature Lemo connector are also mounted on the SQUID PC board. The connector enables the SQUID package to be plugged into a matching connector on the bottom of the model 581P Cryogenic Probe.

The Model 581H SQUID Processor Electronics consists of a miniature (17cm x 7cm x

3.5cm) shielded enclosure containing all of the SQUID closed loop circuitry. This unit can be used as a stand alone unit if power (±15 VDC) is provided or it can be connected to the Model 581S Control/Display Console. When operating the 581H in a stand alone mode, miniature 10 turn potentiometers enable adjustment of the SQUID parameters listed below:

1. SQUID bias current
2. SQUID offset
3. modulation amplitude
4. phase
5. calibration
6. AC gain

In addition, range (1x, 10x, 100x, and 1000x), reset, fast slew, and external or internal feedback modes can all be selected by switches in the Model 581H.

The Model 581S Control/Display Console contains the system power supplies. It also contains two displays; a 4½ digit digital display and a fast 20 element LED bargraph display.

The 4½ digital display can be user selected to show either the SQUID output or the SQUID count output. The bargraph can be configured to show the SQUID output or the modulation amplitude. The latter option is used in the setup mode to enable adjustment of SQUID electronic parameters without using an oscilloscope.

The 581H/581S electronics system is very immune to radio frequency interference (RFI) and power line pickup because all of the SQUID closed loop electronics are located in a highly shielded and filtered enclosure near the SQUID.

The Model 581P Cryogenic Probe provides a convenient method of immersing the SQUID sensor in a cryogenic environment. The probe consists of a flexible multiconductor cable connecting the SQUID sensor with the room temperature electronics. The SQUID sensor is plugged into a miniature 10 pin connector, mounted at the bottom of the flexible cable. A niobium shield also mounts to the probe bottom and provides a shielded environment for the

SQUID sensor. (Extract from Applied Physics manuals).

E.4.2. Technical specifications

- Flux Noise level 5x10-6 Flux unit RMS/Hz
- Energy noise level 6x10-31 joules RMS/Hz
- 1/f Noise corner frequency <0.5 Hz
- Input coupling inductance 1.9 H
- Size 12 mm dia x 56 mm long
- SQUID transformer turns ratio 8:1
- Input coil current sensitivity 0.2A/Flux unit
- Modulation coil sensitivity 1.5A/Flux unit

1. Model 581P Cryogenic Probe
   - Flexible, shielded 0.125" dia Integral RFI filters on all leads
   - Length 122cm
   - Connector (to 581 H) Winchester 9 pin
2. Model 581H SQUID Processor Electronics
   - Center frequency 200 KHz
   - Input coupling transformer ratio 3:1
   - Voltage noise <0.6x10-9 V RMS/Hz
   - Current noise <10-13 A RMS/Hz
   - Internal controls Range, reset, fast slew, modulation type
   - Internal adjustments (10 + potentiometers) AC amp, gain, calibration, phase
   - Size 15cm x 7cm x 3.5cm
   - Power 15VDC @ 150 ma
3. Model 581S Control/Display Console

- ✧ Displays and output
  - 4 digit display of SQUID analog output
  - 4 digit display of SQUID flux count
  - Analog output 10 V for full scale
- ✧ Bargraph analog output ranges
  - 1x 1Flux unit full scale
  - 10x 10Flux unit full scale
  - 100x 100Flux unit full scale
  - 1000x 1000Flux unit full scale

4. Filters (12 db/octave rolloff with selectable corner frequency at 1, 10, 100 Hz). The wideband output is unfiltered.
5. Power 110-130 VAC @ 1A or 220-260 VAC @ 0.5A; 50 or 60 Hz
6. Size 37cm L x 21cm W x 10cm H
7. Weight 11 lbs.